

Nanoparticles for the selective delivery of photosensitisers for photodynamic cancer therapy

Paula García Calavia

School of Chemistry
University of East Anglia
Norwich Research Park
Norwich, UK
November 2016

Thesis submitted in partial fulfilment of the requirements for the degree of
Doctor of Philosophy of the University of East Anglia.

©This copy of the thesis has been supplied on condition that anyone who consults it is understood to recognise that its copyright rests with the author and that use of any information derived from there must be in accordance with current UK Copyright Law. In addition, any quotation or extract must include full attribution.

Declaration

I declare that the work contained in this thesis submitted by myself for the Degree of Doctor of Philosophy is my work, except where due reference is made to other authors, and has not previously been submitted by me for a degree at this or any other university.

Paula García Calavia

Abstract

Photodynamic therapy (PDT) requires a photosensitiser, light and oxygen to generate reactive oxygen species and cell death. The hydrophobicity of photosensitisers can be overcome using nanoparticles. Furthermore, nanoparticles can be functionalised with cancer-specific ligands to increase selectivity towards tumours. The aim of this thesis was to investigate the use of nanoparticles for PDT of breast cancer.

Gold nanoparticles (AuNPs) were functionalised with polyethylene glycol (PEG) and a zinc phthalocyanine photosensitiser (Pc). Two Pcs differing in the length of the carbon chain that connects the Pc to the gold, three (C3Pc) or eleven (C11Pc) carbon atoms, were explored. Fluorescence emission intensity was higher for free C11Pc. Conversely, on the surface of the AuNPs, it was higher for C3Pc. The higher fluorescence emission intensity of C3Pc-PEG-AuNPs correlated with an increased production of singlet oxygen (${}^1\text{O}_2$). SK-BR-3 cells internalised both nanosystems but cell death was enhanced with C3Pc-PEG-AuNPs (80 %), due to metal-enhanced fluorescence, as compared to C11Pc-PEG-AuNPs (10 %). The conjugation of the AuNPs with a breast cancer-specific antibody improved the internalisation and PDT efficacy of both nanosystems.

The potential use of a carbohydrate, lactose, to target the galectin-1 receptor on breast cancer cells was studied. Lactose and either C3Pc or C11Pc were conjugated to AuNPs. Two breast cancer cell lines, SK-BR-3 and MDA-MB-231, were used. While lactose-C11Pc-AuNPs only induced phototoxicity to SK-BR-3 cells, lactose-C3Pc-AuNPs induced effective PDT for both cell lines. Evidence of targeting galectin-1 was only observed for MDA-MB-231 cells.

The use of upconverting nanoparticles (UCNPs) functionalised with the photosensitiser Rose Bengal (RB) for near-infrared PDT was investigated. Energy transfer between the UCNPs and RB upon excitation at 980 nm allowed the generation of ${}^1\text{O}_2$. SK-BR-3 cells successfully internalised the UCNPs and induced effective PDT at 15 $\mu\text{g}/\text{mL}$, leading to minimal dark toxicity and effective cell death following irradiation.

Contents

Declaration.....	ii
Abstract.....	iii
Contents.....	iv
List of acronyms.....	ix
Acknowledgements	xv
Chapter 1. Introduction.....	1
1.1. Photodynamic therapy and its mechanism of action	1
1.1.1. Photosensitisers	6
1.2. Nanoparticles for photodynamic therapy	12
1.2.1. Targeted photodynamic therapy	14
1.2.2. Gold nanoparticles	17
1.2.3. Upconverting nanoparticles.....	30
1.2.4. Conclusions	44
1.3. Thesis outline	45
1.4. References	46
Chapter 2. Experimental	55
2.1. Materials and instruments.....	55
2.1.1. Starting materials and solvents.....	55
2.1.2. Instrumental techniques	56
2.1.3. Buffer solutions and imaging medium.....	58
2.1.4. Cell culture	58
2.1.4.1. Cell passage and cell count	59
2.1.4.2. Freezing cells for long-term storage	60
2.2. Gold nanoparticle enhanced and selective antibody targeting photodynamic therapy of breast cancer cells	60
2.2.1. Synthesis of C11Pc/C3Pc-PEG-AuNPs	60
2.2.2. Functionalisation of Pc-PEG-AuNPs with anti-HER2 antibody ..	62
2.2.3. Nanoparticle characterisation by TEM.....	62
2.2.4. Determination of extinction coefficients of C11Pc and C3Pc ..	63
2.2.5. Fluorescence quantum yields of free Pc and Pc-PEG-AuNPs...	63

2.2.6. Synthesis of control PEG-AuNPs	64
2.2.7. Measurement of singlet oxygen production.....	64
2.2.8. Singlet oxygen quantum yields	65
2.2.9. MTT cell viability assay.....	66
2.2.10. CellTiter-Blue® cell viability assay	67
2.2.11. Confocal laser scanning microscopy	68
2.2.12. Colocalisation studies by confocal laser scanning microscopy	69
2.2.13. InCell ELISA for the detection of the HER2 receptor on SK- BR-3 cells	70
2.2.14. ApoTox-Glo™ Triplex assay	72
2.3. Targeted photodynamic therapy of breast cancer cells using lactose- phthalocyanine gold nanoparticle conjugates.....	74
2.3.1. Synthesis of lactose-C11Pc-AuNPs.....	74
2.3.2. Synthesis of lactose-C3Pc-AuNPs.....	75
2.3.3. Nanoparticle characterisation with TEM	76
2.3.4. Measurement of singlet oxygen production for lactose-Pc- AuNPs	76
2.3.5. Synthesis of C11Pc/C3Pc-sPEG-AuNPs.....	76
2.3.6. Synthesis of control sPEG-AuNPs.....	77
2.3.7. MTT cell viability assay for lactose targeting	77
2.3.8. CellTiter-Blue® cell viability assay for lactose targeting	78
2.3.9. Confocal microscopy – Internalisation and PDT of lactose- C3Pc-AuNPs	79
2.3.10. InCell ELISA to quantify the levels of galectin-1 on the cell surface.....	80
2.3.11. InCell ELISA to detect lactose targeting	81
2.3.12. ApoTox-Glo™ Triplex assay – Targeting with lactose-C3Pc- AuNPs	81
2.4. The potential use of upconverting nanoparticles as drug carriers for photodynamic therapy of cancer.....	82
2.4.1. Synthesis of upconverting nanoparticles	82
2.4.2. Characterisation of the UCNPs.....	83
2.4.3. Measurement of singlet oxygen production by UCNPs.....	83

2.4.4. Internalisation of NaYF ₄ -lysine-RB UCNPs by SK-BR-3 cells – Confocal microscopy and multi-photon microscopy	84
2.4.5. PDT effect of NaYF ₄ -lysine-RB UCNPs on SK-BR-3 cells – Confocal microscopy	85
2.4.6. CellTiter-Blue® cell viability assay – NaYF ₄ -lysine-RB UCNPs ...	86
2.4.7. Determination of the extinction coefficient of Rose Bengal ...	87
2.4.8. ApoTox-Glo™ Triplex assay – NaYF ₄ -lysine-RB UCNPs	87
2.4.9. CellTiter-Blue® cell viability assay – UCNPs in dH ₂ O without Rose Bengal	88
2.4.10. Confocal microscopy – UCNPs in dH ₂ O without Rose Bengal..	88
2.5. References	90

Chapter 3. Gold nanoparticle enhanced and selective antibody targeting photodynamic therapy of breast cancer cells	91
3.1. Introduction	91
3.1.1. Interactions between metal nanoparticles and fluorophores.	91
3.1.2. Human epidermal growth factor receptor 2.....	101
3.1.3. Antibodies	104
3.1.4. Aim of the research reported in this chapter	107
3.2. Results and discussion	108
3.2.1. Zinc phthalocyanine photosensitisers.....	108
3.2.2. Synthesis of gold nanoparticles	112
3.2.3. Fluorescence studies	117
3.2.4. Spectroscopic analysis of singlet oxygen production	125
3.2.5. Singlet oxygen quantum yields	128
3.2.6. Cell viability assays	131
3.2.7. Study of the internalisation of the AuNPs by the SK-BR-3 cells.....	135
3.2.8. Functionalisation of the PEG-AuNPs with anti-HER2 antibody	138
3.2.9. Targeted PDT <i>in vitro</i>	140
3.2.10. Confocal microscopy study of targeted PDT	144
3.2.11. Colocalisation studies.....	148

3.2.12. Toxicity and PDT effect in non-cancerous mammary epithelial cells.....	150
3.2.13. Studies of cell viability 19 h after incubation.....	152
3.2.14. ApoTox-Glo™ Triplex assay for cell death mechanism	154
3.3. Conclusions	158
3.4. References	161

Chapter 4. Targeted photodynamic therapy of breast cancer cells using lactose-phthalocyanine gold nanoparticle conjugates	167
4.1. Introduction	167
4.1.1. Aberrant glycosylation in cancer.....	167
4.1.2. Galectins and their role in cancer	169
4.1.3. Targeting cancer glycosylation.....	174
4.1.4. Aim of the research reported in this chapter	178
4.2. Results and discussion	178
4.2.1. Lactose and galectin-1 levels	178
4.2.2. Synthesis and characterisation of lactose-C11Pc-AuNPs.....	181
4.2.3. Synthesis and characterisation of control C11Pc-sPEG-AuNPs	185
4.2.4. <i>In vitro</i> studies in MDA-MB-231 cells using lactose-C11Pc-AuNPs	186
4.2.5. <i>In vitro</i> studies in SK-BR-3 cells using lactose-C11Pc-AuNPs ...	189
4.2.6. Synthesis and characterisation of lactose-C3Pc-AuNPs.....	193
4.2.7. Synthesis and characterisation of control C3Pc-sPEG-AuNPs..	196
4.2.8. <i>In vitro</i> studies in MDA-MB-231 cells using lactose-C3Pc-AuNPs	197
4.2.9. Studies of lactose-C3Pc-AuNPs internalisation by MDA-MB-231 cells.....	202
4.2.10. <i>In vitro</i> studies in SK-BR-3 cells using lactose-C3Pc-AuNPs	205
4.2.11. Internalisation of lactose-C3Pc-AuNPs and PDT effect in SK-BR-3 cells	209
4.2.12. Mechanism of cell death post-PDT by lactose-C3Pc-AuNPs	211
4.2.13. Effects of lactose-C3Pc-AuNPs in non-cancerous MCF-10A cells.....	214

4.3. Conclusions	215
4.4. References	219
 Chapter 5. The potential use of upconverting nanoparticles as drug carriers for photodynamic therapy of cancer 224	
5.1. Introduction	224
5.1.1. Upconverting nanoparticles	224
5.1.2. Biological applications of UCNPs	229
5.1.3. Aim of the research reported in this chapter	235
5.2. Results and discussion	236
5.2.1. Synthesis and characterisation of the UCNPs	236
5.2.2. Singlet oxygen production by the NaYF ₄ -lysine-RB UCNPs	240
5.2.3. Internalisation studies of the NaYF ₄ -lysine-RB UCNPs by SK-BR-3 cells	241
5.2.4. PDT using NaYF ₄ -lysine-RB UCNPs – CellTiter-Blue® cell viability assays	245
5.2.5. Estimation of the concentration of RB on the UCNPs	248
5.2.6. Evaluation of PDT effect using confocal microscopy	249
5.2.7. ApoTox-Glo™ Triplex assay to investigate the mechanism of cell death	255
5.2.8. Analysis of UCNPs without Rose Bengal	258
5.3. Conclusions	262
5.4. References	265
 Chapter 6. Conclusions and future work 268	
6.1. Gold nanoparticle enhanced and selective antibody targeting photodynamic therapy	268
6.2. Targeting breast cancer cells with lactose	273
6.3. Upconverting nanoparticles for photodynamic therapy	275
6.4. Future work	277
6.5. References	280
 Publications and presentations 282	

List of acronyms

Acronym	Definition
+ve St	Staurosporine, positive control for cytotoxicity
¹ O ₂	Singlet oxygen
³ O ₂	Molecular oxygen
5-ALA	5-aminolevulinic acid
67LR	67 laminin receptor
Ab	Antibody
ABMA	9,10-anthracenediyl-bis (methylene) dimalonic acid
AEP	2-aminoethyl dihydrogen phosphate
AgNPs	Silver nanoparticles
AlPcS	Sulfonated aluminium phthalocyanine
AlPcS ₄	Aluminium (III) phthalocyanine tetrasulfonate
AO	Acridine orange
APBA	3-aminophenylboronic acid
APTE	Addition de photon par transferts d'energie
APTES	(3-aminopropyl)triethoxysilane
AuNPs	Gold nanoparticles
AuNRs	Gold nanorods
BBB	Blood brain barrier
bis-AAF-R110	Bis-alanylalanyl-phenylalanyl-rhodamine 110
BODIPY	Boron-dipyrromethene
<i>b</i> -PCL	<i>Block</i> -poly(caprolactone)
BPE	Bovine pituitary extract
<i>b</i> -PLA	<i>Block</i> -poly(DL)lactic acid
BSA	Bovine serum albumin
C11Pc	(1,1',4,4',8,8',15,15',18,18',22,22'-tetradecakisdecyl-25,25'-(11,11'dithiodiundecyl) diphthalocyanine zinc
C3Pc	(1,1',4,4',8,8',15,15',18,18',22,22'-tetradecakisdecyl-25,25'-(3,3'dithiodiundecyl) diphthalocyanine zinc
CD	Cluster determinant
CDR	Complementarity-determining region
Ce6	Chlorin e6

CNBA	4-(2-carboxy-ethylsulfanyl methyl)-3-nitro-benzoic acid
CNS	Central nervous system
ConA	Concanavalin A
Cp	Camptothecin
CPE	Conjugated polyelectrolyte
CpG-ODN	5'-purine-purine/T-CpG-pyrimidine-pyrimidine-3'-oligodeoxynucleotides
CR	Cross relaxation
CRD	Carbohydrate-recognising domain
CT	Computed tomography
DIC	Differential interference contrast
DMEM	Dulbecco's Modified Eagle Medium
DMSO	Dimethyl sulfoxide
DNA	Deoxyribonucleic acid
DOX	Doxorubicin
ECM	Extracellular matrix
EDC	N-(3-Dimethylaminopropyl)-N'-ethylcarbodiimide hydrochloride
EDTA	Ethylenediaminetetraacetic acid
EGF	Epidermal growth factor
EGFR	Epidermal growth factor receptor
ELISA	Enzyme linked immunosorbent assay
EM	Electromagnetic
EPR	Enhanced permeability and retention effect
ErbB	Erythoblastoma gene B
ESA	Excited state absorption
ETU	Energy transfer upconversion
Fab	Antigen binding site
FBS	Foetal bovine serum
Fc	Basal fragment
FRET	Fluorescence/Förster resonance energy transfer
Gal	Galactose
GF-AFC	Glycyl-phenylalanyl-aminofluorocoumarin
GLUT1	Glucose transporter 1

GSH	Glutathione
H	Thiolated heparin
HSA	Human serum albumin
HBSS	Hank's balanced salt solution
hEGF	Human epidermal growth factor
HEPES	4-(2-hydroxyethyl)piperazine-4-ethanesulfonic acid
HER	Human epidermal growth factor receptor
Hp	Haematoporphyrin
HPA	<i>Helix Pomatia</i> agglutinin
HpD	Haematoporphyrin derivative
HRP	Horseradish peroxidase
Hyal	Hyaluronidase enzyme
I _{1O₂}	Intensity of ¹ O ₂ emission
I _a	Intensity of light absorbed by the sample
IBU	Ibuprofen
ICP-MS	Inductively coupled plasma mass spectrometry
Ig	Immunoglobulin
IONPs	Iron oxide nanoparticles
ISC	Intersystem crossing
JM	Juxtamembrane domain
K _d	Dissociation constant
LAMPs	Lysosome-associated membrane proteins
LGALS	Lectin galactoside-binding soluble
LSPR	Localised surface plasmon resonance
M-540	Merocyanine 540
M6P	Mannose-6-phosphate
M6P/IGF-II	Mannose-6-phosphate/insulin-like growth factor
Man	Mannose
MASL	<i>Maackia amurensis</i>
ME ¹ O ₂	Metal-enhanced ¹ O ₂ production
MEBM	Mammary epithelial basal medium
MEF	Metal-enhanced fluorescence
MeOH	Methanol

MES	2-(N-morpholino)ethanesulfonic acid
MRI	Magnetic resonance imaging
mSiO_2	Mesoporous silica
MSN	Mesoporous silica nanoparticles
mTHPC	Tetra(<i>m</i> -hydroxyphenyl)chlorin
mTHPP	5,10,15,20-tetrakis(3-hydroxyphenyl)porphyrin
MTT	3-(4,5,dimethylthiazol-2-yl)-2,5-diphenyltetrazolium bromide
MWCO	Molecular weight cut-off
NaYF_4	Sodium yttrium fluoride
Nd:YAG	Neodymium-doped yttrium aluminium garnet
NGFs	Neuregulins
NHS	N-hydroxysuccinimide
NIR	Near-infrared
NMM	N-methylmesoporphyrin IX
NO	Nitric oxide
NSET	Nanometal surface energy transfer
OCMC	O-carboxymethylated chitosan
OQPGA	Octadecyl-quaternised polyglutamic acid
PA	Photon avalanche
PAA	Polyacrylic acid
PAAm	Poly(allylamine)
PB	Phosphate buffer
PBS	Phosphate buffered saline
PBS-B	Phosphate buffered saline for biological experiments
Pc	Phthalocyanine
Pc4	Silicon phthalocyanine
PcGal_{16}	Phthalocyanine surrounded by sixteen galactose molecules in a dendrimer
PCI	Photochemical internalisation
PDPN	Podoplanin
PDT	Photodynamic therapy
PEG	Polyethylene glycol
PEI	Polyethylenimine

PES	Polyethersulfone
PF6	5,10,15,20-tetrakis(pentafluorophenyl)-21H,23H-porphine
PheoA	Pheophorbide A
Plk1	Oncogene polo-like kinase 1
PpIX	Protoporphyrin IX
Ppa	Pyropheophorbide A
PPADT	Poly-(1,4-phenyleneacetone dimethylenethioketal)
PS	Photosensitiser
PTK7	Protein tyrosine kinase 7
PTT	Photothermal therapy
QDs	Quantum dots
RB	Rose Bengal
RCA ₁₂₀	<i>Ricis communis</i> agglutinin
RES	Reticuloendothelial system
RGD	Peptide arginine-glycine-aspartic acid
RNA	Ribonucleic acid
ROS	Reactive oxygen species
RP	Radiating plasmon
RTKs	Receptor tyrosine kinases
Ru(bpy) ₃ ²⁺	Tris(bipyridine)ruthenium(II)
S ₀	Ground state
S ₁	Excited singlet state
SAM	Self-assembled monolayer
SD	Standard deviation
SERS	Surface-enhanced Raman scattering
SiO ₂ -AuNCs	Silica coated fluorescent gold nanoclusters
siRNA	Small interfering ribonucleic acid
SOC	<i>N</i> -succinyl- <i>N'</i> -octyl chitosan
SPCD	Silicon phthalocyanine dihydroxide
SPEG	Thiol-dPEG® ₄ -acid
SPP	Surface plasmon polariton
SPR	Surface plasmon resonance
T ₁	Excited triplet state

T antigen	Thomsen-Friedenreich carbohydrate antigen
TBS	Tris buffered saline
TEM	Transmission electron microscopy
TEOS	Tetraethoxysilane
TESPIC	(3-isocyanatopropyl)triethoxysilane
Tf _{pep}	Transferrin peptide
TGF α	Transforming growth factor α
THF	Tetrahydrofuran
TL	Tomato lectin
TMB	3,3',5,5'-tetramethylbenzidine
TNBC	Triple-negative breast cancers
TOAB	Tetraoctylammonium bromide
TPA	Two-photon absorption
TPE	Two-photon excitation
TPP	Tetraphenylporphyrin
UCL	Upconverted luminescence
UCNPs	Upconverting nanoparticles
UK	United Kingdom
USA	United States of America
UV	Ultraviolet
UV-vis	Ultraviolet-visible
VB ₁₂	Vitamin B ₁₂
VR	Vibrational relaxation
WGA	Wheat Germ agglutinin
ZnPc	Zinc phthalocyanine

Acknowledgements

'We are all in the gutter, but some of us are looking at the stars', Oscar Wilde

First, I would like to thank my primary supervisor Professor David Russell for welcoming me in his lab when I was an undergraduate student and giving me the opportunity to pursue a PhD under his guidance. Thank you David for believing in me and for your continued help and support these years. I could not have wished for a better supervisor. Thank you to Professor Mark Searcey, my 'other' primary supervisor, for making us part of his research group after David retired. Thank you to my secondary supervisor Professor Julea Butt for all her guidance and suggestions.

This thesis would not have been possible without the financial support from the School of Chemistry, University of East Anglia. The invaluable technical assistance given by Dr Paul Thomas and Dr Colin Macdonald is hugely appreciated. The assistance of Professor Andrew Beeby at the University of Durham to obtain the singlet oxygen quantum yields is gratefully acknowledged. A special thanks goes to Professor Thomas Hirsch and Dr-to-be Markus Buchner at the University of Regensburg (Germany) for kindly providing the upconverting nanoparticles used in this work. Thank you Thomas for your hospitality during our visit to Regensburg and your support. Thank you Markus for your kindness and for the useful discussions on upconverting nanoparticles.

During this PhD, most of my time was spent in the lab with my colleagues from the Russell group. I would like to thank Dr María José Marín Altaba, Dr Susan van der Heide, Dr Gergis Obaid and Drs-to-be Brydie Moore, María Elisa Alea Reyes and Beth McMurchie. I am especially indebted to María José for her constant help and support these years. Thank you María for being my teacher, my colleague and my friend. I would not have come this far if it wasn't for you and I will be forever grateful. Thank you Susan for introducing me to the research life when I was an undergraduate student and making my first steps easier; and Gergis for sharing, in the distance, your scientific knowledge with me. Brydie, thank you for your friendship, your help and for always keeping a smile on your face and spreading your positivity. María Elisa, thank you for the useful discussions, for our trips to bio and for becoming my friend. Beth, thank you for your company and support, and for introducing us to the best cookies ever made.

I want to acknowledge a few people that I have met during this PhD journey. Dr Teresa Quirós, thank you for your support, Dr Kunal Mahesh Tewari, thank you for your love for gelato, and Drs-to-be Franco Valduga and James Frost for sharing the ups and downs of the PhD life during our demonstrating sessions. A big ‘gracias’ to my friends in Spain who have stayed in touch and shared all the gossip with me, Paloma and Luis.

Special thanks to my partner Andrew for his constant love and support. Thank you for making me part of your life and always being there for me no matter the distance. Thank you for our holidays, our camping trips discovering America, your trips to England, for showing me the American culture and for always having faith in me and being confident that I would finish my PhD.

Last but not least, my biggest gratitude goes to my family. Thank you to my parents for their immeasurable love and support, both emotionally and financially, for the skype calls, the whatsapp conversations, the parcels with much-missed Spanish food, the reminders of home, our Europe trips, our Christmas holidays and for always keeping my feet on the ground. Thank you for always believing in me, even when I didn’t believe in myself. Thank you to my sister, Dr-to-be Noelia García Calavia, for the weekends spent in London, which always provided a fun distraction from the worries of the PhD life, for the nostalgic memories of our teenage years, for the hours spent waiting at airports and for always being there for me. Mamá, papá y Noe, os quiero y siempre os estaré agradecida. This thesis is dedicated to you.

Chapter 1

Introduction

Cancer is a serious health problem. It has a high incidence rate; cancer will be diagnosed to 1 in 2 people in the UK, with cancer cases becoming increasingly common due to the an ageing population, and it is one of the principal causes of death in the world for both men and women.^{1,2} Specifically, lung, stomach, liver, colon and breast cancer lead the number of cancer-related deaths yearly.³ Therefore, it is vital to find treatments for the prevention and therapy of tumours.

Photodynamic action has been known for over 100 years, when it was inadvertently discovered by Raab and von Tappeiner, as described by Anand *et al.*⁴ and Ackroyd *et al.*⁵ These authors realised that photodynamic action is a two-step process that requires a photosensitising molecule and light, together with a suitable amount of molecular oxygen in the environment, in order to induce tissue damage. The investigation of photodynamic therapy has since then attracted great interest, especially for the treatment of malignant tumours.⁴ More recently, the combination of nanotechnology and cancer-specific targeting molecules with photodynamic therapy has gained remarkable attention for an enhanced photodynamic effect.

In this chapter, a review of photodynamic therapy will be explored. Additionally, the choice of photosensitising molecules available for photodynamic therapy as well as the photosensitisation mechanisms that they undergo will be discussed. Targeted photodynamic therapy *via* the introduction of cancer-specific targeting agents will also be covered. Finally, a review on the use of different types of nanoparticles for photodynamic therapy will be studied.

1.1. Photodynamic therapy and its mechanism of action

Photodynamic therapy (PDT) of cancer, sometimes referred to as photochemotherapy of cancer, is a minimally invasive treatment that involves the use of two components, a photosensitiser (PS) and visible light.⁴⁻²² Additionally, the presence of molecular

oxygen is essential for effective PDT. These three elements by themselves, PS, light and oxygen, are non-toxic. During the treatment, the PS is activated with visible light. Reaction of the excited PS with molecular oxygen leads to the production of reactive oxygen species (ROS), capable of inducing toxicity to cells and tissues.⁴⁻²² Advantages of PDT over conventional cancer treatments include cost-effectiveness, low systemic toxicity, the prevention of toxic side effects such as the ones seen after chemotherapy or radiotherapy (*i.e.*, tiredness, weakness, nausea and vomiting, hair loss, dry skin, peripheral neuropathy, infertility and problems in the heart, lungs and bladder) as well as higher cure rates, and excellent cosmetic results following treatment, which is especially important for skin cancer lesions.^{6-9,23} PDT is particularly useful for the treatment of early and localised tumours, due to the selective delivery of the PS towards cancerous tissue.^{6,8} Furthermore, PDT can be easily combined with other therapies, such as conventional chemotherapy, for an improved destruction of tumours.⁶ However, PDT also has its limitations. The main problem related to PDT is the presence of skin photosensitivity, *i.e.*, skin remains sensitive to light, for some time following treatment.⁶ Additionally, complete cure of metastatic tumours is more challenging since irradiation of the whole body is not possible.^{7,8}

During photosensitisation (**Figure 1.1**), the PS is irradiated with light of a specific wavelength, usually between 400-800 nm.¹⁰ The PS in the ground state (S_0) absorbs light, which provides energy for the PS to reach an electronically excited singlet state (S_1). The S_1 state has a short half-life (10^{-9} - 10^{-6} s)¹¹, which is unstable and thus prone to quickly undergo deactivation. Deactivation can occur *via* different pathways, either radiative, such as fluorescence, or non-radiative, such as intersystem crossing (ISC). Both fluorescence and ISC occur from the lowest energy level within the S_1 state, which the PS reaches *via* non-radiative vibrational relaxation (VR). Effective PS follow ISC, which induces a change in spin multiplicity leading to a triplet excited state (T_1). The T_1 state has a longer half-life (10^{-3} - 1 s)¹¹ than S_1 , which allows the PS to go through the next steps of photosensitisation. Two mechanisms of photosensitisation can be followed, type I or type II. Type I involves direct reaction between a PS in the T_1 state and a substrate, which concludes with the formation of free radicals *via* electron or hydrogen transfer. Upon reaction with molecular oxygen (3O_2), ROS are formed, including the superoxide anion, hydrogen peroxide, and the highly reactive hydroxyl

radical. Type II involves the transfer of energy from the PS in the T_1 state to molecular oxygen, producing a highly reactive ROS, singlet oxygen (1O_2). All of these ROS induce oxidative stress in the cells and tissues, which lead to cell death and tumour destruction.^{6,7,9-16}

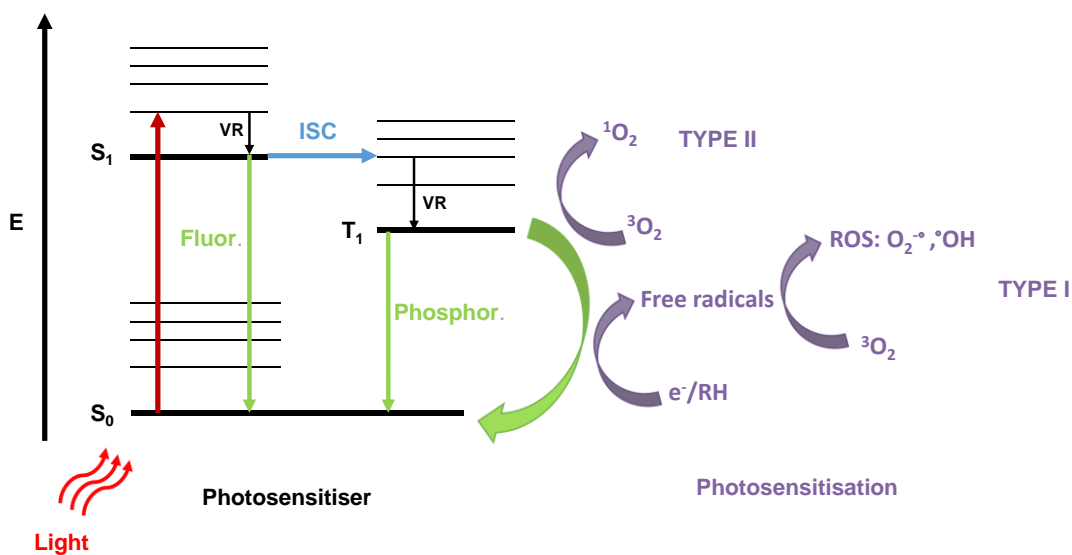


Figure 1.1. Simplified Jablonski diagram including a schematic representation of the PDT photosensitisation mechanisms leading to the production of ROS. The arrows represent excitation (red), fluorescence and phosphorescence (green), intersystem crossing (blue), non-radiative vibrational relaxation (black) and energy transfer (purple).

It is generally accepted that the most common type of photosensitisation that leads to PDT photodamage is Type II.^{6,7,9,13,14,17} However, the ratio by which type I and type II photosensitisation occur during PDT depends on several factors, including the choice of PS, the subcellular localisation of the PS, the binding affinity between the PS and the substrate and the presence of 3O_2 .^{6,9,12,17} As a result, in situations where molecular oxygen is not readily available, known as hypoxia and anoxia, type I is the pathway followed for effective PDT.^{6,7,13} Following production of the ROS, the PS decays back to the ground state and thus multiple cycles of photosensitisation can take place during PDT until the concentration of oxygen in the tissue is depleted.⁸

Given that type II is the most common mechanism followed in PDT, 1O_2 is the most important cytotoxic species that leads to cell death. In the ground state, molecular oxygen presents two unpaired electrons (same spin) in the 2p antibonding orbitals.⁹

However, upon excitation, singlet oxygen presents two paired electrons (different spin) in the 2p antibonding outer orbital. Effective excitation of ${}^3\text{O}_2$ to produce ${}^1\text{O}_2$ requires at least 94.5 kJ/mol of energy (Figure 1.2).^{9,16} The half-life of ${}^1\text{O}_2$ in water is *ca.* 3 μs , but it is diminished in the cytoplasm to *ca.* 10-320 ns.^{9,14,15,24} As a result, the maximum radius of action for ${}^1\text{O}_2$ within the cellular environment is *ca.* 10-55 nm.^{14,24} Considering the diameter of a typical cell ranges between 10-100 μm , it is easily seen that the localisation of the PS inside the cells is vital for an effective photodynamic cell kill.^{9,13,15}

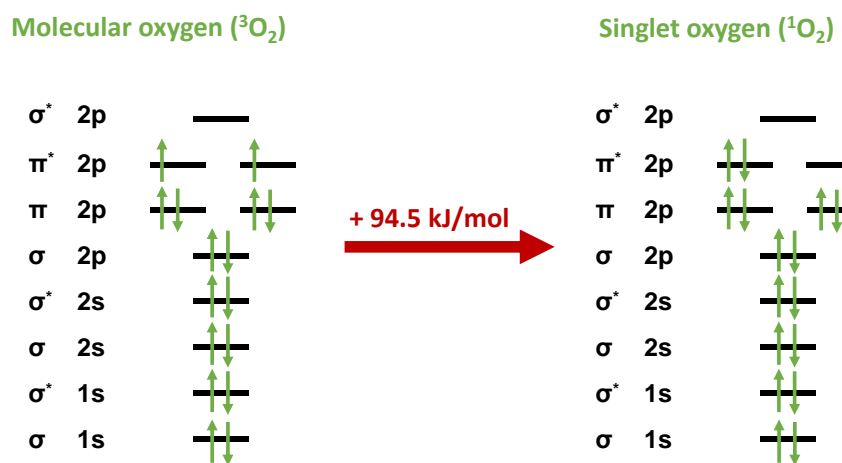


Figure 1.2. Energy level diagrams of molecular oxygen (${}^3\text{O}_2$) and the long-lived ${}^1\Delta_g$ excited state of singlet oxygen (${}^1\text{O}_2$). Energy of at least 94.5 kJ/mol is required for the transition from ${}^3\text{O}_2$ to ${}^1\text{O}_2$.

Following the production of ROS, there are three main mechanisms that can lead to malignant cell death; direct photodamage, vascular shutdown and the activation of an immune response.^{6,7,12,17,18} The ratio in which each of these mechanisms contribute to tumour destruction is dependent on the localisation of the PS, the light dose and the type of tumour being treated.⁶

Photodamage refers to the direct killing of the tumour cells as a result of the cellular damage caused by the ROS.¹² There are three main cell death pathways that can be followed in PDT, apoptosis, necrosis and autophagy.^{14,24} The pathway followed depends not only on the cell type but also on the localisation of the PS within the cells, the light dose and the oxygen concentration available for the treatment.^{6,13,17} Additionally, the localisation of the PS within the cells will depend on the type of PS, its

chemical properties and the concentration at which it is administered.⁶ It has been reported that PS that locate in the mitochondria lead to apoptosis, whereas those PS located in the lysosomes and the plasma membrane are most likely to induce necrosis or autophagy.^{23,25} Direct photodamage has its limitations because the distribution of the PS within the tumour is not always homogeneous. It is further limited by the amount of oxygen in the malignant tissue, most of which is consumed during the PDT treatment itself, which can reduce the direct damage to the cells.¹²

Vascular shutdown refers to damage not to the cancer cells themselves, but to the blood vessels that surround them. These blood vessels are essential for tumour growth, since they provide all the nutrients and oxygen the cells need. Therefore, damage to the blood vessels can lead to cell death. PDT has been shown to induce microvascular collapse, which in turn constraints the oxygen supply to the malignant tissue. As a result, microvascular collapse can lead to vascular constriction, thrombus formation and inhibition of tumour growth.¹² Vascular constriction is easily identified because it leads to haemorrhage and erythema.¹⁷

Finally, some studies have reported that leukocytes, lymphocytes and macrophages have been found in PDT-treated cells and tissue. This implies that PDT could lead to the activation of an immune response against tumour cells, which is characteristic for the stimulation of an inflammatory reaction.^{12,14} Inflammation is manifested *via* a localised gross oedema and it appears as a consequence of damage to the vasculature.¹⁴ It has been suggested that the mechanism followed by the PDT treatment depends on the dose and the incubation time within the tissue.¹²

The efficacy of PDT relies on several parameters, such as the selectivity of the PS towards tumour tissue, the interval between administration of the PS and light irradiation and the wavelength of light and light dose used for the treatment.¹² The accumulation of the PS is partially selective towards tumour cells. The reasoning behind this selectivity is not completely understood but it is most likely related to the special characteristics of the tumour such as the presence of leaky vasculature and the lack of lymphatic drainage. The selectivity of PS towards tumour tissue will be further reviewed in **section 1.2.1**.⁶ Additionally, the use of hydrophobic PS yields more selective accumulation than hydrophilic PS, due to their rapid diffusion into tumour

cells.^{6,24} Further information on the types of PS and their selectivity towards cancer cells will be reviewed in **section 1.1.1**. Light dosimetry is an important concept in PDT as it will determine the uniform distribution of light over the tumour, as well as the potential irradiation of healthy tissue.^{4,26} An ideal dose should minimise irradiation of the healthy cells surrounding the tumour.²⁶ Dosimetry is an important parameter in deciding not only the light dose but also the fluence rate and the time of photoexposure.⁴ Additionally, the selection of the irradiation wavelength plays an important role in PDT.¹⁴ Blue light is the least efficient choice since it penetrates biological tissue only slightly. The most efficient wavelength range is between 600-1,200 nm and the longer the wavelength used, the deeper the penetration into the tissue and thus the ability to reach deeper-lying tumours. However, the production of $^1\text{O}_2$ requires relatively high energy (94.5 kJ/mol) and only the range 600-800 nm is energetic enough to induce its generation. As a result, the most efficient light is red light.¹⁴

1.1.1. Photosensitisers

An ideal PS should have a series of properties in order to enhance its efficacy for PDT while minimising side effects. In order to produce ROS in sufficient concentrations, efficient PS should have a **high quantum yield** for the triplet state together with a relatively long half-life.^{6,9,13,19,24} Furthermore, the PS's **absorption maximum** should be between 680-850 nm.^{6,9,13,14,19,26} This wavelength region ensures a deeper penetration into the target tissue, *ca.* 8 mm but reaching up to 2-3 cm under favourable conditions, while providing enough energy for the effective excitation of molecular oxygen in order to generate ROS.^{6,14,19}

One of the most important properties for an effective PS is the **selectivity** towards the tumour.^{6,9,13,19,26} As reported in **section 1.1**, the mechanism by which some PS are more selectively accumulated in the tumour is poorly understood. However, it has been described to be due to specificities in the tumour's structure. The main factors are the presence of leaky vasculature created around the tumour, a reduction in the lymphatic drainage, a lower pH in the tumour's extracellular compartment and a high affinity of hydrophobic PS for endothelial/cancer cells *via* low-density lipoprotein receptor-

mediated endocytosis.⁹ These factors and the selective accumulation of PS in tumours will be reviewed in **section 1.2.1**. Selectivity towards the target tissue would avoid undesirable toxicity to the healthy tissue surrounding the tumour.¹³

Another important property is **low dark toxicity**.^{6,9,13,14,19,26} Photosensitisers should not be toxic, the toxicity of the treatment should only occur after light irradiation, with the production of ROS. Having **minimal side effects** is also beneficial.^{9,14,26} This includes limited *in vivo* stability for a **fast biological clearance** from the human body so the patient does not need to avoid bright light during the months following PDT (skin photosensitivity).^{19,24,26} Furthermore, the PS should not cause mutagenic effects, which are usually related to the intracellular localisation.^{9,26} Therefore, to avoid this effect, efficient PS will not be located inside the nucleus of the cells.⁹

The chemical properties of the PS are also key for their efficiency. PS should be a **stable**, **chemically pure** compound with a constant composition that will induce a **reliable** PDT treatment.^{6,9,13,24,26} Additionally, the solubility of the PS is another factor to consider.^{9,26} Hydrophobic photosensitisers are efficient for the reaction with the lipid bilayers of the cell membrane, as well as the selective delivery towards tumour tissue. However, hydrophilicity is required for an effective delivery and transport of the PS through the body. As a result, **amphiphilicity** is an important property for PS.⁹

The administration of the PS is also important as it should not lead to toxic effects such as allergic reactions.⁹ Furthermore, the administration of the PS should be fairly easy and pain-free. The pain-free property should be extended throughout the irradiation period.^{9,26} Other important considerations are the **cost**²⁶ and **availability**¹⁹, as well as the potential to use PDT with other therapies. Consequently, ideal PS should not prevent combination therapy. For example, in order to use PDT in combination with fluorescence diagnosis, the PS should have at least some **fluorescence emission**.⁹ According to the time when they were developed and their characteristics, photosensitisers can be divided in two main groups; first generation photosensitisers and second generation photosensitisers.

First generation photosensitisers

First generation photosensitisers refer to haematoporphyrin derivatives (HpD) mainly. The structure of haematoporphyrin and its parent compound the porphyrin, based on a tetrapyrrole backbone, are shown in **Figure 1.3.**²⁴

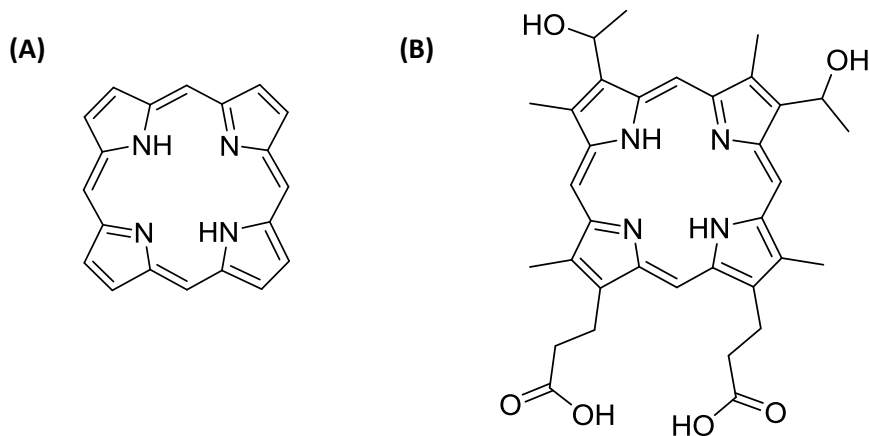


Figure 1.3. Chemical structure of (A) porphyrin and (B) haematoporphyrin, from which haematoporphyrin derivative (HpD) and Photofrin® are derived.

The modern period of PDT started with Schwartz and Lipson in 1960 at the Mayo Clinic (USA).^{4-6,10,12,18} The treatment of haematoporphyrin with acetic acid and sulfuric acid produced a water-soluble mixture of porphyrins known as haematoporphyrin derivative (HpD), which was found to have tumour localising properties. The discovery of the activation of HpD using red light led to the development of HpD for PDT in a variety of clinical trials.^{10,12} HpD was the first approved photosensitiser for PDT and it was later purified, to remove the least active porphyrins, to porfimer sodium, commonly known as Photofrin®.^{4,18} Photofrin was initially approved in Canada for the prophylactic treatment of bladder cancer in 1994.^{6,11} Since then, it has been approved in more than 125 countries⁶ for a variety of lesions including non-small cell lung cancer, oesophageal cancer, early-stage gastric cancer and early-stage cervical cancer.^{11,13} Even though Photofrin is non-toxic, reliable, pain-free and still successfully used in the clinics, it suffers from a series of disadvantages.^{6,11,13,14,19,20,26} Photofrin is a complex mixture of more than 60 compounds, making its reproducibility quite challenging.^{6,13} Photofrin absorbs light at 630 nm with a low extinction coefficient, which means the penetration

into the tissue is limited to *ca.* 5 mm.^{11,13,19} Additionally, the tumour selectivity is limited and the PS is slowly cleared from the body, leading to skin photosensitivity for *ca.* 2-3 months.^{6,11,13,14,19,20} As a result of these drawbacks, improved PS were developed, which are known as second generation photosensitisers.¹¹

Second generation photosensitisers

The second generation of photosensitisers offers certain advantages over the first generation, such as a shorter period of skin photosensitivity, a longer irradiation wavelength (675-800 nm) that allows for a deeper penetration into the tissue, an improved tumour selectivity and higher quantum yields of the triplet excited state and thus of $^1\text{O}_2$ production.^{11,20} Within the porphyrins, a special type of second generation photosensitiser is 5-aminolevulinic acid (5-ALA), **Figure 1.4.** 5-ALA is a naturally occurring prodrug, involved in the biosynthesis of haem.^{5,6,13,20} During the biosynthesis of haem, 5-ALA is a precursor of the photosensitiser protoporphyrin IX (PpIX), **Figure 1.4.**^{5,6} This is an example of endogenous photosensitisation.^{5,6,14} The administration of 5-ALA leads to a porphyria-like phenomenon by which an excess of PpIX is secreted and accumulated within cancerous tissue.^{5,6,11} 5-ALA offers several advantages over HpD, including a shorter photosensitivity period of only 24 h, fast biological clearance and the possibility of oral and topical administration.^{5,6} On the other hand, 5-ALA also presents some drawbacks, the main one being its hydrophilic character, which prevents efficient internalisation and limits its action to superficial tumours.⁶ However, the synthesis of novel 5-ALA-esters is becoming increasingly popular as a way to increase the hydrophobicity of the compound and avoid this problem, including the 5-ALA hexyl ester Hetvix® and the methyl ester-aminolevulinate Metvix®.⁶ Additionally, 5-ALA PDT can be painful.²⁶ Nevertheless, 5-ALA is clinically approved for actinic keratoses of the face and scalp, basal-cell carcinoma, brain, bladder, head and neck and gynaecological tumours.¹²⁻¹⁴

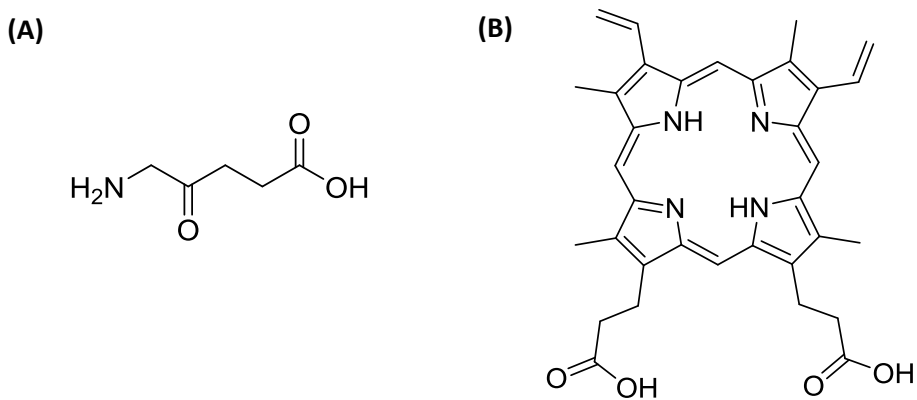


Figure 1.4. Chemical structure of (A) 5-aminolevulinic acid (5-ALA) and (B) the active photosensitiser protoporphyrin IX (PpIX).

Second generation photosensitisers include several families within the tetrapyrrole backbone, such as phthalocyanines, naphthalocyanines, chlorins, bacteriochlorins, texaphyrins, and purpurins.^{11,20} **Figure 1.5** shows the parent compound of the most commonly employed families. These parent compounds give rise to many derivatives that are used as photosensitisers in PDT.

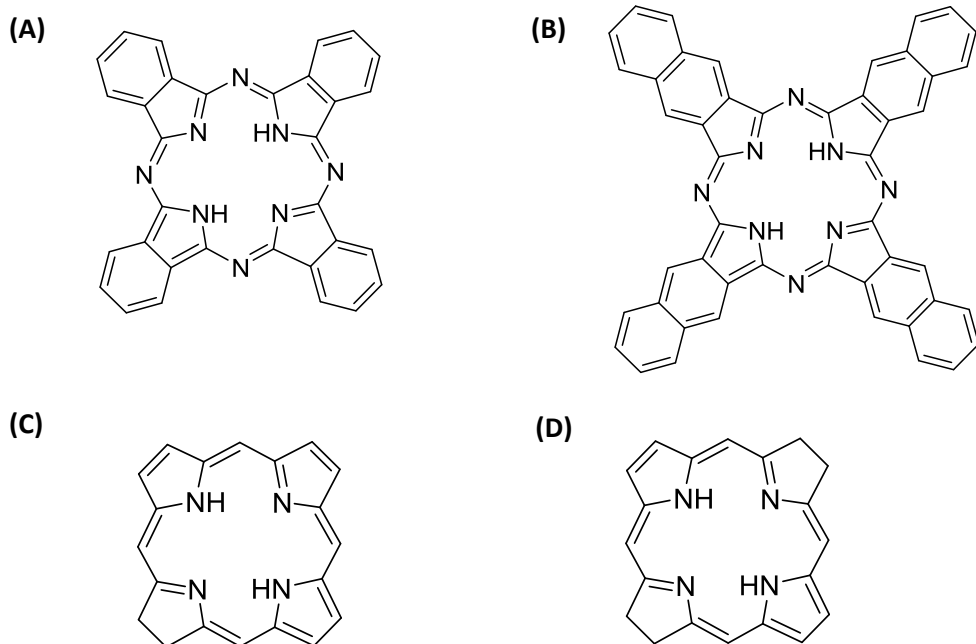


Figure 1.5. Chemical structure of (A) phthalocyanine, (B) naphthalocyanine, (C) chlorin and (D) bacteriochlorin.

Phthalocyanines are the most promising second generation photosensitisers.¹³ Their monomeric form has a strong absorption band at *ca.* 680 nm with a high extinction coefficient. Furthermore, phthalocyanines can be modified by addition of a central metal ion, such as Zn²⁺ or Al³⁺, which can further increase the triplet quantum yield leading to an increased production of ¹O₂.¹³ The silicon phthalocyanine Pc4 is being used for clinical trials in the United States for the treatment of cutaneous T-cell lymphoma.¹⁴ Zinc phthalocyanines are gaining interest for *in vitro* investigations and they are being tested in clinical trials in combination with liposomal formulations.²⁴

There are a couple of clinically approved PS belonging to the chlorin family. The best known chlorin approved for treatment is tetra(*m*-hydroxyphenyl)chlorin (mTHPC), also known as Foscan®. The chlorin mTHPC is 100 times more potent than the first generation PS Photofrin and it leads to effective PDT using low concentration and light dose.¹¹ In Europe, mTHPC is clinically approved for the treatment of neck and head cancers.¹⁴ Other examples include the benzoporphyrin derivative known as verteporfin, and chlorin e6, a naturally occurring chlorophyll derivative.²⁴ The use of verteporfin, commercialised as Visudyne®, has been clinically approved for the treatment of age-related macular degeneration in ophthalmology since 2001 in more than 60 countries.^{6,27} Another photosensitiser that belongs to the chlorins is tin etiopurpurin (Purlytin®). Tin etiopurpurin is clinically approved in the USA for PDT of cutaneous metastatic breast cancer and Kaposi's sarcoma, as well as other non-cancerous diseases.¹¹ Purlytin is derived from the porphyrins but its structure, especially the addition of tin metal, allows for a longer absorption wavelength (650-680 nm), thus making it a more efficient PS.

Other second generation PS not derived from the tetrapyrrole backbone have been investigated.²⁴ Molecules that act as PS and can be classified as synthetic dyes include phenothiazinium salts, Rose Bengal, squaraines, boron-dipyrromethene (BODIPY) dyes, phenalenones and transition metal compounds. Within the phenothiazinium salts, the most commonly used PS is methylene blue (**Figure 1.6**), which is especially used for antimicrobial PDT rather than anticancer PDT. The PS Rose Bengal (**Figure 1.6**), belonging to the xanthenes, is widely used as a photoactive dye with interest in antimicrobial PDT, anticancer PDT and tissue bonding applications.²⁴

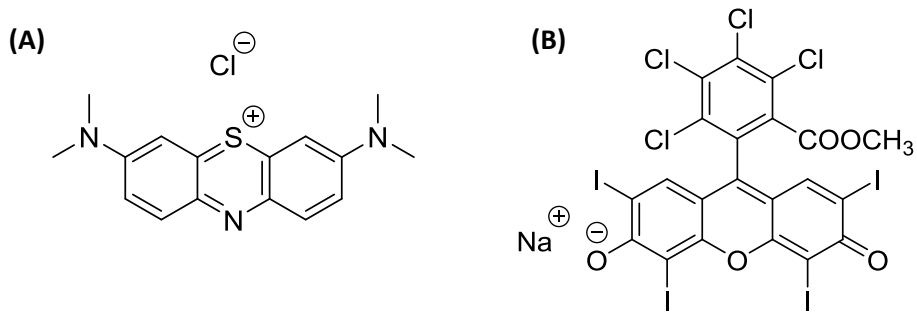


Figure 1.6. Chemical structure of (A) methylene blue and (B) Rose Bengal. Ref. 24.

Natural products can also be used as PS for PDT. The most widely studied ones are hypericin, hypocrellin, riboflavin and curcumin.²⁴ Even though the selectivity towards tumour tissue is improved in the second generation of photosensitisers, it is still limited. In an attempt to increase the PS selectivity to the tumour, third generation photosensitisers are being developed.^{11,14,19} Third generation PS are based on the conjugation of the PS to biological ligands for targeted PDT, which will be reviewed in **section 1.2.1**.

1.2. Nanoparticles for photodynamic therapy

Effective PS are usually hydrophobic in nature, as mentioned in **section 1.1.1**, in order to interact with the lipid bilayers of the cell membrane and be efficiently internalised by the cells.⁹ As a result, the PS delivery and intravenous administration into the body becomes challenging as the PS can easily aggregate in aqueous solutions, leading to a decrease in quantum yield and thus reduced ${}^1\text{O}_2$ production.^{28,29} Additionally, the PS selectivity towards tumour tissue *in vivo* is limited, even for the most recently developed third generation PS, which incorporate a targeting ligand on their surface.^{21,29} Therefore, there is a need to develop PS delivery systems that allow the solubilisation of the hydrophobic PS in aqueous media while increasing the selectivity towards cancerous tissue.²³ The use of nanoparticles as vehicles for the selective delivery of PS in PDT has received significant attention over the past 10-15 years.³⁰ Nanoparticles are ideal candidates for PDT due to their small size (1-100 nm), their high surface area-to-volume ratio, their photophysical and photochemical properties as well

as the extensive possibilities for size and shape control.^{23,28,31,32} Nanoparticles can be made water soluble while the PS they carry retain its hydrophobic properties.²⁸ This provides the amphiphilicity the PS needs in order to circulate through the blood and maintain its monomeric active form without aggregation.^{23,24,29,31,32} Furthermore, nanoparticles enhance the selectivity towards cancerous tissue *via* the enhanced permeability and retention effect (EPR)^{23,25,28-32}, which will be discussed in **section 1.2.1**. The selectivity towards cancer cells can be further improved by the addition of chemical and/or biological ligands with strong binding affinities towards certain cell receptors overexpressed on the surface of tumours.^{23,28-34} This is known as targeted PDT and will be further discussed in **section 1.2.1**.

The high surface area-to-volume ratio of nanoparticles allows for their functionalisation with many different ligands. The nanoparticles can thus accommodate a high number of PS molecules, which increases the amount of PS delivered to the cancer cells and results in an enhanced production of ${}^1\text{O}_2$ and other ROS.^{28,32} Other advantages of the use of nanoparticles for PDT include the possibility of specifically controlling the release of the PS into the target tissue and the possibility to obtain multifunctional nanoparticle platforms.^{23,25,32} Multifunctional nanoparticle platforms are those nanoparticles functionalised with different ligands to allow for theranostic applications, *i.e.*, perform diagnosis and therapy at the same time. Theranostics can refer to the use of the nanoparticle system for both imaging and PDT. Additionally, PDT can be combined with other therapeutic modalities such as photothermal therapy (PTT), chemotherapy and magnetically-guided therapies.^{25,32}

The nanoparticles used for PDT can be divided into two categories, passive and active nanoparticles, based on their participation in the photosensitisation process.^{23,32,35} As defined by their name, passive nanoparticles are only carriers of the PS.^{32,35} Passive nanoparticles can be either biodegradable or non-biodegradable, the main difference between them being that biodegradable nanoparticles effectively release the PS into the cytoplasm whereas non-biodegradable nanoparticles induce the generation of ROS without releasing the PS.^{21,23,29,32,35,36} Biodegradable nanoparticles include liposomes, dendrimers, synthetic polymer-based micelles and natural macromolecules.^{32,36} Non-biodegradable nanoparticles offer some advantages over the biodegradable type,

mainly their resistance to changes in pH and temperature, the tunability in size, shape and porosity during synthesis and the resistance towards microbial attack.^{21,32,36} Non-biodegradable nanoparticles include metallic nanoparticles, silica nanoparticles, magnetic nanoparticles, ceramic-based nanoparticles and polyacrylamide-based nanoparticles.^{23,32} On the contrary, active nanoparticles are involved in the production of ROS and can be further classified into nanoparticles that act as PS by themselves and nanoparticles that generate an energy transfer to the PS.³² Active nanoparticles that act as PS include titanium dioxide (TiO_2) nanoparticles, zinc oxide (ZnO) nanoparticles and fullerenes.^{29,32,35} These nanoparticles have unique absorption properties that allow them to induce the generation of ROS.³² The second class of active nanoparticles are those nanoparticles that not only carry the PS but are also involved in energy transfer processes. These include upconverting nanoparticles, X-ray activatable nanoparticles, quantum dots and two-photon absorbing nanoparticles.³²

This section will focus on a review on the use of gold nanoparticles and upconverting nanoparticles for PDT of cancer, which are the two types of nanoparticles explored during the investigations reported in this thesis.

1.2.1. Targeted photodynamic therapy

As it has been mentioned throughout **Chapter 1**, the selectivity of PS towards cancerous tissue is limited. Such selectivity can be increased by the conjugation of the PS to nanomaterials. The increase in selectivity with the use of nanoparticles is called passive targeting. Passive targeting refers to the preferential internalisation of nanoparticles by cancer cells due to the specific properties of tumours in contrast to healthy tissue, the enhanced permeability and retention effect (EPR). The EPR effect is related to the appearance of fenestrations in the tumour vasculature as well as the lack of lymphatic drainage.³⁷ The uncontrolled growth of cancer cells requires increasing amounts of oxygen and nutrients in order for the cells to survive. As a result, new blood vessels need to be rapidly created, a process known as angiogenesis. Angiogenesis leads to the formation of abnormal, leaky, disorganised and loosely-connected blood vessels with an increased vessel permeability.^{25,36,37} The increased permeability

appears as fenestrations with sizes of 100-600 nm.²⁵ Conversely, fenestrations in the vasculature of healthy tissue are less than 10 nm in size. Therefore, nanoparticles permeate through tumour vasculature more easily than healthy tissue.³⁷ Healthy tissue is continuously drained *via* the lymphatic vessels, allowing for the regeneration of the interstitial fluid. However, tumours present a reduced, minimal lymphatic drainage. Therefore, once nanoparticles have been internalised, they will be retained due to the inability of tumours to renew and clean the interstitial fluid.^{25,36,37} The EPR effect plays an important role in tumour selectivity. Even though the tumour biology is essential for the development of the EPR effect, the physicochemical properties of the PS also influence the effectiveness of selective uptake *via* EPR.³⁷ One of the limitations of the EPR effect is the high variability in vascular permeation in different human tumours. Gastric, pancreatic and highly metastatic cancers typically show low vascularisation, which restricts the nanoparticle accumulation *via* EPR.³⁸

As it was mentioned in **section 1.2**, the use of nanoparticles further provides the opportunity to use biological ligands in order to increase the potential selectivity that occurs through the EPR effect in a complementary manner.³⁷ The use of biomolecules for the selective targeting of cancer cells is known as active targeting.^{25,33,36,37} In contrast to third generation PS, nanoparticles can be functionalised with multiple targeting ligands on their surface, which increases the selectivity.³³ The idea for active targeting is the use of ligands that specifically recognise certain receptors overexpressed on the surface of cancer cells but not on healthy cells.^{33,36} The most typically used receptors for active targeting are, as shown in **Figure 1.7**, the human epidermal growth factor receptor 2 (HER2), the folate receptor, the transferrin receptor, nucleolin, the $\alpha\beta$ integrins, the cluster determinants 44 (CD44), carbohydrates and endogenous lectins.^{25,33,37} One of the carbohydrates is the Thomsen-Friedenreich carbohydrate antigen (T antigen), overexpressed in more than 90 % of primary tumours.³³ The lectin Jacalin, specific towards the T antigen, has been used as the targeting ligand in previous studies.^{33,39}

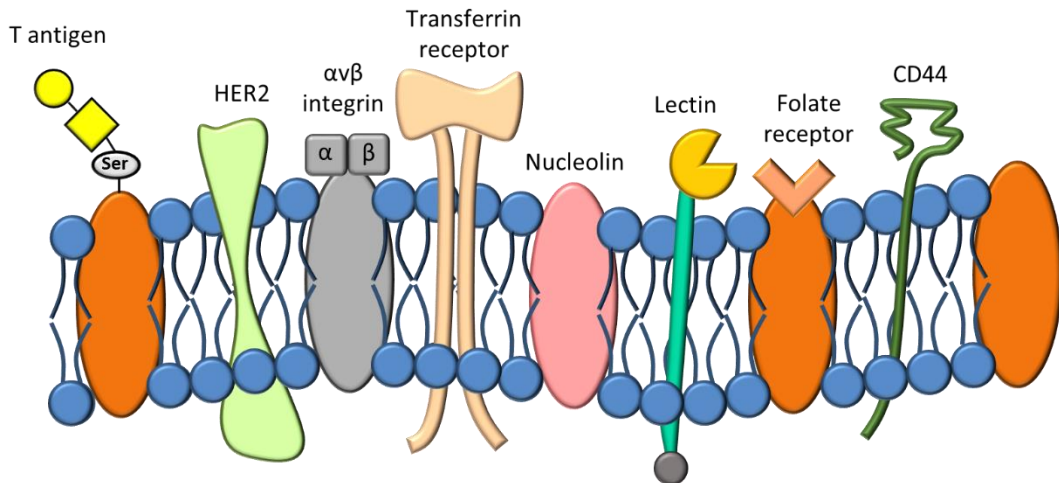


Figure 1.7. Schematic representation of a cell membrane, showing some of the cancer cell receptors that can be used for selective targeting. It should be noted that these receptors are not all present in all cancer cell types. The figure was adapted and modified from Ref. 28.

The HER2 receptor is overexpressed in *ca.* 10-34 % of aggressive breast cancers. It is usually targeted by using a monoclonal antibody, since it has binding affinities in the nanomolar range.³³ The HER2 receptor and its role in cancer will be discussed in **Chapter 3**. The folate receptor, found overexpressed in more than 90 % of ovarian cancers, has been widely chosen for active targeting *via* folic acid due to their selective interaction.^{25,33} The transferrin receptor, upregulated in several malignancies, has become an important target due to its specificity to the glycoprotein transferrin, which is typically used as the targeting ligand.^{37,40,41} Nucleolin has been targeted in previous studies using the vascular targeting F3 peptide as well as nucleolin-specific aptamers, single-stranded oligonucleotides with high specificity.^{25,37,42-44} The αβ integrins are transmembrane proteins used as angiogenic biomarkers that are overexpressed in tumours.⁴⁵ The peptide arginine-glycine-aspartic acid (RGD), in its cyclic form, is recognised by most integrins and thus, the peptide used as the targeting ligand in cancer research.^{45,46} The expression of CD44 glycoproteins in tumours leads to increased metastatic potential.⁴⁷ As such, these receptors can be used for targeted PDT since they selectively bind hyaluronic acid.⁴⁷ Finally, endogenous lectins have also been targeted on cancer cell surfaces. The overexpression of lectins and carbohydrates and their use for targeted PDT will be reviewed in **Chapter 4**.

1.2.2. Gold nanoparticles

The following review on gold nanoparticles (AuNPs) for PDT is an up to date version of a contribution to a textbook on pre-clinical and clinical PDT, published earlier this year.²⁸ The use of gold nanoparticles (AuNPs) in biomedicine, especially PDT, is advantageous because of their excellent biocompatibility and the non-toxic nature of the gold core.⁴⁸ Additionally, AuNPs are highly stable and readily synthesised with good control over the nanoparticle size. The ease by which the surface can be modified with chemical and biological ligands is a further advantage.⁴⁸⁻⁵⁰ The strong interaction between gold and sulfur allows for the self-assembly of thiolated species on the gold core. As a result, surface modification of AuNPs is typically performed in this manner.⁵¹ The functionalisation of AuNPs with PS induces an enhancement in the production of $^1\text{O}_2$, due to the interactions between the PS and the metal nanoparticle. Therefore, AuNPs enable the administration of low doses of the drugs, which in turn leads to a reduction in the possible side effects of the therapy.⁴⁸

The first time that AuNPs were functionalised with a PS for PDT was reported by Russell and co-workers.⁵²⁻⁵⁴ The authors synthesised 2-4 nm AuNPs functionalised with a thiolated zinc phthalocyanine containing a C₁₁ mercaptoalkyl tether (C11Pc). The phase transfer reagent tetraoctylammonium bromide (TOAB) was used to assemble the C11Pc on the surface of the AuNPs. Additionally, TOAB enabled the solubilisation of the AuNPs in polar solvents to facilitate drug administration.⁵³ The authors reported that the C11Pc-AuNPs produced $^1\text{O}_2$ with a 50 % increase as compared to the free C11Pc. This was confirmed by the significantly higher $^1\text{O}_2$ quantum yield of C11Pc-AuNPs ($\phi_\Delta=0.65$) than that of the free C11Pc ($\phi_\Delta=0.45$). The increase in $^1\text{O}_2$ quantum yield in the presence of the AuNPs was assumed to be due to interactions between C11Pc and TOAB.⁵³ *In vitro* studies using HeLa cervical adenocarcinoma cells proved that the C11Pc-AuNPs were effectively internalised by the cells after a 4 h incubation.⁵⁴ The internalised C11Pc-AuNPs were irradiated for 20 min with a 690 nm diode laser, to induce the generation of $^1\text{O}_2$ for PDT. Following PDT treatment, the cells incubated with the C11Pc-AuNPs exhibited a considerable decrease in cell viability (43 %), improving that of the free C11Pc (74 %). Additionally, the PDT efficacy was further confirmed visually by the drastic change in cell morphology due to cell death *via* apoptosis.⁵⁴ The

promising *in vitro* results led to *in vivo* studies for the treatment of a sub-cutaneously implanted amelanotic melanoma, a common type of skin cancer, in mice.⁵² Camerin *et al.* successfully showed inhibition of the tumour growth following application of the PDT treatment, just 3 h after nanoparticle administration. Even though the C11Pc-AuNPs inhibited tumour growth, it was apparent that opsonisation of the C11Pc-AuNPs by the reticuloendothelial system (RES), *i.e.*, removal by the phagocytes, to the liver and spleen occurred. Such opsonisation reduces the average lifetime of C11Pc in the serum, which is key for the success of the PDT treatment. Moreover, the accumulation of AuNPs in both the liver and spleen could lead to undesired toxicity and other side effects.⁵²

In a similar approach, Nombona *et al.* prepared *ca.* 5 nm AuNPs functionalised with 1,6-hexanedithiol tetra substituted zinc phthalocyanine (ZnPc), stabilised *via* the phase transfer reagent TOAB.⁵⁵ The ZnPc-AuNPs were tested *in vitro* in MCF-7 human malignant breast cancer cells, where they were shown to induce good phototoxicity and an increased cell death as compared to studies with healthy fibroblast cells. The major drawback of this system was that the use of AuNPs only induced a moderate increase in PDT efficacy as compared to the free ZnPc. The authors attributed this observation to the limited $^1\text{O}_2$ production in PBS containing 2 % v/v DMSO, likely to be due to the quenching effects of aqueous environments. It was suggested that the synthesis of hydrophilic AuNPs would solve this problem and thus improve the PDT efficacy.⁵⁵

Not only phthalocyanines have been conjugated to AuNPs for PDT; porphyrins have also been studied. The first time a porphyrin was conjugated to gold nanoparticles was reported by Ohyama *et al.*⁵⁶ The authors successfully synthesised gold nanoparticles coated with a porphyrin monolayer *via* a porphyrin tetradeятate passivant.⁵⁶ Following that, the first studies using porphyrin coated gold nanoparticles for PDT were performed by Gamaleia *et al.*⁵⁷ This group synthesised 14.5 and 45 nm AuNPs functionalised with haematoporphyrin (Hp) and stabilised with polyvinylpyrrolidone. The Hp-AuNPs were more effective at producing ROS than the free Hp in solution, which was correlated with a higher PDT efficacy *in vitro* in MT4 T-cells and Jurkat human T-cell leukemia, especially using the 45 nm sized particles.⁵⁷ The functionalisation of

the 14.5 nm AuNPs with the photosensitiser 5,10,15,20-tetrakis(3-hydroxyphenyl)porphyrin (mTHPP) in a multilayer system was performed by Reum *et al.* *via* a layer-by-layer technique.⁵⁸ This technique allows for an effective control of the PS concentration, not only by the number of AuNPs, but also by altering the number of mTHPP monolayers around the AuNPs.⁵⁸

Zaruba *et al.* conjugated two porphyrin-brucine quaternary ammonium salts to 3-mercaptopropanoic acid modified AuNPs as potential agents for PDT.⁵⁹ *In vitro* and *in vivo* studies in PE/CA-PJ34 basaloid squamous cell carcinoma cells showed inconsistencies. *In vitro* studies showed a lower PDT efficacy for the AuNP conjugates than for the free porphyrin-brucine PS, possibly due to the aggregation of the AuNPs in cell culture media. However, *in vivo* studies induced reduction and complete regression of the tumours when the AuNPs were used. The authors speculated that the interaction between AuNPs and plasma proteins, mainly human serum albumin, *in vivo* enhanced the accumulation of the AuNPs in the cancer cells *via* an improved EPR effect.⁵⁹

The prodrug 5-ALA, which leads to the generation of the photosensitiser PpIX, has achieved particular success in PDT. The hydrophilic character of 5-ALA makes penetration through lipophilic biological barriers, such as cell membranes, difficult. The diagnostic success of 5-ALA is thus related to the disruption of epithelial barriers observed in neoplastic diseases, which facilitates 5-ALA penetration through the skin.⁶⁰ The conjugation of 5-ALA with AuNPs for an improved delivery and cytotoxic effect in PDT has been the subject of several studies.⁶¹⁻⁶⁴ Xu *et al.* synthesised 24 nm cationic gold nanoparticles electrostatically functionalised with 5-ALA.⁶¹ The use of these 5-ALA-AuNPs had several advantages over free 5-ALA related to selectivity and ${}^1\text{O}_2$ production. *In vitro* studies in K562 chronic myelogenous cells showed an increased delivery of 5-ALA with a high selectivity for tumour tissue for the 5-ALA-AuNPs. The authors attributed the increase in selectivity to the higher negative-zeta potential of tumour cells over healthy cells, which enables their binding to the cationic AuNPs. Additionally, the production of ${}^1\text{O}_2$ by PpIX was reported to be higher when 5-ALA was combined with AuNPs, as compared to free PpIX. The surface plasmon absorption band of the AuNPs might contribute to an increased absorption of light by the system, which thus results in a higher generation of ${}^1\text{O}_2$. The ability to produce more ${}^1\text{O}_2$ by the 5-ALA-

AuNPs also significantly improved the PDT efficacy.⁶¹ The use of 5-ALA functionalised AuNPs for the treatment of skin cancer, Mel-Rm metastatic melanoma cells, was reported by Mohammadi *et al.*⁶² The results of this study were similar to those obtained by Xu *et al.* since the ideal incubation time was found to be 4 h and the phototoxic damage following PDT was twice as high for the AuNPs as compared to free 5-ALA.⁶² Other research groups^{63,64} have studied the cooperative effect when AuNPs and 5-ALA are used in combination but without actual conjugation between the two. It was reported that the combination of AuNPs with 5-ALA for PDT is beneficial since it requires a smaller amount of 5-ALA to induce good phototoxicity. As a result, the PS can be used in reduced quantities, which can avoid the potential harmful effects of high concentrations on healthy cells.⁶⁴

PpIX has also been directly combined with AuNPs for PDT.⁶⁵⁻⁶⁷ Khaing Oo *et al.* studied the effect of the AuNPs size on the enhancement of ROS production using 19, 66 and 106 nm AuNPs electrostatically functionalised with PpIX.⁶⁵ In solution, the enhancement of the generation of ROS was found to correlate with the increase in AuNP size, with the 106 nm producing the highest levels of ROS. The size-dependence of ROS generation was speculated to be relative to the localised plasmonic field of AuNPs, which is larger in AuNPs of bigger sizes. However, *in vitro* studies with MDA-MB-231 human breast adenocarcinoma cells showed that the 66 nm AuNPs performed the best, producing both the highest ROS and the highest toxicity. This effect was attributed to the low uptake of the large (106 nm) AuNPs by the cells. Nevertheless, the use of AuNPs of any size induced a higher degree of cytotoxicity (> 50 % cell death) compared to free PpIX (22.6 % cell death).⁶⁵ In another study, PpIX was used to functionalise smaller AuNPs (7 nm diameter) *via* 6-mercaptop-1-hexanol ligands attached to the surface of the AuNPs. The conjugates were tested *in vitro* with HeLa cervical cancer cells and were found to be good delivery vehicles to produce a high photodynamic cytotoxicity. The major drawback of this method was the limited selectivity towards the tumour site, which the authors suggested could be improved by the use of active targeting.⁶⁶ Ashjari *et al.* further evaluated the combination of PpIX conjugated to AuNPs *via* cysteine.⁶⁷ The increase in ROS production as well as *in vitro* cytotoxicity, 24 % cell death for free PpIX *versus* 59 % cell death for the PpIX-cysteine-

AuNPs, was found to be a result of the energy transfer from the surface plasmon of the AuNPs to PpIX on their surface.⁶⁷

Studies with other photosensitisers such as bacteriochlorins are less widespread but have also been reported.⁶⁸ As an example, Pantiushenko *et al.* reported the synthesis of a thiolated bacteriochlorophyll a. The combination of this PS with AuNPs increased the circulation time in the blood of rats bearing sarcoma M-1 and increased the specificity towards the tumour tissue due to the EPR effect.⁶⁸

Use of polyethylene glycol for steric stabilisation

From the above studies, it is apparent that using AuNPs as drug carriers has a positive effect in PDT of cancer. However, one of the biggest limitations is the opsonisation of the nanoparticles by the reticuloendothelial system (RES), which leads to a short half-life in the serum and thus rapid clearance from the body. A solution to this problem is the modification of the AuNPs with water soluble polyethylene glycol (PEG), which is approved for human intravenous application.⁶⁹⁻⁷¹ PEG provides stealth-like properties to the AuNPs and it has a high resistance to protein adsorption.^{25,32,70} As a result, the conjugates are not easily taken up by the RES, which leads to an increased circulation time in the blood. This is a clear advantage since rapid clearance by the RES limits the potential of the functionalised AuNPs for selective accumulation within the tumour tissue through the EPR effect, which in turn leads to the accumulation of the AuNPs in the liver, kidney and spleen.^{25,31}

The Burda group^{70,72-74} focused on the use of 5 nm PEGylated gold nanoparticles functionalised with a silicon phthalocyanine (Pc4). Pc4 was non-covalently bound to the AuNPs *via* a N-Au bond to the terminal amine group on the Pc4 axial ligand. This bond is relatively weak and the production of stable Pc4-AuNP conjugates is possible due to the stabilisation provided by the PEG ligands.⁷⁰ PEG stabilises the AuNPs by steric repulsion to avoid aggregation. Furthermore, PEG provides stabilisation to the Pc4 ligand through van der Waals interactions taking place at the PEG end closest to the surface of the AuNPs.⁷² The result is a cage-type structure which can deliver the hydrophobic Pc4 within cells. The nanoparticles enter the tumour tissue *via* the EPR effect and then Pc4 is released into lipid membranes of the cells.^{70,74} Initial *in vitro*

studies using HeLa cancer cells were promising, showing a negligible dark toxicity of the particles but with a phototoxicity of 90 %. The biggest improvement as compared to the use of Pc4 alone was that the incubation time required for accumulation within the target tissue was only 2 h for the nanoparticles, rather than 2 days when non-conjugated Pc4 was administered.⁷⁰ This research group extended their work by studying the excretion pathways of the nanoparticles over a 7-day period. The conjugates were injected in mice, where they were shown to produce no adverse effects, and their pathway was followed using fluorescence. It was suggested that even though some of the AuNPs were retained in the spleen and liver, the most likely excretion route was through the renal and hepatobiliary systems.⁷⁴

Localisation of phthalocyanine-gold nanoparticle conjugates has also been studied *in vivo* by Camerin *et al.* over an 8-week period.⁷⁵ PEGylated AuNPs functionalised with a self-assembled C11Pc photosensitiser (C11Pc-PEG-AuNPs) were intravenously administered to C57/BL6 mice bearing a subcutaneous B78H1 amelanotic melanoma. The C11Pc-PEG-AuNPs were initially found in the serum in high quantities, which is advantageous for a good cytotoxic effect. The mice were treated with light either 3 h or 24 h following injection of the AuNPs. The optimum results were obtained with light irradiation after 3 h, which induced vascular damage to the tumour leading to the mice staying tumour-free for 18 days. Most importantly, 40 % of the mice showed no tumour regrowth and complete survival, up to 45 days after the treatment.⁷⁵ The fate and excretion of the AuNPs was also investigated. The C11Pc-PEG-AuNPs, initially located in the serum in high concentrations, started to move towards the liver and the spleen 1 week after administration. At this time period, there was a maximum accumulation in these organs, which was later decreased by 70 % in the liver and 30 % in the spleen 8 weeks after administration. These results suggest that AuNPs are internalised selectively within the melanoma and subsequently eliminated *via* the bile-gut pathway.⁷⁵

Active targeting for PDT

Another significant advantage of using PEGylated AuNPs is that the terminal carboxylic acid moiety of the PEG can be functionalised with chemical and/or biological ligands for active targeted PDT. Stuchinskaya *et al.* used anti-HER2 antibodies conjugated to

C11Pc-PEG-AuNPs in order to target human epidermal growth factor receptor 2 (HER2) positive breast cancers.⁶⁹ The antibody was attached to the PEG on the surface of the AuNPs *via* an amide linkage between the amine groups of the antibody and the terminal carboxyl group of the PEG ligand. These AuNP conjugates were used *in vitro* in HER2 positive SK-BR-3 human breast adenocarcinoma cells, HER2 negative MDA-MB-231 human breast cancer cells and healthy mammary epithelial MCF-10A cells. Cell cytotoxicity was significantly higher for the HER2 positive SK-BR-3 cells (60 % cell death) as compared to either HER2 negative MDA-MB-231 breast cancer cells (25 % cell death) or the healthy MCF-10A cells (7 % cell death). Therefore, it was concluded that the internalisation of the AuNPs is enhanced by the selective binding of the anti-HER2 antibodies to the HER2 receptors.⁶⁹ Obaid *et al.* used the same C11Pc-PEG-AuNPs conjugates to prove the targeting ability of the lectin Jacalin towards the T antigen overexpressed in HT-29 human colorectal adenocarcinoma cells.^{33,39} Nanoparticle uptake by the colon cancer cells was effectively enhanced with the Jacalin targeting agent. Moreover, the higher selectivity to tumorigenic cells induced a significant increase in PDT efficacy (95-98 % cell death).³⁹ Both the anti-HER2 antibody and the Jacalin conjugated C11Pc-PEG-AuNPs were found to locate in the acidic organelles, *i.e.*, the lysosomes, inside the cells following receptor-mediated endocytosis.³³ A comparative study between the two targeting agents, anti-HER2 antibody and Jacalin, was performed in both SK-BR-3 and HT-29 cells.³³ The levels of cytotoxicity induced by both biomolecules were comparable. However, the main difference was seen in dark toxicity, since the anti-HER2 antibody AuNP conjugates were less toxic than the Jacalin AuNP conjugates in the absence of light.³³

The use of peptides as targeting agents has been studied particularly for brain tumours. Glioma cancer cells overexpress the epidermal growth factor receptor (EGFR) on their surface, which can be specifically targeted using EGF peptides. The Burda group conjugated EGF peptides to their previously developed Pc4-PEG-AuNPs *via* the PEG ligand.^{72,76} *In vitro* studies showed that the drug was taken up by the cells through receptor-mediated endocytosis, with the particles just acting as delivery vehicles and not being internalised by the cells. More importantly, *in vivo* experiments in mice showed that the conjugates successfully go through the blood-brain barrier (BBB). The accumulation and selectivity towards the tumour was reported to be 10 times higher

when the EGFR targeting agents were present. Moreover, only 4 h incubation with the conjugates after drug administration was required for successful PDT.⁷² The EGFR conjugated AuNPs stayed longer in circulation than the untargeted AuNPs and were specifically delivered into the tumour tissue as well as the liver.⁷⁶ Even though the EGF targeted AuNPs circulated longer in the serum, the conjugates were efficiently excreted from the body 7 days after administration *via* the spleen and urinary tracts.⁷⁶ Brain tumours were further targeted by the Broome group using transferrin as the targeting ligand.⁵⁰ The authors used 5 nm AuNPs loaded with Pc4 and a seven amino acid transferrin peptide (Tf_{pep}) to target the overexpressed transferrin receptor in glioma cells. The targeted AuNPs were internalised by the cells only 1 h after incubation, a 2-3 fold improvement compared to the untargeted AuNPs. The enhanced internalisation correlated with an improved phototoxic effect following PDT, both *in vitro* and *in vivo*, with the targeted AuNPs being able to induce effective cell death at concentrations 10 times lower than the untargeted AuNPs.⁵⁰ In an attempt to increase selectivity even further, the Broome group attempted the use of dual targeted AuNPs. The authors functionalised Pc4-AuNPs with both EGF peptides and Tf_{pep}.⁷⁷ Even though the dual targeted AuNPs showed a considerable improvement over untargeted AuNPs in PDT efficacy and *in vivo* delivery crossing the BBB, there was only a slight enhancement over the single targeted AuNPs using either Tf_{pep} or EGF peptides alone.⁷⁷ The use of transferrin as a targeting agent was also explored by Yu *et al.*⁷⁸ These authors synthesised AuNPs functionalised with a polymer layer to which the PS methylene blue and transferrin were attached. HeLa cells overexpressing the transferrin receptor effectively internalised these targeted conjugates *via* receptor-mediated endocytosis three times as much as the non-conjugated AuNPs, which in turn improved the photodynamic efficiency.⁷⁸

The protein nucleolin, found overexpressed in the cytoplasm and plasma membrane of some cancer cells, was targeted using the aptamer AS1411, a guanine-rich nucleotide.^{42,79} In order to bind to the nucleolin receptors on the cells, AS1411 adopts the stable G-quadruplex structure. G-quadruplex structures have been shown to bind intercalatively to cationic porphyrins. Ai *et al.* synthesised 13 nm AuNPs and functionalised these particles with a thiolated AS1411 aptamer conjugated to the PS N-methylmesoporphyrin IX (NMM).⁴² *In vitro* studies with HeLa human cervical cancer

cells, that overexpress nucleolin, showed a high amount of the particles being taken up. The incubation of those same cells with non-conjugated AuNPs showed significantly less uptake, highlighting that the selectivity towards the tumour was increased by the AS1411 aptamer.⁴²

A special type of active targeting was reported by Li *et al.*⁸⁰ The authors took advantage of the glutathione (GSH)-response within cells, which consists of the cleavage of disulfide bonds and it has been reported to be overexpressed in tumour cells as compared to healthy cells. Therefore, the activation of the GSH-response is a potential platform to deliver drugs more selectively to cancer cells. In this study, Li *et al.* developed a GSH-responsive nanoplatform for the selective delivery of the PS pheophorbide A (PheoA).⁸⁰ PheoA was conjugated to a thiolated heparin (H), selected for its good water solubility and biocompatibility as well as its anti-inflammation, anti-angiogenesis and anti-tumour cell proliferation properties. The PheoA-H was attached to the surface of 30 nm AuNPs. The conjugation of PheoA with the AuNPs inhibited the fluorescence and the photo-activity of the PS due to fluorescence resonance energy transfer (FRET) between the light-excited PheoA and the AuNPs, which act as FRET acceptors. *In vitro* studies were performed using A549 adenocarcinomic human alveolar basal epithelial cells, which have a higher level of GSH activity as compared to healthy lung cells. The *in vitro* studies revealed that internalisation of PheoA was enhanced by the conjugation to the AuNPs. Following internalisation, GSH induces the release of H-PheoA by breaking the thiol bond between the PheoA-H and the AuNPs. Consequently, PheoA regains its photoactivity and, upon irradiation with light, can induce phototoxic effects to the cells. These results were further confirmed *in vivo* in A549 tumour-bearing SKH1 mice.⁸⁰

Other gold nanostructures

Other gold nanostructures, including gold nanorods, gold nanoclusters and gold nanostars have also been considered as drug carriers for PDT. Huang *et al.* have used silica coated fluorescent gold nanoclusters (SiO₂-AuNCs) functionalised with the photosensitiser chlorin e6 (Ce6).⁸¹ The silica coating was used to enhance the photostability and chemical stability of the fluorescent AuNCs. *In vivo* experiments in mice showed that the PDT efficacy and thus the tumour regression was improved using

the Ce6-SiO₂-AuNC conjugates as compared to Ce6 alone. Furthermore, the use of NIR fluorescence enabled the location of the AuNCs to be monitored during PDT.⁸¹ Li *et al.*⁸² functionalised gold nanorods (AuNRs) with a sulfonated aluminium phthalocyanine (AlPcS) *via* electrostatic interactions. The conjugation of AlPcS to the AuNRs resulted in a 5-fold increase of its fluorescence due to metal-enhanced fluorescence. The AlPcS-AuNRs were effectively taken up by QGY liver cancer cells and were shown to provide improved PDT efficiency as compared to the free AlPcS.⁸² An aluminium phthalocyanine was also used by Hu *et al.* and attached to gold nanorings in a layer-by-layer approach for effective PDT.⁸³ The use of endoperoxides as a chemical source of ¹O₂ for PDT was explored in combination with AuNRs.⁸⁴ Chemical generation of ¹O₂ by these endoperoxides has the potential to avoid the problems related to the tumour inherent hypoxia and tissue penetration in order to enhance the effects of PDT.⁸⁴

The use of targeted PDT with gold nanostructures other than spheres has also been reported. The use of folic acid in combination with either PpIX-AuNRs⁸⁵ or Chlorin e6-gold nanoclusters⁸⁶ has led to an enhanced and selective internalisation by cancer cells and thus improved PDT efficiency. Additionally, Kuo *et al.* used AuNRs to target A549 human lung carcinoma malignant cells, which overexpress the epidermal growth factor receptor (EGFR) on their surface.⁸⁷ The AuNRs were functionalised with the PS indocyanine green and anti-EGFR antibodies. These conjugates were shown to be efficient PDT agents as well as probes for bioimaging in the NIR region.⁸⁷

Combination therapies

The combination of PDT with other therapies for the treatment of cancer is gaining particular interest. The combination of PDT with immune system activation has been described as promising for the treatment of metastatic breast cancer. Marrache *et al.* synthesised a hybrid nanoparticle platform composed of polymeric nanoparticles conjugated to a ZnPc photosensitiser, which were then coated with AuNPs.⁸⁸ The AuNPs were functionalised with 5'-purine-purine/T-CpG-pyrimidine-pyrimidine-3'-oligodeoxynucleotides (CpG-ODN). The CpG-ODN is a single-stranded DNA immunostimulant capable of activating dendritic cells and thus initiating an immune response. *In vitro* studies using 4T1 metastatic mouse breast carcinoma cells showed

not only a high photodynamic effect following PDT ($IC_{50}=2.8\text{ nM}$), but also substantial immune activation.⁸⁸

The combination of AuNPs-PDT with chemotherapy is also being increasingly studied. Li *et al.* loaded the PS chlorin e6 and the chemotherapeutic agent doxorubicin (DOX) in mesoporous silica coated AuNPs.⁸⁹ HeLa cells effectively internalised the conjugates into the cytoplasm, allowing for the delivery of DOX into the nucleus for effective chemotherapy. Following laser irradiation at 660 nm, the combination of chemotherapy and PDT induced an IC_{50} of $1.152\text{ }\mu\text{g/mL}$, a considerable improvement from either chemotherapy ($IC_{50}=3.215\text{ }\mu\text{g/mL}$) or PDT ($IC_{50}=7.232\text{ }\mu\text{g/mL}$) performed individually.⁸⁹

The largest interest in combination therapies in conjunction with AuNPs lies with the simultaneous use of photothermal therapy (PTT) and PDT. PTT involves the use of light-absorbing molecules or nanoparticles, the photothermal agents, that lead to the heating of the local tumour environment.^{90,91} Following light absorption, the excited photothermal agent releases energy non-radiatively through vibrational modes, which induces an increase in the kinetic energy of the matrix species around the photothermal agent and thus an increase in temperature.⁹⁰ The combination of PDT/PTT with AuNPs has been investigated in a variety of studies.⁹²⁻⁹⁴ Kang *et al.* synthesised a hybrid nanomaterial composed of 5-7 nm AuNPs encapsulated with the PS PheoA, which was conjugated to hyaluronic acid.⁹² The AuNPs act as the PTT agent, the PheoA is responsible for the generation of ROS for PDT, and hyaluronic acid is the targeting agent towards the overexpressed CD44 receptor on lung cancer cells. The hybrid nanomaterial was selectively internalised by the tumour *via* receptor-mediated endocytosis only 3 h after administration and it induced cell death levels of 78.6 % following combined PDT/PTT *in vitro*.⁹² Hari *et al.*⁹³ used the PS acridine orange (AO), which mainly accumulates in lysosomes. *In vitro* studies with MCF-7 breast cancer cells showed that AO-AuNPs were internalised twice as much as free AO. As a result, the efficacy of the PDT/PTT cancer therapy was improved, inducing 78.6 % of cell death.⁹³ Chen *et al.* created core-shell micelles formed by the combination of polymers with the dye 5,10,15,20-tetrakis(pentafluorophenyl)-21H,23H-porphine (PF6), which acts as the PS.⁹⁴ Furthermore, the micelles were decorated with AuNPs as effective PTT agents.

The cells were readily internalised by A549 lung cancer cells and induced 80 % cell death following combined PDT/PTT.⁹⁴

The combination of PTT/PDT with other gold nanostructures has also been extensively studied.⁹⁵⁻¹⁰⁴ Kuo *et al.* used indocyanine green functionalised AuNRs for combined PTT/PDT. The integration of the two therapies was found to effectively enhance the cell killing as compared to the use of PDT on its own.¹⁰⁴ Jang *et al.*⁹⁵ effectively combined near infrared (NIR) fluorescence imaging with PTT/PDT of cancer. The authors used AuNRs with PEG conjugated to the PS aluminium (III) phthalocyanine tetrasulfonate (AlPcS₄). *In vitro* studies in squamous cell carcinoma (SCC7) cells showed that the use of AuNRs improves by 4-fold the internalisation as well as the selectivity towards cancerous cells as compared to free AlPcS₄, which results in an improved photodynamic activity. These *in vitro* results were further confirmed *in vivo* through the treatment of female athymic nude mice with implanted SCC7 squamous cell carcinoma cells. Acute apoptosis and tissue loss was observed for mice treated with the AlPcS₄-AuNR followed by PDT, reducing tumour growth by 79 %. The effect was intensified with dual PTT/PDT therapies, reducing tumour growth by up to 95 %.⁹⁵ The main drawback in this study was the need of two different laser sources for PDT (670 nm) and PTT (810 nm).⁹⁵ NIR combined PTT/PDT was also demonstrated for AuNRs conjugated to a silicon naphthalocyanine with similar positive results.⁹⁶ Additionally, Tham *et al.* further improved the effective use of AuNRs for PTT/PDT by using an external targeting agent, hyaluronic acid, which targets the CD44 receptors overexpressed on cancer cells.⁹⁷ Other studies with gold nanoshells⁹⁸, gold nanorings⁹⁹, gold nanostars¹⁰⁰ and gold nanocages¹⁰¹ have also shown the improved destruction of cancer cells when PDT and PTT are used in combination. Within these studies, it is important to note the advantage of the gold nanocages functionalised with the natural PS hypocrellin.¹⁰¹ In this study, the authors were able to perform PDT and PTT simultaneously using a single laser source at 790 nm, which could induce the generation of ¹O₂ and the production of heat at the same time.¹⁰¹ More importantly, the ability to magnetically guide the drugs to the tumour cells is an additional improvement for combined PTT/PDT. Bhana *et al.* developed gold nanopopcorns with an iron oxide core, which were functionalised with a silicon naphthalocyanine.¹⁰² The iron oxide core provides the paramagnetism that allows the nanopopcorns to be

selectively guided towards the tumours *via* an external magnet for effective PTT/PDT. Indeed, the use of the external magnet induced a 92.9 % cell death compared to only 73.7 % when PTT/PDT were performed without the external guiding.¹⁰² The combination of PDT with other techniques such as surface-enhanced Raman scattering (SERS) imaging^{103,105-107} for theranostics, or gene delivery¹⁰⁸ is also being studied.

Use of AuNPs as photosensitisers

A particularly exciting development is the possibility of AuNPs and other gold nanostructures to act as $^1\text{O}_2$ generators by themselves without the presence of any PS when exposed to light irradiation. The first observation of this effect was reported by Vankayala *et al.* in 2011.¹⁰⁹ These authors reported that the irradiation of metallic nanoparticles, including AuNPs, at their surface plasmon absorption band induced the generation of $^1\text{O}_2$.¹⁰⁹ Since then, other groups have reported similar observations. Misawa *et al.* showed how AuNPs contribute to the production of ROS, including $^1\text{O}_2$, following UV and X-ray irradiation.¹¹⁰ The authors highlighted the possibility of using AuNPs in combination with X-ray radiological and PDT destruction of tumours.¹¹⁰ Jiang *et al.* showed how AuNPs (40 nm) and AuNRs could act as PS and induce the production of $^1\text{O}_2$ when exposed to one- and two-photon excitation.¹¹¹ El-Hussein *et al.* compared the ability to produce $^1\text{O}_2$ by AuNPs and silver nanoparticles (AgNPs).¹¹² Even though both AuNPs and AgNPs were able to induce the generation of $^1\text{O}_2$, AgNPs were found to have a more powerful effect. The better action of AgNPs was thought to be due to the higher absorption efficiency of AgNPs in the therapeutic window as compared to AuNPs.¹¹² Recently, Chadwick *et al.* investigated the reasons why metallic nanoparticles are able to act as PS.¹¹³ These authors found that the behaviour of metallic nanoparticles as PS was due to the presence of 'hot electrons'. The term 'hot electrons' refers to the electrons found in the conduction band, which can reach very high temperatures when they absorb light from a short laser pulse.¹¹³ The use of AuNPs as PS has several potential advantages over conventionally used PS. The most important one is the high extinction coefficients of AuNPs, between 3-5 times higher than that of conventional PS, which could lead to an increased production of $^1\text{O}_2$.¹⁰⁹

1.2.3. Upconverting nanoparticles

Upconverting nanoparticles (UCNPs) have been classified as active nanoparticles for PDT because they actively participate in the generation of ${}^1\text{O}_2$.³² Even though the UCNPs are unable to produce ${}^1\text{O}_2$ by themselves, UCNPs are active in the energy transfer to the PS, which then allows the production of ${}^1\text{O}_2$ and other ROS.²³ UCNPs are excited with near-infrared (NIR) light, which is followed by their emission of higher energy visible light.^{30,31} This property is achieved by the use of rare-earth metals, mainly lanthanides, doped into a solid state host lattice.^{23,31} A description on the synthesis of UCNPs, the choice of host lattice and dopants, as well as the mechanisms of upconversion will be discussed in **Chapter 5**.

The visible light emission of UCNPs following excitation with NIR radiation can be used to excite a PS located near the surface of the UCNPs, which thus leads to the generation of ${}^1\text{O}_2$ (**Figure 1.8**).³⁰⁻³² As a result, the use of NIR light for the excitation of the UCNPs allows for a deeper penetration into the tissue, reaching tumours that are situated further from the skin surface.^{27,30,31} The functionalisation of UCNPs with a PS can be achieved by different techniques, including the encapsulation of the PS in a silica layer that surrounds the core of the UCNPs, the covalent linkage of the PS to the UCNPs, the physical adsorption of the PS to the surface of the UCNPs *via* hydrophobic interactions, the direct coating of the UCNPs with a layer of PS, and the use of electrostatic interactions,^{30,32} as shown in **Figure 1.8**. The use of UCNPs for PDT requires that these nanoparticles are biocompatible and selective towards the cancer tissue.³⁰ The biocompatibility and water dispersibility of the UCNPs can be achieved *via* several methods of surface modification, including the use of a silica layer and the functionalisation of the UCNPs with water-soluble polymers such as PEG. Additionally, the energy transfer between the UCNPs and the PS should be high enough to allow for an efficient photosensitisation and the PS itself should not leak from the nanoparticle.³⁰

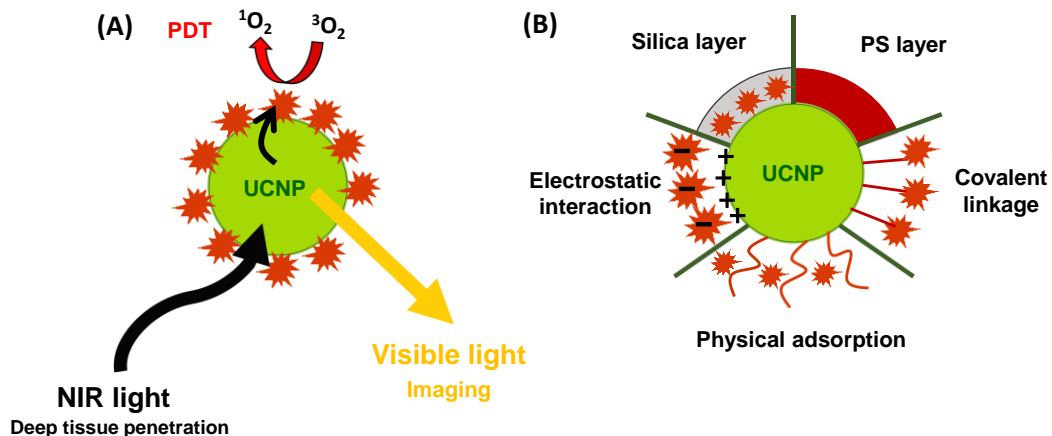


Figure 1.8. (A) Schematic representation of the production of $^1\text{O}_2$ due to the energy transfer taking place between the UCNPs and the PS. Following irradiation with NIR light, the UCNPs emit visible light, which can be used for both excitation of the PS that leads to the generation of $^1\text{O}_2$ and for bioimaging. (B) Schematic representation of the different PS loading mechanisms on the surface of the UCNPs. (A-B) The photosensitiser is shown in red. Figure adapted from Refs. 30-32.

The use of UCNPs for PDT with or without active targeting

A. Silica layer

In 2007, Zhang and co-workers reported the use of silica-coated UCNPs for PDT for the first time.¹¹⁴ These authors synthesised sodium yttrium fluoride (NaYF_4) UCNPs codoped with ytterbium (Yb^{3+}) and erbium (Er^{3+}) with a size ranging between 60-120 nm due to batch-to-batch variations. The UCNPs were coated with a silica layer, in which the photosensitiser merocyanine 540 (M-540) was embedded. Additionally, the UCNPs were conjugated with anti-MUC1/episialin antibody, selective towards the MUC1/episialin receptor overexpressed on the surface of MCF-7/AZ breast cancer cells. Irradiation of these UCNPs with a 974 nm laser induced the emission of light at *ca.* 537 nm and *ca.* 635 nm, which was used to excite M-540 to stimulate the production of $^1\text{O}_2$. *In vitro* studies in MCF-7/AZ cells showed the selective targeting of the UCNPs followed by effective PDT after 36 min NIR irradiation, which induced cell death for the samples treated with the functionalised UCNPs.¹¹⁴ This group also explored the use of other photosensitisers embedded in the silica layer for efficient $^1\text{O}_2$ production. The use of tris(bipyridine)ruthenium(II) ($\text{Ru}(\text{bpy})_3^{2+}$) was found to be efficient for the generation of $^1\text{O}_2$ and thus a potential candidate for use in PDT.¹¹⁵

Even though the use of a silica layer for the encapsulation of the PS in the UCNPs has shown great potential in PDT, it is limited by a series of problems.^{32,116,117} The incorporation of PS within the silica shell is variable and difficult to control because of the weak interaction between the PS and silica, mainly consisting of hydrogen bonds and van der Waals forces.^{32,116,117} The site of action of $^1\text{O}_2$ is also limited since the silica layer blocks the exit of the $^1\text{O}_2$ from the cells.¹¹⁷ Additionally, the possibility of UCNPs aggregation is high due to the low stability of amorphous silica in physiological conditions.³² As a result, the PDT efficiency for silica-coated UCNPs is low.^{116,117} A possibility to enhance the PDT efficacy of silica-coated UCNPs is to modify the interaction between the PS and the silica layer to lead to stronger covalent bonds, so the incorporation of the PS on the silica layer will be improved and more easily controlled.¹¹⁶ Yang *et al.* combined a naturally occurring PS, hypericin, to *ca.* 20 nm silica-coated NaYF_4 (Yb^{3+} , Er^{3+}) UCNPs *via* a strong covalent interaction.¹¹⁶ The covalent interaction was possible due to the conjugation of hypericin with (3-isocyanatopropyl)triethoxysilane (TESPIC). Hypericin-TESPIC was then co-hydrolysed and co-condensed with tetraethoxysilane (TEOS) and (3-aminopropyl)triethoxysilane (APTES) to allow the covalent conjugation between hypericin and the silica layer on the surface of the UCNPs. The authors found that the $^1\text{O}_2$ production for this system was significantly higher than for the UCNPs where hypericin was directly encapsulated within the silica layer, primarily due to the higher loading ability of hypericin *via* covalent conjugation. For selective tumour uptake, the UCNPs were further functionalised with folic acid to selectively target the overexpressed folate receptors on cancer cells. Indeed, *in vitro* studies showed a higher uptake in HeLa cervical cancer cells as compared to healthy human embryonic kidney 293T cells. Furthermore, following NIR irradiation (980 nm) for 10 min, the folic acid-hypericin functionalised UCNPs were effective at inducing cell death *via* apoptosis for the HeLa cell line.¹¹⁶

Another method to enhance the PDT efficacy of silica-coated UCNPs is the use of mesoporous silica materials.^{32,117} Mesoporous silica (mSiO_2) provides improved water solubility than amorphous silica since it allows for a greater efficiency of energy transfer and it has a large surface area and porous structure.^{32,117,118} Guo *et al.* developed 90 nm NaYF_4 (Yb^{3+} , Er^{3+}) UCNPs coated with a mesoporous silica shell and attached a ZnPc into the pores of the mSiO_2 .¹¹⁷ *In vitro* studies in MB49-PSA bladder cancer cells showed

efficient intracellular ${}^1\text{O}_2$ production, which led to ${}^1\text{O}_2$ -induced apoptosis following irradiation at 980 nm, as confirmed by changes in the morphology of the cell nucleus, DNA fragmentation, and cytochrome c release from the mitochondria. The main drawback with this system was the increase in dark toxicity concomitant with an increase in the concentration of UCNPs.¹¹⁷ In another study, Xu *et al.* used vitamin B₁₂ (VB₁₂) as a PS, given its porphyrin-like structure.¹¹⁹ VB₁₂ was conjugated to the 20 nm thick mSiO₂ shell on *ca.* 20 nm NaYF₄ (Yb³⁺, Er³⁺) UCNPs. The PDT effect was evaluated in MDA-MB-231 human breast adenocarcinoma cells. The authors reported that the 980 nm PDT-induced cell death was dependent on the concentration of VB₁₂ within the UCNPs, as well as the irradiation time to which the cells were exposed.¹¹⁹

A problem associated with the use of a mSiO₂ layer to load the PS is the high chance of PS release when the surface of the mesoporous silica layer is unmodified.¹¹⁸ In order to avoid the leaking of the PS from the UCNPs, Hou *et al.* added a cross-linked lipid as the outer layer in the mSiO₂-coated UCNPs.¹¹⁸ The lipid layer was made of an amphiphilic polymer, PEG linked to octadecyl-quaternised polyglutamic acid (OQPGA), to which the peptide arginine-glycine-aspartic acid (RGD) was attached (RGD-PEG-OQPGA). The use of RGD-PEG-OQPGA not only avoided the release of the PS from the UCNPs thanks to the presence of OQPGA, it also increased the circulation time of the UCNPs within the serum with the presence of PEG. Additionally, the RGD-PEG-OQPGA also enhanced the selective uptake of the UCNPs by cancer cells due to the presence of the targeting ligand RGD. The RGD peptide is selective towards the $\alpha\text{v}\beta$ integrin, overexpressed in HeLa cervical cancer cells.¹¹⁸ The result was a triple-layered system made of a 25 nm NaYF₄ (Yb³⁺, Er³⁺) core, a 25 nm mSiO₂ shell in which the PS ZnPc was encapsulated, and a cross-linked lipid outer layer with great potential for PDT treatment.¹¹⁸

One of the first investigations of *in vivo* PDT with UCNPs was performed with mSiO₂-coated UCNPs, as reported by Idris *et al.*¹²⁰ The authors synthesised NaYF₄ (Yb³⁺, Er³⁺) UCNPs covered by a mSiO₂ shell, in which two PS, M-540 and ZnPc, were embedded for a dual-PS approach. The combination of two PS within the same nanoparticle system enhanced the production of ${}^1\text{O}_2$, which was higher than for UCNPs functionalised only with either M-540 or ZnPc alone. The higher production of ${}^1\text{O}_2$ correlated *in vitro* with a higher PDT efficacy in B16-F0 melanoma cells. Additionally, the authors injected

C57BL/6 mice bearing melanoma tumours with the dual-functionalised UCNPs for *in vivo* therapy. Following NIR-PDT at 980 nm, the tumour growth rate was shown to be slower than for the control groups not treated with the UCNPs. In order to improve the *in vivo* efficacy, the UCNPs were further functionalised with PEG and folic acid. The addition of PEG increases the circulation in the blood, as previously mentioned, while the presence of folic acid selectively targets the overexpressed folate receptors on the surface of melanoma cells. The authors found that the active targeting was important to strengthen the therapeutic efficacy and significantly reduce tumour growth in the treated mice. Unfortunately, complete tumour regression was not possible under these conditions.¹²⁰

B. Polyethylene glycol

The use of PEG for the water-solubility of UCNPs has also been reported.¹²¹⁻¹²⁵ PEG does not only provide aqueous solubility, it also induces biocompatibility and increases the circulation time of the UCNPs in the serum, as previously mentioned. The first report on the use of PEG for UCNPs was published in 2009 by Ungun *et al.*¹²¹ These authors synthesised 160 nm NaYF₄ (Er) UCNPs loaded with tetraphenylporphyrin (TPP) and an outer layer of PEG-*block*-poly(caprolactone) (PEG-*b*-PCL), as potential candidates for NIR-PDT.¹²¹ *In vitro* studies were first performed by Shan *et al.*¹²² Their UCNPs were similar to those reported by Ungun *et al.* but using a slightly different PEG copolymer. PEG-*b*-PCL was substituted by PEG-*block*-poly(DL)lactic acid (PEG-*b*-PLA) due to its higher stability in physiological conditions.¹²² The 100 nm NaYF₄ (Yb³⁺, Er³⁺) UCNPs loaded with TPP and PEG-*b*-PLA were tested in HeLa cervical cancer cells. The UCNPs were shown to induce no dark toxicity. However, following 978 nm NIR-PDT (45 min irradiation at 134 W/cm²) those cells treated with the functionalised UCNPs presented 75 % cell death.¹²² The use of PEG without conjugation to other copolymers was reported by González-Béjar *et al.*¹²³ These authors described the synthesis of *ca.* 30 nm oleate-capped NaYF₄ (Yb³⁺, Er³⁺), which they coated with PEG for water-solubility. Additionally, a diiodo substituted BODIPY PS was embedded in the PEG coat. These BODIPY-PEG functionalised UCNPs were shown to generate ¹O₂ following irradiation at 975 nm. *In vitro* studies in human neuroblastoma SH-SY5Y cells confirmed *ca.* 50 % of the treated cells died following PDT (45 min irradiation at 239 mW) *via*

apoptosis. Furthermore, the BODIPY-PEG functionalised UCNPs showed only limited dark toxicity with 10 % death in the absence of NIR irradiation.¹²³

The investigation on the use of PEGylated UCNPs for *in vivo* PDT was first reported by Wang *et al.*¹²⁴ Oleate-capped NaYF₄ (Y³⁺, Yb³⁺, Er³⁺) UCNPs of 30 nm in diameter were functionalised with the amphiphilic polymer PEG-grafted poly (maleic anhydride-alt-1-octadecene), to which the PS chlorin e6 was attached *via* hydrophobic interactions. The synthesised UCNPs were shown to induce good phototoxicity *in vitro* following 980 nm NIR-PDT (10 min irradiation at 0.5 W/cm²). The promising results *in vitro* were further tested *in vivo* using Balc/c mice bearing 4T1 murine breast tumour. Intratumoural injection of the functionalised UCNPs was followed by 980 nm NIR-PDT (30 min irradiation at 0.5 W/cm²). Out of the 10 treated mice, the tumours of 7 were completely eliminated over a 2-week period, reaching survival periods of more than 60 days. The fate of the functionalised UCNPs was also studied, reaching the conclusion that the UCNPs are initially located around the injection site but move towards the liver and spleen two weeks later due to opsonisation by the RES system. Complete clearance from these organs was seen 60 days after injection. The advantages of using NIR-PDT was further investigated by blocking the tumours on the mice using 8 mm thick pork tissue. While PDT using a 660 nm laser induced no reduction in tumour growth, 980 nm-PDT led to a slower tumour progression.¹²⁴

The use of an inorganic photosensitiser, titanium dioxide (TiO₂), was reported by Zhang and co-workers.^{125,126} Core-shell 25 nm NaYF₄ (Yb³⁺, thulium (Tm³⁺)) UCNPs were synthesised and functionalised with a thin layer of TiO₂. Excitation at 980 nm confirmed the production of hydroxyl radicals, superoxide anions and hydrogen peroxide, but not ¹O₂, showing that TiO₂ follows Type I photosensitisation.¹²⁶ However, *in vitro* studies of this nanosystem only induced 53-58 % cell death. As a result, the authors conjugated the UCNPs with maleimide-PEG-silane for further stability and PDT efficacy.¹²⁵ *In vitro* studies with oral squamous carcinoma cells showed significantly enhanced cell death when the PEG was present, reaching values of up to 78 % cell death. Additionally, the authors performed *in vivo* studies by intratumourally injecting female balb/c mice with the UCNPs. There was significant decrease in tumour growth following PDT, especially with the PEG-UCNPs.¹²⁵

C. Other functionalisation methods

The Gu group investigated the use of the polysaccharide chitosan as a potential ligand to induce hydrophilicity to UCNPs, due to its low toxicity and high biocompatibility.^{127,128} The authors synthesised oleate-capped NaYF_4 (Yb^{3+} , Er^{3+}) UCNPs and functionalised them with amphiphilic *N*-succinyl-*N'*-octyl chitosan (SOC) and ZnPc *via* hydrophobic interactions.¹²⁷ Following excitation at 980 nm, efficient production of $^1\text{O}_2$ by energy transfer from the UCNPs to the ZnPc correlated with a good phototoxic effect *in vitro* in MCF-7 human breast adenocarcinoma cells with no dark toxicity. *In vivo* studies were performed on female Kunming mice bearing a S180 tumour model. PDT treatment at 980 nm for 15 min (0.4 W/cm²) in mice treated with the UCNPs reduced the tumour progression rate by 76 % as compared to the saline-treated mice. During the 14-day period, over which the mice were monitored, there was not one death for the ZnPc-SOC-UCNPs treated mice, whereas the control groups showed 14-day survival rates of 50-67 %.¹²⁷ To further enhance the selectivity towards tumour tissue, the Gu group conjugated their ZnPc-SOC-UCNPs with folic acid.¹²⁸ The presence of folic acid was proven to be essential for an enhanced internalisation *via* receptor-mediated endocytosis, both *in vitro* and *in vivo*.¹²⁸ In another study, Zhou *et al.* used O-carboxymethylated chitosan (OCMC) to coat NaYF_4 (Yb^{3+} , Er^{3+}) UCNPs.¹²⁹ The PS pyropheophorbide a (Ppa) was then loaded with the targeting peptide cyclic RGD. Two cell lines with either high expression of $\alpha\text{v}\beta$ integrin, U87-MG human glioblastoma cancer cells, or low expression of $\alpha\text{v}\beta$ integrin, MCF-7 human breast cancer cells, were tested for *in vitro* PDT efficacy. The presence of cyclic RGD on the UCNPs, which selectively targets the $\alpha\text{v}\beta$ integrin on the surface of the cells, led to the Ppa-OCMC UCNPs being internalised by the U87-MG cells much better than MCF-7 cells. This translated into an improved PDT efficacy for the U87-MG cells, reaching cell death values of up to 50 % following 980 nm NIR-PDT (5 min irradiation at 0.5 W/cm²).¹²⁹

The use of the prodrug 5-ALA conjugated to UCNPs for PDT was evaluated by Punjabi *et al.*.¹³⁰ The authors used a shell of calcium fluoride (CaF_2) to coat cubic NaYF_4 (Yb^{3+} , Er^{3+}) UCNPs (*ca.* 26 nm), to which 5-ALA was attached using a covalent hydrazone linkage. The use of CaF_2 increases the stability and biocompatibility of the system and prevents the leakage of the PS. The hydrazone linkage between 5-ALA and the UCNPs

is pH sensitive, which allows for the release of 5-ALA inside the cells due to the low pH in cancer. In this study, the red emission of the UCNPs was maximised by modulating the amount of Yb^{3+} in the system, finding that 80 % is the ideal concentration. The optimal functionalised UCNPs were studied *in vitro* and *in vivo*. In both cases, the functionalised UCNPs following 980 nm NIR-PDT (0.5 W/cm^2) were found to induce good phototoxicity. Additionally, the use of NIR-PDT was advantageous over direct excitation of 5-ALA given that NIR light can penetrate pork tissue placed between the laser and the tumour up to 1.2 cm thick.¹³⁰

Other studies on UCNPs for PDT have explored the use of nucleotides as templates for their synthesis¹³¹ and the use of electrospun fibres to encapsulate UCNPs,¹³² which would stabilise the emission of the UCNPs. Even though the most common types of UCNPs synthesised and reported for PDT involve the host lattice NaYF_4 , investigations on other structures such as LiYF_4 have also been reported.^{133,134}

The use of UCNPs for PDT and bioimaging

As it can be seen in **Figure 1.8**, the visible light emitted from the UCNPs can not only be used to excite a PS for PDT, but also for tumour imaging. Therefore, numerous studies have become interested in the investigation of the simultaneous use of imaging and PDT.¹³⁵⁻¹⁴⁷ Silica-coated UCNPs have been reported to be potential candidates for multimodal imaging and PDT.¹³⁵⁻¹³⁷ However, as specified earlier, the use of silica results in a low loading of the PS within the system and thus low PDT efficacy. As a result, the use of other water-solubility methods, such as PEG, are encouraged.

The Zhang group developed 20 nm NaYF_4 (Yb^{3+} , Er^{3+}) UCNPs, made hydrophilic by addition of 2-aminoethyl dihydrogen phosphate (AEP), and covalently conjugated to the PS Rose Bengal.¹³⁸ Additionally, a PEG ligand was attached in order to include the targeting molecule folic acid for the selective detection of cancer cells. This nanosystem was found to be internalised by JAR choriocarcinoma cells, which overexpress the folate receptor, and cell viability was decreased only after 980 nm NIR-PDT (1.5 W/cm^2). As a result, the synthesised UCNPs hold great potential for theranostics acting as dual agents for cancer cell imaging and therapy.¹³⁸ In a similar study, the Zhang group used NaYF_4 (Yb^{3+} , Er^{3+}) UCNPs functionalised with poly(allylamine) (PAAm) for

water-solubility and covalently conjugated to a monomalonic fullerene acting as PS.¹³⁹ A PEG ligand and folic acid targeting ligand were also included in the system. Similar results were obtained as the functionalised UCNPs were only internalised by folate receptor overexpressing HeLa cells, leading to efficient cell death following 980 nm NIR-PDT (1.37 W/cm²).¹³⁹ The use of *ca.* 31 nm PEGylated core-shell NaYF₄ (Yb³⁺, Er³⁺)@NaYF₄ (Yb³⁺, Er³⁺) UCNPs conjugated with chlorin e6 by physical adsorption was reported by Chen *et al.*¹⁴⁰ These UCNPs were easily internalised and effective at inducing cell death following 980 nm NIR-PDT (1.5 W/cm²) *in vitro* without the need of a targeting agent.¹⁴¹ The main problem with these studies was the high radiation doses needed for effective PDT, much higher than the 980 nm continuous-wave laser maximum permissible skin exposure of 0.73 W/cm² permitted by the American National Standard for Safe Use of Lasers.^{30,130} In order to reduce the high radiation doses needed, the Zhang group synthesised a similar system to those previously reported; *ca.* 30 nm NaYF₄ (Yb³⁺, Er³⁺) UCNPs made hydrophilic by addition of PAAm and covalently conjugated to the PS ZnPc.¹⁴¹ As previously, PEG was attached in order to include folic acid for targeted PDT. This system could be simultaneously used for cell imaging, due to their emission at 540 nm, and PDT, due to their emission at 660 nm, used to excite ZnPc. Promising results both *in vitro* and *in vivo* were obtained *via* folate targeting by using a much lower laser dose of 0.39 W/cm². The ability to kill cells at such low doses was possible due to the addition of the doping ion Yb³⁺ at high concentrations (25 %), which led to enhanced red luminescence emission.¹⁴¹

Other groups have also reported the use of polymer-coated UCNPs for *in vitro* theranostics.¹⁴²⁻¹⁴⁷ Dou *et al.* developed NaYF₄ (Yb³⁺, Tm³⁺) UCNPs made hydrophilic by the addition of (3-aminopropyl) triethoxysilane (APTES) and covalently conjugated to chlorin e6.¹⁴² Even though the UCNPs were efficiently internalised by MCF-7 human breast cancer cells, good PDT efficacy (*ca.* 50 % cell death) was only achieved with higher radiation doses of 2.43 W/cm².¹⁴² Improved results were obtained by Yuan *et al.* using a G4-aptamer for targeted imaging and PDT.¹⁴³ The G4-aptamer was created by linking a guanine-rich DNA fraction with the sgc8 aptamer that selectively binds the protein tyrosine kinase 7 (PTK7) overexpressed on the surface of CCRF-CEM lymphoblastic leukaemia cells. The conjugation of the G4-aptamer to 15 nm sodium lutetium fluoride (NaLuF₄) (Gd³⁺, Yb³⁺, Er³⁺) UCNPs allowed for the attachment of the

PS TMPyP4, a porphyrin derivative. The G4-aptamer has a high affinity for PTK7, ($k_d=0.8$ nM), which induced effective targeted bioimaging as well as effective targeted PDT. Indeed, CEM cells reached up to 89.6 % cell death following 980 nm NIR-PDT (0.5 W/cm²). The use of the targeting G4-aptamer was proven to be essential since cells without PTK7 overexpression only reached 15 % cell death at the same concentration.¹⁴³ Dual-targeting bioimaging and PDT was reported by Wang *et al.* with the use of 3-aminophenylboronic acid (APBA), specific towards polysialic acid, and hyaluronic acid, specific towards CD44 receptors.¹⁴⁴ These authors synthesised NaYF₄ (Yb³⁺, Gd³⁺, Tm³⁺) functionalised with APBA and a hyaluronated fullerene, where fullerene acts as the PS. The authors concluded that the use of a dual-targeting nanosystem was beneficial for the increased selectivity towards cancer cells over single-targeting nanosystems.¹⁴⁴ The use of amphiphilic polymers for the stabilisation of UCNP, with or without targeting ligands, have also been shown to be good candidates for combined bioimaging and PDT.¹⁴⁵⁻¹⁴⁷

The use of multi-imaging modalities has become an important area of research. In particular, the combination of imaging from the emitted luminescence of UCNP (UCL) with magnetic resonance imaging (MRI) has been explored. Imaging *via* the non-invasive MRI requires the presence of contrast agents.¹⁴⁸ The lanthanide gadolinium (Gd) has magnetic properties due to the seven inner 4f unpaired electrons shielded by outer electrons, which enhances the electronic relaxation time and magnetic moment of Gd.¹⁴⁸ Therefore, the use of UCNP doped with Gd³⁺ opens the possibility for multimodal imaging including MRI.¹⁴⁸⁻¹⁵² Qiao *et al.* developed NaGdF₄ (Yb³⁺, Er³⁺) UCNP coated with CaF₂ and a shell of mSiO₂.¹⁴⁸ The PS, either haematoporphyrin or silicon phthalocyanine dihydroxide (SPCD), was covalently attached to the pores of the mSiO₂ shell. The PDT treatment and UCL imaging were both found to be efficient in HeLa cells. Additionally, the magnetic relaxivity (r_1) and relaxation time (t_1) were comparable to those of commercially available contrast agents based on Gd. The T1-weighted MR images were of good quality and slightly better for the UCNP functionalised with SPCD.¹⁴⁸ In another study, the Gd was present in the shell rather than the core of the UCNP.¹⁴⁹ Park *et al.* synthesised rod-shaped NaYF₄ (Yb³⁺, Er³⁺)@NaGdF₄ UCNP conjugated to PEG for water-solubility and the PS chlorin e6 *via* physical adsorption. This nanosystem was tested *in vivo* in balb/c mice injected with a

U87-MG glioblastoma tumour and was proven to be efficient for PDT, T1-weighted MRI and UCL.¹⁴⁹ The combination of active targeting with PDT/MRI/UCL was reported by Zhang *et al.*¹⁵⁰ The authors prepared NaGdF₄ (Yb³⁺, Tm³⁺) UCNPs covered with a silica shell and a shell of the PS TiO₂. Furthermore, the UCNPs were modified with APTES, to which the targeting ligand folic acid was conjugated. This nanosystem was biocompatible and efficient for the treatment of MCF-7 tumours *via* 980 nm NIR-PDT (0.6 W/cm² during 20 min), reaching cell death values of up to 69 % *in vitro* and 88.6 % tumour reduction *in vivo* as compared to control samples. Additionally, Gd efficiently acted as a good T1-weighted MRI agent.¹⁵⁰

The use of Gd as a MRI contrast agent in combination with UCNPs has been reported in different structural systems.^{151,152} Wei *et al.* used UCNPs based on a ZnO host lattice doped with Gd³⁺, Er³⁺ and Yb³⁺.¹⁵¹ The r_1 of this nanosystem was found to be larger than that of commercially available Gd-based contrast agents. As a result, the ZnO-UCNPs (Gd³⁺, Er³⁺, Yb³⁺) have been shown to have great potential for T1-weighted MRI. Additionally, in combination with methylene blue, the nanosystem can also be used for PDT due to its low cytotoxicity in the absence of 980 nm light.¹⁵¹ In another study by Li *et al.*, the UCNPs were based on a Gd₂O₃ host lattice doped with Yb³⁺ and Er³⁺.¹⁵² Similarly, in combination with either methylene blue or 5-ALA, the nanosystem was found to be a useful agent for combined PDT/MRI.¹⁵²

Other possibilities for the synthesis of MRI-active UCNPs include the use of an iron oxide (Fe₃O₄) core.¹⁵³ Zeng *et al.* synthesised NaYF₄ (Yb³⁺, Er³⁺) UCNPs containing a Fe₃O₄ core to which the PS AlPcS₄ was electrostatically attached. The functionalised UCNPs were effective for T2-weighted MRI, due to the presence of Fe₃O₄, UCL imaging and PDT, reaching values of up to 70 % cell death *in vitro* following 980 nm NIR-PDT (20 mW/cm² for 3 min).¹⁵³ Huang *et al.* studied the use of Na_xYbF_{3+x} UCNPs loaded with a shell of strontium fluoride (SrF₂) for combined MRI and computed tomography (CT) due to the high transverse relaxivity of the Yb³⁺ ions.¹⁵⁴ In combination with ZnPc, the nanosystem could also be used for 915 nm NIR-PDT.¹⁵⁴ Finally, the use of UCNPs doped with manganese (Mn²⁺) has also been studied as a potential contrast agent for MRI.¹⁵⁵

The use of combination therapies with UCNPs

The synthesis and application of multifunctional UCNPs to perform various cancer therapies simultaneously is an important advance. PDT has been combined with gene therapy by Wang *et al.*¹⁵⁶ These authors synthesised *ca.* 30 nm oleate-capped NaGdF₄ (Gd³⁺, Yb³⁺, Er³⁺) UCNPs functionalised with a multilayer of various polymers. For PDT, the PS chlorin e6 was attached *via* hydrophobic interactions. For the gene therapy, a small interfering RNA (siRNA) was bound to the functionalised UCNPs. The siRNA is selective towards the oncogene polo-like kinase 1 (Plk1), overexpressed in numerous types of cancer. The downregulation of Plk1 with siRNA leads to the activation of cell apoptosis. *In vitro* studies in HeLa cancer cells showed that the combination of 980 nm NIR-PDT (0.8 W/cm² for 20 min) with gene therapy induced higher levels of cell death than either of the therapies on their own.¹⁵⁶

As discussed with the AuNPs explained in **section 1.2.2**, the combination of PDT with PTT has received increasing interest for UCNPs.¹⁵⁷⁻¹⁵⁹ Chen *et al.* synthesised NaGdF₄ (Yb³⁺, Er³⁺) UCNPs modified with bovine serum albumin for biocompatibility.¹⁵⁷ The addition of the PDT agent Rose Bengal and the PTT agent IR825, a NIR-absorbing dye was performed *via* hydrophobic interactions. Two lasers were required to induce PDT (980 nm at 0.4 W/cm²) and PTT (808 nm at 0.5 W/cm²). While either therapy alone only induced partial tumour destruction *in vivo*, combination of the two therapies induced severe tumour damage.¹⁵⁷ The combination of PTT and PDT using the same laser irradiation would be beneficial. Therefore, He *et al.* prepared 25 nm PEGylated silica-coated NaYF₄ (Yb³⁺, Er³⁺) with a ZnPc embedded in the silica layer and modified with gold clusters that would act as the PTT agents.¹⁵⁸ The combination of PDT/PTT with a single laser light (980 nm at 15.9 W/cm²) was possible for enhanced cell killing, leading to 20 % more cell death than PTT alone. However, the main drawback of this method was the high laser power required for effective therapy.¹⁵⁸ Additionally, Lv *et al.* also performed PDT/PTT with a single 980 nm laser using a TiO₂-based compound.¹⁵⁹

The combination of PDT and chemotherapy is an effective method to induce enhanced cancer cell death. Chemotherapy drug release can be achieved by different methods, including pH-sensitive UCNPs,¹⁶⁰ polymer degradation due to the NIR light activation of UCNPs¹⁶¹⁻¹⁶⁴ or the combination of the two.^{165,166} Tian *et al.* synthesised *ca.* 20-30 nm

NaYF_4 (Yb^{3+} , Er^{3+}) UCNPs modified with α -cyclodextrin and conjugated to the PS chlorin e6 and the chemotherapeutic drug doxorubicin (DOX) *via* hydrophobic interactions.¹⁶⁰ At acidic conditions, DOX becomes more hydrophilic and it is easily released from the UCNPs. This pH-sensitive release mechanism is advantageous for tumours since tumour tissue presents low pH in its surroundings. The authors confirmed that the combination of PDT and pH-chemotherapy induces more cell death following NIR irradiation than either of the therapies alone.¹⁶⁰ The use of biodegradable polymers for the release of DOX has also been investigated. The Chang group developed silica-coated NaYF_4 (Yb^{3+} , Er^{3+}) UCNPs to which the PS Rose Bengal and the polymer poly-(1,4-phenyleneacetone dimethylenethioketal) (PPADT) conjugated to DOX were covalently attached.¹⁶¹ Yang *et al.* chose to covalently conjugate silica-coated $\text{NaY}(\text{Mn})\text{F}_4$ (Yb^{3+} , Er^{3+}) UCNPs with a PEGylated polymer, the PS chlorin e6 and DOX.¹⁶² Zhang *et al.* selected the polymer 4-(2-carboxy-ethylsulfanyl methyl)-3-nitro-benzoic acid (CNBA), which was attached to the PS hypocrellin A doped silica-coated NaYF_4 (Yb^{3+} , Tm^{3+}) UCNPs.¹⁶³ In these three cases, 980 nm irradiation induces the biodegradation of the polymers, which in turn enables the release of DOX into the cells. Release of DOX, together with the generation of ${}^1\text{O}_2$ by the respective PS, induces more cell death than either chemotherapy or PDT alone in all three studies.¹⁶¹⁻¹⁶³ A novel type of polymer degradation was reported by Zhang *et al.*¹⁶⁴ These authors used chlorin e6 covalently conjugated to silica-coated NaYF_4 (Yb^{3+} , Er^{3+}) UCNPs, to which a thioketal linker and DOX were attached. In this case, the degradation of thioketal is not directly related to the NIR excitation, rather it depends on the generation of ROS by the PS, which induces the breakage of the thioketal linker and allows the release of DOX into the environment.¹⁶⁴ The combination of pH- and NIR-sensitive release mechanisms for DOX and targeted cell delivery have been investigated. Yuan *et al.* used DOX covalently linked to a PEGylated conjugated polyelectrolyte (CPE) to hydrophobically encapsulate NaYF_4 (Yb^{3+} , Tm^{3+}) UCNPs, which were further functionalised with the targeting ligand cyclic RGD.¹⁶⁵ Additionally, Zeng *et al.* conjugated a PEGylated APTES polymer to TiO_2 -coated NaYF_4 (Yb^{3+} , Tm^{3+}) UCNPs further functionalised with folic acid.¹⁶⁶ In these two examples, the release of DOX was triggered by both the excitation with NIR-light and the presence of an acidic environment. Furthermore, the cancer cell uptake was enhanced by the inclusion of targeting agents in both systems.^{165,166} In another study, Yin *et al.* reported

a similar release mechanism.¹⁶⁷ In this case, silica-coated NaGdF₄ (Yb³⁺, Tm³⁺) UCNPs were functionalised with a TiO₂ layer, hyaluronic acid and DOX. Hyaluronic acid acted not only as the targeting ligand but also induced the release of DOX due to its degradation when conjugated to the hyaluronidase (Hyal) enzyme. The presence of Hyal, together with an acidic environment, induces the degradation of hyaluronic acid and thus DOX release.¹⁶⁷

To end this section, it is important to mention that the combination of more than two therapies is also being investigated. The combination of PDT, chemotherapy and radiotherapy was reported by Fan *et al.* for an enhanced therapeutic effect as compared to mono- or dual-therapeutic approaches.¹⁶⁸ Additionally, the combination of PDT/PTT with chemotherapy has also been reported by the Lin group.^{169,170} These authors not only combined these three therapies together, they also opened the possibility for multimodal imaging (UCL, CT and MRI) within the same system.^{169,170}

The use of 808 nm NIR-PDT

The majority of UCNPs used for biomedical applications, including PDT, use Yb³⁺ ion as the energy donor.¹⁷¹ As a result, the excitation wavelength is usually *ca.* 980 nm, as seen throughout this section. The main problem associated with this wavelength is the notable absorption of water, which leads to an overheating effect and limits the penetration depth.¹⁷¹ The absorption of water is minimised at *ca.* 800 nm and the development of UCNPs with excitation within this region is being studied. The use of neodymium ion (Nd³⁺) as the energy donor facilitates excitation at 808 nm and thus a minimal overheating effect and increased penetration depth.¹⁷¹ Several investigations on the development of UCNPs for PDT at 808 nm have been reported.¹⁷¹

Ai *et al.* synthesised chlorin e6 functionalised core-shell-shell UCNPs based on NaYbF₄ (Nd³⁺)@NaGdF₄ (Yb³⁺, Er³⁺)@NaGdF₄ and compared their excitation at conventional 976 nm with excitation at 808 nm.¹⁷¹ The use of 808 nm as the excitation source not only reduced the laser toxicity at longer irradiation periods, it also allowed for a deeper penetration. Studies for the production of ¹O₂ using a 15 mm thick pork muscle tissue located between the UCNPs and the laser showed that only excitation at 808 nm was able to generate ¹O₂ under such conditions, suggesting that deeper penetration is only

possible with the shorter wavelength.¹⁷¹ A similar approach was reported by Wang *et al.*¹⁷² These authors synthesised Rose Bengal functionalised core-shell-shell UCNPs based on NaYF_4 (Yb^{3+} , holmium (Ho^{3+}))@ NaYF_4 (Nd^{3+})@ NaYF_4 . Comparison between excitation at 808 nm and 980 nm yielded better results and lower overheating effect for the shorter excitation wavelength.¹⁷² The Lin group also showed the superiority of 808 nm excitation using a core NaYF_4 (Yb^{3+} , Tm^{3+}) covered by four shells NaGdF_4 (Yb^{3+}), NaNdF_4 (Yb^{3+}), NaGdF_4 and a final mSiO_2 shell functionalised with the PS TiO_2 .¹⁷³ The nature of this nanosystem allowed for enhanced PDT at 808 nm and also for multimodal imaging, UCL, MRI and CT.¹⁷³ Their work was further improved by the functionalisation of UCNPs with two PS, TiO_2 and hypocrellin A, which was able to inhibit tumour growth *in vivo* more effectively than UCNPs with one single PS.¹⁷⁴

1.2.4. Conclusions

Numerous studies highlight the advantages of using nanoparticles for PDT. Gold nanoparticles are easily synthesised with great potential for surface functionalisation. Upconverting nanoparticles offer further advantages due to their ability to convert NIR light into visible light, which offers an increased penetration depth to reach deeper-lying tumours. The functionalisation of both AuNPs and UCNPs with water soluble moieties such as PEG enables the delivery of hydrophobic photosensitisers in aqueous media. Additionally, the use of PEG increases the circulation time in the serum while preventing opsonisation by the RES. As a result, the PS is selectively delivered into the tumour *via* the EPR effect. Tumour selectivity can be further enhanced by conjugation of the nanoparticles with active targeting ligands. Both AuNPs and UCNPs hold great potential for combination therapies. For AuNPs, the combination of PDT with PTT has been particularly studied for improved tumour destruction. For UCNPs, the use of PDT in combination with PTT and chemotherapy has been shown to induce effective tumour death. Additionally, UCNPs can be doped with ions with magnetic properties and thus be used as contrast agents for MRI. The use of UCNPs for theranostics is not only limited to MRI because UCNPs can also be used for UCL and CT imaging. It is clear that nanoparticles, especially AuNPs and UCNPs, will play an important role in the future of photodynamic therapy.

1.3. Thesis outline

The research presented in this thesis focuses on the use of gold nanoparticles functionalised with two different zinc phthalocyanine derivatives for photodynamic therapy. Additionally, the use of upconverting nanoparticles for photodynamic therapy was investigated.

A detailed description of the materials, instruments and experimental procedures performed throughout this research is given in **Chapter 2**. The comparison of two zinc phthalocyanines conjugated to gold nanoparticles for PDT is reported in **Chapter 3**. The comparison of the two photosensitisers leads to the investigation of metal-enhanced fluorescence as a potential approach to improve PDT efficacy. Additionally, the targeting of breast cancer with anti-HER2 antibody is explored. Cell viability assays and confocal laser scanning microscopy are used to study the internalisation and PDT efficacy of the synthesised functionalised gold nanoparticles for PDT.

Chapter 4 describes the use of lactose as a potential targeting ligand for the galectin-1 receptor in breast cancer cells. The expression of galectin-1 in two breast cancer cell lines, SK-BR-3 and MDA-MB-231 cells, is quantified with an InCell enzyme-linked immunosorbent assay (ELISA). Gold nanoparticles functionalised with lactose are synthesised and their PDT efficacy assessed *via* cell viability assays. Additionally, the potential selective targeting between lactose and galectin-1 on the surface of the breast cancer cells is investigated.

The use of upconverting nanoparticles for PDT is explored in **Chapter 5**. Upconverting nanoparticles functionalised with Rose Bengal, kindly provided by Markus Buchner from Dr Thomas Hirsch's group at the University of Regensburg (Germany), are used for PDT in breast cancer cells. Multi-photon microscopy is required for the visualisation of the UCNPs internalisation by the cells. Additionally, the PDT efficacy of the functionalised UCNPs is investigated *in vitro* using cell viability assays and confocal laser scanning microscopy.

Finally, **Chapter 6** provides a summary of the results and final conclusions for the research reported throughout this thesis. Suggestions for future experiments to continue research in this area are described.

1.4. References

- (1) Cancer Research UK <http://www.cancerresearchuk.org/health-professional/cancer-statistics/risk/lifetime-risk> [Accessed Nov 7th, 2016].
- (2) Berger, N. A.; Savvides, P.; Koroukian, S. M.; Kahana, E. F.; Deimling, G. T.; Rose, J. H.; Bowman, K. F.; Miller, R. H. *Trans. Am. Clin. Climatol. Assoc.* **2006**, *117*, 147.
- (3) Decock, J.; Thirkettle, S.; Wagstaff, L.; Edwards, D. R. *J. Cell. Mol. Med.* **2011**, *15*, 1254.
- (4) Anand, S.; Ortel, B. J.; Pereira, S. P.; Hasan, T.; Maytin, E. V. *Cancer Lett.* **2012**, *326*, 8.
- (5) Ackroyd, R.; Kelty, C.; Brown, N.; Reed, M. *Photochem. Photobiol.* **2001**, *74*, 656.
- (6) Juarranz, Á.; Jaén, P.; Sanz-Rodríguez, F.; Cuevas, J.; González, S. *Clin. Transl. Oncol.* **2008**, *10*, 148.
- (7) Alemany-Ribes, M.; García-Díaz, M.; Acedo, P.; Agut, M.; Nonell, S.; Sagristá, M. L.; Mora, M.; Cañete, M.; Villanueva, Á.; Stockert, J. C.; Semino, C. E. *J. Anal. Bioanal. Tech.* **2013**, *S1*.
- (8) Brown, S. B.; Brown, E. A.; Walker, I. *Lancet Oncol.* **2004**, *5*, 497.
- (9) Plaetzer, K.; Krammer, B.; Berlanda, J.; Berr, F.; Kiesslich, T. *Lasers Med. Sci.* **2009**, *24*, 259.
- (10) Celli, J. P.; Spring, B. Q.; Rizvi, I.; Evans, C. L.; Samkoe, K. S.; Verma, S.; Pogue, B. W.; Hasan, T. *Chem. Rev.* **2010**, *110*, 2795.
- (11) Josefsen, L. B.; Boyle, R. W. *Theranostics* **2012**, *2*, 916.
- (12) Dolmans, D. E. J. G. J.; Fukumura, D.; Jain, R. K. *Nat. Rev. Cancer* **2003**, *3*, 380.
- (13) Allen, C. M.; Sharman, W. M.; van Lier, J. E. *J. Porphyrins Phthalocyanines* **2001**, *5*, 161.
- (14) Agostinis, P.; Berg, K.; Cengel, K. A.; Foster, T. H.; Girotti, A. W.; Gollnick, S. O.; Hahn, S. M.; Hamblin, M. R.; Juzeniene, A.; Kessel, D.; Korbelik, M.; Moan, J.; Mroz, P.; Nowis, D.; Piette, J.; Wilson, B. C.; Golab, J. *CA-Cancer J. Clin.* **2011**, *61*, 250.
- (15) Ochsner, M. *J. Photochem. Photobiol. B.* **1997**, *39*, 1.
- (16) Spring, B. Q.; Rizvi, I.; Xu, N.; Hasan, T. *Photochem. Photobiol. Sci.* **2015**, *14*, 1476.
- (17) Henderson, B. W.; Dougherty, T. J. *Photochem. Photobiol.* **1992**, *55*, 145.
- (18) Dougherty, T. J.; Gomer, C. J.; Henderson, B. W.; Jori, G.; Kessel, D.; Korbeil, M.; Moan, J.; Peng, Q. *J. Natl. Cancer Inst.* **1998**, *90*, 890.

(19) Wöhrle, D.; Hirth, A.; Bogdahn-Rai, T.; Schnurpfeil, G.; Shopova, M. *Russ. Chem. Bull.* **1998**, *47*, 807.

(20) Hopper, C. *Lancet Oncol.* **2000**, *1*, 212.

(21) Bechet, D.; Couleaud, P.; Frochot, C.; Viriot, M.-L.; Guillemin, F.; Barberi-Heyob, M. *Trends Biotechnol.* **2008**, *26*, 612.

(22) Mallidi, S.; Spring, B. Q.; Hasan, T. *Cancer J.* **2015**, *21*, 194.

(23) Chatterjee, D. K.; Fong, L. S.; Zhang, Y. *Adv. Drug Delivery Rev.* **2008**, *60*, 1627.

(24) Abrahamse, H.; Hamblin, M. R. *Biochem. J.* **2016**, *473*, 347.

(25) Obaid, G.; Broekgaarden, M.; Bulin, A.-L.; Huang, H.-C.; Kuriakose, J.; Liu, J.; Hasan, T. *Nanoscale* **2016**, *8*, 12471.

(26) Allison, R. R.; Downie, G. H.; Cuenca, R.; Hu, X.-H.; Childs, C. J. H.; Sibata, C. H. *Photodiagn. Photodyn. Ther.* **2004**, *1*, 27.

(27) Cheng, L.; Wang, C.; Feng, L.; Yang, K.; Liu, Z. *Chem. Rev.* **2014**, *114*, 10869.

(28) García Calavia, P.; Russell, D. A. In *Photodynamic Medicine: From Bench to Clinic*; Kostron, H., Hasan, T., Eds.; The Royal Society of Chemistry: Croydon, 2016, p 113.

(29) Wang, S.; Gao, R.; Zhou, F.; Selke, M. *J. Mater. Chem.* **2004**, *14*, 487.

(30) Marín, M. J.; Russell, D. A. In *Near-infrared Nanomaterials: Preparation, Bioimaging and Therapy Applications*; Zhang, F., Ed.; The Royal Society of Chemistry: Croydon, 2016, p 192.

(31) Obaid, G.; Russell, D. A. In *Handbook of photomedicine*; Hamblin, M. R., Huang, Y.-Y., Eds.; Taylor & Francis: Boca Raton, 2013, p 365.

(32) Lucky, S. S.; Soo, K. C.; Zhang, Y. *Chem. Rev.* **2015**, *115*, 1990.

(33) Obaid, G.; Chambrier, I.; Cook, M. J.; Russell, D. A. *Photochem. Photobiol. Sci.* **2015**, *14*, 737.

(34) Hong, E. J.; Choi, D. G.; Shim, M. S. *Acta Pharm. Sin. B* **2016**, *6*, 297.

(35) Smith, L.; Kuncic, Z.; Ostrikov, K. K.; Kumar, S. *J. Nanomater.* **2012**, *2012*, 1.

(36) Shirasu, N.; Nam, S. O.; Kuroki, M. *Anticancer Res.* **2013**, *33*, 2823.

(37) Bertrand, N.; Wu, J.; Xu, X.; Kamaly, N.; Farokhzad, O. C. *Adv. Drug Delivery Rev.* **2014**, *66*, 2.

(38) Blau, R.; Krivitsky, A.; Epshtain, Y.; Satchi-Fainaro, R. *Drug Resist. Updates* **2016**, *27*, 39.

(39) Obaid, G.; Chambrier, I.; Cook, M. J.; Russell, D. A. *Angew. Chem., Int. Ed.* **2012**, *51*, 6158.

(40) Daniels, T. R.; Bernabeu, E.; Rodríguez, J. A.; Patel, S.; Kozman, M.; Chiappetta, D. A.; Holler, E.; Ljubimova, J. Y.; Helguera, G.; Penichet, M. L. *Biochim. Biophys. Acta, Gen. Subj.* **2012**, *1820*, 291.

(41) Tortorella, S.; Karagiannis, T. C. *J. Membr. Biol.* **2014**, *247*, 291.

(42) Ai, J.; Xu, Y.; Lou, B.; Li, D.; Wang, E. *Talanta* **2014**, *118*, 54.

(43) Reddy, G. R.; Bhojani, M. S.; McConville, P.; Moody, J.; Moffat, B. A.; Hall, D. E.; Kim, G.; Koo, Y.-E. L.; Woolliscroft, M. J.; Sugai, J. V.; Johnson, T. D.; Philbert, M. A.; Kopelman, R.; Rehemtulla, A.; Ross, B. D. *Clin. Cancer Res.* **2006**, *12*, 6677.

(44) Yin, M.; Li, Z.; Liu, Z.; Ren, J.; Yang, X.; Qu, X. *Chem. Commun.* **2012**, *48*, 6556.

(45) Backer, M. V.; Backer, J. M. *Theranostics* **2012**, *2*, 502.

(46) Chen, K.; Chen, X. *Theranostics* **2011**, *1*, 189.

(47) Zöller, M. *Nat. Rev. Cancer* **2011**, *11*, 254.

(48) Nyokong, T.; Antunes, E. *Coord. Chem. Rev.* **2013**, *257*, 2401.

(49) Daniel, M.-C.; Astruc, D. *Chem. Rev.* **2004**, *104*, 293.

(50) Dixit, S.; Novak, T.; Miller, K.; Zhu, Y.; Kenney, M. E.; Broome, A.-M. *Nanoscale* **2015**, *7*, 1782.

(51) Xie, J.; Lee, S.; Chen, X. *Adv. Drug Delivery Rev.* **2010**, *62*, 1064.

(52) Camerin, M.; Magaraggia, M.; Soncin, M.; Jori, G.; Moreno, M.; Chambrier, I.; Cook, M. J.; Russell, D. A. *Eur. J. Cancer* **2010**, *46*, 1910.

(53) Hone, D. C.; Walker, P. I.; Evans-Gowing, R.; FitzGerald, S.; Beeby, A.; Chambrier, I.; Cook, M. J.; Russell, D. A. *Langmuir* **2002**, *18*, 2985.

(54) Wieder, M. E.; Hone, D. C.; Cook, M. J.; Handsley, M. M.; Gavrilovic, J.; Russell, D. A. *Photochem. Photobiol. Sci.* **2006**, *5*, 727.

(55) Nombona, N.; Maduray, K.; Antunes, E.; Karsten, A.; Nyokong, T. *J. Photochem. Photobiol. B* **2012**, *107*, 35.

(56) Ohyama, J.; Hitomi, Y.; Higuchi, Y.; Shinagawa, M.; Mukai, H.; Kodera, M.; Teramura, K.; Shishido, T.; Tanaka, T. *Chem. Commun.* **2008**, 6300.

(57) Gamaleia, N. F.; Shishko, E. D.; Dolinsky, G. A.; Scherbakov, A. B.; Usatenko, A. V.; Kholin, V. V. *Exp. Oncol.* **2010**, *32*, 44.

(58) Reum, N.; Fink-Straube, C.; Klein, T.; Hartmann, R. W.; Lehr, C.-M.; Schneider, M. *Langmuir* **2010**, *26*, 16901.

(59) Zaruba, K.; Kralova, J.; Rezanka, P.; Pouckova, P.; Veverkova, L.; Kral, V. *Org. Biomol. Chem.* **2010**, *8*, 3202.

(60) Donnelly, R. F.; McCarron, P. A.; Woolfson, A. D. *Perspect. Med. Chem.* **2007**, *1*, 49.

(61) Xu, H.; Liu, C.; Mei, J.; Yao, C.; Wang, S.; Wang, J.; Li, Z.; Zhang, Z. *Int. J. Nanomed.* **2012**, *7*, 5029.

(62) Mohammadi, Z.; Sazgarnia, A.; Rajabi, O.; Soudmand, S.; Esmaily, H.; Sadeghi, H. R. *Photodiagn. Photodyn. Ther.* **2013**, *10*, 382.

(63) Amini, S. M.; Kharrazi, S.; Hadizadeh, M.; Fateh, M.; Saber, R. *IET Nanobiotechnol.* **2013**, *7*, 151.

(64) Benito, M.; Martín, V.; Blanco, M. D.; Teijón, J. M.; Gómez, C. J. *Pharm. Sci.* **2013**, *102*, 2760.

(65) Khaing Oo, M. K.; Yang, Y.; Hu, Y.; Gomez, M.; Du, H.; Wang, H. *ACS Nano* **2012**, *6*, 1939.

(66) Eshghi, H.; Sazgarnia, A.; Rahimizadeh, M.; Attaran, N.; Bakavoli, M.; Soudmand, S. *Photodiagn. Photodyn. Ther.* **2013**, *10*, 304.

(67) Ashjari, M.; Dehfuly, S.; Fatehi, D.; Shabani, R.; Koruji, M. *RSC Adv.* **2015**, *5*, 104621.

(68) Pantiushenko, I. V.; Rudakovskaya, P. G.; Starovoytova, A. V.; Mikhaylovskaya, A. A.; Abakumov, M. A.; Kaplan, M. A.; Tsygankov, A. A.; Majouga, A. G.; Grin, M. A.; Mironov, A. F. *Biochemistry (Moscow)* **2015**, *80*, 752.

(69) Stuchinskaya, T.; Moreno, M.; Cook, M. J.; Edwards, D. R.; Russell, D. A. *Photochem. Photobiol. Sci.* **2011**, *10*, 822.

(70) Cheng, Y.; C. Samia, A.; Meyers, J. D.; Panagopoulos, I.; Fei, B.; Burda, C. *J. Am. Chem. Soc.* **2008**, *130*, 10643.

(71) Paciotti, G. F.; Kingston, D. G. I.; Tamarkin, L. *Drug Dev. Res.* **2006**, *67*, 47.

(72) Cheng, Y.; Meyers, J. D.; Agnes, R. S.; Doane, T. L.; Kenney, M. E.; Broome, A.-M.; Burda, C.; Basilion, J. P. *Small* **2011**, *7*, 2301.

(73) Cheng, Y.; Samia, A. C.; Li, J.; Kenney, M. E.; Resnick, A.; Burda, C. *Langmuir* **2010**, *26*, 2248.

(74) Cheng, Y.; Meyers, J. D.; Broome, A.-M.; Kenney, M. E.; Basilion, J. P.; Burda, C. *J. Am. Chem. Soc.* **2011**, *133*, 2583.

(75) Camerin, M.; Moreno, M.; Marín, M. J.; Schofield, C. L.; Chambrier, I.; Cook, M. J.; Coppelotti, O.; Jori, G.; Russell, D. A. *Photochem. Photobiol. Sci.* **2016**, *15*, 618.

(76) Meyers, J. D.; Cheng, Y.; Broome, A.-M.; Agnes, R. S.; Schluchter, M. D.; Margevicius, S.; Wang, X.; Kenney, M. E.; Burda, C.; Basilion, J. P. *Part. Part. Syst. Charact.* **2015**, *32*, 448.

(77) Dixit, S.; Miller, K.; Zhu, Y.; McKinnon, E.; Novak, T.; Kenney, M. E.; Broome, A.-M. *Mol. Pharmaceutics* **2015**, *12*, 3250.

(78) Yu, J.; Hsu, C.-H.; Huang, C.-C.; Chang, P.-Y. *ACS Appl. Mater. Interfaces* **2015**, *7*, 432.

(79) Soundararajan, S.; Wang, L.; Sridharan, V.; Chen, W.; Courtenay-Luck, N.; Jones, D.; Spicer, E. K.; Fernandes, D. *J. Mol. Pharmacol.* **2009**, *76*, 984.

(80) Li, L.; Nurunnabi, M.; Nafiuojjaman, M.; Lee, Y.-k.; Huh, K. M. *J. Controlled Release* **2013**, *171*, 241.

(81) Huang, P.; Lin, J.; Wang, S.; Zhou, Z.; Li, Z.; Wang, Z.; Zhang, C.; Yue, X.; Niu, G.; Yang, M.; Cui, D.; Chen, X. *Biomaterials* **2013**, *34*, 4643.

(82) Li, L.; Chen, J.-Y.; Wu, X.; Wang, P.-N.; Peng, Q. *J. Phys. Chem. B* **2010**, *114*, 17194.

(83) Hu, Y.; Yang, Y.; Wang, H.; Du, H. *ACS Nano* **2015**, *9*, 8744.

(84) Kolemen, S.; Ozdemir, T.; Lee, D.; Kim, G. M.; Karatas, T.; Yoon, J.; Akkaya, E. U. *Angew. Chem., Int. Ed.* **2016**, *55*, 3606.

(85) Nair, L. V.; Nazeer, S. S.; Jayasree, R. S.; Ajayaghosh, A. *ACS Nano* **2015**, *9*, 5825.

(86) Zhang, C.; Li, C.; Liu, Y.; Zhang, J.; Bao, C.; Liang, S.; Wang, Q.; Yang, Y.; Fu, H.; Wang, K.; Cui, D. *Adv. Funct. Mater.* **2015**, *25*, 1314.

(87) Kuo, W.-S.; Chang, C.-N.; Chang, Y.-T.; Yang, M.-H.; Chien, Y.-H.; Chen, S.-J.; Yeh, C.-S. *Angew. Chem., Int. Ed.* **2010**, *49*, 2711.

(88) Marrache, S.; Choi, J. H.; Tundup, S.; Zaver, D.; Harn, D. A.; Dhar, S. *Integr. Biol.* **2013**, *5*, 215.

(89) Li, H.; Li, Z.; Liu, L.; Lu, T.; Wang, Y. *RSC Adv.* **2015**, *5*, 34831.

(90) Camerin, M.; Rello, S.; Villanueva, Á.; Ping, X.; Kenney, M. E.; Rodgers, M. A. J.; Jori, G. *Eur. J. Cancer* **2005**, *41*, 1203.

(91) Huang, X.; Jain, P. K.; El-Sayed, I. H.; El-Sayed, M. A. *Lasers Med. Sci.* **2007**, *23*, 217.

(92) Kang, S. H.; Nafiuojjaman, M.; Nurunnabi, M.; Li, L.; Khan, H. A.; Cho, K. J.; Huh, K. M.; Lee, Y.-k. *Macromol. Res.* **2015**, *23*, 474.

(93) Hari, K.; Pichaimani, A.; Kumpati, P. *RSC Adv.* **2013**, *3*, 20471.

(94) Chen, R.-J.; Chen, P.-C.; Prasannan, A.; Vinayagam, J.; Huang, C.-C.; Chou, P.-Y.; Weng, C.-C.; Tsai, H. C.; Lin, S.-Y. *Mater. Sci. Eng. C* **2016**, *63*, 678.

(95) Jang, B.; Park, J.-Y.; Tung, C.-H.; Kim, I.-H.; Choi, Y. *ACS Nano* **2011**, *5*, 1086.

(96) Bhana, S.; O'Connor, R.; Johnson, J.; Ziebarth, J. D.; Henderson, L.; Huang, X. *J. Colloid Interface Sci.* **2016**, *469*, 8.

(97) Tham, H. P.; Chen, H.; Tan, Y. H.; Qu, Q.; Sreejith, S.; Zhao, L.; Venkatraman, S. S.; Zhao, Y. *Chem. Commun.* **2016**, *52*, 8854.

(98) Chung, U. S.; Kim, J.-H.; Kim, B.; Kim, E.; Jang, W.-D.; Koh, W.-G. *Chem. Commun.* **2016**, *52*, 1258.

(99) Chih-Ken, C.; Yi-Chou, T.; Jen-Hung, H.; Jian-He, Y.; Chih-Kang, Y.; Shih-Yang, C.; Po-Hao, T.; Shuai, C.; Yean-Woei, K.; Yang, C. C. *Nanotechnology* **2016**, *27*, 115102.

(100) Wang, S.; Huang, P.; Nie, L.; Xing, R.; Liu, D.; Wang, Z.; Lin, J.; Chen, S.; Niu, G.; Lu, G.; Chen, X. *Adv. Mater.* **2013**, *25*, 3055.

(101) Gao, L.; Fei, J.; Zhao, J.; Li, H.; Cui, Y.; Li, J. *ACS Nano* **2012**, *6*, 8030.

(102) Bhana, S.; Lin, G.; Wang, L.; Starring, H.; Mishra, S. R.; Liu, G.; Huang, X. *ACS Appl. Mater. Interfaces* **2015**, *7*, 11637.

(103) Seo, S.-H.; Kim, B.-M.; Joe, A.; Han, H.-W.; Chen, X.; Cheng, Z.; Jang, E.-S. *Biomaterials* **2014**, *35*, 3309.

(104) Kuo, W.-S.; Chang, Y.-T.; Cho, K.-C.; Chiu, K.-C.; Lien, C.-H.; Yeh, C.-S.; Chen, S.-J. *Biomaterials* **2012**, *33*, 3270.

(105) Fales, A. M.; Yuan, H.; Vo-Dinh, T. *Langmuir* **2011**, *27*, 12186.

(106) Zhao, L.; Kim, T.-H.; Kim, H.-W.; Ahn, J.-C.; Kim, S. Y. *Acta Biomater.* **2015**, *20*, 155.

(107) Simon, T.; Potara, M.; Gabudean, A.-M.; Licarete, E.; Banciu, M.; Astilean, S. *ACS Appl. Mater. Interfaces* **2015**, *7*, 16191.

(108) Vankayala, R.; Kuo, C.-L.; Nuthalapati, K.; Chiang, C.-S.; Hwang, K. C. *Adv. Funct. Mater.* **2015**, *25*, 5934.

(109) Vankayala, R.; Sagadevan, A.; Vijayaraghavan, P.; Kuo, C.-L.; Hwang, K. C. *Angew. Chem., Int. Ed.* **2011**, *50*, 10640.

(110) Misawa, M.; Takahashi, J. *Nanomed. Nanotech. Biol. Med.* **2011**, *7*, 604.

(111) Jiang, C.; Zhao, T.; Yuan, P.; Gao, N.; Pan, Y.; Guan, Z.; Zhou, N.; Xu, Q.-H. *ACS Appl. Mater. Interfaces* **2013**, *5*, 4972.

(112) El-Hussein, A.; Mfouo-Tynga, I.; Abdel-Harith, M.; Abrahamse, H. *J. Photochem. Photobiol. B* **2015**, *153*, 67.

(113) Chadwick, S. J.; Salah, D.; Livesey, P. M.; Brust, M.; Volk, M. *J. Phys. Chem. C* **2016**, *120*, 10647.

(114) Zhang, P.; Steelant, W.; Kumar, M.; Scholfield, M. *J. Am. Chem. Soc.* **2007**, *129*, 4526.

(115) Guo, Y.; Kumar, M.; Zhang, P. *Chem. Mater.* **2007**, *19*, 6071.

(116) Yang, X.; Xiao, Q.; Niu, C.; Jin, N.; Ouyang, J.; Xiao, X.; He, D. *J. Mater. Chem. B* **2013**, *1*, 2757.

(117) Guo, H.; Qian, H.; Idris, N. M.; Zhang, Y. *Nanomed. Nanotech. Biol. Med.* **2010**, 6, 486.

(118) Hou, B.; Zheng, B.; Gong, X.; Wang, H.; Wang, S.; Liao, Z.; Li, X.; Zhang, X.; Chang, J. *J. Mater. Chem. B* **2015**, 3, 3531.

(119) Xu, F.; Ding, L.; Tao, W.; Yang, X.-z.; Qian, H.-s.; Yao, R.-s. *Mater. Lett.* **2016**, 167, 205.

(120) Idris, N. M.; Gnanasammandhan, M. K.; Zhang, J.; Ho, P. C.; Mahendran, R.; Zhang, Y. *Nat. Med.* **2012**, 18, 1580.

(121) Ungun, B.; Prud'homme, R. K.; Budijono, S. J.; Shan, J.; Lim, S. F.; Ju, Y.; Austin, R. *Opt. Express* **2009**, 17, 80.

(122) Shan, J.; Budijono, S. J.; Hu, G.; Yao, N.; Kang, Y.; Ju, Y.; Prud'homme, R. K. *Adv. Funct. Mater.* **2011**, 21, 2488.

(123) González-Béjar, M.; Liras, M.; Frances-Soriano, L.; Voliani, V.; Herranz-Pérez, V.; Durán-Moreno, M.; García-Verdugo, J. M.; Alarcón, E. I.; Scaiano, J. C.; Pérez-Prieto, J. *J. Mater. Chem. B* **2014**, 2, 4554.

(124) Wang, C.; Tao, H.; Cheng, L.; Liu, Z. *Biomaterials* **2011**, 32, 6145.

(125) Lucky, S. S.; Muhammad Idris, N.; Li, Z.; Huang, K.; Soo, K. C.; Zhang, Y. *ACS Nano* **2015**, 9, 191.

(126) Idris, N. M.; Lucky, S. S.; Li, Z.; Huang, K.; Zhang, Y. *J. Mater. Chem. B* **2014**, 2, 7017.

(127) Cui, S.; Chen, H.; Zhu, H.; Tian, J.; Chi, X.; Qian, Z.; Achilefu, S.; Gu, Y. *J. Mater. Chem.* **2012**, 22, 4861.

(128) Cui, S.; Yin, D.; Chen, Y.; Di, Y.; Chen, H.; Ma, Y.; Achilefu, S.; Gu, Y. *ACS Nano* **2013**, 7, 676.

(129) Zhou, A.; Wei, Y.; Wu, B.; Chen, Q.; Xing, D. *Mol. Pharmaceutics* **2012**, 9, 1580.

(130) Punjabi, A.; Wu, X.; Tokatli-Apollon, A.; El-Rifai, M.; Lee, H.; Zhang, Y.; Wang, C.; Liu, Z.; Chan, E. M.; Duan, C.; Han, G. *ACS Nano* **2014**, 8, 10621.

(131) Zhou, L.; Li, Z.; Liu, Z.; Yin, M.; Ren, J.; Qu, X. *Nanoscale* **2014**, 6, 1445.

(132) Watkins, Z.; Taylor, J.; D'Souza, S.; Britton, J.; Nyokong, T. *J. Fluoresc.* **2015**, 25, 1417.

(133) Jesu Raj, J. G.; Quintanilla, M.; Vetrone, F. *J. Mater. Chem. B* **2016**, 4, 3113.

(134) Wang, M.; Chen, Z.; Zheng, W.; Zhu, H.; Lu, S.; Ma, E.; Tu, D.; Zhou, S.; Huang, M.; Chen, X. *Nanoscale* **2014**, 6, 8274.

(135) Qian, H. S.; Guo, H. C.; Ho, P. C.-L.; Mahendran, R.; Zhang, Y. *Small* **2009**, 5, 2285.

(136) Wang, F.; Yang, X.; Ma, L.; Huang, B.; Na, N.; E, Y.; He, D.; Ouyang, J. *J. Mater. Chem.* **2012**, 22, 24597.

(137) Liang, L.; Care, A.; Zhang, R.; Lu, Y.; Packer, N. H.; Sunna, A.; Qian, Y.; Zvyagin, A. V. *ACS Appl. Mater. Interfaces* **2016**, *8*, 11945.

(138) Liu, K.; Liu, X.; Zeng, Q.; Zhang, Y.; Tu, L.; Liu, T.; Kong, X.; Wang, Y.; Cao, F.; Lambrechts, S. A. G.; Aalders, M. C. G.; Zhang, H. *ACS Nano* **2012**, *6*, 4054.

(139) Liu, X.; Zheng, M.; Kong, X.; Zhang, Y.; Zeng, Q.; Sun, Z.; Buma, W. J.; Zhang, H. *Chem. Commun.* **2013**, *49*, 3224.

(140) Chen, X.; Zhao, Z.; Jiang, M.; Que, D.; Shi, S.; Zheng, N. *New J. Chem.* **2013**, *37*, 1782.

(141) Xia, L.; Kong, X.; Liu, X.; Tu, L.; Zhang, Y.; Chang, Y.; Liu, K.; Shen, D.; Zhao, H.; Zhang, H. *Biomaterials* **2014**, *35*, 4146.

(142) Dou, Q. Q.; Teng, C. P.; Ye, E.; Loh, X. J. *Int. J. Nanomed.* **2015**, *10*, 419.

(143) Yuan, Q.; Wu, Y.; Wang, J.; Lu, D.; Zhao, Z.; Liu, T.; Zhang, X.; Tan, W. *Angew. Chem., Int. Ed.* **2013**, *52*, 13965.

(144) Wang, X.; Yang, C.-X.; Chen, J.-T.; Yan, X.-P. *Anal. Chem.* **2014**, *86*, 3263.

(145) Wang, H.; Wang, S.; Liu, Z.; Dong, C.; Yang, J.; Gong, X.; Chang, J. *Nanotechnology* **2014**, *25*, 155103.

(146) Wang, H.; Liu, Z.; Wang, S.; Dong, C.; Gong, X.; Zhao, P.; Chang, J. *ACS Appl. Mater. Interfaces* **2014**, *6*, 3219.

(147) Wang, H.; Dong, C.; Zhao, P.; Wang, S.; Liu, Z.; Chang, J. *Int. J. Pharm.* **2014**, *466*, 307.

(148) Qiao, X.-F.; Zhou, J.-C.; Xiao, J.-W.; Wang, Y.-F.; Sun, L.-D.; Yan, C.-H. *Nanoscale* **2012**, *4*, 4611.

(149) Park, Y. I.; Kim, H. M.; Kim, J. H.; Moon, K. C.; Yoo, B.; Lee, K. T.; Lee, N.; Choi, Y.; Park, W.; Ling, D.; Na, K.; Moon, W. K.; Choi, S. H.; Park, H. S.; Yoon, S.-Y.; Suh, Y. D.; Lee, S. H.; Hyeon, T. *Adv. Mater.* **2012**, *24*, 5755.

(150) Zhang, L. e.; Zeng, L.; Pan, Y.; Luo, S.; Ren, W.; Gong, A.; Ma, X.; Liang, H.; Lu, G.; Wu, A. *Biomaterials* **2015**, *44*, 82.

(151) Wei, X.; Wang, W.; Chen, K. *J. Phys. Chem. C* **2013**, *117*, 23716.

(152) Li, H.; Song, S.; Wang, W.; Chen, K. *Dalton Trans.* **2015**, *44*, 16081.

(153) Zeng, L.; Xiang, L.; Ren, W.; Zheng, J.; Li, T.; Chen, B.; Zhang, J.; Mao, C.; Li, A.; Wu, A. *RSC Adv.* **2013**, *3*, 13915.

(154) Huang, Y.; Xiao, Q.; Hu, H.; Zhang, K.; Feng, Y.; Li, F.; Wang, J.; Ding, X.; Jiang, J.; Li, Y.; Shi, L.; Lin, H. *Small* **2016**, *12*, 4200.

(155) Wang, C.; Cheng, L.; Liu, Y.; Wang, X.; Ma, X.; Deng, Z.; Li, Y.; Liu, Z. *Adv. Funct. Mater.* **2013**, *23*, 3077.

(156) Wang, X.; Liu, K.; Yang, G.; Cheng, L.; He, L.; Liu, Y.; Li, Y.; Guo, L.; Liu, Z. *Nanoscale* **2014**, *6*, 9198.

(157) Chen, Q.; Wang, C.; Cheng, L.; He, W.; Cheng, Z.; Liu, Z. *Biomaterials* **2014**, *35*, 2915.

(158) He, L.; Dragavon, J.; Cho, S.; Mao, C.; Yildirim, A.; Ma, K.; Chattaraj, R.; Goodwin, A. P.; Park, W.; Cha, J. *N. J. Mater. Chem. B* **2016**, *4*, 4455.

(159) Lv, R.; Zhong, C.; Li, R.; Yang, P.; He, F.; Gai, S.; Hou, Z.; Yang, G.; Lin, J. *Chem. Mater.* **2015**, *27*, 1751.

(160) Tian, G.; Ren, W.; Yan, L.; Jian, S.; Gu, Z.; Zhou, L.; Jin, S.; Yin, W.; Li, S.; Zhao, Y. *Small* **2013**, *9*, 1929.

(161) Zhou, F.; Zheng, B.; Zhang, Y.; Wu, Y.; Wang, H.; Chang, J. *Nanotechnology* **2016**, *27*, 235601.

(162) Yang, S.; Li, N.; Liu, Z.; Sha, W.; Chen, D.; Xu, Q.; Lu, J. *Nanoscale* **2014**, *6*, 14903.

(163) Zhang, T.; Lin, H.; Cui, L.; An, N.; Tong, R.; Chen, Y.; Yang, C.; Li, X.; Qu, F. *RSC Adv.* **2016**, *6*, 26479.

(164) Zhang, T.; Lin, H.; Cui, L.; An, N.; Tong, R.; Chen, Y.; Yang, C.; Li, X.; Liu, J.; Qu, F. *Eur. J. Inorg. Chem.* **2016**, *2016*, 1206.

(165) Yuan, Y.; Min, Y.; Hu, Q.; Xing, B.; Liu, B. *Nanoscale* **2014**, *6*, 11259.

(166) Zeng, L.; Pan, Y.; Tian, Y.; Wang, X.; Ren, W.; Wang, S.; Lu, G.; Wu, A. *Biomaterials* **2015**, *57*, 93.

(167) Yin, M.; Ju, E.; Chen, Z.; Li, Z.; Ren, J.; Qu, X. *Chem. Eur. J.* **2014**, *20*, 14012.

(168) Fan, W.; Shen, B.; Bu, W.; Chen, F.; He, Q.; Zhao, K.; Zhang, S.; Zhou, L.; Peng, W.; Xiao, Q.; Ni, D.; Liu, J.; Shi, J. *Biomaterials* **2014**, *35*, 8992.

(169) Lv, R.; Yang, P.; He, F.; Gai, S.; Li, C.; Dai, Y.; Yang, G.; Lin, J. *ACS Nano* **2015**, *9*, 1630.

(170) Lv, R.; Yang, P.; He, F.; Gai, S.; Yang, G.; Dai, Y.; Hou, Z.; Lin, J. *Biomaterials* **2015**, *63*, 115.

(171) Ai, F.; Ju, Q.; Zhang, X.; Chen, X.; Wang, F.; Zhu, G. *Sci. Rep.* **2015**, *5*, 10785.

(172) Wang, D.; Xue, B.; Kong, X.; Tu, L.; Liu, X.; Zhang, Y.; Chang, Y.; Luo, Y.; Zhao, H.; Zhang, H. *Nanoscale* **2015**, *7*, 190.

(173) Yang, G.; Yang, D.; Yang, P.; Lv, R.; Li, C.; Zhong, C.; He, F.; Gai, S.; Lin, J. *Chem. Mater.* **2015**, *27*, 7957.

(174) Hou, Z.; Deng, K.; Li, C.; Deng, X.; Lian, H.; Cheng, Z.; Jin, D.; Lin, J. *Biomaterials* **2016**, *101*, 32.

Chapter 2

Experimental

This chapter details the materials and experimental procedures used for the experiments described throughout this thesis.

2.1. Materials and instruments

2.1.1. Starting materials and solvents

All reagents were of analytical grade, used as received and purchased from Sigma-Aldrich (UK) unless otherwise stated. Tetrahydrofuran (THF), toluene, sterile deionised water (dH₂O) and sodium hydrogen orthophosphate dehydrate (Na₂HPO₄·2H₂O) were purchased from Fisher Scientific (UK). Sodium dihydrogen orthophosphate dihydrate (NaH₂PO₄·2H₂O), sodium chloride (NaCl), phosphate buffered saline (PBS) tablets, foetal bovine serum (FBS), 75 cm² Nunc Easy tissue culture flasks with porous caps, Nunc 6-well multidishes, Nunc Nunclon™ Δ Surface 96-well white-bottom and clear-bottom microplates, 18 mm diameter glass coverslips, Nunc cryo tubes (1.8 mL), a cryogenic freezing container and InCell ELISA colorimetric detection kit were purchased from Thermo Fisher Scientific (UK). Costar™ sterile disposable reagent reservoirs, sterile centrifuge tubes and sterile disposable serological pipettes were purchased from Corning B.V. Life Sciences (The Netherlands). Trypsin 0.25 % with ethylenediaminetetraacetic acid (EDTA), trypsin 0.05 % with EDTA, Gibco™ Molecular Probes™ soybean trypsin inhibitor, McCOY's 5A phenol red-free medium containing L-glutamine, McCOY's 5A medium containing phenol red, high glucose phenol red-free Dulbecco's Modified Eagle Medium (DMEM), L-glutamine (200 mM), sodium pyruvate and Lysensor™ green DND-189 (1 mM in DMSO) were all purchased from Invitrogen (UK). Mammary epithelial basal medium (MEBM) and its supplements bovine pituitary extract (BPE), hydrocortisone, human epidermal growth factor (hEGF) and insulin were purchased from Lonza (UK). CellTiter-Blue® cell viability assay and ApoTox-Glo™ Triplex assay were purchased from Promega (UK). Millex GP syringe driven filter units

(0.22 µm) were purchased from Millipore Corporation (USA). Sodium hydrogen carbonate (NaHCO₃) was purchased from BDH Laboratory Supplied Poole (UK). Vivaspin™ 500 (100 kDa MWCO; PES membrane) centrifuge columns were purchased from Sartorius Stedim Biotech (UK). The α -thio- ω -carboxy polyethylene glycol (3,000 Da; PEG) was purchased from Iris Biotech GmbH (Germany). Thiol-dPEG®-acid (sPEG) was purchased from Stratech (UK). Staurosporine free base (> 99 %) was purchased from LC Laboratories (USA). Rat monoclonal anti-ErbB2 antibody, rabbit monoclonal anti-galectin-1 antibody and recombinant human galectin-1 protein were purchased from Abcam (UK). Holey carbon film 300 mesh copper grids were obtained from Agar Scientific (UK). A JDS Uniphase 633 nm Helium-Neon (HeNe) laser (10 mW) was purchased from Edmund Optics (USA). A 980 nm near-infrared (NIR) laser (200 mW) was purchased from Picotronic (Germany).

SK-BR-3 human breast adenocarcinoma cells were purchased from LGC Standards and kindly provided by Prof Dylan R. Edwards (Norwich Medical School, University of East Anglia, UK). MDA-MB-231 human breast adenocarcinoma cells and MCF-10A human mammary epithelial cells were purchased from ATCC in partnership with LGC Standards.

2.1.2. Instrumental techniques

The instrumental techniques used were ultraviolet-visible (UV-vis) spectroscopy, fluorescence spectroscopy, transmission electron microscopy (TEM), confocal laser scanning microscopy, multi-photon microscopy and time-resolved luminescence spectroscopy.

UV-vis spectra of the samples were recorded using a Hitachi U-300 spectrophotometer at room temperature. Quartz cuvettes with a 1 cm path length were used. Fluorescence excitation and emission spectra of the samples were obtained using a Hitachi F-4500 fluorescence spectrometer in quartz cuvettes with a 1 cm path length. For the plate assays, absorbance, fluorescence and luminescence measurements were performed using a CLARIOstar® (BMG Labtech) microplate reader at room temperature.

TEM images were obtained using a JEOL JEM-2010 Electron Microscope operating at 200 kV. The samples were deposited on holey carbon film 300 mesh copper grids. Assistance of Dr Colin McDonald (School of Chemistry, University of East Anglia, Norwich, UK) to obtain the TEM images is gratefully acknowledged.

Centrifugation of Eppendorf tubes (1.5 mL) and vivaspin™ 500 columns was performed using a Beckman Coulter *Allegra™* X-22R centrifuge. Centrifugation of biological samples in 15-50 mL centrifuge tubes was performed using an Eppendorf 5810R centrifuge.

Confocal microscopy was performed using a Carl Zeiss LSM 510 META confocal laser scanning microscope. The images were acquired with a plan-apochromat 63x/1.4 Oil DIC objective and processed using ImageJ/Fiji software.

Multi-photon microscopy was performed using a TriM Scope II multi-photon microscope (LaVision BioTec, Bielefeld, Germany). The images were acquired with a 63x/1.4 NA PlanApochromat objective lens (Carl Zeiss Ltd., Cambridge, UK). The images were processed using InspectorPro and ImageJ/Fiji software. Assistance of Dr Paul Thomas (School of Biological Sciences, University of East Anglia, Norwich, UK) to obtain the multi-photon microscopy images is gratefully acknowledged.

Time-resolved luminescence spectroscopic measurements were performed to obtain information regarding the singlet oxygen quantum yields of the phthalocyanine nanoparticle conjugates, with the kind assistance of Prof Andrew Beeby (Department of Chemistry, University of Durham, Durham, UK). The samples were irradiated at 355 nm using the third harmonic of a Q-switched Nd:YAG laser (Spectra Physics GCR 150-10) with pulse energies between 0.05-1.00 mJ/pulse. The luminescence was collected at 90 ° and passed through a narrow band-pass interference filter at 1,270 nm. The luminescent signal was detected by a germanium photodiode (North Coast EO-817P) previously cooled with liquid nitrogen. The signal was recorded and averaged over 2-32 shots with a digital oscilloscope (Tektronix TDS320).

2.1.3. Buffer solutions and imaging medium

Phosphate buffered saline (PBS) was prepared in 10 mM phosphate buffer (PB) containing NaCl (150 mM) and calcium chloride dihydrate ($\text{CaCl}_2 \cdot 2\text{H}_2\text{O}$; 100 μM). The 10 mM PB was prepared using $\text{NaH}_2\text{PO}_4 \cdot 2\text{H}_2\text{O}$ and $\text{Na}_2\text{HPO}_4 \cdot 2\text{H}_2\text{O}$ stock solutions (200 mM). The pH of the PBS was adjusted to 7.4 using aqueous solutions of sodium hydroxide (NaOH; 5 M) and hydrochloric acid (HCl; 0.6 M).

Phosphate buffered saline for the biological experiments (PBS-B) was prepared by dissolving 10 PBS tablets in dH₂O (1 L). The solution was sterilised by autoclaving at 110 °C for 10 min. The final PBS solution contained Na_2HPO_4 (8 mM), potassium phosphate monobasic (KH_2PO_4 ; 1 mM), NaCl (160 mM), potassium chloride (KCl; 3 mM) and a pH of 7.3.

MES buffer was prepared in dH₂O containing 2-(N-morpholino)ethanesulfonic acid (MES; 50 mM) and Tween-20 (0.05 %). The pH of the MES buffer was adjusted to 5.5 using aqueous solutions of NaOH (5 M) and HCl (0.6 M).

Imaging medium based on Hank's balanced salt solution (HBSS) for the biological experiments was prepared in dH₂O containing NaCl (120 mM), KCl (5 mM), $\text{CaCl}_2 \cdot 2\text{H}_2\text{O}$ (2 mM), magnesium chloride hexahydrate ($\text{MgCl}_2 \cdot 6\text{H}_2\text{O}$; 1 mM), NaH_2PO_4 (1 mM), NaHCO_3 (1 mM), 4-(2-hydroxyethyl)piperazine-4-ethanesulfonic acid (HEPES; 25 mM), D-glucose (11 mM) and bovine serum albumin (BSA; 1 mg/mL). The pH of the imaging medium was adjusted to 7.4 using an aqueous solution of NaOH (1 M).

Prior to use, all buffer solutions and imaging media were sterilised by filtration through Millex GP syringe driven filter units (0.22 μm).

2.1.4. Cell culture

SK-BR-3 human breast adenocarcinoma cells were routinely cultured in McCoy's 5A phenol red-free medium containing L-glutamine and supplemented with FBS (10 %). MDA-MB-231 human breast adenocarcinoma cells were routinely cultured in high glucose DMEM phenol red-free medium supplemented with L-glutamine (1 %), FBS

(10 %) and sodium pyruvate (1 mM). MCF-10A human mammary epithelial cells were routinely cultured in MEBM medium supplemented with BPE (2 mL), hydrocortisone (0.5 mL), hEGF (0.5 mL), insulin (0.5 mL) and cholera toxin (100 ng/mL). All cells were grown in an incubator at 37 °C under a 5 % CO₂ atmosphere.

2.1.4.1. Cell passage and cell count

SK-BR-3 cells, MDA-MB-231 cells and MCF-10A cells were defrosted by rapidly warming a cryo tube containing 1 mL of the cells in freezing medium (90 % complete cell culture medium and 10 % culture grade DMSO) in a water bath at 37 °C. The cells were transferred to a centrifuge tube containing complete cell culture medium (9 mL). The cells were centrifuged at 21 °C at either 1,000 relative centrifugal force (rcf) for 5 min for the human breast adenocarcinoma cell lines, or at 130 rcf for 7 min for the MCF-10A cells. Following centrifugation, the supernatant was discarded and the pellet containing the cells was resuspended in the appropriate complete cell culture medium (12 mL) and transferred to a 75 cm² Nunc Easy flask. Subcultures were made by dislodging the cells from the flask surface by trypsinization, as explained below.

SK-BR-3 and MDA-MB-231 cells were subcultured (1:4) every 5 days, when they reached near confluence in the 75 cm² flasks. The culture medium was discarded and the cells were washed with PBS-B (5 mL). The cells were dislodged from the flasks by addition of trypsin 0.25 % (1x) EDTA (5 mL) and incubation for 5 min at 37 °C under a 5 % CO₂ atmosphere. Trypsin was deactivated by addition of the respective culture medium (5 mL) and removed by centrifugation at 800 rcf for 5 min at 21 °C. The pellets containing the cells were then resuspended in their respective complete cell culture medium and transferred to two 75 cm² Nunc Easy flasks.

MCF-10A cells were subcultured (1:3) every 5 days, when they reached near confluence in the 75 cm² flasks. The culture medium was discarded and the cells were washed with PBS-B (5 mL). The cells were dislodged from the flasks by addition of trypsin 0.05 % (1x) EDTA (5 mL) and incubation for 15 min at 37 °C under a 5 % CO₂ atmosphere. Trypsin was deactivated by addition of soybean trypsin inhibitor (5 mL; 1 mg/mL in PBS) and removed by centrifugation at 130 rcf for 7 min at 21 °C. The pellet containing the cells

was then resuspended in complete MEBM medium and transferred to two 75 cm² Nunc Easy flasks.

Following trypsinisation, cells resuspended in complete culture medium were counted with a *Neubauer* haemocytometer. The haemocytometer was cleaned with 70 % ethanol and the coverslip assembled. The sample (20 µL) was then pipetted inside the chamber. Under the microscope, the haemocytometer gridlines are seen. Cells in the four sets of sixteen corner squares are counted with a hand tally counter. The average of the four sets was then multiplied by 10⁴ to give the final result in cells per mL.

2.1.4.2. Freezing cells for long-term storage

SK-BR-3, MDA-MB-231 and MCF-10A cells were trypsinised as explained above in **section 2.1.4.1**. Following trypsin removal, the cells were resuspended in freezing medium (10.5 mL). Freezing medium consists of 90 % complete cell culture medium and 10 % culture grade DMSO. Each cell line was placed in 1.8 mL Nunc cryo tubes (1 mL per tube). The cryo tubes were placed in a cryogenic freezing container previously filled with isopropanol and stored at -80 °C overnight. The following day, the cryo tubes were removed from the cryogenic container and stored in a sample box either at -80 °C or in liquid nitrogen.

2.2. Gold nanoparticle enhanced and selective targeting photodynamic therapy of breast cancer cells

2.2.1. Synthesis of C11Pc/C3Pc-PEG-AuNPs

Two zinc phthalocyanines (Pc) composed of either a three carbon-atom chain (C3Pc) or an eleven carbon-atom chain (C11Pc) connecting the macrocycle to the sulfur, see **Figure 3.5**, were kindly provided by Dr Isabelle Chambrier (School of Chemistry, University of East Anglia, Norwich, UK).^{1,2} Gold nanoparticles (*ca.* 3-5 nm; AuNPs) were synthesised by sodium borohydride (NaBH₄) reduction and functionalised with a mixed monolayer of PEG (3,073 Da) together with either C11Pc or C3Pc; using a previously described method³ but with modifications.

C11Pc (2.43 mg; 0.95 μ mol) or C3Pc (2.22 mg; 0.95 μ mol) were dissolved in dry THF (1 mL) and left to stir for 5 min at room temperature. Then, PEG (7.5 mg; 2.5 μ mol) was dissolved in dry THF (2 mL), added to the phthalocyanine solution and stirred at room temperature for 5 min. Gold (III) chloride trihydrate (HAuCl₄·3H₂O; 1.2 mg; 3.0 μ mol) was dissolved in dry THF (1.2 mL), added to the Pc-PEG mixtures and stirred at room temperature for a further 5 min. Finally, a solution of NaBH₄ (1.5 mg; 39.65 μ mol) was prepared in dH₂O (1.2 mL) and added to the Pc-PEG-HAuCl₄ mixture rapidly and under vigorous stirring. The reaction was stirred overnight (*ca.* 17 h) at room temperature in the dark at moderate speed.

The resulting solution was a mixture of free Pc, AuNPs functionalised with Pc only, AuNPs functionalised with PEG only and AuNPs functionalised with both Pc and PEG. To purify the mixture, excess dry THF (5.4 mL) was added rapidly and under vigorous stirring, followed by centrifugation in Eppendorf tubes (1.5 mL) at 1,300 rpm for 2 min at 4 °C. The supernatant was collected and the brown pellet containing AuNPs functionalised only with PEG was discarded. The solvent mixture in the supernatant was evaporated by rotary evaporation under reduced pressure at 70 °C. At this point, MES buffer (5 mL) was added and the mixture was solubilised using an ultrasonic bath. The solution was centrifuged in Eppendorf tubes (1.5 mL) at 14,000 rpm for 30 min at 4 °C. The pellet containing free Pc and AuNPs functionalised only with Pc, and thus not soluble in an aqueous solution, was discarded. The supernatant containing the Pc-PEG-AuNPs was collected, filtered through a Millex GP syringe driven filter unit (0.22 μ m) and stored at 4 °C.

The synthesised Pc-PEG-AuNPs were characterised using UV-vis and fluorescence spectroscopies and TEM. The UV-vis extinction spectrum was recorded between 300-800 nm. The fluorescence emission spectrum was recorded using an excitation wavelength of 633 nm between 653-850 nm. The fluorescence excitation spectrum was recorded, using an emission wavelength of 780 nm, between 500-750 nm.

2.2.2. Functionalisation of Pc-PEG-AuNPs with anti-HER2 antibody

C11Pc-PEG-AuNPs and C3Pc-PEG-AuNPs were further functionalised with anti-HER2 antibody. The antibody was conjugated to the PEG on the surface of the AuNPs *via* the terminal carboxyl groups in the PEG ligand using a previously reported method but with modifications.^{3,4} The conjugation was performed *via* an amide linkage through N-(3-Dimethylaminopropyl)-N'-ethylcarbodiimide hydrochloride (EDC) and N-hydroxysuccinimide (NHS) coupling.⁵ EDC (0.8 µL) and NHS (1.2 mg) were added to the Pc-PEG-AuNPs in MES buffer (1 mL; *ca.* 2 µM Pc) and stirred for 30 min at room temperature in the dark. Excess EDC/NHS was removed by ultrafiltration in vivaspin™ 500 columns at 14,000 rpm for 30 min at 4 °C. The NHS-ester functionalised Pc-PEG-AuNPs were redispersed in PBS (1 mL) and anti-HER2 antibody (5 µL; 1 mg/mL) was added to give a final antibody concentration of 65 nM. The solutions were stirred overnight (*ca.* 17 h) at room temperature in the dark.

Following overnight incubation, unbound anti-HER2 antibody was removed by ultrafiltration in vivaspin™ 500 columns by centrifuging at 14,000 rpm for 30 min at 4 °C. The washes at the bottom of the vivaspin™ 500 columns were removed and the AuNPs pellets retained in the vivaspin™ 500 columns were resuspended in PBS (500 µL). This purification step was repeated until no more unbound antibody was left. The end point was measured using the UV-vis absorbance of the washes between 200-500 nm to monitor the decrease in antibody absorption band at *ca.* 250 nm. The final AuNPs pellets were redispersed in FBS-free McCoy's 5A medium containing L-glutamine and the samples were stored at 4 °C.

2.2.3. Nanoparticle characterisation by TEM

The size and morphology of the AuNPs was characterised using TEM. A droplet of the AuNPs (20 µL) in MES buffer was placed onto a holey carbon film 300 mesh copper grid and left for 2 min to allow the AuNPs to sediment onto the grid. Excess MES buffer was then removed by gently poking the side of the grid with filter paper. The grid was left to completely dry before imaging.

2.2.4. Determination of extinction coefficients of C11Pc and C3Pc

C11Pc (2.27 mg) was dissolved in THF (2 mL) giving an initial concentration of 443 μ M. C3Pc (24.5 mg) was dissolved in THF (5 mL) giving an initial concentration of 2,094 μ M. This initial C11Pc and C3Pc solutions were then further diluted with THF to obtain concentrations ranging from 0-5 μ M. These dilutions were prepared in volumetric flasks (2 mL). The dilutions were analysed by UV-vis spectroscopy between 300-800 nm starting with the lowest concentration. A calibration curve at 698 nm was created and a value for the extinction coefficient for each phthalocyanine was obtained.

2.2.5. Fluorescence quantum yields of free Pc and Pc-PEG-AuNPs

The fluorescence quantum yield for both the free Pc and the Pc-PEG-AuNPs were obtained using UV-vis and fluorescence spectroscopies. Zinc 2,9,16,23-tetra-tert-butyl-29H,31H-phthalocyanine (ZnPc) was used as a reference, as it is known to have a fluorescence quantum yield of 0.33 in toluene.⁶

Free C3Pc (0.52 mg) was dissolved in THF (2 mL) to give an initial concentration of 111 μ M. C3Pc-PEG-AuNPs dissolved in MES buffer at an initial concentration of 3.6 μ M were used. Free C11Pc (2.27 mg) was dissolved in THF (2 mL) to give an initial concentration of 443 μ M. C11Pc-PEG-AuNPs dissolved in MES buffer at an initial concentration of 1.3 μ M were used. The reference standard ZnPc (0.66 mg) was dissolved in toluene (2 mL) to give an initial concentration of 411 μ M. All samples were further diluted to give concentrations ranging from 0-1.2 μ M. Five dilutions were analysed for each sample. The UV-vis absorption spectra of all samples were recorded and the absorbance intensity at 640 nm was noted. Then, the fluorescence emission spectra of the samples, using an excitation wavelength of 640 nm, were recorded between 660-850 nm.

The fluorescence quantum yields were obtained by the creation of a calibration curve of integrated fluorescence intensity (*i.e.*, area under the curve) *vs* absorbance at the excitation wavelength, 640 nm. The calibration curve produces a straight line with gradient *m* and intercept 0. The gradient is proportional to the fluorescence quantum yield of the sample. By comparing the gradient of the unknown samples to the gradient

of the reference standard, the fluorescence quantum yields can be estimated. The equation used to calculate the fluorescence quantum yields is shown in **section 3.2.3**.

2.2.6. Synthesis of control PEG-AuNPs

The synthesis of AuNPs (*ca.* 2-4 nm) functionalised with PEG (PEG-AuNPs) of a similar size to the Pc-PEG-AuNPs was performed. PEG (15.2 mg; 4.95 μ mol) was dissolved in dH₂O (15 mL) and left to stir at room temperature. Then, HAuCl₄·3H₂O (1.2 mg; 3.0 μ mol) was dissolved in THF (1.2 mL), added to the PEG solution and stirred at room temperature for 5 min. A fresh solution of NaBH₄ (1.5 mg; 39.65 μ mol) in dH₂O (0.5 mL) was prepared and added to the PEG-HAuCl₄ mixture. The reaction was stirred for a further 4 h at room temperature. Purification of the AuNPs was then performed. Firstly, the THF was evaporated by rotary evaporation under reduced pressure at 60 °C. The final solution in dH₂O was transferred to vivaspin™ 500 columns and centrifuged at 14,000 rpm for 10 min at 4 °C. The PEG-AuNPs were resuspended in MES buffer (16.7 mL) and filtered through a Millex GP syringe driven filter unit (0.22 μ m). The UV-vis extinction spectrum was recorded between 250-800 nm. The PEG-AuNPs were stored at room temperature.

2.2.7. Measurement of singlet oxygen production

Production of singlet oxygen (${}^1\text{O}_2$) was measured using the singlet oxygen probe 9,10-anthracenediyl-bis (methylene) dimalonic acid (ABMA). ABMA (0.63 mg) was dissolved in methanol (MeOH; 3 mL) to give an initial concentration of 0.512 mM.

The Pc-PEG-AuNPs (511 μ L) in MES buffer were placed in a 1.5 mL quartz cuvette together with ABMA (1 μ L; 1 μ M) and a magnetic stirrer bar. Oxygen was bubbled through the solution and the quartz cuvette was stoppered. The fluorescence emission spectrum of the initial solution was recorded using an excitation wavelength of 380 nm between 390-600 nm. The sample was then irradiated at 633 nm using a 10 mW HeNe laser for 40 min with continuous stirring. The laser was placed 50 cm away from the cuvette. The fluorescence emission spectrum of the sample was recorded every 5 min.

2.2.8. Singlet oxygen quantum yields

The singlet oxygen quantum yields of the free Pcs as well as the Pc-PEG-AuNPs were measured. The assistance of Prof Andrew Beeby (Department of Chemistry, University of Durham, Durham, UK) is gratefully acknowledged. Perinaphthenone was used as the reference sample as it is known to have a singlet oxygen quantum yield of 1.0 in toluene.⁷

The free C3Pc and C11Pc, as well as perinaphthenone were dissolved in toluene. Three dilutions of each sample with absorbance values of ≈ 0.16 , ≈ 0.21 and ≈ 0.32 at 355 nm were prepared. For each set of dilutions, the samples were placed in a 1.5 cm stoppered quartz cuvette and irradiated at 355 nm using the third harmonic of a Q-switched Nd:YAG laser with pulse energies in the range 0.05-1.00 mJ per pulse. The luminescence was collected at 90° and passed through a narrow band-pass interference filter at 1,270 nm. Only light with a wavelength of 1,270 nm, *i.e.* the luminescence signal from $^1\text{O}_2$, will be collected. Detection was performed with a germanium photodiode, which had been previously cooled with liquid nitrogen for 1.5 h. The luminescence signal from $^1\text{O}_2$ was recorded and averaged over 2-32 shots using a digital oscilloscope. The intensity of $^1\text{O}_2$ ($I_{^1\text{O}_2}$) emission was recorded at different laser power intensities, ranging from 1.24-28.1 mV.

The $^1\text{O}_2$ quantum yields were obtained by the creation of a calibration curve of $I_{^1\text{O}_2}$ vs intensity of light absorbed by the sample (I_a). The calibration curve produces a straight line with gradient m , which is proportional to the $^1\text{O}_2$ quantum yield. By comparing the gradient of the unknown samples to the gradient of the reference standard, the $^1\text{O}_2$ quantum yields can be estimated. The equation used for the comparison is shown in **section 3.2.5**.

The measurement of $^1\text{O}_2$ quantum yield for the Pc-PEG-AuNPs was more challenging. The AuNPs were dissolved in an aqueous solution, MES buffer. Aqueous solutions lead to the quenching of the $I_{^1\text{O}_2}$ signal. As a result, the signal was too low to be able to estimate a value for the $^1\text{O}_2$ quantum yield. In an attempt to minimise the quenching effect and increase the intensity of the $I_{^1\text{O}_2}$ signal, C11Pc-PEG-AuNPs and C3Pc-PEG-AuNPs were dissolved in D_2O . However, the signal in D_2O was also too low to estimate

a value for the ${}^1\text{O}_2$ quantum yields. C11Pc-PEG-AuNPs and C3Pc-PEG-AuNPs, dissolved in D_2O , were diluted to an absorbance value of ≈ 0.28 at 355 nm. The decay of ${}^1\text{O}_2$ production was recorded with pulse energies of 4.0 mJ and 4.5 mJ. To confirm that the low signals seen were due to the production of ${}^1\text{O}_2$ by the samples, both AuNPs samples were deoxygenated by bubbling He through them for 5 min. The signal was again recorded after the removal of the majority of the oxygen in the solutions had taken place.

2.2.9. MTT cell viability assay

SK-BR-3 human breast adenocarcinoma cells were trypsinised and counted as described in **section 2.1.4.1**. The cells were seeded onto two white-bottom Nunc Nunclon™ Δ Surface 96- well microplates at a concentration of 20×10^4 cells/mL (100 μL /well). The cells were incubated for *ca.* 48 h at 37 °C under a 5 % CO_2 atmosphere.

The culture medium was removed using a micropipette and the cells were washed once with PBS-B (100 μL). The nanoparticle samples, anti-HER2 antibody conjugated or non-conjugated C11Pc-PEG-AuNPs and C3Pc-PEG-AuNPs at various Pc concentrations in FBS-free McCoy's 5A medium containing L-glutamine were then added (50 μL /well). Additionally, a solution of staurosporine (1 mM in DMSO) dispersed in FBS-free McCoy's 5A medium containing L-glutamine (50 μL ; 20 μM) was also used as a positive control for cytotoxicity.⁸ Control cells without any AuNPs loaded were treated with FBS-free McCoy's 5A medium containing L-glutamine. The cells were incubated with the samples and controls for 3 h at 37 °C under a 5 % CO_2 atmosphere.

Following incubation with the AuNPs, the samples were removed and the cells were washed with PBS-B (100 μL) three times. The cells were then resuspended in complete McCoy's 5A medium (100 μL) containing L-glutamine and supplemented with FBS (10 %). At this point, one of the plates was irradiated at 633 nm using a 10 mW HeNe laser fitted with a biconvex diverging lens for 6 min per well. The laser was located 50 cm above the 96-well plate, giving an irradiance of 29 mW/cm² and a total light dose of 10.5 J/cm². The plate not being irradiated was kept covered in aluminium foil in the

dark. The cells were further incubated for *ca.* 48 h at 37 °C under a 5 % CO₂ atmosphere prior to measuring cell viability.

MTT reagent (3-(4,5-dimethylthiazol-2-yl)-2,5-diphenyltetrazolium bromide) (10 µL; 5 mg/mL in PBS) was added to each well and incubated for 4 h at 37 °C under a 5 % CO₂ atmosphere.^{9,10} The medium was then removed from the wells using a micropipette and the MTT formazan crystals were washed with PBS-B (100 µL) once and dissolved in culture-grade DMSO (200 µL). The contents of the wells were transferred to clear-bottom Nunc Nunclon™ Δ Surface 96- well microplates. The absorbance intensity was then measured at 560 nm. Background absorbance was corrected by subtracting the absorbance measurement from McCOY's 5A medium alone incubated with MTT. Cell viability was calculated as a percentage of non-treated, non-irradiated cells. All samples were analysed in triplicates. Statistical significance between means was determined using a two-tailed Student's *t*-test and P values < 0.05 were considered significant.¹¹

2.2.10. CellTiter-Blue® cell viability assay

SK-BR-3 human breast adenocarcinoma cells and MCF-10A human mammary epithelial cells were trypsinised and counted as described in **section 2.1.4.1**. The cells were seeded and treated with the AuNPs samples as detailed in **section 2.2.9**.

Following incubation post-PDT treatment, CellTiter-Blue® reagent¹² (20 µL) was added to each well and incubated for 4 h at 37 °C under a 5 % CO₂ atmosphere. Fluorescence emission was then measured at 594 nm following excitation at 561 nm. Background fluorescence was corrected by subtracting fluorescence emission from McCOY's 5A medium alone incubated with CellTiter-Blue®. Cell viability was calculated as a percentage of non-treated, non-irradiated cells. All samples were analysed in triplicates. Statistical significance between means was determined using a two-tailed Student's *t*-test and P values < 0.05 were considered significant.¹¹

2.2.11. Confocal laser scanning microscopy

For imaging experiments, SK-BR-3 cells were cultured in McCoy's 5A medium containing phenol red and supplemented with L-glutamine (1 %) and FBS (10 %). SK-BR-3 cells were trypsinised and counted as described in **section 2.1.4.1**. The cells were then seeded onto 18 mm diameter glass coverslips inside Nunc 6-well multidishes at a concentration of 2×10^4 cells/mL (3 mL/well). The cells were incubated for *ca.* 48 h at 37 °C under a 5 % CO₂ atmosphere.

The culture medium was removed and the cells were washed once with PBS-B (1 mL). The nanoparticle samples, anti-HER2 antibody conjugated or non-conjugated C11Pc-PEG-AuNPs and C3Pc-PEG-AuNPs (0.15 µM or 0.23 µM Pc) in FBS-free McCoy's 5A medium supplemented with L-glutamine (1 %), were then added (1 mL/well). Control cells not loaded with any AuNP samples were treated with FBS-free McCoy's 5A medium supplemented with L-glutamine (1 %). The cells were incubated with the samples and controls for 3 h at 37 °C under a 5 % CO₂ atmosphere.

Following incubation with the samples, the cells were washed with PBS-B (1 mL) three times. They were then resuspended in complete McCoy's 5A medium (2 mL) supplemented with L-glutamine (1 %) and FBS (10 %). At this point, the cells were irradiated at 633 nm using a 10 mW HeNe laser fitted with a biconvex diverging lens for 6 min per coverslip. The non-irradiated plates were left covered in aluminium foil in the dark. Following irradiation, the cells were further incubated for 19 h at 37 °C under a 5 % CO₂ atmosphere.

For imaging in the confocal microscope, the 18 mm coverslips were placed in a Ludin chamber, which was securely tightened. The cells in the coverslips were washed with imaging medium (*ca.* 1 mL) three times and finally resuspended in imaging medium (*ca.* 1 mL). The Ludin chamber was fitted on a heating stage at 37 °C in the confocal microscope. A 633 nm HeNe laser was used to excite the Pc on the AuNPs and the fluorescence emission was collected in the red channel with a 650 nm long pass filter. Differential interference contrast (DIC) images were collected simultaneously using a 488 nm argon-ion laser.^{13,14} To test for dead cells, the dead cell marker propidium iodide was used. Propidium iodide (5 µL; 1 mg/mL in PBS) was dissolved in imaging

medium (1 mL). The solution was directly added to the coverslips, which had been previously placed in the Ludin chamber and mounted on the heating stage. The propidium iodide solution was incubated with the cells at 37 °C for 5 min in the dark. A 543 nm HeNe laser was used to excite propidium iodide and the fluorescence emission was collected in the pink channel with a band pass filter between 560-615 nm.^{13,15}

2.2.12. Colocalisation studies by confocal laser scanning microscopy

For imaging experiments, SK-BR-3 cells were cultured in McCoy's 5A medium containing phenol red and supplemented with L-glutamine (1 %) and FBS (10 %). SK-BR-3 human breast adenocarcinoma cells were dislodged from the flasks by trypsinization and counted as explained in **section 2.1.4.1**. The cells were then seeded on 18 mm diameter glass coverslips and treated with anti-HER2 antibody conjugated C11Pc-PEG-AuNPs and C3Pc-PEG-AuNPs (0.15 µM Pc) as described in **section 2.2.11**, but no irradiation was performed.

For the colocalisation studies, LysoSensor™ Green DND-189 was used to mark the acidic organelles inside the cells. Prior to imaging, LysoSensor™ Green (2 µL; 1 mM in DMSO) was added to the coverslips in the 6-well plates containing McCoy's 5A medium (2 mL) supplemented with L-glutamine and FBS (10 %). The cells were incubated with LysoSensor™ Green for 30 min at 37 °C under a 5 % CO₂ atmosphere. For imaging, the coverslips were placed in a Ludin chamber, which was mounted on a heated stage in the confocal microscope, as explained in **section 2.2.11**. A 458 nm argon-ion laser was used to excite the LysoSensor™ Green and the fluorescence emission was collected in the green channel with a band pass filter between 475-525 nm. Simultaneously, a 633 nm HeNe laser was used to excite the Pc on the AuNPs and the fluorescence emission was collected in the red channel with a 650 nm long pass filter. Additionally, DIC images were also collected at the same time using a 458 nm argon-ion laser.

2.2.13. InCell ELISA for the detection of the HER2 receptor on SK-BR-3 cells

An InCell Enzyme Linked Immunosorbent Assay (ELISA) was performed to study the targeting ability of anti-HER2 antibody towards the HER2 receptor overexpressed on the surface of SK-BR-3 cells.¹⁶ SK-BR-3 cells were dislodged from the flasks by trypsinization and counted as described in **section 2.1.4.1**. The cells were seeded onto a clear-bottom Nunc Nunclon™ Δ Surface 96-well microplate at a concentration of 10×10^4 cells/mL (100 µL/well). The cells were incubated overnight at 37 °C under a 5 % CO₂ atmosphere.

The culture medium was removed and the cells were washed with PBS-B (100 µL) once. The nanoparticle samples, anti-HER2 antibody conjugated or non-conjugated C11Pc-PEG-AuNPs and C3Pc-PEG-AuNPs (0.20 µM Pc) in FBS-free McCoy's 5A medium containing L-glutamine, were then added (50 µL/well). Additionally, a solution of staurosporine (1 mM in DMSO) dispersed in FBS-free McCoy's 5A medium containing L-glutamine (50 µL; 20 µM) was used as a positive control for cytotoxicity. Control cells not loaded with any AuNP samples were treated with FBS-free McCoy's 5A medium containing L-glutamine (50 µL). The cells were incubated with the samples and controls for 3 h at 37 °C under a 5 % CO₂ atmosphere.

During the incubation period, the required buffers for the InCell ELISA were prepared. Tris buffered saline (1X; TBS) was prepared by addition of 20X TBS (2.5 mL) to dH₂O (47.5 mL). Formaldehyde (4 %) was prepared by addition of MeOH-free formaldehyde (16 %; 1.5 mL) to 1X TBS (4.5 mL). Permeabilisation buffer was prepared by addition of Surfact-Amps X-100 detergent (110 µL) to 1X TBS (11 mL). Quenching solution was prepared by addition of hydrogen peroxide (H₂O₂; 30 %; 380 µL) to 1X TBS (11 mL). Washing buffer (1X) was prepared by addition of 20X TBS (7.5 mL) and Surfact-Amps 20 detergent (1.5 mL) to dH₂O (141 mL). Finally, the solution in which the primary antibody was diluted (blocking-washing solution) was prepared by addition of blocking buffer (3 mL) to washing buffer (1X; 3 mL).

Following incubation with the AuNPs, the samples were removed and the cells were washed with PBS-B (100 µL) three times and resuspended in McCoy's 5A medium (100 µL) containing L-glutamine and supplemented with FBS (10 %). The first part of

the assay involved fixing the cells prior to addition of the primary antibody. From this point onwards, all incubation steps were performed with gentle shaking of the microplate and the plate contents were always removed using a micropipette to minimise cell loss. The culture medium was removed and formaldehyde (4 %; 100 μ L) was added to each well and incubated with the cells for 15 min at room temperature. The formaldehyde solution was removed and the plate was washed with 1X TBS (100 μ L) twice. Permeabilisation buffer (100 μ L) was added to each well and incubated with the cells for 15 min at room temperature. The permeabilisation buffer was removed and the cells were washed with 1X TBS (100 μ L) once. Quenching solution (100 μ L) was added to each well and incubated with the cells for 20 min at room temperature. The quenching solution was then removed and the cells were washed with 1X TBS (100 μ L) once. Following the fixing of the cells, blocking buffer (100 μ L) was added and incubated with the cells for 30 min at room temperature.

While the cells were being incubated with blocking buffer, the anti-HER2 primary antibody solution was prepared. Anti-HER2 antibody (5 μ L; 1 mg/mL in PBS containing 0.02 % sodium azide) was diluted in the blocking-washing solution (5 mL) previously prepared, as explained above, to give a final concentration of 1 μ g/mL. Following incubation of the cells with blocking buffer, the blocking buffer was removed and anti-HER2 antibody (50 μ L; 1 μ g/mL) was added to each well. Non-specific signal control wells, *i.e.*, cells not incubated with primary antibody, were incubated with blocking-washing solution (50 μ L) instead. The microplate was sealed with a plate sealer and the cells were incubated with the primary antibody overnight (*ca.* 17 h) at 4 °C.

The second part of the assay involved the development of an absorbance intensity signal for the levels of HER2 present in each sample. Following overnight incubation with the primary antibody, the blocking-washing solution was removed and the cells were washed with washing buffer (100 μ L) three times. HRP conjugate (15 μ L) was diluted with washing buffer (6 mL). The diluted HRP conjugate (100 μ L) was added to each well and incubated with the cells for 30 min at room temperature. Following incubation, the HRP conjugate was removed and the plate was washed with washing buffer (200 μ L) three times. The substrate 3,3',5,5'-tetramethylbenzidine (100 μ L; TMB) was added to each well and the plate was covered with aluminium foil. The plate was

then incubated for 20 min at room temperature in the dark. TMB stop solution (100 μ L) was then added to stop the reaction between the TMB Substrate and the HRP conjugate. The absorbance intensity was measured at 450 nm. Background absorbance was corrected by subtracting the absorbance measurement from the non-specific signal controls. All samples were analysed in triplicates.

The third part of the assay involved the whole-cell staining of each well so the values of the HER2 receptor could be normalised to cell number. The plate contents were emptied and the plate was washed with dH₂O (200 μ L) twice. Janus Green Whole-Cell Stain (100 μ L) was added to each well and incubated for 5 min at room temperature. The stain was then removed and the plate was washed with dH₂O (200 μ L) five times to remove all excess stain. Elution buffer (100 μ L) was added to each well and incubated for 10 min at room temperature. The absorbance intensity was then measured at 615 nm. Background absorbance was corrected by subtracting the absorbance measurement from McCoy's 5A medium alone. All samples were analysed in triplicates. To obtain the values of HER2 expression normalised to cell number in each well, the corrected absorbance values at 450 nm were divided by the corrected absorbance values at 615 nm.

2.2.14. ApoTox-Glo™ Triplex assay

SK-BR-3 cells were trypsinised and counted as described in **section 2.1.4.1**. The cells were seeded onto two white-bottom Nunc Nunclon™ Δ Surface 96-well microplates at a concentration of 18×10^4 cells/mL (100 μ L/well). The cells were incubated for *ca.* 48 h at 37 °C under a 5 % CO₂ atmosphere.

The culture medium was removed using a micropipette and the cells were washed once with PBS-B (100 μ L). The nanoparticle samples, anti-HER2 antibody conjugated or non-conjugated C11Pc-PEG-AuNPs (0.16 μ M C11Pc) and C3Pc-PEG-AuNPs (0.15 μ M Pc) in FBS-free McCoy's 5A medium containing L-glutamine, were then added (50 μ L/well). Additionally, a solution of Staurosporine (1 mM in DMSO) dispersed in FBS-free McCoy's 5A medium containing L-glutamine (50 μ L; 20 μ M) was also used as a positive control for cytotoxicity *via* apoptosis. Control cells without any AuNPs loaded were

treated with FBS-free McCoy's 5A medium containing L-glutamine. The cells were incubated with the samples and controls for 3 h at 37 °C under a 5 % CO₂ atmosphere.

Following incubation with the AuNPs, the samples were removed and the cells were washed with PBS-B (100 µL) three times. The cells were then resuspended in complete McCoy's 5A medium (100 µL) containing L-glutamine and supplemented with FBS (10 %). At this point, one of the plates was irradiated at 633 nm using a 10 mW HeNe laser fitted with a biconvex diverging lens for 6 min per well, giving an irradiance of 29 mW/cm² and a total light dose of 10.5 J/cm². The laser was located 50 cm above the 96-well plate. The plate not being irradiated was kept covered in aluminium foil in the dark. Following irradiation, the cells were further incubated for either 4 h or 48 h at 37 °C under a 5 % CO₂ atmosphere.

The ApoTox-Glo™ Triplex assay was then performed.^{17,18} The assay buffer, glycyl-phenylalanyl-aminofluorocoumarin (GF-AFC) substrate and bis-alanylalanyl-phenylalanyl-rhodamine 110 (bis-AAF-R110) substrate were thawed in a water bath at 37 °C. The Caspase-Glo® 3/7 substrate and buffer were thawed at room temperature. Once all the reagents had reached room temperature, the Viability/Cytotoxicity reagent was prepared by adding GF-AFC substrate (10 µL) and bis-AAF-R110 substrate (10 µL) to the assay buffer (2 mL). The mixture was vortex-mixed to ensure a homogeneous distribution. The Viability/Cytotoxicity reagent (20 µL) was added to each well and the plate was mixed by orbital shaking at 300 rpm for 30 seconds. The plate was then incubated at 37 °C under a 5 % CO₂ atmosphere for 1 h. Fluorescence intensity was then measured at two wavelength sets. The fluorescence emission from the viability component was measured at 505 nm following excitation at 400 nm. The fluorescence emission from the cytotoxicity component was measured at 520 nm following excitation at 485 nm.

The Caspase-Glo® 3/7 reagent was prepared by adding the Caspase-Glo® 3/7 buffer (10 mL) to the bottle containing the lyophilized Caspase-Glo® 3/7 substrate. The reagent was thoroughly mixed before use. The Caspase-Glo® reagent (100 µL) was then added to each well and the plate was mixed by orbital shaking at 300 rpm for 30 seconds. The plate was incubated at room temperature for 30 min. The luminescence signal was then measured using an integration time of 1 second.

2.3. Targeted photodynamic therapy of breast cancer cells using lactose-phthalocyanine gold nanoparticle conjugates

2.3.1. Synthesis of lactose-C11Pc-AuNPs

Gold nanoparticles (AuNPs) were synthesised by NaBH₄ reduction and functionalised with a mixed monolayer of C11Pc and lactose. Initially, a version of the method described in **section 2.2.1** for the synthesis of C11Pc-PEG-AuNPs was used but replacing the PEG ligand with the thiolated lactose ligand.

C11Pc (2.43 mg; 0.95 µmol) was dissolved in dry THF (1 mL) and left to stir at room temperature. Then, lactose (2 mL; 1.31 mM in dH₂O) was added to the C11Pc solution and stirred at room temperature for 5 min. HAuCl₄·3H₂O (1.2 mg; 3.0 µmol) was dissolved in dH₂O (1.2 mL), added to the C11Pc-lactose mixture and stirred at room temperature for a further 5 min. Finally, a solution of NaBH₄ (1.5 mg; 39.65 µmol) was prepared in dH₂O (1.2 mL) and added to the previous mixtures rapidly and under vigorous stirring. The reaction was stirred overnight (*ca.* 17 h) at room temperature in the dark at moderate speed.

The resulting solution was a mixture of free Pc, AuNPs functionalised with Pc only, AuNPs functionalised with lactose only and AuNPs functionalised with both Pc and lactose. To purify the mixture, excess dry THF (6 mL) was added rapidly and under vigorous stirring, followed by centrifugation in Eppendorf tubes (1.5 mL) at 1,300 rpm for 2 min at 4 °C. The supernatant was collected and the brown pellet containing AuNPs functionalised only with lactose was discarded. The solvent mixture in the supernatant was evaporated by rotary evaporation under reduced pressure at 70 °C. For further purification, more excess THF (5.4 mL) was added, followed by the same centrifugation and evaporation steps as explained previously. Once all the THF had been evaporated, MES buffer (3 mL) was added and the solubilisation was assisted using an ultrasonic bath. However, most of the solution appeared white, which suggested there was no Pc attached to the lactose-AuNPs. The solution was centrifuged in Eppendorf tubes (1.5 mL) at 14,000 rpm for 30 min at 4 °C. The pellet containing free Pc and AuNPs functionalised only with Pc, and thus not soluble in an aqueous solution, was discarded. The supernatant containing the lactose-Pc-AuNPs was collected and filtered through a

Millex GP syringe driven filter unit (0.22 μm). The synthesised lactose-Pc-AuNPs were characterised using UV-vis spectroscopy between 300-800 nm. The yield for the resulting lactose-C11Pc-AuNPs was low as the solution looked colourless and the UV-vis extinction spectrum showed a small absorption band for C11Pc at 698 nm.

In an attempt to increase the loading of C11Pc on the lactose-AuNPs, the amount of lactose used was reduced. Additionally, the amount of THF in the reaction mixture was increased to provide a higher solubility of C11Pc in the mixture. C11Pc (2.43 mg; 0.95 μmol) was dissolved in dry THF (1.45 mL) and left to stir at room temperature. Then, lactose (1 mL; 1.31 mM in dH₂O) was added to the C11Pc solution and stirred at room temperature for 5 min. HAuCl₄·3H₂O (1.2 mg; 3.0 μmol) was dissolved in dry THF (1.2 mL), added to the C11Pc-lactose mixture and stirred at room temperature for a further 5 min. Finally, a solution of NaBH₄ (1.5 mg; 39.65 μmol) was prepared in dH₂O (1.2 mL) and added to the previous mixtures rapidly and under vigorous stirring. The reaction was stirred overnight (*ca.* 17 h) at room temperature in the dark at moderate speed. The purification of the mixture was performed in the same way as that described above for the initial synthetic method. The resulting lactose-C11Pc-AuNPs were filtered through a Millex GP syringe driven filter unit (0.22 μm) and they were characterised using UV-vis spectroscopy between 300-800 nm. The final solution was stored at 4 °C.

2.3.2. Synthesis of lactose-C3Pc-AuNPs

Gold nanoparticles were synthesised by NaBH₄ reduction and functionalised with a mixed monolayer of C3Pc and lactose. C3Pc (2.22 mg; 0.95 μmol) was dissolved in dry THF (1.45 mL) and left to stir at room temperature. The synthesis followed the improved method for the synthesis of lactose-C11Pc-AuNPs described at the end of **section 2.3.1**, where the amount of lactose within the reaction mixture was reduced while the amount of THF was increased in order to increase the loading of Pc immobilised on the surface of the lactose-AuNPs.

2.3.3. Nanoparticle characterisation with TEM

The synthesised lactose-C11Pc-AuNPs and lactose-C3Pc-AuNPs were characterised using TEM, as described previously in **section 2.2.3**.

2.3.4. Measurement of singlet oxygen production for lactose-Pc-AuNPs

Production of $^1\text{O}_2$ was measured using the singlet oxygen probe ABMA, as previously explained in **section 2.2.7**.

2.3.5. Synthesis of C11Pc/C3Pc-sPEG-AuNPs

Gold nanoparticles were synthesised by NaBH_4 reduction and functionalised with a mixed monolayer of either C11Pc or C3Pc and thiol-dPEG®-acid (sPEG), a PEG ligand with a chain simulating the length of the lactose ligand. C11Pc (2.43 mg; 0.95 μmol) or C3Pc (2.22 mg; 0.95 μmol) were dissolved in dry THF (1 mL) and left to stir at room temperature. Then, sPEG (0.51 mg; 1.8 μmol) was dissolved in dH_2O (1.9 mL), added to the phthalocyanine solutions and stirred at room temperature for 5 min. $\text{HAuCl}_4 \cdot 3\text{H}_2\text{O}$ (1.2 mg; 3.0 μmol) was dissolved in dH_2O (1.2 mL), added to the Pc-sPEG mixtures and stirred at room temperature for a further 5 min. Finally, a solution of NaBH_4 (1.5 mg; 39.65 μmol) was prepared in dH_2O (1.2 mL) and added to the previous mixtures rapidly and under vigorous stirring. The reaction was stirred overnight (*ca.* 17 h) at room temperature in the dark at moderate speed.

The resulting solution was a mixture of free Pc, AuNPs functionalised with Pc only, AuNPs functionalised with sPEG only and AuNPs functionalised with both Pc and sPEG. To purify the mixture, excess dry THF (5.4 mL) was added rapidly and under vigorous stirring, followed by centrifugation in Eppendorf tubes (1.5 mL) at 1,300 rpm for 2 min at 4 °C. The supernatant was collected and the brown pellet containing AuNPs functionalised only with sPEG was discarded. The solvent mixture in the supernatant was evaporated by rotary evaporation under reduced pressure at 70 °C. For further purification, more excess THF (5.4 mL) was added, followed by the same centrifugation

and evaporation steps as explained previously. Once all the THF had been evaporated, MES buffer (5 mL) was added and the solubilisation was assisted using an ultrasonic bath. The solution was centrifuged in Eppendorf tubes (1.5 mL) at 14,000 rpm for 30 min at 4 °C. The pellet containing free Pc and AuNPs functionalised only with Pc, and thus not soluble in an aqueous solution, was discarded. The supernatant containing the Pc-sPEG-AuNPs was collected and filtered through a Millex GP syringe driven filter unit (0.22 µm). The synthesised Pc-sPEG-AuNPs were characterised using UV-vis spectroscopy between 300-800 nm and the solutions were stored at 4 °C.

2.3.6. Synthesis of control sPEG-AuNPs

Control AuNPs functionalised with sPEG but without photosensitiser were synthesised following the method described in **section 2.2.6**. A solution of sPEG (1.44 mg; 5.1 µmol) in dH₂O (15 mL) was prepared and left to stir at room temperature. Then, HAuCl₄·3H₂O (1.2 mg; 3.0 µmol) was dissolved in THF (1.2 mL), added to the sPEG solution and stirred at room temperature for 5 min. A fresh solution of NaBH₄ (1.5 mg; 39.65 µmol) in dH₂O (0.5 mL) was prepared and added to the sPEG-HAuCl₄ mixture. The reaction was stirred for a further 4 h at room temperature. Purification of the AuNPs was then performed. Firstly, the THF was evaporated by rotary evaporation under reduced pressure at 60 °C. The final solution in dH₂O was transferred to vivaspin™ 500 columns and centrifuged at 14,000 rpm for 10 min at 4 °C. The sPEG-AuNPs were resuspended in McCoy's 5A phenol red-free, FBS free medium (2 mL) containing L-glutamine and filtered through a Millex GP syringe driven filter unit (0.22 µm). The UV-vis extinction spectrum was recorded between 250-800 nm. The sPEG-AuNPs were stored at room temperature.

2.3.7. MTT cell viability assay for lactose targeting

SK-BR-3 human breast adenocarcinoma cells and MDA-MB-231 human breast adenocarcinoma cells were dislodged from the flasks by trypsination and counted as described in **section 2.1.4.1**. The cells were then seeded following the procedure

described in **section 2.2.9** and incubated for *ca.* 48 h at 37 °C under a 5 % CO₂ atmosphere.

The culture medium was removed using a micropipette and the cells were washed once with PBS-B (100 µL). The nanoparticle samples, lactose-C11Pc-AuNPs and control C11Pc-sPEG-AuNPs together with lactose-C3Pc-AuNPs and control C3Pc-sPEG-AuNPs, dissolved in FBS-free McCoy's 5A medium containing L-glutamine at various Pc concentrations were then added (50 µL/well). Additionally, a solution of staurosporine (1 mM in DMSO) dispersed in FBS-free McCoy's 5A medium containing L-glutamine (50 µL; 20 µM) was used as a positive control for cytotoxicity. Control cells without any AuNPs loaded were treated with FBS-free McCoy's 5A medium containing L-glutamine. SK-BR-3 cells were incubated with the samples and controls for 3 h at 37 °C under a 5 % CO₂ atmosphere. MDA-MB-231 cells were incubated with the samples and controls for 24 h at 37 °C under a 5 % CO₂ atmosphere.

Following incubation with the AuNPs and controls, the subsequent steps in these MTT assays, including cell irradiation, post-PDT incubation and MTT addition and reading, were performed following the procedure described in **section 2.2.9**. Statistical significance between means was determined using a two-tailed Student's *t*-test and P values < 0.05 were considered significant.¹¹

2.3.8. CellTiter-Blue® cell viability assay for lactose targeting

SK-BR-3 human breast adenocarcinoma cells, MDA-MB-231 human breast adenocarcinoma cells and MCF-10A human mammary epithelial cells were dislodged from the flasks by trypsinization and counted as explained in **section 2.1.4.1**. The cells were then seeded following the procedure described in **section 2.2.9** and incubated for *ca.* 48 h at 37 °C under a 5 % CO₂ atmosphere.

The cells were treated with the lactose-C11Pc-AuNPs, lactose-C3Pc-AuNPs, C11Pc-sPEG-AuNPs and C3Pc-sPEG-AuNPs samples as well as the control samples as explained in **section 2.3.7**. SK-BR-3 and MDA-MB-231 cells were incubated with the samples and controls as described previously in **section 2.3.7**. MCF-10A cells were incubated with the samples and controls for either 3 h or 24 h at 37 °C under a 5 % CO₂ atmosphere.

Following incubation with the AuNPs and controls, the subsequent steps for these CellTiter-Blue® cell viability assays were performed following the procedures described in **section 2.2.9**, for cell irradiation and post-PDT incubation, and **section 2.2.10**, for CellTiter-Blue® addition and reading. Statistical significance between means was determined using a two-tailed Student's *t*-test and P values < 0.05 were considered significant.¹¹

2.3.9. Confocal microscopy – Internalisation and PDT of lactose-C3Pc-AuNPs

The internalisation of lactose-C3Pc-AuNPs by SK-BR-3 and MDA-MB-231 human breast adenocarcinoma cells was studied using confocal laser scanning microscopy. For the following imaging experiments, SK-BR-3 cells were cultured in phenol red-free McCoy's 5A medium containing L-glutamine and supplemented with FBS (10%). MDA-MB-231 cells were cultured in high glucose DMEM medium supplemented with L-glutamine (1%), FBS (10%) and sodium pyruvate (1 mM).

SK-BR-3 and MDA-MB-231 cells were dislodged from the flasks by trypsinisation and counted as explained in **section 2.1.4.1**. The cells were then seeded onto 18 mm diameter glass coverslips inside Nunc 6-well multidishes at a concentration of 2×10^4 cells/mL (3 mL/well). The cells were incubated for *ca.* 48 h at 37 °C under a 5 % CO₂ atmosphere. The culture medium was removed and the cells were washed with PBS-B (1 mL) once. Lactose-C3Pc-AuNPs (0.17 µM C3Pc) dissolved in FBS-free McCoy's 5A medium containing L-glutamine were added (1 mL/well). Control cells not loaded with AuNPs were treated with FBS-free McCoy's 5A medium containing L-glutamine (1 mL). SK-BR-3 cells were incubated with the lactose-C3Pc-AuNPs and the control for 3 h at 37 °C under a 5 % CO₂ atmosphere. MDA-MB-231 cells were incubated with the lactose-C3Pc-AuNPs and the control for either 3 h or 24 h at 37 °C under a 5 % CO₂ atmosphere. Following incubation with the samples, the subsequent steps in these confocal microscopy experiments follow the procedure already described in **section 2.2.11**, including irradiation, post-PDT incubation, imaging conditions and testing with propidium iodide.

2.3.10. InCell ELISA to quantify the levels of galectin-1 on the cell surface

An InCell ELISA was performed to study the difference in the levels of the galectin-1 receptor on the surface of MDA-MB-231 cells and SK-BR-3 cells. MDA-MB-231 and SK-BR-3 cells were dislodged from the flasks by trypsinization and counted as explained in **section 2.1.4.1**. The cells were seeded onto a clear-bottom Nunc Nunclon™ Δ Surface 96- well microplate at a concentration of 10×10^4 cells/mL (100 μ L/well). The cells were incubated overnight at 37 °C under a 5 % CO₂ atmosphere.

The culture medium was removed for both cell lines and the cells were washed with PBS-B (100 μ L) once. A solution of staurosporine (1 mM in DMSO) dispersed in FBS-free McCoy's 5A medium containing L-glutamine (50 μ L; 20 μ M) was used as a positive control for cytotoxicity. Control cells, to detect the levels of galectin-1, were treated with FBS-free McCoy's 5A medium containing L-glutamine (50 μ L). Both cell lines were incubated with the samples and controls for 3 h at 37 °C under a 5 % CO₂ atmosphere.

During the incubation period, the required buffers for the InCell ELISA were prepared, as described in **section 2.2.13**. Following incubation with the positive control, the samples were removed and the cells were washed with PBS-B (100 μ L) three times and resuspended in the appropriate complete cell culture media, McCoy's 5A for SK-BR-3 cells and DMEM for MDA-MB-231 cells. The cells were then fixed with formaldehyde and treated with blocking buffer as described in **section 2.2.13**. While the cells were incubated with blocking buffer, the primary antibody was appropriately diluted. In this experiment, the primary antibody used was anti-galectin-1 antibody. Anti-galectin-1 antibody (1 μ L; 1.604 mg/mL in a solution containing PBS (49 %), sodium azide (0.01 %), glycerol (50 %) and BSA (0.05 %)) was diluted in the blocking-washing solution (1.603 mL) previously prepared, to give a final concentration of 1 μ g/mL. Following incubation of the cells with blocking buffer, the blocking buffer was removed with a micropipette and anti-galectin-1 antibody (50 μ L; 1 μ g/mL) was added to each well. Non-specific signal control wells, *i.e.*, cells not incubated with primary antibody, were incubated with blocking-washing solution (50 μ L) not containing the antibody instead. The microplate was sealed with a plate sealer and the cells were incubated with the primary antibody overnight (*ca.* 17 h) at 4 °C. Following incubation with the primary antibody, the development of an absorbance signal for the levels of galectin-1 present

in each sample was obtained following the procedure outlined in **section 2.2.13**. Additionally, whole-cell staining to normalise the values of galectin-1 to cell number in each well was also performed in the same way as described in **section 2.2.13**.

2.3.11. InCell ELISA to detect lactose targeting

An InCell ELISA to study the targeting ability of lactose towards the galectin-1 receptor on the surface of MDA-MB-231 and SK-BR-3 cells was performed. MDA-MB-231 and SK-BR-3 cells were seeded onto a clear-bottom Nunc Nunclon™ Δ Surface 96-well microplate as described in **section 2.3.10**.

The culture medium was removed with a micropipette and the cells were washed with PBS-B (100 µL) once. The nanoparticle samples, lactose-C11Pc-AuNPs and C11Pc-sPEG-AuNPs together with lactose-C3Pc-AuNPs and C3Pc-sPEG-AuNPs (0.2 µM Pc), dissolved in FBS-free McCoy's 5A medium containing L-glutamine, were then added (50 µL/well). Additionally, a solution of staurosporine (1 mM in DMSO) dispersed in FBS-free McCoy's 5A medium containing L-glutamine (50 µL; 20 µM) was used as a positive control for cytotoxicity. Control cells not loaded with any AuNPs samples were treated with FBS-free McCoy's 5A medium containing L-glutamine (50 µL). The cells were incubated with the samples and controls for either 3 or 24 h at 37 °C under a 5 % CO₂ atmosphere. Following incubation with the AuNPs samples, the InCell ELISA was performed following the procedure described in **section 2.2.13**. The primary anti-galectin-1 antibody solution was prepared as explained previously in **section 2.3.10**.

2.3.12. ApoTox-Glo™ Triplex assay – Targeting with lactose-C3Pc-AuNPs

SK-BR-3 and MDA-MB-231 cells were dislodged from the flasks by trypsinisation and counted as explained in **section 2.1.4.1**. The cells were seeded onto two white-bottom Nunc Nunclon™ Δ Surface 96-well microplates at 18×10⁴ cells/mL (100 µL/well) and incubated for *ca.* 48 h at 37 °C under a 5 % CO₂ atmosphere.

The culture medium was removed using a micropipette and the cells were washed once with PBS-B (100 µL). The nanoparticle samples, lactose-C3Pc-AuNPs and C3Pc-sPEG-

AuNPs (0.2 μ M) in FBS-free McCoy's 5A medium containing L-glutamine, were then added (50 μ L/well). Additionally, a solution of staurosporine (1 mM in DMSO) dispersed in FBS-free McCoy's 5A medium containing L-glutamine (50 μ L; 20 μ M) was used as a positive control for cytotoxicity *via* apoptosis. Control cells without any AuNPs loaded were treated with FBS-free McCoy's 5A medium containing L-glutamine. SK-BR-3 cells were incubated with the samples and controls for 3 h at 37 $^{\circ}$ C under a 5 % CO₂ atmosphere. MDA-MB-231 cells were incubated with the samples and controls for 24 h at 37 $^{\circ}$ C under a 5 % CO₂ atmosphere. Following incubation with the AuNPs samples and the controls, the subsequent steps of the ApoTox-Glo™ triplex assay including irradiation, post-PDT incubation and addition of the assay components, were performed following the procedure described in **section 2.2.14**.

2.4. The potential use of upconverting nanoparticles as drug carriers for photodynamic therapy of cancer

2.4.1. Synthesis of upconverting nanoparticles

All the upconverting nanoparticles (UCNPs) used throughout this thesis were synthesised by Markus Buchner, PhD student in the group of Dr Thomas Hirsch (Institute for Analytical Chemistry, University of Regensburg, Regensburg, Germany).

The first type of UCNPs studied were dispersed in dimethyl sulfoxide (DMSO). UCNPs made of sodium yttrium fluoride (NaYF₄) doped with 20 % ytterbium (Yb³⁺), 2 % erbium (Er³⁺) and 20 % gadolinium (Gd³⁺) were synthesised. The UCNPs were further modified with a NaYF₄ shell, giving rise to 17.2 nm UCNPs. The core-shell UCNPs were then surface-modified to be functionalised with lysine and the photosensitiser Rose Bengal (NaYF₄-lysine-RB UCNPs).

The second type of UCNPs studied were dispersed in dH₂O. UCNPs made of NaYF₄ doped with 20 % Yb³⁺, 2 % Er³⁺ and 10 % Gd³⁺ were synthesised. The UCNPs were further modified with a NaYF₄ shell, giving rise to 28 nm UCNPs. The ligand polyacrylic acid (PAA) was used to modify the surface of the UCNPs in order to provide aqueous

solubility to the system. The resulting UCNPs (NaYF_4 -PAA UCNPs) were only functionalised with PAA and no Rose Bengal.

2.4.2. Characterisation of the UCNPs

The UCNPs were characterised using TEM and luminescence spectroscopy, all obtained by Markus Buchner at the University of Regensburg.

TEM images were obtained using a Philips CM12 Electron Microscope (MicroCal) operating at 120 kV and analysed using ImageJ and Origin 8 software. Luminescence spectra of the samples were recorded using an Amicon Bowman Series 2 spectrometer (Thermo Electron Corporation) coupled with a 200 mW continuous-wave laser ($\lambda_{\text{ex}} = 980$ nm) between 400-700 nm.

2.4.3. Measurement of singlet oxygen production by UCNPs

Production of singlet oxygen (${}^1\text{O}_2$) was measured using the singlet oxygen probe ABMA, as described in **section 2.2.7**. The 17.2 nm NaYF_4 -lysine-RB UCNPs in DMSO and the 28 nm NaYF_4 -PAA UCNPs in dH_2O were tested for ${}^1\text{O}_2$ production with ABMA at various concentrations. Each solution (511 μL) was placed in a 1.5 mL quartz cuvette together with ABMA (1 μL ; 0.512 mM in MeOH) and a magnetic stirrer bar. Oxygen was bubbled through the solutions and the stoppers were fitted on the quartz cuvettes. The fluorescence emission intensity of the initial solutions was recorded, between 390-600 nm, using an excitation wavelength of 380 nm. The samples were then irradiated at 980 nm using a 200 mW NIR laser for 40 min with continuous stirring. The laser was placed at *ca.* 5 cm from the samples. A NIR detector card was placed behind the cuvettes during irradiation to be able to place the laser light passing through the sample inside the cuvette. The fluorescence emission spectrum of the samples was recorded every 5 min.

2.4.4. Internalisation of NaYF₄-lysine-RB UCNPs by SK-BR-3 cells – Confocal microscopy and multi-photon microscopy

The internalisation of the 17.2 nm NaYF₄-lysine-RB UCNPs in DMSO by SK-BR-3 cells was studied using both confocal microscopy and multi-photon microscopy. SK-BR-3 cells were cultured in phenol red-free McCoy's 5A medium containing L-glutamine and supplemented with FBS (10 %) for these imaging experiments. The SK-BR-3 cells were seeded on 18 mm glass coverslips and incubated for *ca.* 48 h at 37 °C under a 5 % CO₂ atmosphere, as described in **section 2.2.11**.

The cells were then washed with PBS-B (1 mL) once. The cells were treated with a 25 µg/mL solution of the 17.2 nm NaYF₄-Lysine-RB UCNPs in DMSO dispersed in FBS-free McCoy's 5A medium (1 mL) containing L-glutamine. The control cells, not loaded with any UCNPs, were treated with FBS-free McCoy's 5A medium (1 mL) containing L-glutamine. The cells were incubated for 3 h at 37 °C under a 5 % CO₂ atmosphere. Following incubation, the cells were washed three times with PBS (1 mL) and kept in McCoy's 5A medium (2 mL) containing L-glutamine and supplemented with FBS (10 %). Subsequently, the cells were imaged. For imaging, the 18 mm coverslips were placed in a Ludin chamber, which was securely tightened. The coverslips were washed with imaging medium (*ca.* 1 mL) three times and finally resuspended in imaging medium (*ca.* 1 mL). The Ludin chamber was fitted on a heating stage at 37 °C in either the confocal microscope or the multi-photon microscope.

For imaging using the confocal microscope, a 543 nm HeNe laser was used to excite the Rose Bengal on the surface of the NaYF₄-lysine-RB UCNPs. The fluorescence emission was collected in the red channel with a band pass filter between 560-615 nm. DIC images were collected simultaneously using a 488 nm argon-ion laser.

For imaging using the multi-photon microscope, the 880 nm line from a Vision II Ti:Sapphire laser (Coherent Ltd., Ely, UK) was used to excite the Rose Bengal on the surface of the NaYF₄-lysine-RB UCNPs. The fluorescence emission was collected in the green channel at 550 ± 42.5 nm. DIC images were collected simultaneously with the same 880 nm laser. Additionally, the 980 nm line from the Vision II Ti:Sapphire laser was used to collect the luminescence of the UCNPs. The emission was collected with

two non-descanned GaAsP detectors in the green channel at 550 ± 42.5 nm and in the red channel at 655 ± 20 nm.

2.4.5. PDT effect of NaYF₄-lysine-RB UCNPs on SK-BR-3 cells – Confocal microscopy

The PDT effect of the 17.2 nm NaYF₄-lysine-RB UCNPs in DMSO on SK-BR-3 cells was studied using confocal microscopy. SK-BR-3 cells were cultured in phenol red-free McCoy's 5A medium containing L-glutamine and supplemented with FBS (10 %) for these imaging experiments. The SK-BR-3 cells were seeded on 18 mm glass coverslips, in two 6-well multidishes, and incubated for *ca.* 48 h at 37 °C under a 5 % CO₂ atmosphere, as described in **section 2.2.11**. The cells were then washed with PBS-B (1 mL) once. The cells were treated with a 15 µg/mL solution of the 17.2 nm NaYF₄-lysine-RB UCNPs in DMSO dispersed in FBS-free McCoy's 5A medium (1 mL) containing L-glutamine. The control cells, not loaded with any UCNPs, were treated with FBS-free McCoy's 5A medium (1 mL) containing L-glutamine. All solutions, control and UCNPs, contained a 0.25 % culture grade DMSO. The cells were incubated for 3 h at 37 °C under a 5 % CO₂ atmosphere.

Following incubation, the cells were washed three times with PBS (1 mL) and kept in McCoy's 5A medium (2 mL) containing L-glutamine and supplemented with FBS (10 %). At this point, one of the 6-well multidishes was irradiated at 980 nm using a 200 mW NIR laser for 6 min per coverslip. The laser was located 5 cm above the 6-well multidish. A NIR detector card was placed under the well containing the coverslip during the irradiation of the sample to be able to place the laser light at the centre of the treated coverslip. The other 6-well multidishes, which were not irradiated, were kept covered in aluminium foil in the dark during irradiation. Following irradiation, the cells were further incubated for *ca.* 24 h at 37 °C under a 5 % CO₂ atmosphere prior to imaging. For imaging, the cells were treated, placed on the confocal microscope and analysed using the same conditions as described in **section 2.4.4**. Propidium iodide, to test for dead cell staining, was also added and analysed under the same conditions as those described in **section 2.2.11**.

2.4.6. CellTiter-Blue® cell viability assay – NaYF₄-lysine-RB UCNPs

The 17.2 nm NaYF₄-lysine-RB UCNPs in DMSO were tested for PDT of SK-BR-3 human breast adenocarcinoma cells. SK-BR-3 cells were dislodged from the flasks by trypsinization and counted as described in section 2.1.4.1. The cells were then seeded following the procedure described in **section 2.2.9** and incubated for ca. 48 h at 37 °C under a 5 % CO₂ atmosphere.

The culture medium was removed using a micropipette and the cells were washed once with PBS-B (100 µL). The NaYF₄-lysine-RB UCNPs in DMSO were dispersed in FBS-free McCoy's 5A medium containing L-glutamine at concentrations ranging from 5-25 µg/mL (50 µL/well). All samples with varying concentrations of UCNPs contained a constant amount of 0.25 % DMSO, to account for possible solvent effects on the cells. Two solvent control consisting of culture grade DMSO (0.25 %) or culture grade DMSO (100 %) dispersed in FBS-free McCoy's 5A medium containing L-glutamine (50 µL) were also used to test the effect of DMSO alone on the cells. Control cells, not loaded with any UCNPs, were treated with FBS-free McCoy's 5A medium containing L-glutamine. Additionally, a solution of staurosporine (1 mM in DMSO) dispersed in FBS-free McCoy's 5A medium containing L-glutamine (50 µL; 20 µM) was used as a positive control for cytotoxicity. The samples and controls were incubated with the SK-BR-3 cells for 3 h at 37 °C under a 5 % CO₂ atmosphere.

Following incubation with the UCNPs and controls, the samples were removed and the cells were washed with PBS-B (100 µL) three times. The cells were then resuspended in complete McCoy's 5A medium (100 µL) containing L-glutamine and supplemented with FBS (100 %). At this point, one of the plates was irradiated at 980 nm using a 200 mW NIR laser for 6 min per well. The laser was located 5 cm above the 96-well plate. The plate not being irradiated was kept covered in aluminium foil in the dark. Following irradiation, the cells were further incubated for ca. 48 h at 37 °C under a 5 % CO₂ atmosphere. Addition of the CellTiter-Blue® reagent, incubation and fluorescence measurements were performed following the procedure explained in **section 2.2.10**.

2.4.7. Determination of the extinction coefficient of Rose Bengal

Rose Bengal (2 mg) was dissolved in dH₂O (5 mL) giving an initial concentration of 393 µM. This initial RB solution was then further diluted with dH₂O to obtain concentrations ranging from 0-3 µM. These dilutions were prepared in volumetric flasks (1 mL). The dilutions were analysed by UV-vis spectroscopy between 300-800 nm starting with the lowest concentration. A calibration curve at 549 nm was created and a value for the extinction coefficient was obtained.

2.4.8. ApoTox-Glo™ Triplex assay – NaYF₄-lysine-RB UCNPs

SK-BR-3 cells were dislodged from the flasks by trypsination and counted as explained in **section 2.1.4.1**. The cells were seeded onto two white-bottom Nunc Nunclon™ Δ Surface 96-well microplates at a concentration of 18×10^4 cells/mL (100 µL/well). The cells were incubated for *ca.* 48 h at 37 °C under a 5 % CO₂ atmosphere. The culture medium was removed using a micropipette and the cells were washed once with PBS-B (100 µL). The cells were treated with a 15 µg/mL solution of the 17.2 nm NaYF₄-lysine-RB UCNPs in DMSO dispersed in FBS-free McCoy's 5A medium containing L-glutamine (50 µL). The control cells not loaded with any UCNPs were treated with FBS-free McCoy's 5A medium containing L-glutamine (50 µL). Additionally, a solution of staurosporine (1 mM in DMSO) dispersed in FBS-free McCoy's 5A medium containing L-glutamine (50 µL; 20 µM) was used as a positive control for cytotoxicity *via* apoptosis. All solutions, control and UCNPs, contained a 0.25 % culture grade DMSO. The cells were incubated with the samples and controls for 3 h at 37 °C under a 5 % CO₂ atmosphere.

Following incubation with the UCNPs samples and the controls, the samples were removed and the cells were washed with PBS-B (100 µL) three times. The cells were then resuspended in complete McCoy's 5A medium (100 µL) containing L-glutamine and supplemented with FBS (10 %). At this point, one of the plates was irradiated at 980 nm using a 200 mW NIR laser for 6 min per well. The laser was located 5 cm above the 96-well plate. The plate not being irradiated was kept covered in aluminium foil in the dark. Prior to measuring cell viability, cytotoxicity and apoptosis, the cells were

further incubated for 4 h at 37 °C under a 5 % CO₂ atmosphere. The subsequent steps of the ApoTox-Glo™ triplex assay including reagent preparation and addition of the assay components, were performed following the procedure described in **section 2.2.14.**

2.4.9. CellTiter-Blue® cell viability assay – UCNPs in dH₂O without Rose Bengal

The 28 nm NaYF₄-PAA UCNPs in dH₂O were tested *in vitro* using SK-BR-3 cells to determine their cytotoxicity before and after irradiation at 980 nm. SK-BR-3 cells were seeded in white-bottom 96-well plates following the procedure described in **section 2.2.9.** Following the seeding of the cells, the NaYF₄-PAA UCNPs samples in dH₂O were dispersed in FBS-free McCoy's 5A medium containing L-glutamine at concentrations ranging from 10-25 µg/mL. All samples with varying concentrations of UCNPs contained a constant amount of 0.63 % dH₂O. Additionally, a solvent control consisting of dH₂O (0.63 %) dispersed in FBS-free McCoy's 5A medium containing L-glutamine (50 µL) was used to test the effect of dH₂O alone on the cells. A positive control, consisting of a solution of staurosporine (1 mM in DMSO) dispersed in FBS-free McCoy's 5A medium containing L-glutamine (50 µL; 20 µM) was used as a positive control for cytotoxicity. Negative control cells, not loaded with any UCNPs samples, were treated with FBS-free McCoy's 5A medium containing L-glutamine (50 µL). The samples and controls were incubated with the SK-BR-3 cells for 3 h at 37 °C under a 5 % CO₂ atmosphere. Following incubation with the UCNPs and the controls, the samples were treated and irradiated following the procedure described in **section 2.4.6.** Addition of the CellTiter-Blue® reagent, incubation time and measurement of the fluorescence emission intensity were performed following the procedure explained in **section 2.2.10.**

2.4.10. Confocal microscopy – UCNPs in dH₂O without Rose Bengal

The toxicity of the 28 nm NaYF₄-PAA UCNPs in dH₂O was further studied using confocal microscopy, to confirm the visual appearance of the cells following incubation with the UCNPs samples. SK-BR-3 cells were cultured in phenol red-free McCoy's 5A medium containing L-glutamine and supplemented with FBS (10 %) for these imaging

experiments. The SK-BR-3 cells were seeded on 18 mm glass coverslips in two 6-well multidishes and incubated for *ca.* 48 h at 37 °C under a 5 % CO₂ atmosphere, as described in **section 2.2.11**.

The cells were then washed with PBS-B (1 mL) once. The cells were treated with a 25 µg/mL solution of the 28 nm NaYF₄-PAA UCNPs in dH₂O dispersed in FBS-free McCoy's 5A medium containing L-glutamine (1 mL). The control cells not loaded with any UCNPs were treated with FBS-free McCoy's 5A medium containing L-glutamine (1 mL). The cells were incubated for 3 h at 37 °C under a 5 % CO₂ atmosphere.

Following incubation with the UCNPs and the control, the cells were irradiated, placed on the confocal microscope and analysed using the same conditions as described in **section 2.4.5**. Propidium iodide, to test for dead cell staining, was also added and analysed under the same conditions as those described in **section 2.2.11**.

2.5. References

- (1) Chambrier, I.; Cook, M. J.; Russell, D. A. *Synthesis* **1995**, 10, 1283.
- (2) Revell, D. J.; Chambrier, I.; Cook, M. J.; Russell, D. A. *J. Mater. Chem.* **2000**, 10, 31.
- (3) Stuchinskaya, T.; Moreno, M.; Cook, M. J.; Edwards, D. R.; Russell, D. A. *Photochem. Photobiol. Sci.* **2011**, 10, 822.
- (4) Obaid, G.; Chambrier, I.; Cook, M. J.; Russell, D. A. *Photochem. Photobiol. Sci.* **2015**, 14, 737.
- (5) Grabarek, Z.; Gergely, J. *Anal. Biochem.* **1990**, 185, 131.
- (6) Staniford, M. C.; Lezhnina, M. M.; Gruener, M.; Stegemann, L.; Kuczus, R.; Bleicher, V.; Strassert, C. A.; Kynast, U. H. *Chem. Comm.* **2015**, 51, 13534.
- (7) Hone, D. C.; Walker, P. I.; Evans-Gowing, R.; FitzGerald, S.; Beeby, A.; Chambrier, I.; Cook, M. J.; Russell, D. A. *Langmuir* **2002**, 18, 2985.
- (8) Bertrand, R.; Solary, E.; O'Connor, P.; Kohn, K. W.; Pommier, Y. *Exp. Cell Res.* **1994**, 211, 314.
- (9) Mosmann, T. *J. Immunol. Methods* **1983**, 65, 55.
- (10) Roy, I.; Ohulchanskyy, T. Y.; Pudavar, H. E.; Bergey, E. J.; Oseroff, A. R.; Morgan, J.; Dougherty, T. J.; Prasad, P. N. *J. Am. Chem. Soc.* **2003**, 125, 7860.
- (11) Rodriguez, L.; Vallercosa, P.; Battah, S.; Di Venosa, G.; Calvo, G.; Mamone, L.; Sáenz, D.; Gonzalez, M. C.; Batlle, A.; MacRobert, A. J.; Casas, A. *Photochem. Photobiol. Sci.* **2015**, 14, 1617.
- (12) O'Brien, J.; Wilson, I.; Orton, T.; Pognan, F. *Eur. J. Biochem.* **2000**, 267, 5421.
- (13) Obaid, G.; Chambrier, I.; Cook, M. J.; Russell, D. A. *Angew. Chem., Int. Ed.* **2012**, 51, 6158.
- (14) Marín, M. J.; Galindo, F.; Thomas, P.; Russell, D. A. *Angew. Chem., Int. Ed.* **2012**, 124, 9795.
- (15) Sasaki, D. T.; Dumas, S. R.; Engleman, E. G. *Cytometry* **1987**, 8, 413.
- (16) Thermo Fisher Scientific. InCell ELISA Colorimetric Detection Kit – Catalog number 62200 <https://www.thermofisher.com/order/catalog/product/62200> [Accessed Jan 13th, 2017].
- (17) Promega. ApoTox-Glo™ Triplex Assay – Catalog number G6320 https://www.promega.co.uk/products/cell-health-and-metabolism/apoptosis-assays/apotox_glo_triplex_assay/ [Accessed Jan 13th, 2017].
- (18) Niles, A. L.; Moravec, R. A.; Hesselberth, P. E.; Scurria, M. A.; Daily, W. J.; Riss, T. L. *Anal. Biochem.* **2007**, 366, 197.

Chapter 3

Gold nanoparticle enhanced and selective antibody targeting photodynamic therapy of breast cancer cells

This chapter describes the use of gold nanoparticles functionalised with a zinc phthalocyanine photosensitiser for photodynamic therapy (PDT) of breast adenocarcinoma cells. Two zinc phthalocyanines differing in the length of the carbon chain that connects the macrocycle to the surface of the gold nanoparticles were compared in terms of singlet oxygen production and PDT efficacy. Additionally, the selectivity towards breast cancer cells was increased by addition of a targeting agent, anti-HER2 antibody.

3.1. Introduction

3.1.1. Interactions between metal nanoparticles and fluorophores

The synthesis and applications of metal nanoparticles have become the subject of numerous studies over the years.¹ The optical, electronic and chemical properties of metal nanoparticles change dramatically from those properties encountered in the bulk metal and are dependent on both the size and shape of the synthesised nanoparticles.^{1,2} A particularly interesting property in metal nanoparticles is their ability to interact with fluorophores anchored to their surface. Consequently, the study of the metal nanoparticle-fluorophore interactions is of particular interest amongst the scientific community. Several studies confirm the quenching ability of metal nanoparticles on the surrounding fluorophores, while other studies show the opposite behaviour, an enhancement in the fluorescence of the fluorophore.³

One of the most important characteristics of metal nanoparticles, that is significant in the study of metal nanoparticles-fluorophore interactions, is surface plasmon resonance (SPR).⁴ The SPR refers to the collective oscillation of the electrons in the conduction band of the metal upon interaction with electromagnetic (EM) energy.^{2,4-6}

The oscillating electrons, referred to as plasmons, oscillate at the same frequency as the electromagnetic wave.⁴ These oscillations are dependent on the size and shape of the nanoparticles, but also on the dielectric constants of both the metal and the surrounding material.¹ The SPR is responsible for the strong ultraviolet-visible (UV-vis) absorption bands, the intense colours seen in solutions of metal nanoparticles as well as the ability of metal nanoparticles to both absorb and scatter light.^{2,4,5} Two types of SPR are seen, localised SPR (LSPR) and propagating surface plasmon polaritons (SPPs).⁷ LSPR are the confined, non-propagating oscillations while the SPPs are the propagating charge oscillations of the electrons on the surface of the metals.^{7,8}

The SPR and plasmon field created by metal nanoparticles, dependent on the field strength upon exposure to incident light, are responsible for the effects observed in the fluorescence of fluorophores placed near-by.⁹ Metal nanoparticles have a reputation for being strong fluorescence quenchers, which has been shown experimentally in a variety of studies.^{5,10-16} However, the potential use of metal nanoparticles as fluorescence enhancers has also been studied.^{7,8,17-20} The concept of fluorescence enhancement by metallic surfaces was introduced in the 1960s by Drexhage and co-workers when they discovered that the decay times of a fluorophore could be altered in the presence of a metallic film in a distance-dependent manner.^{19,21,22} Research has continued^{18,23-29} but it was not until 2002 that the term metal-enhanced fluorescence (MEF) was coined by Geddes and Lakowicz.¹⁸ Since then, the interest in the theory and applications of MEF has gained more attention and other researchers have referred to MEF as surface-enhanced fluorescence, plasmon-enhanced fluorescence and metal-induced fluorescence enhancement.^{19,30} MEF refers to the phenomenon by which metal surfaces and metal nanoparticles increase the fluorescence intensity of the fluorophores in the near-field (*i.e.*, near the metal surface, usually found within 10 nm), due to an enhanced excitation of the fluorophores.^{8,18} This fluorescence intensity is accompanied by an increase in the fluorescence quantum yield (ϕ_F), a decrease in the fluorescence lifetime and a higher photostability for the fluorophore.^{18,30} Applications in which MEF could be useful include biological sensors, activatable probes, fluorescence microscopy and also PDT.^{5,7,8,19,31} For PDT, several studies have been performed to understand whether this metal-enhanced fluorescence could lead to an enhancement in the formation of singlet oxygen, which

would thus lead to a higher cell kill.³²⁻³⁵ Indeed, these studies have found a correlation between MEF and a higher production of ${}^1\text{O}_2$. In 2006, Geddes and co-workers experimentally showed metal-enhanced phosphorescence at low temperature for the photosensitiser Rose Bengal in the presence of silver island films.³⁴ Following this, in 2007 the Geddes' group published the first report of metal-enhanced ${}^1\text{O}_2$ production ($\text{ME}{}^1\text{O}_2$) by Rose Bengal in close proximity to such silver island films.³³ Furthermore, $\text{ME}{}^1\text{O}_2$ was further highlighted in photosensitisers other than Rose Bengal and it was shown that certain properties, such as the size and shape of the nanoparticles, the distance of the fluorophore and the excitation wavelength of the photosensitiser could be modified in order to optimise the extent of $\text{ME}{}^1\text{O}_2$.³⁵ Huang *et al.* additionally showed the application of $\text{ME}{}^1\text{O}_2$ *in vitro* for PDT by using gold nanorods functionalised with the photosensitiser chlorin e6.³¹ MEF and $\text{ME}{}^1\text{O}_2$ in this system contributed to a higher internalisation by HeLa cells and a higher phototoxicity and cell death. Therefore, the use of nanotechnology in PDT could lead to increased productions of ${}^1\text{O}_2$, which in turn could potentially produce an increased photodynamic efficiency.³¹

The mechanism by which MEF occurs is still a subject of discussion.³⁰ The groups of Geddes and Lakowicz have both proposed mechanisms, with slight differences, by which MEF can take place.^{18,30,36,37} Geddes and Lakowicz proposed the existence of three known pathways of interaction between fluorophores and metals.^{18,19,37} The first is non-radiative energy transfer from the fluorophore to the metal, which leads to fluorescence quenching. Non-radiative energy transfer is a dipole-dipole dominated transfer and is inversely proportional to the distance between the metal and the fluorophore (d^{-3}) and thus it primarily occurs at small distances.^{18,19,37,38} The second pathway is the “antenna effect” by which metallic nanoparticles concentrate the incident electromagnetic field near the fluorophore, *i.e.*, an increase in the rate of excitation, leading to an increase in emission intensity.^{18,19,37} In the third pathway, the metal increases the radiative decay rate of the fluorophore, leading to enhanced fluorescence quantum yields and thus fluorescence enhancement.^{18,19,37} **Figure 3.1** shows a schematic representation of the Jablonski diagram of the fluorophore with and without the presence of a metal, which is useful to understand the second and third pathways of interaction between metals and fluorophores.

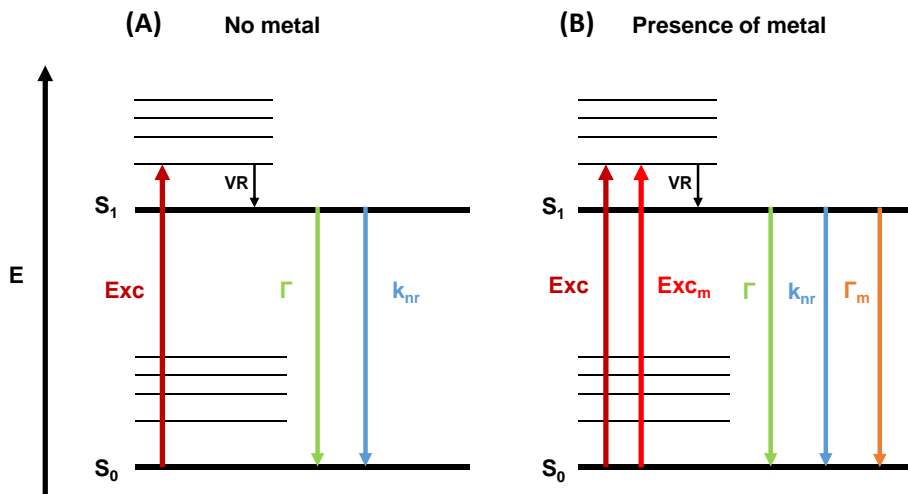


Figure 3.1. Jablonski diagram for (A) a free fluorophore and (B) a fluorophore in the presence of a conducting metal. **Exc** represents the excitation rate, **Exc_m** the metal-enhanced excitation rate and **VR** the non-radiative vibrational relaxation. Additionally, the decay rates of the fluorophore are given by the radiative decay rate Γ , the metal-enhanced radiative decay rate Γ_m , and the non-radiative decay rate k_{nr} . The diagram was adapted from Ref. 18.

Considering the three mechanisms of interaction between fluorophores and metals, it was initially proposed that the mechanism of MEF was mainly related to the modification of the radiative decay rate of the fluorophore by the close proximity to the metal.^{18,30} Therefore, MEF was thought to be dependent on the fluorescence quantum yield of the free fluorophore in solution, *i.e.*, weakly fluorescence molecules lead to higher MEF efficiencies while the fluorescence of fluorophores with high quantum yields cannot be further enhanced.^{37,39} However, more recently, Geddes and co-workers have proposed a different mechanism underlying the complex interactions between fluorophores and metallic surfaces.^{30,36,40,41} The authors reported that MEF results from a combination of electric field effects and induced plasmon effects.³⁶ The fluorophore and metal are coupled in the ground and excited states. Therefore, the energy of the excited state of the distal fluorophore is partially transferred to the surface plasmon of the metal, *i.e.*, the fluorophore radiates through the scattering mode of the metal nanoparticle. The surface plasmon then radiates the coupled emission, known as quanta.^{30,42} The electric field and plasmon effects thus result in an increased absorption and emission of the fluorophores, an increase in the fluorescence emission by the coupled fluorophore-metal system and a decrease in the fluorescence

lifetime.³⁶ In this new model, MEF is no longer dependent on the fluorescence quantum yield of the free fluorophore; instead there is a wavelength-dependence factor.^{40,41}

There are different variables that can determine the way in which a fluorophore and a metal can interact, thus leading to either fluorescence quenching or enhancement, including the choice of metal, the nanoparticle size and shape, the distance between the fluorophore and the metal nanoparticle, the nature of the anchor chain that connects the fluorophore to the metal core, the geometry adopted by the fluorophore relative to the metal nanoparticle, the orientation of the fluorophore's molecular dipole relative to the nanoparticle surface and the spectral overlap between the metal nanoparticle and the fluorophore.^{5,7,8,10,13,22,37} The choice of the metal nanoparticle, either silver or gold, can affect the efficiency of MEF. The majority of the published reports describing MEF have chosen silver nanoparticles, which have been shown to produce high MEF efficiency.⁴³ The use of gold nanoparticles for MEF has been overlooked due to gold being a strong fluorescence quencher, even at long distances.⁴⁴ However, recently the use of gold nanoparticles for MEF is becoming increasingly popular since it has several advantages over silver, including the high chemical stability, ease of synthesis and ease to modify the gold surface with biomolecules.⁴⁴ The first report of the use of gold nanoparticles for MEF was performed by Geddes and co-workers.⁴³ By controlling the size of the nanoparticles and the position of the fluorophore relative to the gold nanoparticles, MEF was successfully obtained.⁴³

The radiating plasmon (RP) model developed by Lakowicz discussed the effect of nanoparticle size.²⁰ As it was previously mentioned, metal nanoparticles have the ability to both absorb and scatter light. The size of the nanoparticle is the most important parameter that influences the efficiency of the absorption and scattering of the light. In small spherical nanoparticles (< 40 nm for gold nanoparticles; < 20 nm for silver nanoparticles), the light is mainly absorbed, while in larger nanoparticles (> 40 nm and especially > 80 nm for gold nanoparticles; > 30 nm for silver nanoparticles) the scattering component becomes more relevant.^{4,5,20,45,46} The RP model states that the absorption of light will lead to fluorescence quenching and the scattering will lead to fluorescence enhancement.²⁰ As a result, small nanoparticles will induce the quenching of the fluorescence, whereas larger nanoparticles will be more

likely to induce MEF. The RP model suggested the ideal nanoparticle size for maximum fluorescence enhancement, for both silver and gold nanoparticles, to be *ca.* 40 nm.^{5,20} However, other authors have reported the ideal size to be larger than 15 nm for MEF.⁷ Recently, Xie and co-workers have challenged the assumption of nanoparticle size being relevant for MEF.⁸ These authors speculated that the extinction properties of metallic nanoparticles refer to isolated nanoparticles and not in the presence of a coupled system with a fluorophore.⁸ The shape of the nanoparticles can also influence the MEF efficiency to a given fluorophore.³⁷ Lakowicz reported that the largest fluorescence enhancement is observed for spheroids.³⁷ Spherical nanoparticles are not as efficient fluorescence enhancers and the fluorescence enhancement abilities of elongated spheroids are even lower.³⁷ In accordance with Lakowicz, the group of Halas experimentally showed that the fluorescence quantum yield of a near-infrared fluorophore (IR800; $\phi_F = 7\%$) was enhanced in the presence of gold nanoshells ($\phi_F = 86\%$) with greater efficiency as compared to gold nanorods ($\phi_F = 74\%$).⁴⁵ Additionally, Swierczewska *et al.* have reported that, in the case of gold nanoparticles, the spherical shape induces the highest fluorescence quenching efficiency.⁵

Another important consideration for the quenching or enhancement of the fluorescence is the distance between the fluorophore and the metal core of the nanoparticles, as shown in **Figure 3.2**.² If the fluorophore is placed too close to the metal (≤ 5 nm), all the fluorescence will be quenched due to the reduction in the oscillating dipole of the fluorophore, electron transfer and non-radiative energy transfer from the fluorophore to the metal. The mechanisms of energy transfer that best explain this phenomenon are nanometal surface energy transfer (NSET) and Förster resonance energy transfer (FRET).⁵ Quenching by electron usually occurs in small nanoparticles (< 5 nm) since these particles present a weak SPR absorption band and thus spectral overlap with the fluorophore is poor, which limits the energy transfer between the fluorophore and the metal.⁴⁷ On the other hand, if the fluorophore is placed too far from the metal there will be no real change in the fluorescence as the distance is too large for any effect to occur. The key for fluorescence enhancement is to find an intermediate optimum distance (*ca.* 5-20 nm; usually ≥ 10 nm) in which there

is an effective transfer of the free electrons of the fluorophore to the SPP in the metal due to the strong Purcell effect, and thus the fluorescence is enhanced.^{1-3,9,10,25,37,40,41,47}

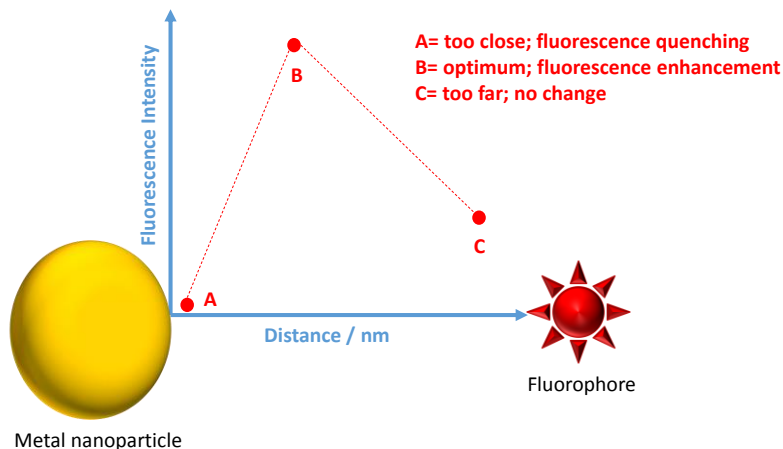


Figure 3.2. Schematic representation showing the distance dependence between a metal nanoparticle and a fluorophore, leading to either fluorescence quenching or enhancement.

The distance dependence between the metal and the fluorophore has not only been proven theoretically, but it has also been shown experimentally in several studies.^{3,6,9,48-50} Anger *et al.* showed the first report of the variable fluorescence behaviour depending on the distance between the nanoparticle and the fluorophore.³ These authors found an optimal distance of 5 nm between 80 nm gold nanoparticles and a fluorescent molecule, which led to the maximum rate of fluorescence enhancement. Additionally Kang *et al.* studied the distance-dependence between the fluorescent dye cypate and 10 nm gold nanoparticles and they revealed similar results.⁹ The fluorescence of cypate was completely quenched when it was placed directly on the surface of the gold, the fluorescence was significantly increased when it was located approximately 5 nm away but started to decrease again when the distance increased further. The effect of distance dependence for fluorescence quenching or enhancement has also been studied with other metals, especially silver. Cheng and Xu showed results for silver nanoparticles to be comparable to those reported for gold nanoparticles.⁵⁰ The fluorescence of fluorescein isothiocyanate was studied as a function of its distance from 75 nm silver nanoparticles. The distance was modified using a silica (SiO_2) spacer. When no spacer was used, the fluorescence was effectively quenched. However, when the SiO_2 spacer was added, a maximum fluorescence

enhancement was found at a distance of 21 nm. This fluorescence enhancement decreased after reaching this optimal value upon further increasing the distance between the metal and the fluorophore.⁵⁰ Also using silver as the metal, the Geddes group studied the distance dependence of MEF and found a similar trend of quenching and enhancement to that which had previously been reported.⁴⁹ Of particular importance to the work reported in this thesis, a recent study by Planas *et al.* has shown that this distance-dependence not only influences MEF but also ME¹O₂.⁶ The authors synthesised 67 nm silver nanoparticles coated with a silica layer, which was modified with (3-aminopropyl)triethoxysilane (APTES). The photosensitiser Rose Bengal was then attached to the primary amines of APTES *via* carbodiimide coupling. The production of ¹O₂ by the Rose Bengal functionalised core-shell silver nanoparticles was studied. The thickness of the silica layer was modified from 5-100 nm to change the distance between the metal and the Rose Bengal. As previously stated, at short distances, there was complete quenching of the production of ¹O₂. However, as the distance was increased, the production of ¹O₂ reappeared, reaching a maximum value when the Rose Bengal was placed 11 nm away from the silver core. After this optimum distance of 11 nm was further increased, the production of ¹O₂ started to decrease.⁶

The orientation adopted by the fluorophore and its molecular dipole relative to the metallic nanoparticle plays an important role in distance-dependent MEF. A perpendicular orientation relative to the surface of the nanoparticles can induce the maximum fluorescence-enhancement, due to the minimised possibility of non-radiative energy transfer from the fluorophore to the metal nanoparticle.³⁷ In a parallel orientation, quenching is allowed not only because of the possibility of energy transfer being enhanced but also due to the dipole in the metal cancelling the dipole in the fluorophore. The cancellation of the dipole further slows the radiative decay and favours the quenching of the fluorescence.³⁷ The orientation of the fluorophore depends on the angle at which the chain connecting the fluorophore to the metal is positioned with respect to the metal core. Even though the angle between fluorophores and metal nanoparticles has not been widely studied, numerous researchers have reported investigations on the possible orientation of alkanethiol monolayers on gold surfaces.⁵¹⁻⁵⁵ Russell and co-workers have studied the relative orientation of a zinc phthalocyanine self-assembled monolayer (SAM) on gold

surfaces.^{51,52} The phthalocyanines were connected to the gold surface *via* an alkyl chain containing 3, 8 or 11 carbon atoms. The authors reported that the chains in all three phthalocyanines were *ca.* 20-30 ° tilted from the gold surface. However, the orientation of the macrocycles adopted a parallel configuration relative to the gold surface for the C3 chain, in contrast to the longer chains, which adopted a more perpendicular orientation. As a result, the distance for the C3, C8 and C11 phthalocyanines from the surface was 4 Å, 10 Å and 13 Å, respectively. The authors found that the fluorescence was quenched for the C3 chain significantly, due to the closeness to the gold surface (4 Å), followed by the C8 (10 Å) and C11 (13 Å) chains, respectively. Additionally, the odd-even effect, *i.e.*, whether the chain is composed of an odd or even number of carbon atoms, was found to be an important parameter that would determine the final position of each chain. If it is assumed that the chains are in an all-*trans* extended configuration, then the position of the phthalocyanine macrocycle will be different depending on the odd or even nature of the carbon chain. In fact, the C8 macrocycle was found to adopt a configuration that was not as perpendicular as the C11 nor as parallel as the C3.⁵¹ The odd-even effect has not only been reported in this study, it is a well-known phenomenon for SAMs on gold and silver surfaces.⁵⁶ A more recent study by Battistini *et al.* was similar in that it compared the same molecule, a pyrene, linked to gold nanoparticles by a carbon chain that differed in length, either 4 carbon atoms (C4) or 11 carbon atoms (C11).⁴⁸ In contrast to the study by Russell and co-workers, these authors found a decreased quenching effect for the molecule closer to the gold core (C4) as compared to the molecule that was placed further away (C11). This behaviour was also attributed to the angle between the gold surface and the fluorescent molecules, which was governed by the intra- and inter-molecular interactions, but was found to be unrelated to the odd-even effect. The nature of the chain that connects the fluorophore to the nanoparticle core was found to be the main parameter to determine the relative position of the pyrene with respect to the nanoparticle surface. The nature of the chain influences the stronger or weaker interactions between chains, such as van der Waals forces, which will induce the chains to be closer or further away from one another.⁴⁸ In this study, it was reported that when the chain was shorter the chain-chain interaction was minimal, but this interaction became more important as the chain length increased. As a result, the C4

chain was tilted *ca.* 20 ° from the nanoparticle surface, leading to the pyrene molecule adopting a more perpendicular position relative to the gold core in order to maximise fluorophore-fluorophore interactions. On the other hand, the C11 chain was tilted *ca.* 45-48 ° from the nanoparticle surface in order to maximise chain-chain interactions, leading the pyrene molecules to lie closer to the gold core, which effectively increases the quenching of the fluorescence due to non-radiative energy transfer as previously described.⁴⁸ Even though the authors reported that the odd-even effect was not an important parameter, the study of a pyrene connected to a short odd carbon chain, *i.e.*, C3 or C5, should be performed for confirmation. These two studies by Russell and co-workers and Battistini *et al.* produced conflicting results. However, it is important to consider that one study used SAMs on a planar gold surface, whereas the other focused on the use of gold nanoparticles. The difference between the planar surface *versus* the nanoparticle can have an effect in the fluorescence behaviour of the fluorophores. In fact, Lakowicz already observed that fluorophores are quenched at short distances from a planar metal surface but not quenched at short distances from metal nanoparticles.²⁰ Lakowicz suggested that the fluorescence quenching was originated from the oscillations created in metals being unable to radiate due to the presence of optical restrictions at the metal-fluorophore interface.²⁰

The nature of the anchor group, such as a thiol, connecting the chain to the metal surface has also been reported to influence the higher or lower MEF efficiency.^{16,57} Additionally, another factor that should be considered is how closely the fluorophores are packed on the surface of the metal nanoparticles, which could lead to dimerisation and aggregation and thus induce self-quenching of the fluorescence.^{10,51}

To summarise, metal nanoparticles can produce different effects on the fluorescence of fluorophores anchored onto their surface. The size of the nanoparticles is an important consideration, where small particles will lead to fluorescence quenching whereas larger particles will have a role in fluorescence enhancement. However, the size is not a sole definite measure of how the fluorescence will behave. The distance between the fluorophore and the metal nanoparticle is also important to consider. As discussed, short distances lead to fluorescence quenching and fluorescence enhancement will only be achieved at intermediate optimum distances between the

two. Another important parameter to be considered is the orientation at which the fluorophore and its molecular dipole are located relative to the metal surface, which will determine how close the fluorophore lies towards the metal core. As discussed, the orientation is influenced by the nature of the chain connecting the fluorophore to the metal core, the nature of the anchor group and whether it has an odd or even number of carbon atoms. Additionally, the choice of the metal for the nanoparticles as well as the choice of the fluorophore can have a profound effect on the efficiency of MEF.

3.1.2. Human epidermal growth factor receptor 2

The human epidermal growth factor receptor 2 (HER2) is a 1,255 amino acid transmembrane glycoprotein (185 KDa) encoded by the proto-oncogene HER2 located on chromosome 17q12.⁵⁸⁻⁶² The HER2 receptor belongs to the family of receptor tyrosine kinases (RTKs), known as erythoblastoma gene B (ErbB) receptors.^{58,59,63} The term ErbB was coined when the first growth factor receptor was discovered in 1978 due to its origin in the ErbB gene, responsible for avian erythroblastosis virus.⁵⁹ The ErbB family is composed of four members; the epidermal growth factor receptor (EGFR/HER1/ErbB1), HER2/ErbB2/*neu*, HER3/ErbB3 and HER4/ErbB4.^{58,59,63}

The four members of the ErbB family are homologous, which means their basic structure is the same, as shown in **Figure 3.3**. The receptors are made up of three parts, the extracellular domain, the transmembrane domain and the intracellular domain.⁵⁸ The extracellular domain is divided into four subdomains (I, II, III and IV also known as L1, S1, L2 and S2). Two of these subdomains (L1 and L2) constitute the ligand-binding sites, while the other two (S1 and S2) are the homologous cysteine-rich domains. The transmembrane lipophilic domain enters the cell membrane connecting the extracellular and intracellular domains. The intracellular domain is located in the cytoplasm and it contains a juxtamembrane domain (JM), a protein kinase domain, with tyrosine kinase catalytic activity, and the carboxyl end containing the phosphorylation sites.^{58,59,63,64}

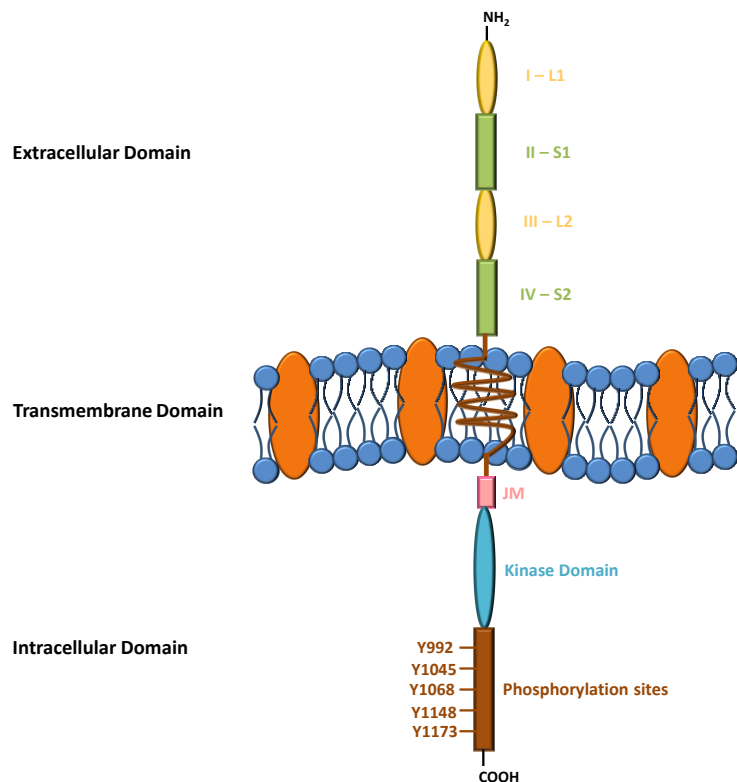


Figure 3.3. Basic structure of the ErbB receptors. The extracellular domain is composed of two cysteine-rich domains (S1, S2) and two ligand-binding sites (L1, L2). The intracellular domain is composed of the juxtamembrane domain (JM), the protein kinase domain and the autophosphorylation sites located within the carboxyl end. The diagram was adapted from Refs. 58 and 64.

The role of the ErbB receptors is essential for human life, including normal cell growth, proliferation and differentiation, wound healing and apoptosis.^{58,59,63} These processes are regulated through the activation of RTKs, which initiates several signal transduction pathways.^{59,63} Activation of the RTKs occurs upon binding of a specific ligand to the extracellular domain of the ErbB receptors. When there is no ligand in the environment, the receptors stay inactive and in a monomeric form. However, when the ligand becomes available and it binds the receptor, dimerisation and oligomerisation start to occur. Dimerisation leads to an increase in the kinase catalytic activity and initiates phosphorylation, thus inducing the activation of the intracellular signalling.^{58,59,65,66} Dimerisation, which is favoured by the higher stability of the dimer complexes as compared to the monomers, can be of two types, either homodimerisation, *i.e.*, the same two receptors are bound, or heterodimerisation, *i.e.*, two different receptors are

bound. The resulting activation signal is much stronger for heterodimers, especially when HER2 is involved, as compared to homodimers, which produce weaker signals.⁶⁵ Activation of each receptor is triggered by specific ligands. HER1 is activated by epidermal growth factor (EGF), transforming growth factor α (TGF α), amphiregulin, heparin-binding EGF-like growth factor, betacellulin and epiregulin. HER3 and HER4 are activated by binding neuregulins (NGFs) 1-4. On the other hand, the only exception is HER2, which is an orphan receptor as there is no known ligand that binds specifically to it.^{58,59,63,65} As a result, HER2 stays in a structural conformation that is always able to interact with other ErbB receptors to form heterodimers, thus allowing the activation of the ligand-less receptor.⁵⁸

The members of the ErbB receptor family can play an important role in the development of human cancers due to overexpression, underexpression or mutation.⁵⁸ The HER2 receptor is particularly important in the development of cancer. Its role in cancer was discovered in rat neuroblastoma, where the name *neu* comes from.⁶³ A point mutation from valine to glutamate was found in the position 664 of the protein sequence, mediated by the increasing ability of HER2 to form dimers. Even though this mutation is not found in humans, it has served as a basis to understand the role HER2 plays in human tumours. Indeed, HER2 is commonly found in a dimeric state within cancer cells, in contrast to healthy cells where the inactive form is always found as a monomer.⁶³ The high dimerisation rate of HER2 in cancer cells is related to HER2 being overexpressed in certain types of cancer, primarily in breast cancer in approximately 10-34 % of the cases.⁶⁰ HER2 overexpression is mainly due to ErbB2 gene amplification, which leads to a 100-fold increase in the HER2 protein expression.⁶⁵ The overexpression of HER2 leads to a higher production of HER2 heterodimers, but also to the appearance of HER2 homodimers, which stimulate aberrant malignant growth. As a result, HER2 overexpression is linked to poor prognosis, aggressive tumour growth and increased metastatic potential.^{62,65} In fact, the median survival for patients with HER2 positive breast cancers is 3 years, whereas it goes up to 6-7 years for non-HER2 breast cancers.⁶² Furthermore, HER2 overexpression is thought to increase brain metastasis to 9 % as compared to only 1.9 % when the breast cancers are not HER2 positive.⁶⁷

Additionally, it has recently been found that HER2 is also overexpressed in other types of cancer, including gastric (10-30 %), ovarian (20-30 %), colon (60-80 %), uterine serous endometrial carcinoma (14-85 %), lung (20 %), head and neck, oesophagus and bladder cancers.^{59,68}

3.1.3. Antibodies

An organism reacts to foreign molecules by producing antibodies, serum recognition elements that bind selectively to these molecules, referred to as antigens, and neutralise their effects. Antibodies bind to a specific site of the antigen, the epitope or antigenic determinant, and have an important role in the immune system.⁶⁹⁻⁷¹

Antibodies are glycoproteins from the immunoglobulin (Ig) family. In humans, Ig are divided into five classes; IgG, IgA, IgM, IgD and IgE. The differences between the Ig classes are mainly related to size, charge and composition, both in amino acid sequences and carbohydrates.⁷² All types of antibodies, independent of which Ig class they belong to, are made up of four polypeptide chains, two heavy and two light chains, which conform a Y-shaped molecule. The chains are subsequently divided into domains, each of which contains approximately 110 amino acids.^{71,72}

The most common antibodies found in blood serum are those belonging to the IgG class, found in approximately 80 %, which are involved in secondary immune responses.^{71,73} IgG antibodies are composed of one single Y-shaped molecule, structure shown in **Figure 3.4**, and have an average weight of 150 kDa. The G label stands for gamma (γ) heavy chains. The two identical heavy chains are linked between them by one to five disulfide bonds and subsequently linked to the two identical light chains by one disulfide bond and non-covalent interactions.⁷¹⁻⁷³ The amount of inter-heavy chain disulfide bonds present in the antibody differentiates the four IgG subgroups.⁷² The chains are divided into constant and variable domains. Heavy chains contain three constant domains and one variable domain, whereas light chains have one domain of each type. As their name indicates, constant domains have a relatively constant amino acid sequence among all IgG antibodies and are involved in the effector functions of the antibody. On the other hand, variable domains have a more variable amino acid

sequence since they are responsible for the specificity towards antigens. There are three hypervariable regions, also known as complementarity-determining regions (CDRs). These CDRs, located at the end of each arm of the Y-shape, constitute the antigen binding site (Fab) on each antibody and thus are chemically complementary with the antigen they recognise.^{71,72} The lower part of the antibody at the base, containing the C_H2 and C_H3 domains, is known as basal fragment (Fc). The Fc crystallises readily, binds to cell surface receptors and is active in the lysis of target cells but it does not bind to antigens.^{71,73}

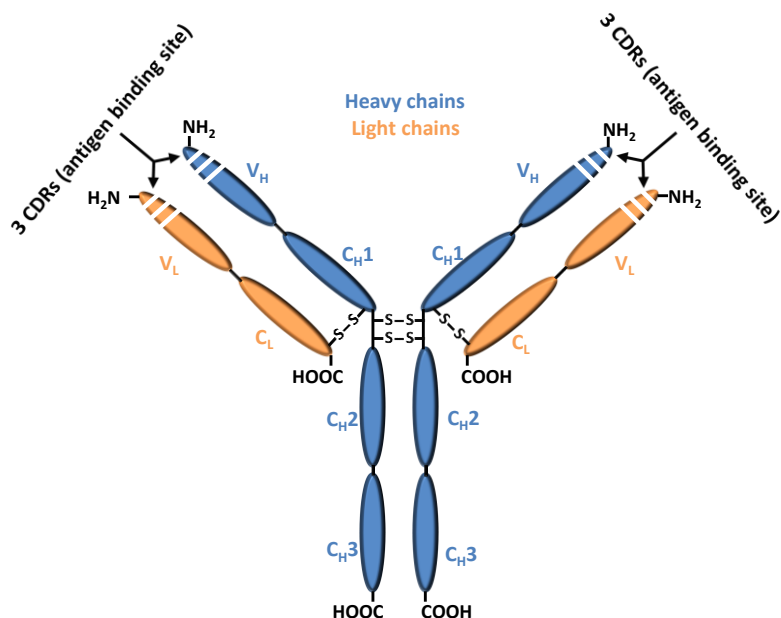


Figure 3.4. Structure of a typical IgG antibody, where V and C represent the variable and constant domains, respectively; H and L represent the heavy and light chains, respectively and CDRs represent the complementarity-determining regions or antigen-binding sites. The figure was adapted from Refs. 71-72.

The second most common type of antibodies found in serum belongs to the IgA class, making up between 10-15 %.⁷³ The A label stands for alpha (α) heavy chains. While IgA antibodies are found in a monomeric structure in the serum, *i.e.*, one Y-shaped molecule similar to IgG, they form a dimer in secretions, *i.e.*, two Y-shaped molecules linked by a J chain. Following IgA antibodies, IgM antibodies are found in the serum in 5-8 % and they are the most important antibodies in primary immune responses since they are the first antibodies to be made in the organism.^{71,73} The M label stands for mu

(μ) heavy chains. IgM antibodies, with an average molecular weight of 900 KDa, form a pentamer made up of five Y-shaped molecules, linked together by disulfide bonds and one J chain. In contrast to previous antibody types, the heavy chains of each Y-shaped molecule in IgM antibodies contain four constant domains and one variable domain.^{72,73} Finally, IgD and IgE antibodies make up less than 1 % of the antibody content in the serum and they are both based on monomeric structures, similar to IgG. The D and E labels stand for delta (δ) and epsilon (ϵ) heavy chains, respectively.⁷³

Throughout the research reported in this thesis, IgG antibodies were used. IgG antibodies are the most widely used type of antibody for immunoassays since they are the most commonly found in serum, they have a high affinity towards antigen epitopes and remain stable during their purification.⁷² On the other hand, IgM antibodies are mainly reserved for applications related to immunohistochemistry, since they have less affinity towards antigen epitopes and are more difficult to purify as compared to IgG antibodies. The other Ig classes, IgA, IgD and IgE, are rarely used not only due to their low affinity towards antigen epitopes but also to the minimal amounts found in the serum.⁷²

Production of IgG antibodies is derived from B lymphocytes.^{69,72} B lymphocytes always hold one specific antibody on their surface. Upon recognition of an antigen, B lymphocytes attract T cells, start to divide and create plasma cells, which can then produce many new antibodies.⁷² There are mainly two types of commercially available antibodies, polyclonal and monoclonal antibodies. Polyclonal antibodies are created by introduction of an antigen in an earlier sensitised animal, a method which produces a mixture of related antibodies with different epitope affinities. Therefore, polyclonal antibodies can recognise multiple epitopes on one antigen, which leads to a lower specificity and makes them more prone to batch-to-batch variability.⁷² On the contrary, monoclonal antibodies are identical antibodies able to recognise only one epitope in the antigen of interest. Monoclonal antibodies are created using hybridoma cells in a method developed by Köhler and Milstein in 1975.⁷⁴ Hybridoma cells are a fusion between B lymphocytes and immortal myeloma cancer cells, which gives them the ability to induce the production of antibodies as well as grow indefinitely, similar to cancer cells.^{70,72} Monoclonal antibodies are therefore produced in an identical manner

in all batches and consequently have a higher specificity than polyclonal antibodies. The main disadvantage with the use of monoclonal antibodies is that they are often too specific to recognise the antigen of interest and they can be vulnerable to the loss of epitope occurring after chemical treatment of the antigen.

The use of antibodies for cancer treatment is being widely studied. It is important to choose antibodies that target specific antigens that are only overexpressed on malignant cancer cells, but not on healthy cells.⁷⁵ Antibodies can, by themselves, be used as therapeutic agents. This is the case of the antibody Trastuzumab (Herceptin®), a humanised IgG antibody used to target the overexpressed HER2 receptor on breast cancer cells. Trastuzumab is thought to work in three different ways; inducing antibody-dependent cell cytotoxicity, decreasing the amount of HER2 receptors on the surface of the cancer cells by antibody internalisation that leads to lysosomal destruction, and preventing the dimerisation of the HER2 receptors.⁷⁶ Additionally, trastuzumab can be combined with therapies such as chemotherapy, which increases response to the treatment and decreases cancer progression thus leading to higher survival rates.⁶⁷ The main problems with the use of therapeutic antibodies is that the cancer cells are prone to create resistance to them. The use of trastuzumab leads to breast cancer recurrence one year after treatment with the antibody therapy.⁶⁷ Therefore, the use of antibodies as carriers for drug delivery is becoming more popular. In this mechanism, antibodies bind to the specific receptors overexpressed on the surface of cancer cells and are subsequently internalised *via* receptor-mediated endocytosis.^{75,76} The use of the anti-HER2 antibody as a targeting agent for breast cancer has been combined with nanotechnology in previous studies.^{77,78}

3.1.4. Aim of the research reported in this chapter

As discussed in **Chapter 1**, gold nanoparticles have been and still are widely used for the delivery of photosensitisers for PDT of cancer. The synthesis of gold nanoparticles (*ca.* 3-5 nm; AuNPs) functionalised with a mixed monolayer of PEG and a zinc phthalocyanine photosensitiser separated from the gold core by a carbon chain consisting of 11 carbon atoms has been previously reported (C11Pc).⁷⁷⁻⁷⁹ In this chapter, a second zinc phthalocyanine will be introduced, which possesses the same

macrocycle as C11Pc but is separated from the gold core by a carbon chain of only 3 carbon atoms (C3Pc). As a result, when AuNPs are functionalised with PEG and C3Pc, the phthalocyanine lies closer to the gold core as compared to the C11Pc. The goal of the research reported in this chapter was to compare both nanoparticle systems and their efficiency for PDT.

As it was reported in **section 3.1.1**, the interaction between metal nanoparticles and fluorophores can lead to different effects in the fluorescence of the fluorophore anchored onto their surface. The effects of the AuNPs on the fluorescence of C11Pc and C3Pc were studied. Furthermore, the production of ${}^1\text{O}_2$ by the two different systems was also studied. Finally, *in vitro* PDT of SK-BR-3 human breast adenocarcinoma cells using C11Pc-PEG-AuNPs and C3Pc-PEG-AuNPs was analysed and compared. The rate of phototoxicity and cell death of the breast cancer cell line using each of the nanoparticle systems were investigated.

In the second part of the research, the use of the anti-HER2 antibody as a targeting agent was explored. Anti-HER2 antibody was conjugated to the C11Pc-PEG-AuNPs and also to the C3Pc-PEG-AuNPs to selectively target HER2 overexpressing SK-BR-3 cells. The use of anti-HER2 antibody was shown to increase the uptake of the AuNPs and to reduce the differences between C11Pc-PEG-AuNPs and C3Pc-PEG-AuNPs observed during the first part of the research presented in this chapter.

3.2. Results and discussion

3.2.1. Zinc phthalocyanine photosensitisers

In this study, two zinc phthalocyanine photosensitisers were explored. The structures of both phthalocyanines are shown in **Figure 3.5**. Both phthalocyanines are dimeric structures composed of two macrocycles linked to one another by a disulfide bond. The difference in the two photosensitisers relies on the length of the carbon chain that connects the macrocycle to the sulfur bond. One photosensitiser is connected *via* three carbons (C3Pc), whereas the other is connected *via* eleven carbons (C11Pc). During nanoparticle synthesis, the disulfide bond will lead to self-assembly of the

photosensitiser onto the gold nanoparticle surface. The self-assembly will cause the disulfide bond to break, leading to the functionalisation of the gold core with monomeric structures, consisting of only one macrocycle. As a result, C3Pc is expected to be much closer to the gold core than the C11Pc.

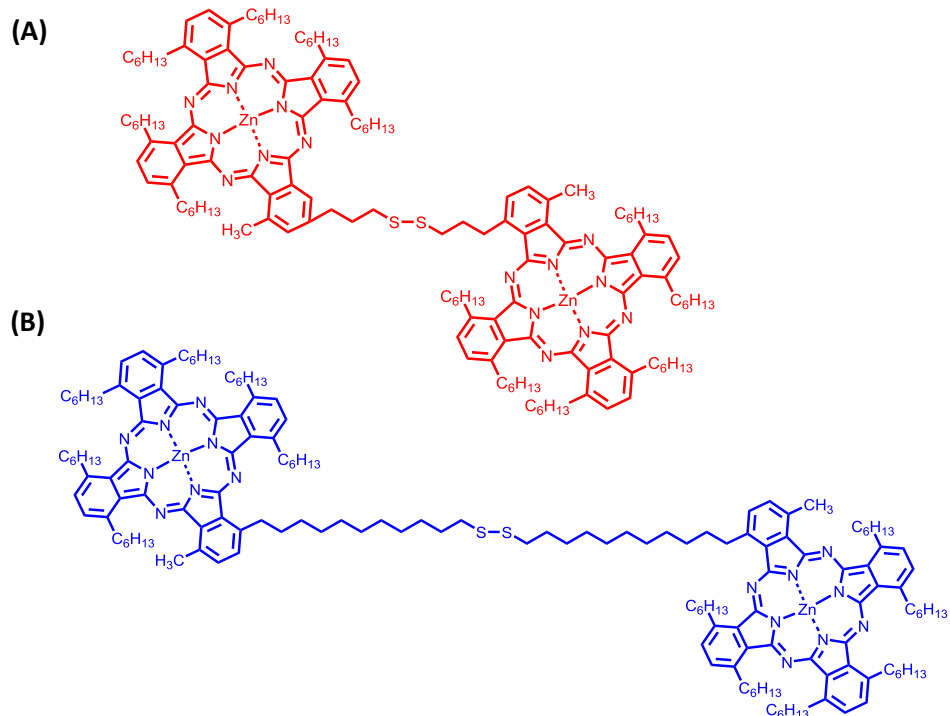


Figure 3.5. Structure of the two phthalocyanines, (A) C3Pc and (B) C11Pc.

The extinction coefficients for both C11Pc and C3Pc were calculated by creating a calibration curve, as explained in **section 2.2.4**. The experimental procedure for the C11Pc was straightforward, since the C11Pc was provided as a dry solid, it was easily weighed and a value for the extinction coefficient was calculated readily. The corresponding calibration curve for C11Pc is shown in **Figure 3.6**. On the other hand, the experimental procedure for C3Pc proved to be more problematic. During the addition of the zinc metal to the phthalocyanine post-synthesis, the final C3Pc compound was obtained in THF, which was then evaporated under reduced pressure using a rotary evaporator. However, the C3Pc solid could not be completely dried as it became particularly difficult to remove all the excess THF. As a result, weighing the C3Pc to obtain an accurate value was difficult. An initial value for the extinction

coefficient was obtained, **Figure 3.7 A-B**. However, to obtain a more accurate value, C3Pc was further dried under vacuum in the rotary evaporator for *ca.* 2 h. Following this procedure, the final C3Pc solid appeared drier than the previous sample. Therefore, a second value for the extinction coefficient was obtained, **Figure 3.7 C-D**. The numerical values of the extinction coefficients obtained experimentally are shown in **Table 3.1** for both C11Pc and C3Pc.

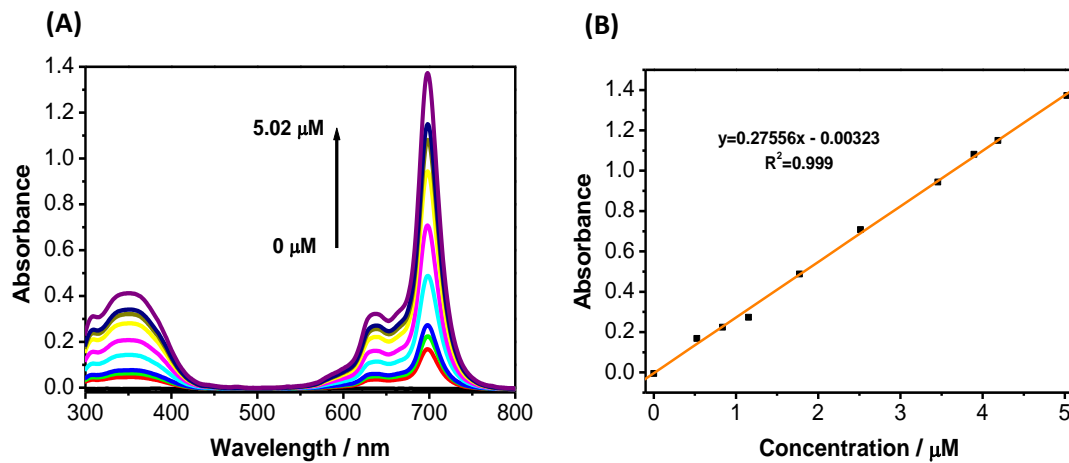


Figure 3.6. (A) UV-vis absorbance spectra of C11Pc in THF at various concentrations and **(B)** the corresponding calibration curve measured using an absorbance intensity at 698 nm.

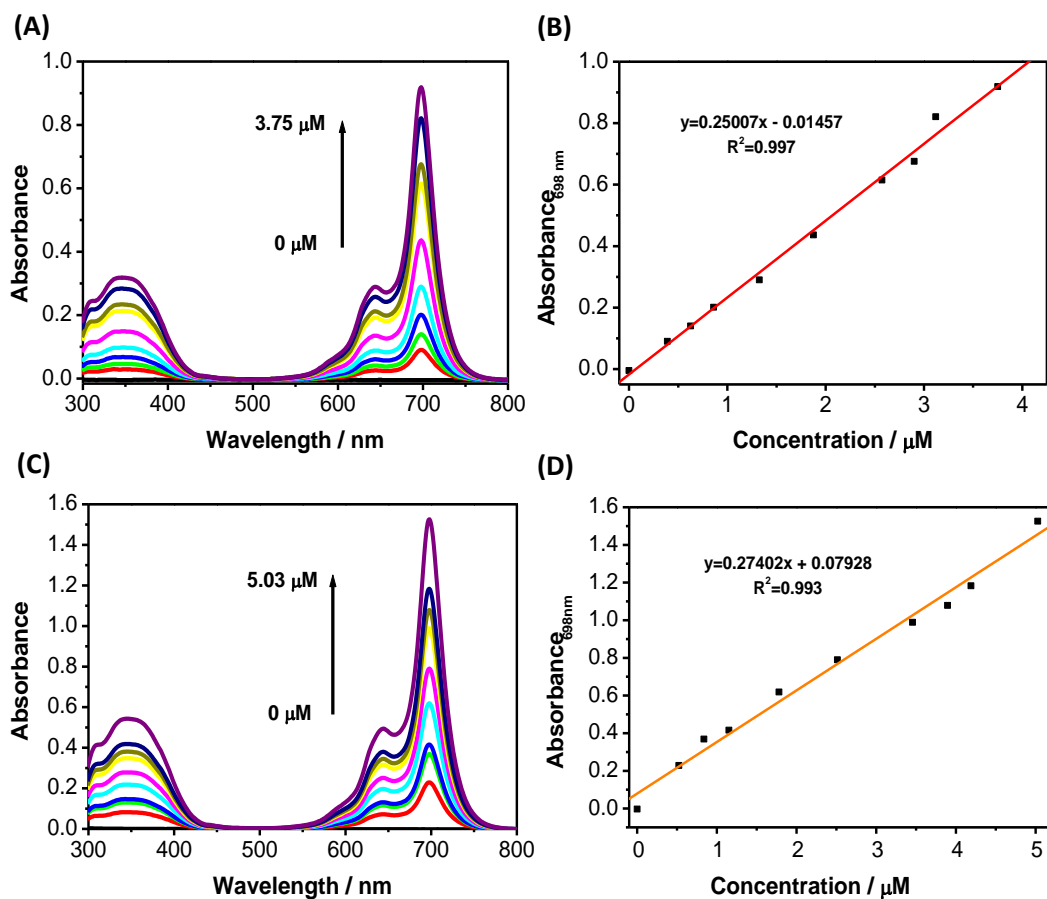


Figure 3.7. (A, C) UV-vis absorbance spectra of C3Pc in THF at various concentrations and (B, D) the corresponding calibration curves measured using an absorbance intensity at 698 nm.

Table 3.1. Extinction coefficients obtained for C11Pc and C3Pc.

Sample	$\epsilon / M^{-1} \cdot cm^{-1}$	Confidence interval (95 %)	R^2
C11Pc	2.75×10^5	3,731	0.999
C3Pc A	2.50×10^5	6,839	0.997
C3Pc B	2.74×10^5	11,112	0.993

For the purpose of this thesis, it will be assumed that the value of the extinction coefficient for C3Pc is $2.74 \times 10^5 M^{-1} \cdot cm^{-1}$, the value obtained after thoroughly drying the C3Pc to eliminate as much excess THF as possible. The structures of C11Pc (calculated $\epsilon = 2.75 \times 10^5 M^{-1} \cdot cm^{-1}$) and C3Pc are identical in the macrocycle of the phthalocyanine. As a result, it is expected that their extinction coefficients would be similar to one another.

3.2.2. Synthesis of gold nanoparticles

Gold nanoparticles (*ca.* 3-5 nm) were simultaneously synthesised and functionalised with a mixed monolayer of one of the two phthalocyanines and PEG by sodium borohydride reduction, as described in **section 2.2.1**. The functionalisation of the nanoparticles with PEG allows for the aqueous dispersibility of the phthalocyanines within the system. A schematic representation of the synthesised AuNPs is shown in **Figure 3.8**.

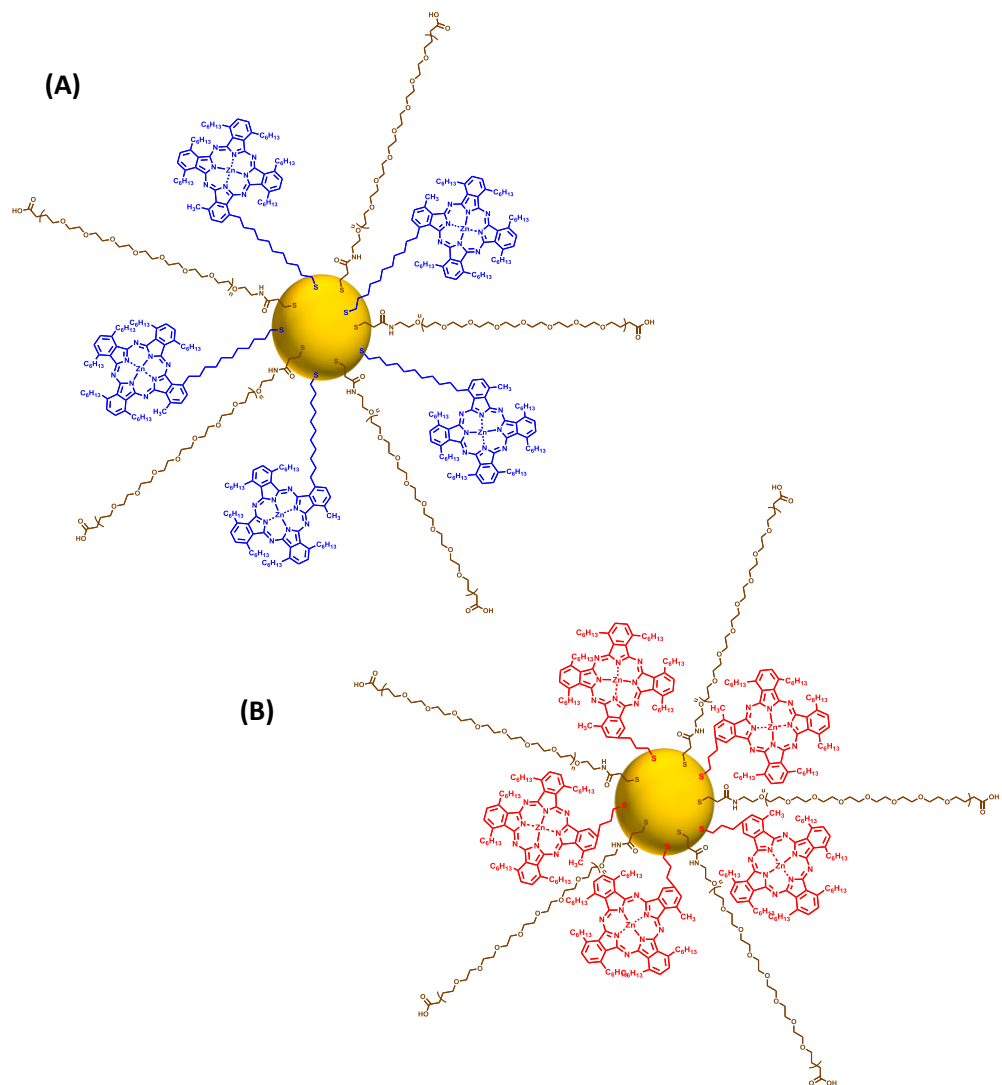


Figure 3.8. Schematic representation of (A) C11Pc-PEG-AuNPs and (B) C3Pc-PEG-AuNPs.

The synthesised nanoparticles were resuspended in MES buffer. The AuNPs were characterised by recording the UV-vis extinction spectra (**Figure 3.9 A**). The UV-vis extinction band at *ca.* 698 nm is characteristic of the monomeric form of zinc phthalocyanines, while the band centered at *ca.* 645 nm is characteristic of the dimeric form. The fact that the band at 698 nm is much higher than the one at 645 nm, for both C11Pc-PEG-AuNPs and C3Pc-AuNPs, indicates that most of the phthalocyanine is present in the active monomeric form.^{77,79} Furthermore, the absence of an extinction band in the 500 nm region suggests the nanoparticles are smaller than 10 nm in diameter. Both nanoparticle solutions presented a light blue colour, characteristic of substituted zinc phthalocyanines (**Figure 3.9 B**).^{77,80,81}

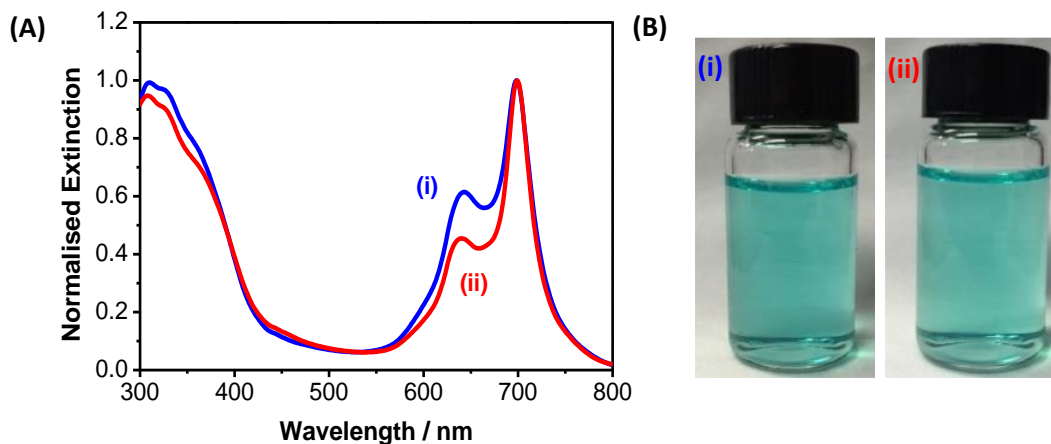


Figure 3.9. (A) UV-vis extinction spectra of C11Pc-PEG-AuNPs (i) and C3Pc-PEG-AuNPs (ii) in MES buffer. **(B)** Image showing the solution of nanoparticles functionalised with C11Pc (i) and C3Pc (ii), respectively.

The nanoparticles, dissolved in MES buffer, were further characterised by transmission electron microscopy (TEM) to evaluate the size. Analysis of the TEM for the C3Pc-PEG-AuNPs indicated that the nanoparticles have an average diameter of 3.83 ± 0.99 nm, following analysis of 562 nanoparticles, with a median value of 3.76 ± 0.99 nm. TEM images of the C3Pc-PEG-AuNPs, together with a histogram showing their size distribution, are shown in **Figure 3.10**. Analysis of the TEM for the C11Pc-PEG-AuNPs indicated that the nanoparticles have an average diameter of 3.41 ± 1.16 nm, following analysis of 282 nanoparticles, with a median value of 3.21 ± 1.35 nm. TEM images of

the C11Pc-PEG-AuNPs, together with a histogram showing their size distribution, are shown in **Figure 3.11**. The size distribution for C11Pc-PEG-AuNPs is slightly skewed. Therefore, the median value of 3.76 ± 0.99 nm could be a better representation of the average size of the C11Pc-PEG-AuNPs.⁸² It is important to note that, in both cases, for C3Pc-PEG-AuNPs and C11Pc-PEG-AuNPs, the batch-to-batch reproducibility was very high, with extinction spectra, TEM images and size distributions being very similar every time the nanoparticles were synthesised.

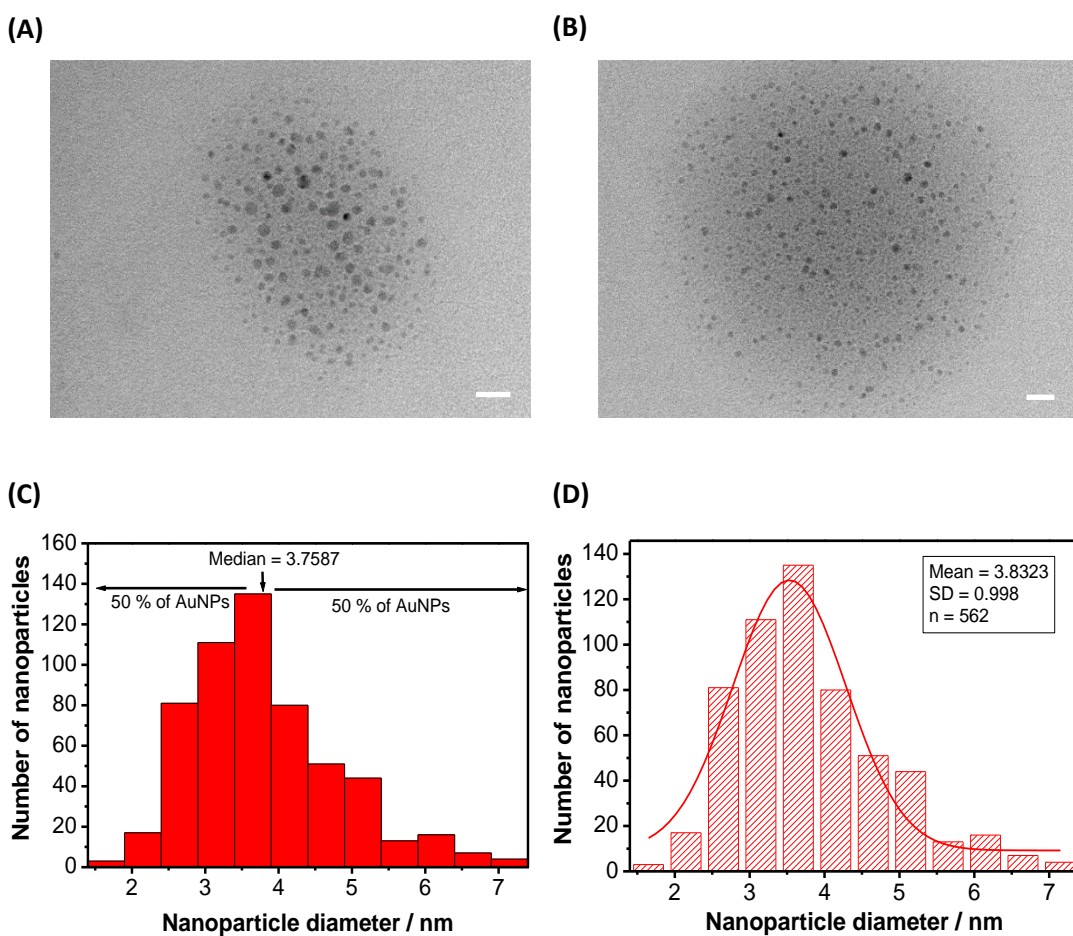


Figure 3.10. (A-B) Transmission electron micrographs of a sample of C3Pc-PEG-AuNPs, where the scale bars represent 20 nm. (C) Histogram of the C3Pc-PEG-AuNPs with a median value of 3.76 ± 0.99 nm ($n = 562$). (D) Size distribution of the C3Pc-PEG-AuNPs showing the Gaussian fit, with an average size of 3.83 ± 0.99 nm ($n = 562$).

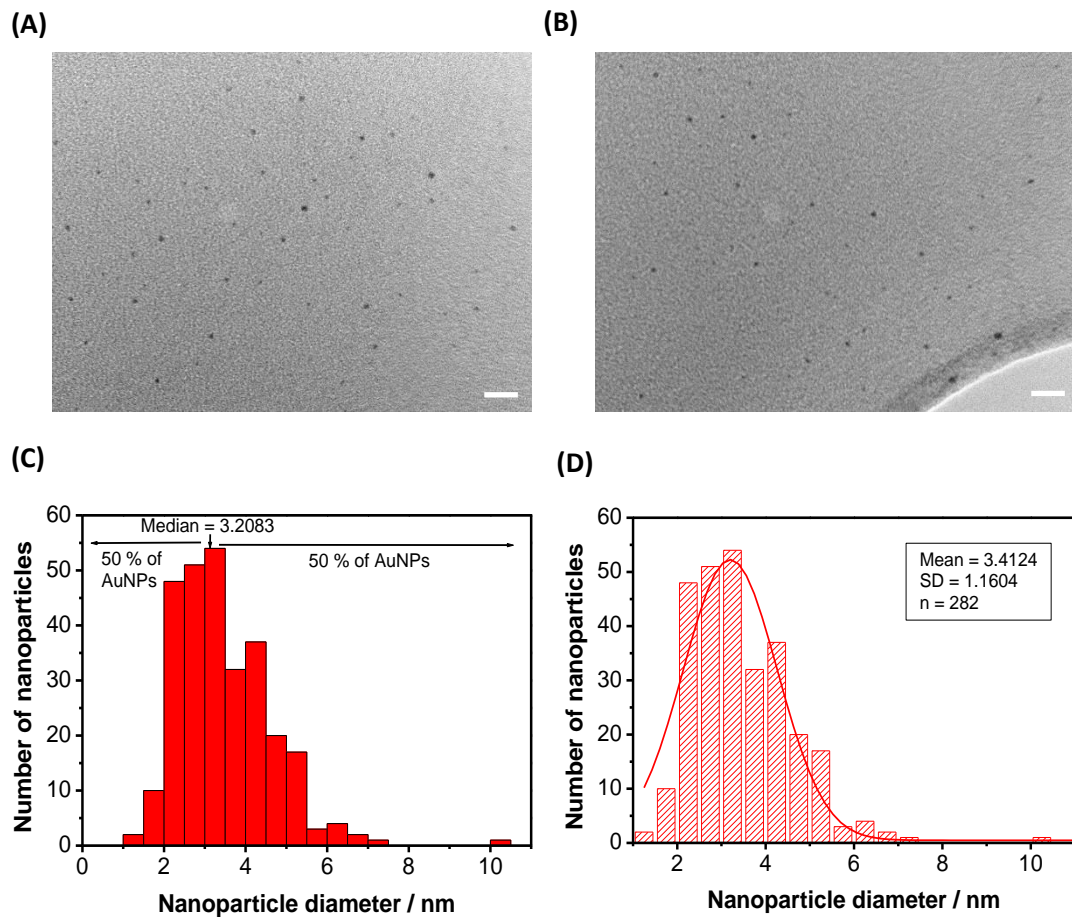


Figure 3.11. (A-B) Transmission electron micrographs of a sample of C11Pc-PEG-AuNPs, where the scale bars represent 20 nm. (C) Histogram of the C11Pc-PEG-AuNPs with a median value of 3.21 ± 1.35 nm ($n = 282$). (D) Size distribution of the C11Pc-PEG-AuNPs showing the Gaussian fit, with an average size of 3.41 ± 1.16 nm ($n = 282$).

The synthesised C11Pc-PEG-AuNPs and C3Pc-PEG-AuNPs were prepared following the same synthetic procedure with identical concentrations of Pc, PEG, gold chloride and sodium borohydride. However, the immobilisation of either of the phthalocyanines, C11Pc or C3Pc, on the surface of the AuNPs could be different due to the difference in the carbon chain length. The difference in the length of the carbon chain can lead to a different orientation of each Pc on the surface of the AuNPs, as previously reported by Revell *et al.*⁵¹ In order to obtain a ratio of the concentration of Pc to the concentration of AuNPs in the sample, the concentrations of both the Pc and the AuNPs need to be calculated. For the phthalocyanines, the extinction coefficients reported in **section 3.2.1** together with the extinction intensity at 698 nm (**Figure 3.9 A**) can be used to

obtain the concentration of the *Pc* in the sample *via* the Beer-Lambert law (**Equation 3.1**).

$$A = \varepsilon \cdot c \cdot l$$

Equation 3.1. Beer-Lambert law. *A* is the absorbance intensity; ε is the extinction coefficient ($M^{-1} \cdot cm^{-1}$) *c* is the concentration (M); and *l* is the path length of the quartz cuvette (1 cm).

The concentration of the AuNPs in the sample cannot be directly calculated due to the absence of a SPR absorption band in the extinction spectrum of the AuNPs with diameters smaller than 10 nm. For this purpose, an estimation of the concentration of AuNPs in the sample was performed following the procedure described by Haiss *et al.*⁸³ These authors experimentally determined the values for the extinction coefficients at 450 nm of AuNPs with a diameter of 2-100 nm. Additionally, the authors reported that it was possible to calculate the concentration of uncoated spherical AuNPs in water using the ε_{450} and the absorbance intensity at 450 nm, as shown in **Equation 3.2**. This method is more accurate for AuNPs larger than 5 nm in diameter, due to the surface effects taking place in smaller AuNPs. Considering that the AuNPs reported in this study are smaller than 5 nm and are not uncoated, this method can only give an estimation of the possible concentration of AuNPs in the sample and thus an estimation of the ratio of *Pc* to AuNPs. The data required to calculate the concentrations of *Pc* and AuNPs, as well as the results of the ratio of *Pc* to AuNPs are shown in **Table 3.2**.

$$c = \frac{A_{450}}{\varepsilon_{450}}$$

Equation 3.2. Equation used to calculate the concentration of AuNPs in an aqueous solution, as reported by Haiss *et al.* (Ref. 83).

Table 3.2. Estimation of the ratio of Pc to AuNPs.

Sample	A_{450}	$[\text{AuNP}] / \text{M}$	A_{698}	$[\text{Pc}] / \text{M}$	Ratio
C3Pc-PEG-AuNPs	0.137	3.78×10^{-8}	1.026	3.75×10^{-6}	99
C11Pc-PEG-AuNPs	0.101	2.79×10^{-8}	0.886	3.22×10^{-6}	115

For 4 nm AuNPs, $\epsilon_{450} = 3.62 \times 10^6 \text{ M}^{-1} \cdot \text{cm}^{-1}$. Value obtained from Ref. 83.

The results in **Table 3.2** suggest that the C3Pc-PEG-AuNPs have less phthalocyanines immobilised per AuNP (*ca.* 99) as compared to C11Pc-PEG-AuNPs, which will have more phthalocyanines per AuNP (*ca.* 115). As a result, at the same concentration of phthalocyanine, the C11Pc-PEG-AuNPs sample will contain less AuNPs than the C3Pc-PEG-AuNPs sample. An accurate value for the number of phthalocyanines immobilised per AuNPs can be obtained by performing inductively coupled plasma mass spectrometry (ICP-MS) on each of the samples, as previously reported.^{77,79} ICP-MS measurements should be performed in the future for confirmation.

3.2.3. Fluorescence studies

The fluorescence emission of the free phthalocyanines was analysed and compared to the fluorescence emission obtained from the functionalised gold nanoparticles. In order to be able to compare the emission spectra of the samples, all were required to be at the same concentration. Therefore, the UV-vis extinction of all samples was initially recorded to ensure this was the case. The solutions were excited at 633 nm and the fluorescence emission was collected between 650 and 850 nm. The free phthalocyanines were dissolved in THF, whereas the functionalised nanoparticles were dissolved in MES buffer for the analysis. The fluorescence emission spectra are shown in **Figure 3.12 A**. **Figure 3.12 B-C** shows the normalised fluorescence emission spectra of the free phthalocyanines and the Pc-PEG-AuNPs, respectively, so that the change in fluorescence can be more readily compared. The normalised fluorescence emission was calculated by taking the fluorescence of the more fluorescent sample to be 100 %

at the emission maximum. The fluorescence measurement and analysis were repeated five times, obtaining the same results on each occasion.

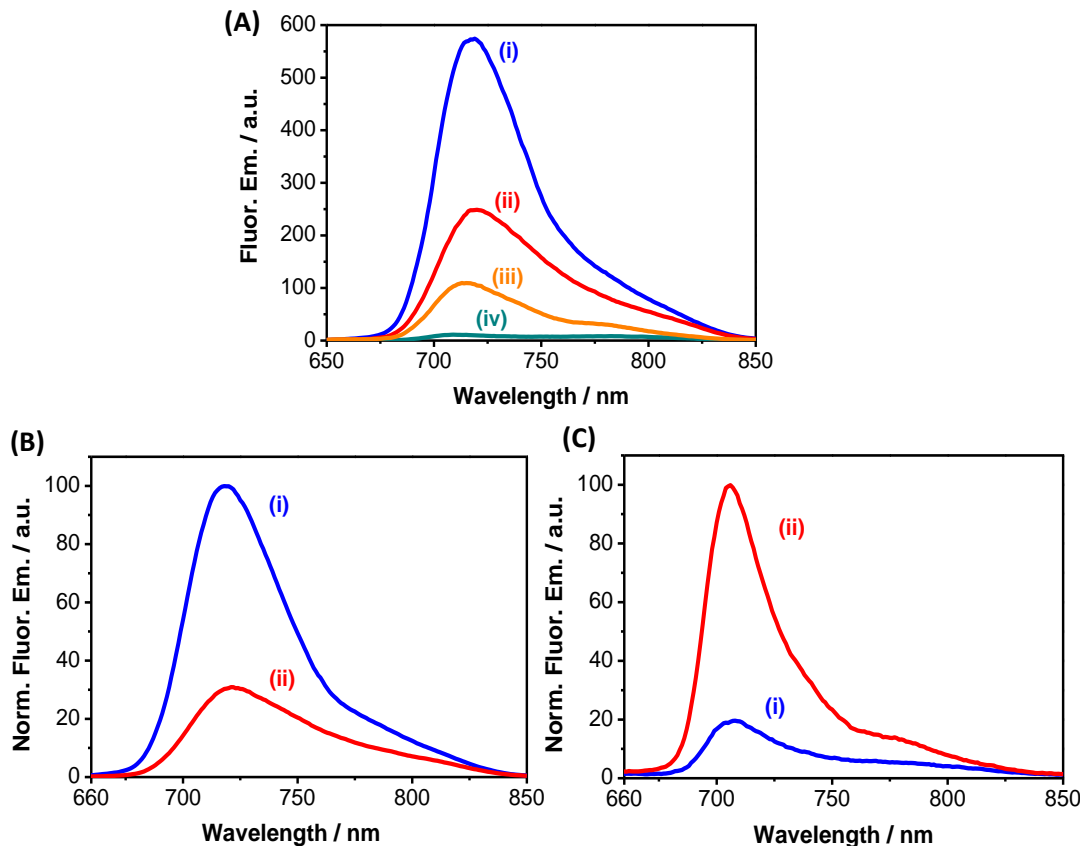


Figure 3.12. (A) Fluorescence emission spectra of free C11Pc (i), free C3Pc (ii), C3Pc-PEG-AuNPs (iii) and C11Pc-PEG-AuNPs (iv). (B) Normalised fluorescence emission spectra of free C11Pc (i) and free C3Pc (ii). (C) Normalised emission spectra of C11Pc-PEG-AuNPs (i) and C3Pc-PEG-AuNPs (ii).

As observed in **Figure 3.12 A-B**, the fluorescence emission intensity of C3Pc in solution is much lower than that of C11Pc. These results are in agreement with the finding of a higher extinction coefficient for C11Pc as compared to C3Pc. However, when the phthalocyanines are self-assembled on the AuNPs, the opposite effect is observed. Gold nanoparticles functionalised with C3Pc produce more fluorescence than those functionalised with C11Pc (**Figure 3.12 C**). The functionalisation of the AuNPs with C11Pc and C3Pc induces a quenching in the fluorescence for both phthalocyanines (**Figure 3.12 A**). This quenching effect by the metal centre is significantly lower for C3Pc, which is closer to the gold core, than for C11Pc. The quenching effect observed for the phthalocyanines self-assembled on the AuNPs could be due to the solvent in which they

are dissolved. While the free phthalocyanines are dissolved in THF, the AuNPs samples are dissolved in an aqueous buffer. Additionally, the presence of the gold metal could be contributing to the reported quenching of the *Pc*-PEG-AuNPs as compared to the free *Pcs*. To confirm these results, fluorescence quantum yields were recorded for both the free phthalocyanines in THF and the functionalised gold nanoparticles in MES buffer. Zinc 2,9,16,23-tetra-tert-butyl-29H,31H-phthalocyanine (ZnPc) was used as the reference sample as it has been reported to have a fluorescence quantum yield of 0.33 (33 %) in toluene.⁸⁴ This reference sample has absorbance and fluorescence emission spectra similar to those of C11Pc and C3Pc, which allows for their comparison. The structure and UV-vis absorption and fluorescence emission spectra of ZnPc can be seen in **Figure 3.13**.

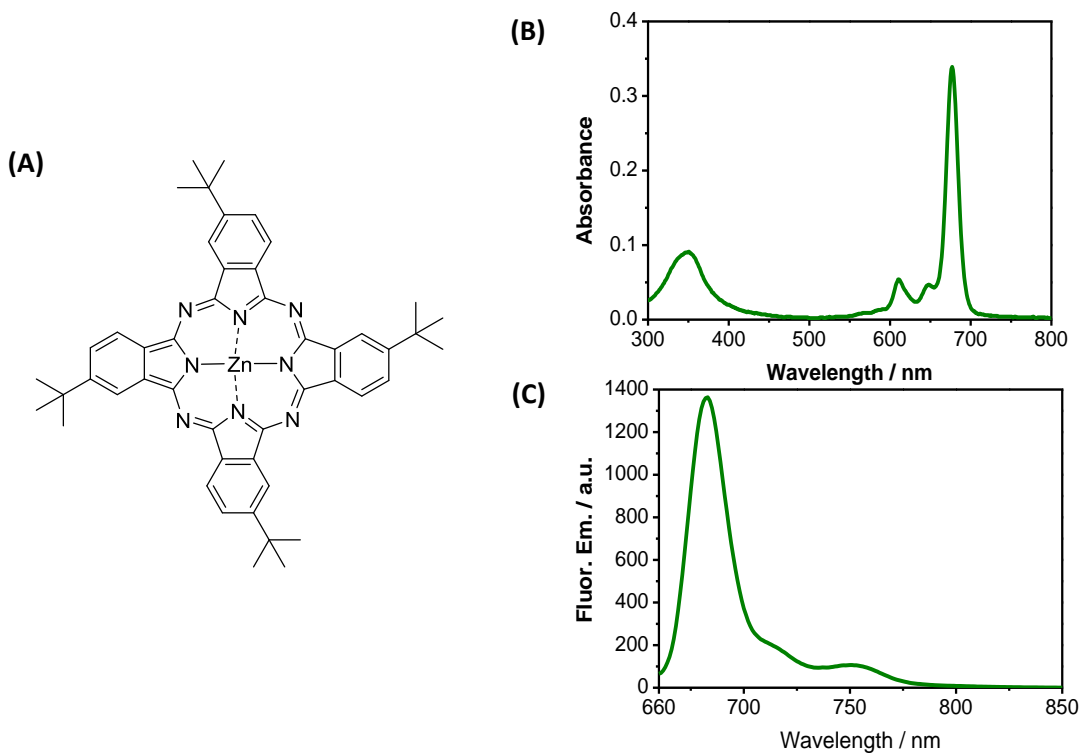


Figure 3.13. (A) Structure of ZnPc. (B) Absorption spectrum of ZnPc in toluene. (C) Fluorescence emission spectrum of ZnPc in toluene ($\lambda_{\text{ex}} = 640$ nm).

Fluorescence quantum yields were recorded for the free phthalocyanines and the phthalocyanines attached to the surface of the gold nanoparticles. The quantum yields were obtained *via* a calibration curve, as explained in **section 2.2.5**. The absorbance and fluorescence emission of each sample were recorded at different concentrations

to produce the calibration curve. Then, the gradients of each calibration curve were used to calculate the final value for the quantum yield, following **Equation 3.3**. The calibration curves obtained are shown in **Figure 3.14**, and the final numerical fluorescence quantum yield values are shown in **Table 3.3**.

$$\phi_x = \phi_{ref} \left(\frac{Grad_x}{Grad_{ref}} \right) \left(\frac{n_x^2}{n_{ref}^2} \right)$$

Where:

ϕ = Fluorescence quantum yield

ref = Reference sample

x = Experimental samples

Grad = Gradient

n = Refractive index of solvent

Equation 3.3. Equation used to calculate the fluorescence quantum yields *via* the calibration method.

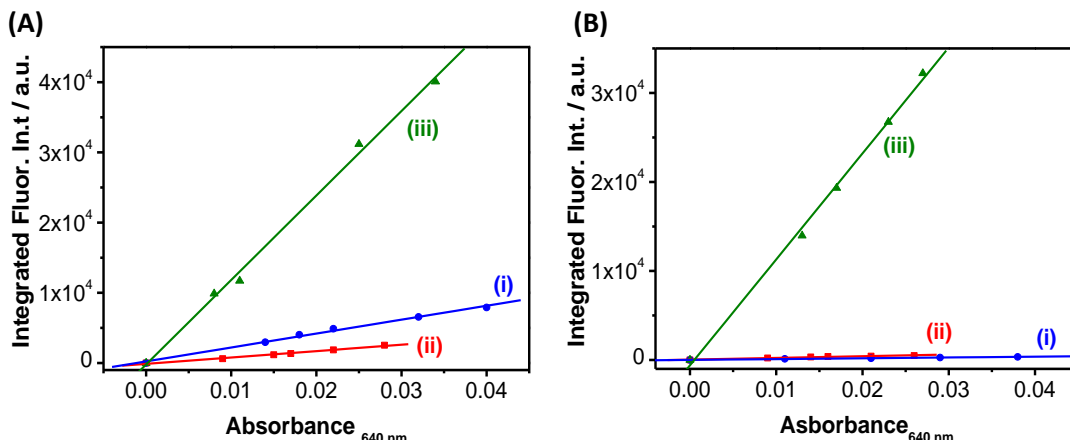


Figure 3.14. (A) Calibration curves for the free C11Pc (i) and C3Pc (ii) in THF together with ZnPc in toluene (iii). (B) Calibration curves for C11Pc-PEG-AuNPs (i) and C3Pc-PEG-AuNPs (ii) in MES buffer, together with ZnPc in toluene (iii).

Table 3.3. Values obtained for the fluorescence quantum yields.

Figure	Sample	Gradient	R ² value	Φ / %
3.14 A	ZnPc	1.20×10^6	0.998	33.00
	Free C11Pc	1.89×10^5	0.997	4.80
	Free C3Pc	9.08×10^4	0.994	2.60
3.14 B	ZnPc	1.19×10^6	0.999	33.00
	C11Pc-PEG-AuNPs	9.11×10^3	0.998	0.20
	C3Pc-PEG-AuNPs	1.91×10^4	0.980	0.42

$n_{THF}^{85} = 1.407$; $n_{Toluene}^{86} = 1.496$; $n_{H_2O}^{87} = 1.330$

The fluorescence quantum yields for the free phthalocyanines are rather low; 4.8 % for C11Pc and 2.6 % for C3Pc. A possible explanation for the low values obtained for the fluorescence quantum yields of the Pc in solution could be related to the dimeric structure of the phthalocyanines, as shown in **Figure 3.5**. Previous studies have reported that the strong fluorescence of monomeric phthalocyanines is usually quenched upon dimerisation and aggregation.⁸⁸⁻⁹⁰ As an example, the Zefirov group reported the synthesis of a magnesium phthalocyanine (2-hydroxy-9(10), 16(17), 23(24)-tri-*tert*-butylphthalocyanine [Mg]) and its corresponding dimer.⁸⁹ The authors found that the fluorescence quantum yield of the dimer was 1.4 %, a value smaller than half that obtained for the monomeric form (4.8 %).⁸⁹ Additionally, the Zefirov group also reported the synthesis of a zinc phthalocyanine (2-hydroxy-9(10), 16(17), 23(24)-tri-*tert*-butyl-29H,31H-phthalocyanine [zinc]) and its corresponding dimer.⁹⁰ The authors found that the fluorescence quantum yield of the dimer was reduced by 1.5-3 times as compared to the fluorescence quantum yield of the monomer in THF. The decrease in fluorescence quantum yield was found to be solvent-dependent and it was attributed to the energy transfer between the macrocycles upon excitation, which induces changes in the flexible structure of the dimeric phthalocyanine in the S₁ excited state.⁹⁰ However, it is also important to note that other studies have reported the successful synthesis of dimeric phthalocyanines with fluorescence quantum yield values exactly the same as for their monomeric counterparts.⁹¹ Relevant to the present study, the fluorescence quantum yield of the monomeric C11Pc phthalocyanine has been reported to be 12 %.⁹² This value is slightly more than double of the value obtained for the dimeric C11Pc in this study, in accordance with the reports of the Zerifov group. A value for the fluorescence quantum yield of the monomeric C3Pc phthalocyanine has not been reported in the literature. However, it could be assumed that the fluorescence quantum yield of the monomeric C3Pc would likely be more than double that of the dimeric C3Pc.

The fluorescence quantum yields estimated for the Pc-PEG-AuNPs are low, 0.42 % for C3Pc-PEG-AuNPs and 0.20 % for C11Pc-PEG-AuNPs. It is important to note that the refractive index of the MES buffer in which the nanoparticles were dissolved was taken to be the same as that of water (1.33), as reported in **Table 3.3**. However, MES buffer contains MES (50 nM) and Tween-20 (0.05 %). It has been reported that the presence

of MES increases the refractive index of water, and this increase in refractive index is concomitant with an increase in the concentration of MES buffer in the sample.⁹³ As a result, the refractive index of MES buffer could be slightly higher than that of water, which would lead to slightly higher values of the fluorescence quantum yields for the Pc-PEG-AuNPs than those reported here.

The estimated fluorescence quantum yields confirm the results obtained with the analysis of the fluorescence spectra as described above. The fluorescence quantum yield is higher for the free C11Pc (4.8 %) as compared to the free C3Pc (2.6 %). When the phthalocyanines are attached to the AuNPs, there is a quenching of the fluorescence in both C11Pc and C3Pc. Additionally, the fluorescence quantum yield for C11Pc-PEG-AuNPs (0.2 %) is lower than that of C3Pc-PEG-AuNPs (0.42 %). This behaviour can be explained by analysing the interaction between the fluorophores and the metal nanoparticles, as discussed in **section 3.1.1**. The RP model developed by Lakowicz suggests that small spherical nanoparticles (< 40 nm) will quench the fluorescence of the fluorophores since such nanoparticles primarily absorb light.²⁰ This explains the quenching effect seen for both C11Pc and C3Pc when they are attached to the AuNPs as compared to the quantum yield values obtained in solution.

The second result, by which the fluorescence from C3Pc is not quenched as much as that of C11Pc on the surface of the AuNPs, can be explained by the distance-dependence and the orientation-dependence parameter between the fluorophores and the metal nanoparticles. The distance-dependent parameter states that there are three regions where the fluorescence emission intensity behaves differently in the presence of the metal nanoparticles. Firstly, when the fluorophores are placed directly on the surface of the AuNPs or close to it (≤ 5 nm), the fluorescence is quenched. However, if the fluorophore is placed at an intermediate distance (*ca.* 5-20 nm, usually ≥ 10 nm), the fluorescence will be enhanced. Finally, if the fluorophore is placed too far away (≥ 20 nm) from the metal centre, there will be no interaction between the two, which leads to no effect in the fluorescence emission intensity.^{2,3,9} Additionally, as discussed in **section 3.1.1**, the orientation adopted by the fluorophores relative to the metal nanoparticles is also an important parameter. In 2007 Battistini *et al.* reported similar observations to that observed in the present study.⁴⁸ In their work, a pyrene

fluorophore was connected to the AuNPs by either a 4 atom-carbon chain or 11 atoms and the fluorescence of the C4 was not quenched as much as that of C11. The authors attributed this effect to the angle in which each chain is positioned in respect to the AuNPs. For the C4 molecule, the chain was *ca.* 20 ° tilted relative to the normal of the nanoparticle surface and thus the fluorophore was thought to be placed almost perpendicular to the AuNPs. On the contrary, the C11 molecule was thought to be at an angle much flatter towards the AuNPs, 45 °. As a result, the C11 molecule lies closer to the metal surface, which effectively quenches the fluorescence since non-radiative energy transfer and charge transfer between the pyrene in close contact with the AuNPs are more likely to occur as compared to the C4.⁴⁸ In conflict with these results is a previous study reported by Russell and co-workers in which the same C3Pc and C11Pc used in the present study were analysed as SAMs on a planar gold surface.⁵¹ These authors observed the tilting angle to be the same for both chains (*ca.* 20 °) but the orientation of the Pc macrocycle was more perpendicular for the C11Pc than for the C3Pc, leading to them being 13 Å and 4 Å away from the metal surface, respectively. As a result, the fluorescence from the C3Pc was quenched more efficiently than for the longer chain, and the fluorescence became stronger as the chain length increased.⁵¹

In the present study, a direct comparison with the study by Russell and co-workers cannot be done since, even though the phthalocyanines used have the same structure, the metal surface consists of gold nanoparticles rather than a planar gold surface. The results obtained in the present study suggest that the different structure of the metal surface affects the relative orientation adopted by the anchor chains. The fluorescence intensity of the C3Pc was found to be greater than the C11Pc on the surface of the AuNPs, suggesting that the C11Pc lies more parallel relative to the gold core as compared to the C3Pc, as speculated by Battistini *et al.* for the pyrenes C4 and C11 chains. Battistini *et al.* speculated that intermolecular interactions were the driving force for the final orientation of the chains; and it was unrelated to the odd or even number of carbons present in each chain. Considering that the fluorescence quenching in the study by Battistini *et al.* and since the present study follows the same trend, *i.e.*, enhanced quenching for the C11 longer chain, the present results suggest that the odd-even effect has a minimal effect as compared to the intra- and inter-molecular interactions, which is the overriding parameter deciding the orientation of the chains

and hence the macrocycles. In the present study, it is possible that the C11Pc chain will adopt a more parallel configuration relative to the AuNPs in order to maximise interactions between the chains. On the other hand, the C3Pc chain adopts a more perpendicular orientation due to the short nature of the chain, in which chain-chain interactions will be minimal. The presence of the PEG on the surface of the AuNPs is another factor to consider. Given the large size and flexible nature of the PEG chain used in this study, it is expected that there will be minimal interaction between the phthalocyanines and the PEG since the chains, even for the longer C11Pc, are a lot shorter than that of the PEG. Additionally, the phthalocyanines are expected to be oriented in a ‘face-to-face’ orientation relative to one another so that aggregation and dimerisation are minimised, consistent with the extinction spectrum indicative of monomeric phthalocyanines obtained for both C3Pc-PEG-AuNPs and C11Pc-PEG-AuNPs (see **Figure 3.9**). The closer angle in which the C11Pc lies towards the AuNPs is an indication that the C11Pc will be more closely packed on the surface of the AuNPs as compared to the C3Pc. The more densely packed structure would further maximise intermolecular chain interactions and is consistent with the estimation of the number of C11Pc and C3Pc per AuNPs shown in **section 3.2.2**, by which more C11Pc than C3Pc molecules are immobilised on the surface of AuNPs.

To summarise, the gold nanoparticles reported in the present study are of small size (*ca.* 4 nm in diameter) and thus, according to Lakowicz’s RP model, are expected to quench the fluorescence of fluorophores placed near-by.²⁰ Additionally, the orientation of the phthalocyanines and their molecular dipoles relative to the gold core is an important consideration. The results of Battistini *et al.*, together with the results presented in this chapter, suggest that the C11Pc lies at a more horizontal angle towards the gold core than the C3Pc. Therefore, the macrocycle in C11Pc is speculated to be in a parallel orientation relative to the gold nanoparticles, while the C3Pc will be placed more perpendicular. The parallel orientation enhances the quenching effect seen for C11Pc due to the cancellation in the molecular dipoles of the phthalocyanine and the AuNPs, which radiate out of phase and thus decrease the radiative rate of the phthalocyanines.^{12,37} Furthermore, the parallel orientation of the C11Pc would cause the C11Pc to lie closer to the gold core as compared to the C3Pc, thus facilitating electron transfer between the C11Pc and the small AuNPs, leading to a higher

quenching effect.⁴⁷ On the contrary, the perpendicular orientation of the C3Pc would be ideal for metal-enhanced fluorescence. However, the fluorescence intensity of C3Pc on the surface of the AuNPs does not seem to be enhanced in comparison to the free C3Pc in solution. Even though part of this quenching effect is expected to be due to the different solvents in which the samples were dissolved, as previously discussed, it is speculated that the small size of the nanoparticles used in this study, together with the distance between the AuNPs and the C3Pc are enhancing the quenching efficiency of the phthalocyanine. The use of AuNPs of larger size should be studied in the future to confirm whether MEF can be seen with C3Pc.

3.2.4. Spectroscopic analysis of singlet oxygen production

Results from the fluorescence analysis, together with the literature review in **section 3.1.1**, suggest that C3Pc-PEG-AuNPs might be more efficient at producing singlet oxygen (${}^1\text{O}_2$) than the C11Pc-PEG-AuNPs. In order to test this possibility, the production of ${}^1\text{O}_2$ by each of the two systems was spectroscopically studied. Firstly, the production of ${}^1\text{O}_2$ was measured using the probe 9,10-anthracenediyl-bis(methylene) dimalonic acid (ABMA). ABMA is a water soluble fluorescent anthracene derivative. It selectively reacts with ${}^1\text{O}_2$, which causes the photobleaching of the probe, leading to the formation of a non-fluorescent 9,10-endoperoxide product.⁹⁴ The reaction between ABMA and ${}^1\text{O}_2$ is shown in **Figure 3.15**. When ${}^1\text{O}_2$ is present, fluorescence emission and absorbance intensity from ABMA are quenched due to the photobleaching reaction. The change in the spectra are best appreciated in the fluorescence emission spectrum.

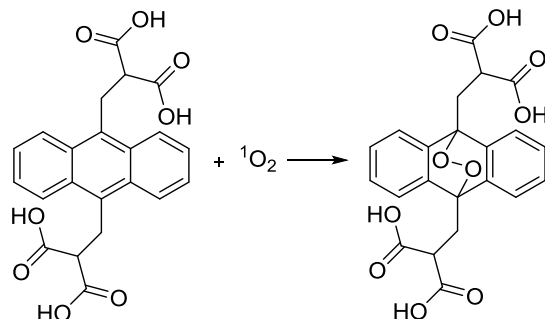


Figure 3.15. Reaction between ABMA and ${}^1\text{O}_2$ to give the corresponding non-fluorescent 9,10-endoperoxide product. The fluorescence of the endoperoxide product is quenched compared to the initial ABMA.

Before $^1\text{O}_2$ production was measured, ABMA was characterised using fluorescence spectroscopy. By doing this, the optimum conditions for excitation ($\lambda_{\text{em}} = 430 \text{ nm}$) and emission ($\lambda_{\text{ex}} = 380 \text{ nm}$) were found. As explained in **section 2.2.7**, the phthalocyanine samples were mixed with ABMA (1 μM). The samples were then irradiated at 633 nm using a HeNe laser for 40 min. The laser was located 50 cm from the cuvette. The fluorescence emission spectrum of ABMA was recorded every 5 min. To confirm that the production of $^1\text{O}_2$ is possible due to the presence of the photosensitiser in the sample, control PEG-AuNPs were synthesised and production of $^1\text{O}_2$ by these control particles was also measured. The results for both C11Pc-PEG-AuNPs and C3Pc-PEG-AuNPs dissolved in MES buffer confirm that $^1\text{O}_2$ is being produced, as there is a decrease in ABMA fluorescence, typical of the photobleaching caused by the formation of the non-fluorescent 9,10-endoperoxide product (**Figure 3.16**).

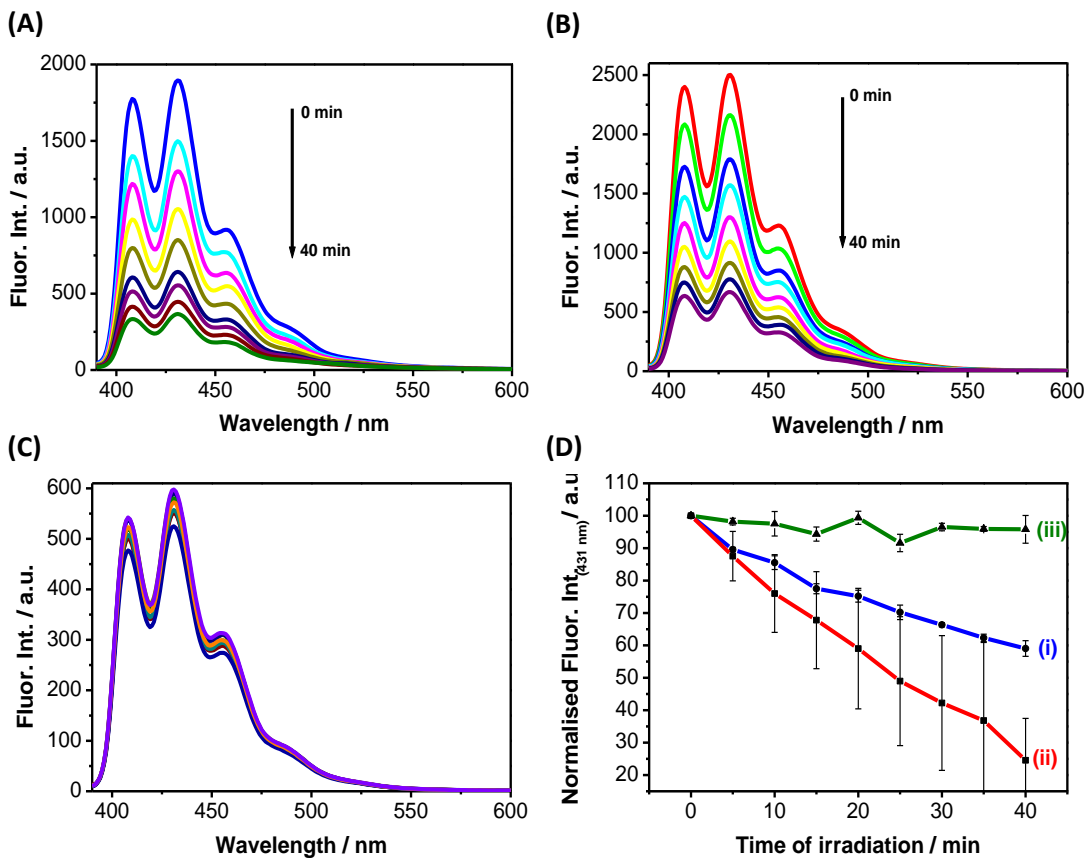


Figure 3.16. Fluorescence emission spectra of ABMA showing the quenching of the fluorescence, thus confirming the formation of $^1\text{O}_2$ in **(A)** C11Pc-PEG-AuNPs and **(B)** C3Pc-PEG-AuNPs in MES buffer. **(C)** No quenching of ABMA is observed in the presence of control PEG-AuNPs. **(D)** Photobleaching of ABMA in the presence of C11Pc-PEG-AuNPs **(i)** or C3Pc-PEG-AuNPs **(ii)** (1 μM Pc) as a function of time; and no photobleaching observed for control PEG-AuNPs **(iii)**. Error bars represent the SD ($n = 3$) within a 95 % confidence interval.

The maximum amount of ABMA photobleaching for each phthalocyanine was calculated and normalised to the concentration of Pc using **Equation 3.4**.⁹⁵ The values obtained for each of the gold nanoparticle conjugates are shown in **Table 3.4** below.

$$\% \text{ ABMA photobleaching} = \frac{(\% \text{ Fluor}_{431\text{nm}} t = 0 \text{ min}) - (\% \text{ Fluor}_{431\text{nm}} t = m \text{ min})}{m \text{ min} \times [\text{Pc}] / \mu\text{M}}$$

Equation 3.4. Equation used to calculate the maximum amount of ABMA photobleaching for the gold nanoparticle conjugates.

Table 3.4. Maximum amount of ABMA photobleaching for each nanoparticle

Time / min	Sample	[Pc] / μM	% Fluor $t=0\text{min}$	% Fluor $t=m\text{ min}$	% ABMA
5	C11Pc-PEG-AuNPs	1.0	100	89.6 \pm 0.7	2.1 \pm 0.1
40				59.0 \pm 2.4	1.0 \pm 0.1
5	C3Pc-PEG-AuNPs	1.0	100	87.5 \pm 7.6	2.5 \pm 1.5
40				24.6 \pm 12.9	1.9 \pm 0.3

The results on **Table 3.4** show the maximum amount of ABMA photobleaching (*i.e.*, after the first 5 min) to be 2.5 % for the C3Pc-PEG-AuNPs and 2.1 % for the C11Pc-PEG-AuNPs. These results indicate that the photobleaching of ABMA is higher in the presence of C3Pc-PEG-AuNPs. The use of ABMA to detect the production of ${}^1\text{O}_2$ is usually a qualitative measurement and the fluorescence measurements can be subject to high errors. Taking the errors into consideration, 2.5 ± 1.5 % for C3Pc-PEG-AuNPs and 2.1 ± 0.1 % for C11Pc-PEG-AuNPs, the results could mean that the maximum amount of ABMA photobleaching and thus production of ${}^1\text{O}_2$ by both systems is similar. However, by looking at the photobleaching of ABMA over time (**Figure 3.16 D**), it can be clearly seen that the C3Pc-PEG-AuNPs induce more photobleaching (1.9 ± 0.3 %) of ABMA than the C11Pc-PEG-AuNPs (1.0 ± 0.1 %) after 40 min, even when the errors are taken into consideration. The higher photobleaching of ABMA in the presence of the C3Pc-PEG-AuNPs over time is a strong indication that the C3Pc-PEG-AuNPs produce more ${}^1\text{O}_2$. In order to better understand the production of ${}^1\text{O}_2$ by both systems, the quantum yield of singlet oxygen was studied, as explained in the following section.

3.2.5. Singlet oxygen quantum yields

The measurement of ${}^1\text{O}_2$ quantum yield was analysed for the free phthalocyanines initially, to check for possible differences between the two photosensitisers. Perinaphthenone was used as a reference, which is known to have a ${}^1\text{O}_2$ quantum yield of 1.0 in toluene.⁸⁰ The singlet oxygen quantum yield was measured *via* time-resolved luminescence. As explained in **section 2.2.8**, the samples were irradiated at 355 nm using the third harmonic of a Q-switched Nd:YAG laser. The luminescence was then collected at 90° and passed through a narrow band-pass interference filter (1,270 nm). Finally, the signal due to ${}^1\text{O}_2$ was detected by a germanium photodiode, cooled with liquid nitrogen. The intensity of ${}^1\text{O}_2$ emission (I_{1O_2} ; mV) was plotted against the intensity of light absorbed by the system (I_{A} ; mV), which produced a calibration curve. By comparing the slope of the curves, the quantum yield of ${}^1\text{O}_2$ in the unknown samples can be calculated. The intensity of light absorbed by the system was calculated using the Beer-Lambert law, **Equation 3.5**. The results are shown in **Figure 3.17**.

$$I_{\text{A}} = I_0(1 - 10^4)$$

Equation 3.5. Beer-Lambert law equation used to calculate I_{A} .

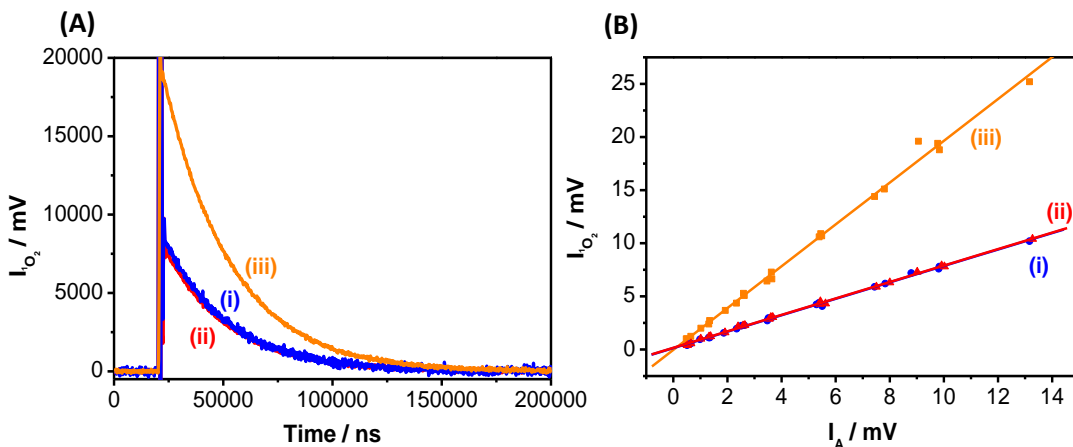


Figure 3.17. (A) Example of the intensity of ${}^1\text{O}_2$ emission *versus* time for C11Pc (i), C3Pc (ii) and perinaphthenone (iii). (B) Calibration curves for C11Pc (i), C3Pc (ii) and perinaphthenone (iii) used to calculate the ${}^1\text{O}_2$ quantum yields.

Following **Equation 3.6**, the quantum yields were calculated and the results are shown in **Table 3.5**.

$$\phi_x = \phi_{ref} \left(\frac{Grad_x}{Grad_{ref}} \right) \left(\frac{n_x^2}{n_{ref}^2} \right)$$

Where:

ϕ = $^1\text{O}_2$ quantum yield
 ref = Reference sample
 x = Experimental samples
 $Grad$ = Gradient
 n = Refractive index of solvent

Equation 3.6. Equation used to calculate the fluorescence quantum yields *via* the calibration method.

Table 3.5. Values obtained for the $^1\text{O}_2$ quantum yields.

Sample	Gradient	R^2 value	$\Phi_\Delta / \%$
Perinaphthenone	1.968	0.998	100
Free C11Pc	0.773	0.999	40
Free C3Pc	0.774	0.999	40

$n_{Toluene}^{86} = 1.496$

The $^1\text{O}_2$ quantum yields obtained for the free phthalocyanines in solution were found to be 40 %, the same for C11Pc and C3Pc. This result is in agreement with a previously reported value for the $^1\text{O}_2$ quantum yield of C11Pc, which was found to be 45 %.⁸⁰

The measurement of $^1\text{O}_2$ quantum yield for the AuNPs was more complex. The nanoparticles are dispersed in an aqueous solution, MES buffer. The presence of water produces a quenching effect of the $^1\text{O}_2$ emission, thus making it difficult for the signal to be seen spectroscopically. Therefore, the calculation of the quantum yield was not possible. In an attempt to solve this problem, the nanoparticles were dispersed in deuterium oxide (D_2O). Following irradiation at 355 nm, as previously described, the signal recorded for $^1\text{O}_2$ was low for both samples. As a result, the calculation of a numerical value for the quantum yield was not possible. The signal was recorded at two different laser powers, 4 and 4.5 mJ, (**Figure 3.18**). The absorbance intensity values at the excitation wavelength were the same for C11Pc-PEG-AuNPs ($A_{355\text{ nm}} = 0.278$) and C3Pc-PEG-AuNPs ($A_{355\text{ nm}} = 0.280$). In order to confirm that the signal seen was due to

$^1\text{O}_2$, the samples were deoxygenated with helium. This confirmed that the signal was indeed produced due to $^1\text{O}_2$, as shown in **Figure 3.18**.

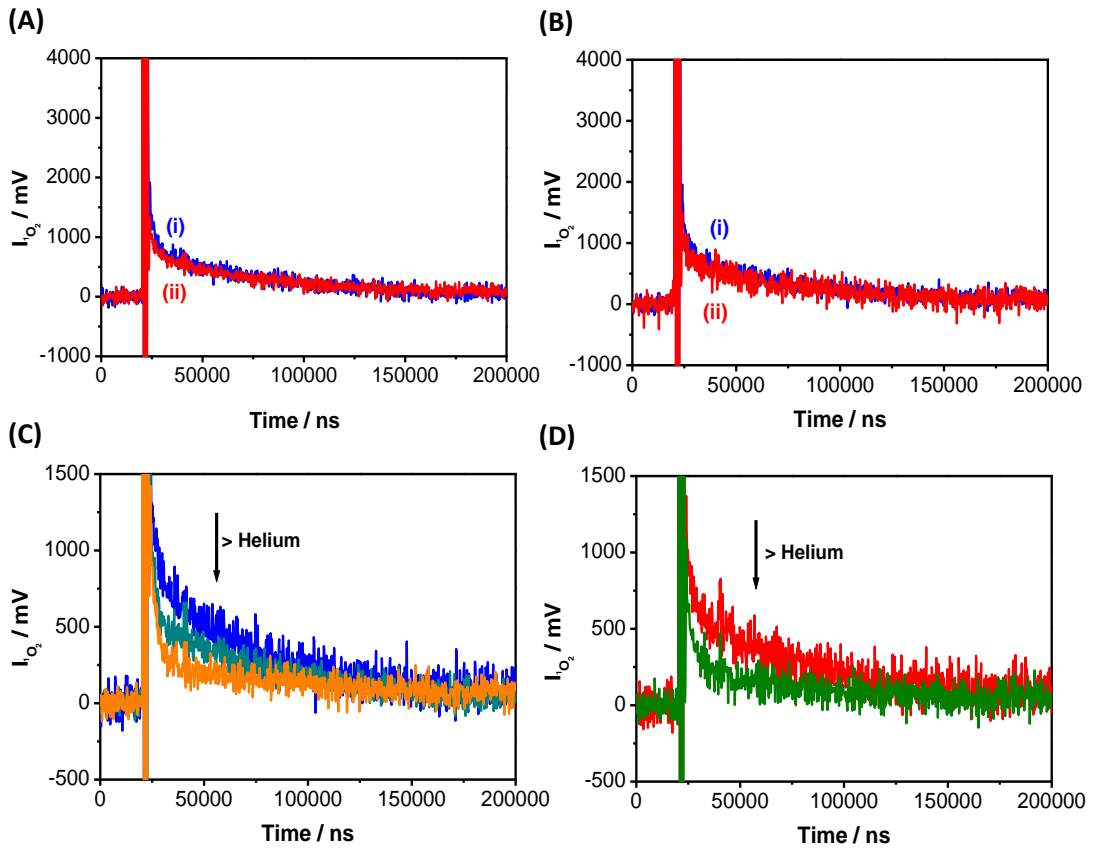


Figure 3.18. Intensity of $^1\text{O}_2$ emission versus time for (i) C11Pc-PEG-AuNPs and (ii) C3Pc-PEG-AuNPs, using a laser power of (A) 4 mJ or (B) 4.5 mJ. (C, D) Decrease in the $^1\text{O}_2$ emission signal due to the deoxygenation of C11Pc-PEG-AuNPs (C) or C3Pc-PEG-AuNPs (D) with helium.

The results in **Figure 3.18 C-D** confirm that $^1\text{O}_2$ is being produced by the AuNPs, as the intensity of the $^1\text{O}_2$ signal decreases as the samples are deoxygenated with helium. However, a numerical value for the $^1\text{O}_2$ quantum yield could not be obtained due to the low signals observed (**Figure 3.18 A-B**). Even though the signal of $^1\text{O}_2$ emission in D_2O is too low to obtain a value for the quantum yield, the results suggest that both samples produce a similar amount of $^1\text{O}_2$. The $^1\text{O}_2$ emission (**Figure 3.18 A-B**) for both samples, at the same Pc concentration, overlap, showing that the production of $^1\text{O}_2$ by the two nanoparticle samples is similar. However, the results are not conclusive and further experiments should be performed.

3.2.6. Cell viability assays

Cell viability was measured on SK-BR-3 human breast adenocarcinoma cells using two different cytotoxicity assays, MTT and CellTiter-Blue®. Initially, the MTT assay was used. MTT (3-(4,5-dimethylthiazol-2-yl)-2,5-diphenyltetrazolium bromide) is a reagent used to assess cell viability.⁹⁶ MTT is water soluble and non-toxic to the cells. In the presence of metabolically active cells (*i.e.*, viable cells), MTT is reduced to MTT formazan. MTT formazan appears in the form of crystals since it is insoluble in aqueous media. However, the MTT formazan can be dissolved in organic solvents such as dimethyl sulfoxide (DMSO). The MTT molecule presents a yellow colour, whereas the reduced MTT formazan product appears pink-purple. The absorbance spectrum of MTT formazan can be measured between 500-600 nm. The reaction scheme is shown in **Figure 3.19.**⁹⁶

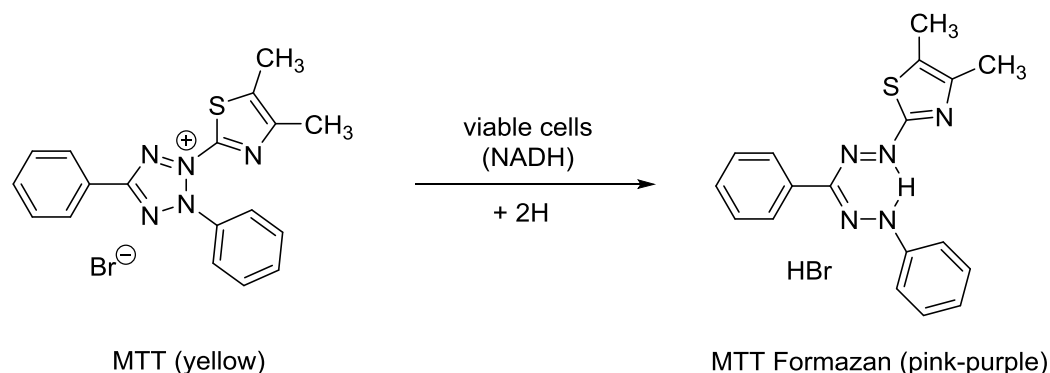


Figure 3.19. Reduction reaction of MTT when in contact with metabolically active cells, to produce MTT formazan.

As described in **section 2.2.9**, SK-BR-3 cells were incubated for 3 h with varying concentrations of C11Pc-PEG-AuNPs or C3Pc-PEG-AuNPs, ranging between 0 - 0.25 μ M of each phthalocyanine. All samples were dispersed in serum-free McCoy's 5A phenol red-free medium, to avoid interference between the absorbance of phenol red and that of MTT, which overlap in the same region. A positive control for cytotoxicity to induce cell apoptosis, consisting of a solution of staurosporine (1 mM in DMSO) dispersed in serum-free McCoy's 5A phenol red-free medium to give a final concentration of 20 μ M was also used.^{79,97,98} Following incubation with the samples, the cells were either

irradiated at 633 nm using a HeNe laser for 6 mins, or non-irradiated. The results for both C11Pc-PEG-AuNPs and C3Pc-PEG-AuNPs are shown in **Figure 3.20**.

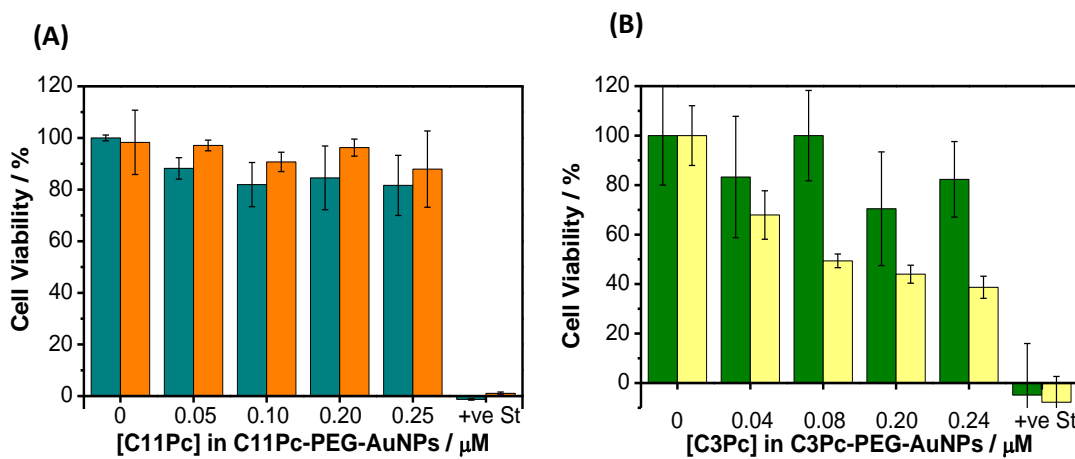


Figure 3.20. MTT cell viability assay for SK-BR-3 cells incubated with **(A)** C11Pc-PEG-AuNPs or **(B)** C3Pc-PEG-AuNPs. Cells were either irradiated with a 633 nm HeNe laser (**A** orange, **B** yellow) or non-irradiated (**A** dark cyan, **B** green). Staurosporine (+ve St) was used as a positive control for cytotoxicity. Error bars represent the SD ($n = 3$) within a 95 % confidence interval.

As can be seen in **Figure 3.20**, neither the C11Pc-PEG-AuNPs nor the C3Pc-PEG-AuNPs appear to produce dark toxicity, which means that the AuNPs are not toxic in the absence of light. When the samples are irradiated with the 633 nm laser, there is a significant difference between the C11Pc-PEG-AuNPs and C3Pc-PEG-AuNPs. Cells treated with C11Pc-PEG-AuNPs remain viable and unharmed following irradiation. On the contrary, the C3Pc-PEG-AuNPs induce cell death following irradiation. The increase in cell death is concomitant with the increase in C3Pc concentration. These results show that PDT with the C3Pc-PEG-AuNPs is more efficient as compared to the C11Pc-PEG-AuNPs. However, these MTT assays show negative values of cytotoxicity for the positive control, +ve St. Furthermore, the samples, especially the non-irradiated cells, show high error bars. In order to eliminate these problems and confirm the results obtained with the MTT assay, a different assay, CellTiter-Blue® cell viability assay, was performed.

CellTiter-Blue® is a fluorescence-based cell viability assay. It contains the non-fluorescent blue reagent resazurin. In the presence of viable cells, resazurin is reduced to the highly fluorescent resorufin, which is pink in colour. The fluorescence of

resorufin can be measured at 594 nm following excitation at 560 nm. On the contrary, non-viable cells, which have lost their metabolic capacity, cannot reduce resazurin and thus do not generate a fluorescence signal.⁹⁹ The reduction reaction of resazurin to resorufin is shown in **Figure 3.21**.¹⁰⁰

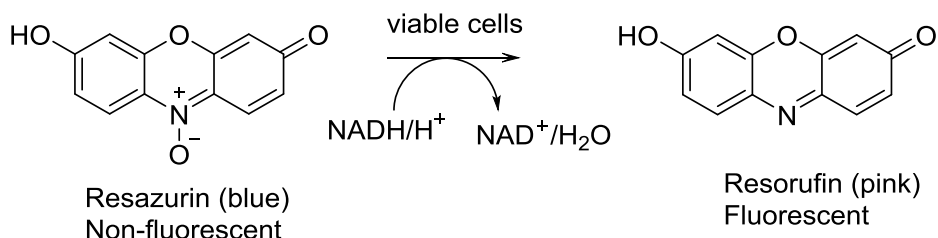


Figure 3.21. Reduction reaction of resazurin in contact with metabolically active cells, to produce resorufin.

SK-BR-3 cells were treated with the C11Pc-PEG-AuNPs and C3Pc-PEG-AuNPs following the procedure previously described for the MTT assay. The results of the assay are shown in **Figure 3.22**. The results from the CellTiter-Blue® assay are in agreement with those of the MTT assay. There is no dark toxicity for either of the nanoparticle conjugates, C11Pc-PEG-AuNPs and C3Pc-PEG-AuNPs, as cell viability remains high with minimal cell death following incubation with the AuNPs. Furthermore, cells subjected to PDT after incubation with the C11Pc-PEG-AuNPs are also undamaged, as no cell death is observed. On the other hand, cells subjected to PDT after incubation with the C3Pc-PEG-AuNPs show increasing levels of cell death as the concentration of C3Pc is increased, reaching up to 85 % cell death. These results not only confirmed the MTT assay results, but the assay significantly improved signal and reduced background noise. The staurosporine positive control no longer produces negative cell viability values and the variability (*i.e.*, the error bars) is reduced. As a result, the CellTiter-Blue® assay was found to provide results that were more reliable than the MTT assay. The CellTiter-Blue® assay was repeated five times and the results were reproducible in 4 of the 5 repeats.

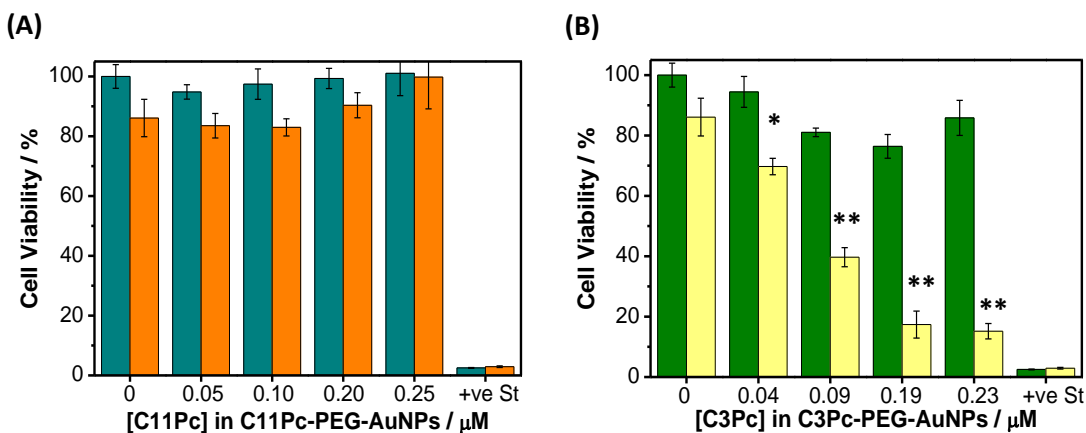


Figure 3.22. CellTiter-Blue® cell viability assay for SK-BR-3 cells incubated with **(A)** C11Pc-PEG-AuNPs or **(B)** C3Pc-PEG-AuNPs. Cells were either irradiated with a 633 nm HeNe laser (**A** orange, **B** yellow) or non-irradiated (**A** dark cyan, **B** green). Staurosporine (+ve St) was used as a positive control for cytotoxicity. Error bars represent the SD ($n = 3$) within a 95 % confidence interval. Statistically significant difference between C11Pc-PEG-AuNPs and C3Pc-PEG-AuNPs is indicated by * at $P < 0.008$ and ** at $P < 0.0001$, obtained using a two-tailed Student's *t*-test, where $P < 0.05$ is considered statistically significant.

These results shown in **Figure 3.22** indicate that at the same concentrations, the C3Pc conjugated nanoparticles are more effective at producing cytotoxicity following light irradiation, as confirmed by the *P* values that show statistical significance between C11Pc-PEG-AuNPs and C3Pc-PEG-AuNPs. There are two possible explanations for this observation. The first is related to the higher fluorescence quenching of C11Pc than that of C3Pc on the surface of the AuNPs, as shown in **section 3.2.3**. The cell viability results suggest that there is an enhanced production of ${}^1\text{O}_2$ by the C3Pc-PEG-AuNPs, which leads to a more efficient PDT effect. However, this possibility could not be confirmed since the measurement of ${}^1\text{O}_2$ quantum yields, as shown in **section 3.2.5**, were inconclusive. A second explanation for these results could be that the C3Pc-PEG-AuNPs are better internalised by the SK-BR-3 cells than the C11Pc-PEG-AuNPs. Such increased uptake would lead to a higher concentration of the C3Pc-PEG-AuNPs inside the cells with a consequent greater photodynamic effect. To assess the internalisation of both C11Pc-PEG-AuNPs and C3Pc-PEG-AuNPs, confocal microscopy was used, as described in the following section.

3.2.7. Study of the internalisation of the AuNPs by the SK-BR-3 cells

To confirm that the enhanced cell death following PDT seen for the C3Pc-PEG-AuNPs is indeed due to a higher production of ${}^1\text{O}_2$, the internalisation of the AuNPs by the SK-BR-3 cells was studied. Internalisation studies were performed *via* confocal laser scanning microscopy, as explained in **section 2.2.11**, using a concentration of 0.23 μM Pc. Additionally, the cell death was also visualised using propidium iodide. Propidium iodide is a dead cell marker that intercalates with the DNA in the nucleus once the cell membrane is broken, therefore it can only stain dead cells.¹⁰¹ **Figure 3.23** shows the results of SK-BR-3 control cells incubated with McCoy's 5A FBS-free medium (**Figure 3.23 A-B**) and SK-BR-3 cells incubated with either C11Pc-PEG-AuNPs (**Figure 3.23 C-D**) or C3Pc-PEG-AuNPs (**Figure 3.23 E-F**) both before and after irradiation with a 633 nm HeNe laser.

The internalisation of C11Pc-PEG-AuNPs (**Figure 3.23 C**) and C3Pc-PEG-AuNPs (**Figure 3.23 E**) at 0.23 μM appear to be similar. Both types of AuNPs are efficiently internalised by the cells, as shown by the red fluorescence seen from within the cells and not in the extracellular space. Additionally, following light irradiation, the SK-BR-3 cells treated with the C11Pc-PEG-AuNPs (**Figure 3.23 D**) are mostly viable, as shown by the minimal staining with propidium iodide. On the contrary, the SK-BR-3 cells treated with the C3Pc-PEG-AuNPs and irradiated with 633 nm light (**Figure 3.23 F**) show high levels of cell death as most cells within the samples are stained with propidium iodide, and the cell membranes appear to be disintegrated. This result is a further indication that the C3Pc-PEG-AuNPs are producing more ${}^1\text{O}_2$ than the C11Pc-PEG-AuNPs. This is because the C11Pc-PEG-AuNPs, which are shown to be efficiently internalised by the SK-BR-3 cells, do not lead to any cell death, as shown by the assay results in **Figure 3.22**. The most likely explanation for this is that the production of ${}^1\text{O}_2$ by the C11Pc-PEG-AuNPs is not sufficient to induce cytotoxicity. On the other hand, the C3Pc-PEG-AuNPs are inducing up to 85 % cell death at this same concentration. Control cells not incubated with any AuNPs appear undamaged and are not stained with propidium iodide either before (**Figure 3.23 A**) or after (**Figure 3.23 B**) light irradiation, showing that the 633 nm HeNe laser light does not induce toxicity to the SK-BR-3 cells.

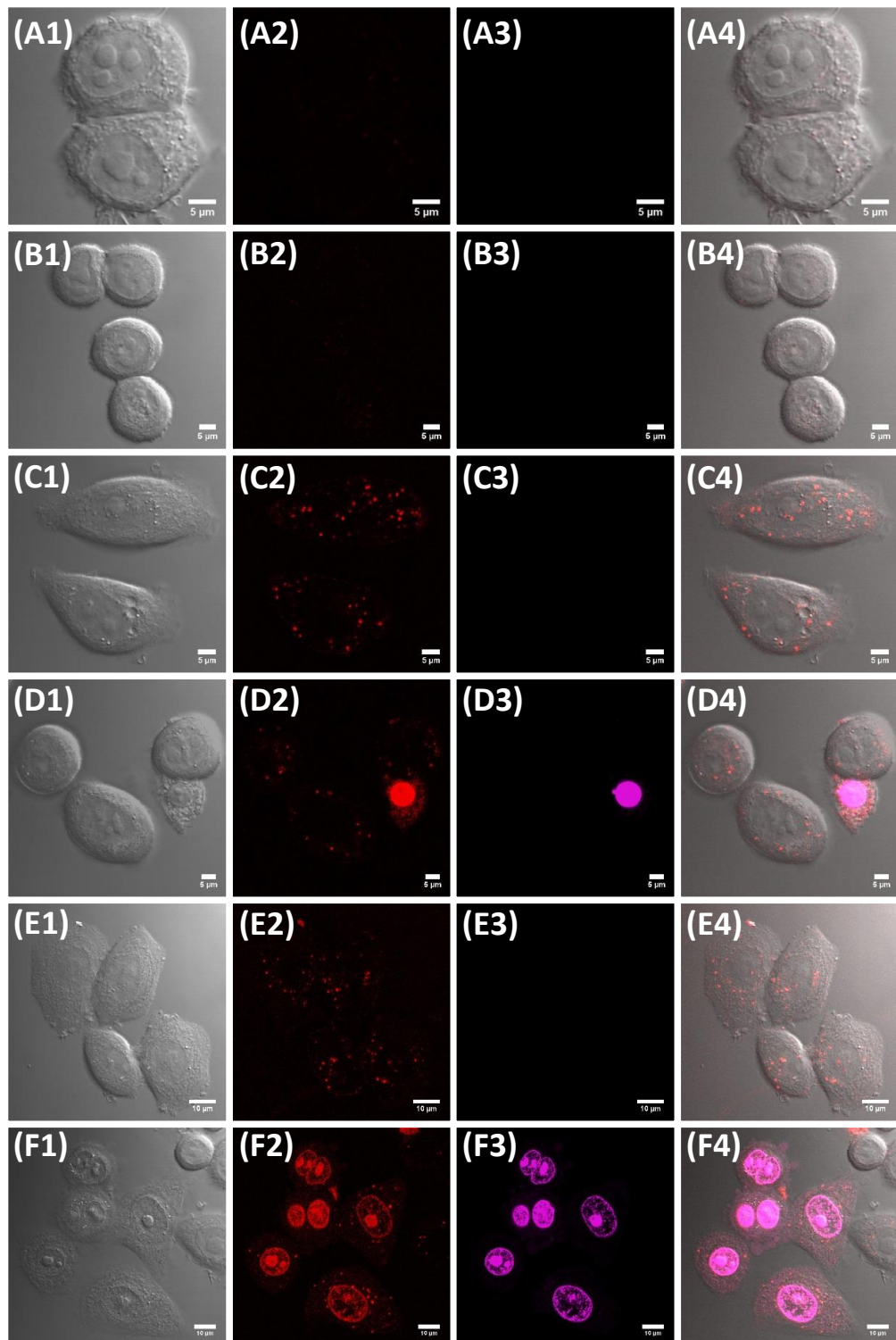


Figure 3.23. Confocal fluorescence microscopy images of SK-BR-3 cells control samples (**A-B**), incubated with C11Pc-PEG-AuNPs (**C-D**) or C3Pc-PEG-AuNPs (**E-F**) (0.23 μ M Pc). The samples were either non-irradiated (**A, C, E**) or irradiated (**B, D, F**) with a 633 nm HeNe laser. Images taken from **1**) DIC, **2**) fluorescence from C11Pc or C3Pc collected in the red channel ($\lambda_{ex} = 633$ nm; above 650 nm), **3**) fluorescence from propidium iodide collected in the pink channel ($\lambda_{ex} = 543$ nm; 560-615 nm) and **4**) composite images of DIC, red channel and pink channel. Scale bars (**A-D**) 5 μ m and (**E, F**) 10 μ m.

The C11Pc-PEG-AuNPs were incubated with SK-BR-3 cells at higher concentrations to determine whether an elevated concentration could induce phototoxicity, as shown in **Figure 3.24**. At a concentration of 1.2 μ M C11Pc, dead cells were found over the coverslip following irradiation, which was confirmed by the staining with propidium iodide (**Figure 3.24 D**). C11Pc-PEG-AuNPs can also induce cell cytotoxicity, however it seems that a higher concentration is required as compared to the C3Pc-PEG-AuNPs. The healthy appearance of control cells before and after irradiation (**Figure 3.24 A-B**) and cells treated with C11Pc-PEG-AuNPs but non-irradiated (**Figure 3.24 C**), together with the absence of propidium iodide staining, shows that the laser does not induce toxicity and the C11Pc-PEG-AuNPs do not induce dark toxicity at high concentrations.

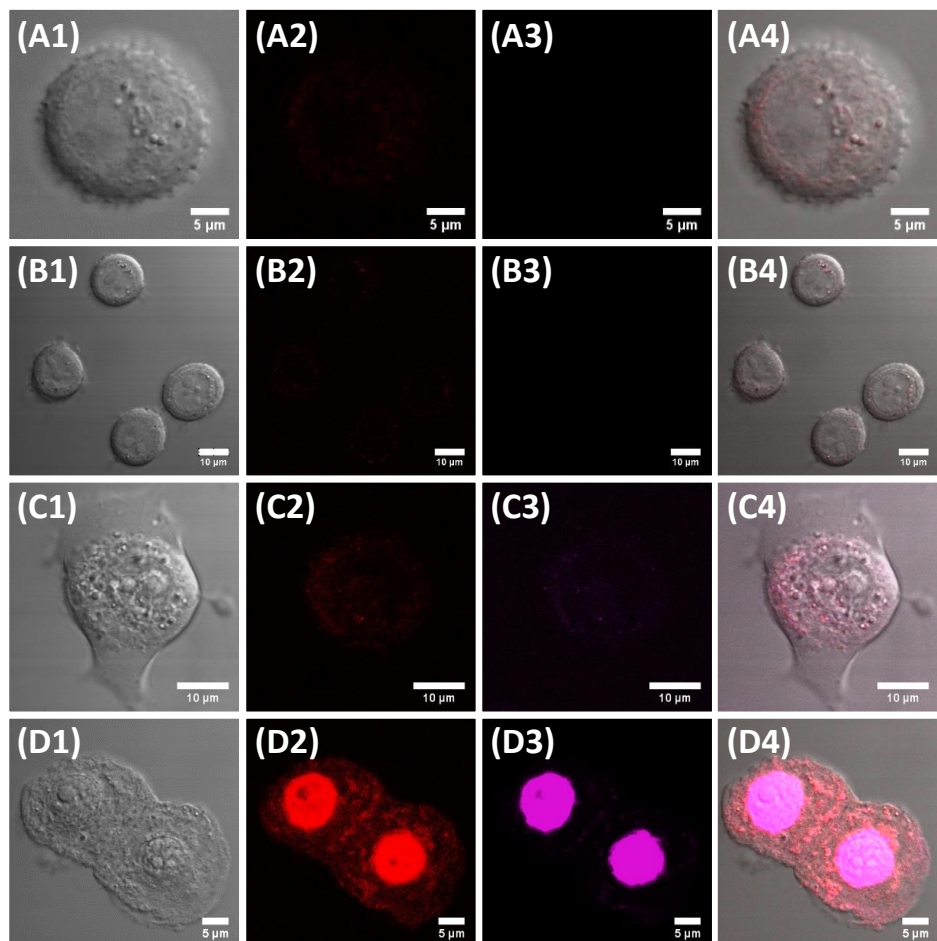


Figure 3.24. Confocal fluorescence microscopy images of SK-BR-3 cells control samples (**A-B**) or incubated with 1.2 μ M C11Pc-PEG-AuNPs (**C-D**). The samples were either non-irradiated (**A, C**) or irradiated (**B, D**) with a 633 nm HeNe laser. Images taken from **1**) DIC, **2**) fluorescence from C11Pc collected in the red channel ($\lambda_{\text{ex}} = 633$ nm; above 650 nm), **3**) fluorescence from propidium iodide collected in the pink channel ($\lambda_{\text{ex}} = 543$ nm; 560-615 nm) and **4**) composite images of DIC, red channel and pink channel. Scale bars (**A, D**) 5 μ m and (**B, C**) 10 μ m.

3.2.8. Functionalisation of the Pc-PEG-AuNPs with anti-HER2 antibody

The large surface area of the gold nanoparticles allows for their functionalisation with multiple ligands. As a result, gold nanoparticles can be functionalised with biological ligands in order to target specific types of cancer. As explained in **section 3.1.2**, between 10-34 % of breast cancers are HER2 positive.⁶⁰ HER2 positive breast cancers, including SK-BR-3 cells, overexpress the HER2 receptor on their surface, which makes them highly invasive and metastatic cancers.^{62,63,65} Anti-HER2 antibody (anti-HER2-Ab) has been previously used to target the HER2 receptor in breast cancer cells for increased PDT efficacy.^{77,78}

Both C11Pc-PEG-AuNPs and C3Pc-PEG-AuNPs were functionalised with anti-HER2-Ab *via* the PEG ligand. The terminal carboxyl group of the PEG ligand was conjugated to the amine groups on the antibody *via* amide coupling. The amide coupling was performed using EDC/NHS.⁷⁷ EDC and NHS react with the carboxyl group at the terminus of the PEG, forming an N-hydroxysuccinimidyl ester at the end of the PEG ligand. This ester then reacts with the amine groups of the antibody, creating the amide coupling that links the antibody to the PEG and thus to the surface of the AuNPs. The reaction scheme is shown in **Figure 3.25**.¹⁰²

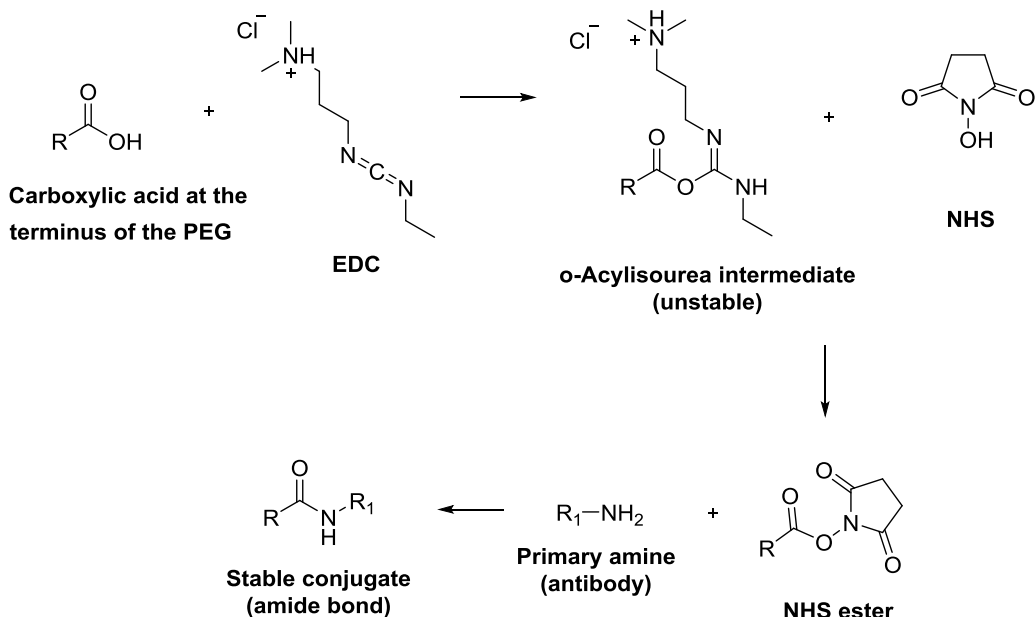


Figure 3.25. Reaction between the terminal carboxyl group in PEG, EDC, NHS and the primary amine of an antibody to give the final amide bond that links the PEG and the antibody.

Anti-HER2-Ab was conjugated to both C11Pc-PEG-AuNPs and C3Pc-PEG-AuNPs. Following the conjugation reaction, the AuNP conjugates were washed until no excess unbound antibody was present. This was confirmed *via* UV-vis spectroscopy, by monitoring the decrease of unbound antibody absorbance intensity between 200-500 nm in each of the washing steps (**Figure 3.26 A-B**). The purified anti-HER2-Ab functionalised AuNPs were then resuspended in serum-free McCoy's 5A phenol red-free medium and the UV-vis extinction spectra were recorded (**Figure 3.26 C**).

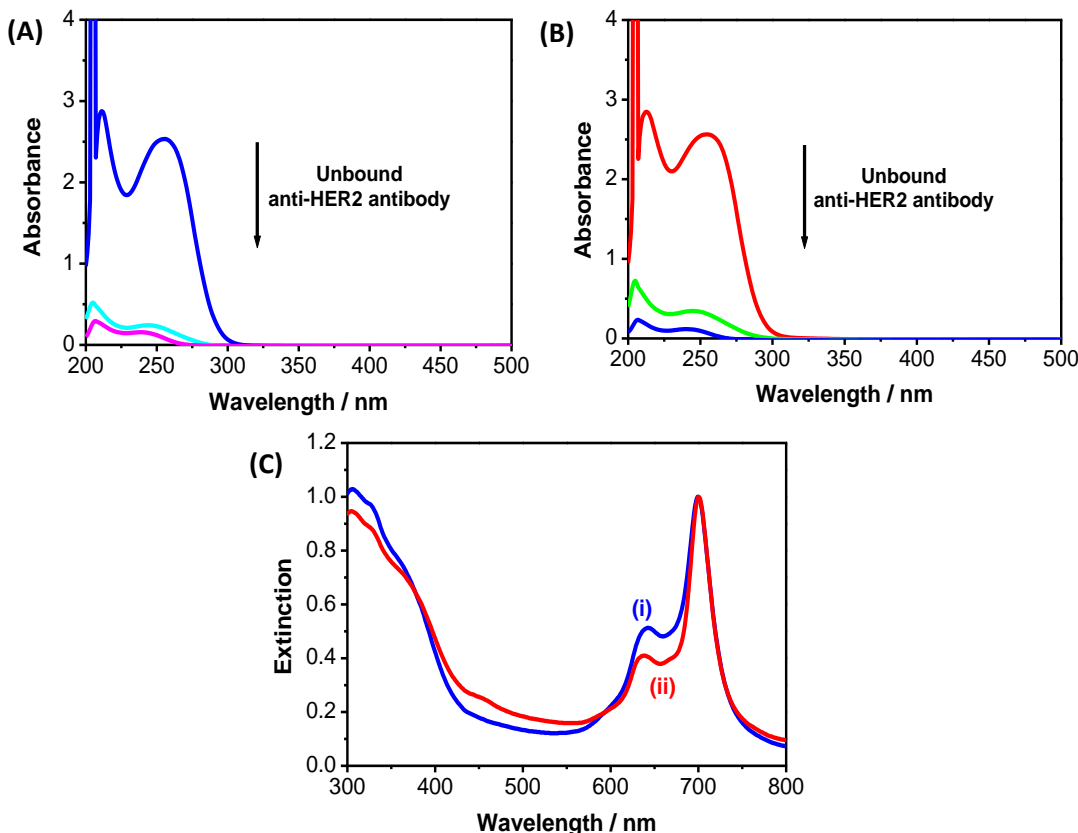


Figure 3.26. Decrease in absorbance intensity of the unbound antibody in the washes of (A) C11Pc-PEG-AuNPs and (B) C3Pc-PEG-AuNPs. (C) Extinction spectra of anti-HER2-Ab functionalised C11Pc-PEG-AuNPs (i) and anti-HER2-Ab functionalised C3Pc-PEG-AuNPs (ii).

The number of antibodies immobilised per AuNP can be estimated. In **section 3.2.2**, an estimation of the ratio of Pc to AuNPs was calculated and it was found that C11Pc-PEG-AuNPs contain *ca.* 115 C11Pc per AuNPs while C3Pc-PEG-AuNPs contain *ca.* 99 C3Pc per AuNPs. Considering the number of Pc per AuNPs and the concentration of the solutions of the C11Pc-PEG-AuNPs and C3Pc-PEG-AuNPs (**Table 3.6**), the concentration of AuNPs

in each solution can be estimated (**Table 3.6**). Then, the ratio of the concentration of anti-HER2 antibody initially used to the concentration of AuNPs in the sample can be calculated (**Table 3.6**), following the method reported by Obaid *et al.*⁷⁸ The calculations estimate that a maximum of *ca.* 3 and *ca.* 2 anti-HER2 antibodies are immobilised on the C11Pc-PEG-AuNPs and C3Pc-PEG-AuNPs, respectively.

Table 3.6. Ratio of anti-HER2 antibody to AuNPs.

Sample	[Pc] / nM	Ratio Pc per AuNP	[AuNPs] / nM	[Antibody] / nM	Ratio
C11Pc-PEG-AuNPs	2.40×10^3	115	20.87	65	3.11
C3Pc-PEG-AuNPs	2.68×10^3	99	27.07	65	2.40

3.2.9. Targeted PDT *in vitro*

The anti-HER2-Ab functionalised AuNPs were tested *in vitro* using SK-BR-3 cells, in the same manner as for the non-functionalised AuNPs as reported in **section 3.2.6**. SK-BR-3 cells are HER2 positive and thus it was expected that a higher amount of AuNPs would be internalised, leading to a higher proportion of cell death. MTT assays were initially performed, but the results showed high error bars and some negative values of cell viability for several samples, including the positive control. Therefore, as previously used for the analysis of non-functionalised AuNPs, CellTiter-Blue® assay was performed to minimise error and increase accuracy of the cell viability assay. The results of the CellTiter-Blue® assay are shown in **Figure 3.27**.

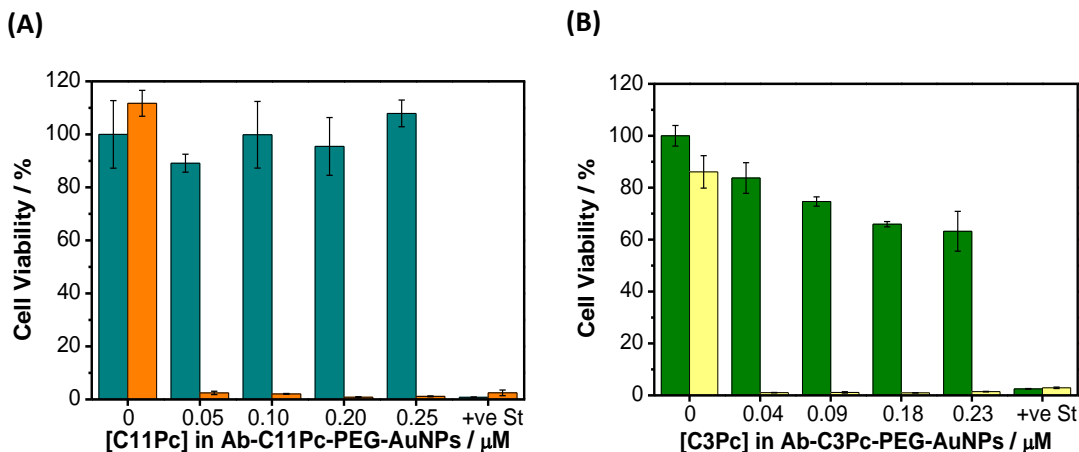


Figure 3.27. CellTiter-Blue® cell viability assay for SK-BR-3 cells incubated with **(A)** anti-HER2-Ab-C11Pc-PEG-AuNPs or **(B)** anti-HER2-Ab-C3Pc-PEG-AuNPs. Cells were either irradiated with a 633 nm HeNe laser (**A** orange, **B** yellow) or non-irradiated (**A** dark cyan, **B** green). Staurosporine (+ve St) was used as a positive control for cytotoxicity. Error bars represent the SD ($n = 3$) within a 95 % confidence interval.

Following irradiation with a 633 nm HeNe laser, cells treated with either anti-HER2-Ab-C11Pc-PEG-AuNPs (**Figure 3.27 A**) or anti-HER2-Ab-C3Pc-PEG-AuNPs (**Figure 3.27 B**) show a high degree of cell death, a significant improvement of cell phototoxicity from the results seen with the non-functionalised AuNPs (**Figure 3.22, section 3.2.6**). Additionally, the levels of cell death are similar for anti-HER2-Ab-C11Pc-PEG-AuNPs and anti-HER2-Ab-C3Pc-PEG-AuNPs, both showing cytotoxicity in up to 99 % of the treated cells. These results indicate that anti-HER2-Ab is effectively targeting the HER2 receptor on the surface of the SK-BR-3 cells. As a result, cytotoxicity following PDT treatment is increased from 0 % with 0.25 μM C11Pc-PEG-AuNPs (**Figure 3.22 A**) to 99 % with 0.25 μM anti-HER2-Ab-C11Pc-PEG-AuNPs (**Figure 3.27 A**); and from 85 % with 0.23 μM C3Pc-PEG-AuNPs (**Figure 3.22 B**) to 99 % with 0.23 μM anti-HER2-Ab-C3Pc-PEG-AuNPs (**Figure 3.27 B**).

On the other hand, the cells incubated with the anti-HER2-Ab functionalised AuNPs, but not subjected to PDT treatment (*i.e.*, not irradiated with light), show different results for the C11Pc and the C3Pc photosensitisers. Dark toxicity in the cells treated with anti-HER2-Ab-C11Pc-PEG-AuNPs (**Figure 3.27 A**) is negligible. However, cells treated with anti-HER2-Ab-C3Pc-PEG-AuNPs (**Figure 3.27 B**) show increasing levels of dark toxicity with increasing concentration of C3Pc. In **section 3.2.2**, an estimation of

the ratio of Pc to AuNPs was performed. It was estimated that there would be *ca.* 115 C11Pc per AuNP and *ca.* 99 C3Pc per AuNP. As a result, at the same concentration of phthalocyanine, the C3Pc-PEG-AuNPs sample contains more AuNPs than the C11Pc-PEG-AuNPs sample. The higher amount of gold nanoparticles internalised by the SK-BR-3 cells could lead to the increase in dark toxicity seen in **Figure 3.27 B**. These results suggest that, even though both nanoparticle systems induce the same levels of cytotoxicity (*ca.* 99 %), anti-HER2-Ab-C11Pc-PEG-AuNPs should be used in preference since they do not induce any dark toxicity.

The results indicate that the anti-HER2-Ab functionalised AuNPs are internalised by SK-BR-3 cells more readily and in increased amounts than the non-functionalised AuNPs. In order to confirm that this increased uptake is due to the specific interaction between anti-HER2-Ab and the HER2 receptor overexpressed on the surface of SK-BR-3 cells, an InCell ELISA was performed. InCell ELISA is a type of indirect ELISA used to assess protein levels on the surface of cells. During an InCell ELISA, the cells are immobilised on 96-well microplates. An antibody, selective to the receptor in question, is then added to the cells. The antibody will bind to the free receptors on the surface of the cells. A secondary antibody bound to HRP is then added, which will bind to all the primary antibodies already immobilised on the surface of the cells. Interaction of HRP with a substrate such as 3,3',5,5'-tetramethylbenzidine (TMB) leads to the development of a coloured solution, with an absorbance intensity at 450 nm proportional to the amount of antibody bound to the cells, and thus to the amount of receptor present on the surface of the cells. In this study, the interest relies on the specific receptor-mediated endocytosis of the anti-HER2-Ab functionalised AuNPs. Therefore, prior to addition of the anti-HER2 primary antibody, the cells were treated with the anti-HER2-Ab functionalised AuNPs for 3 h. This treatment leads to the targeting of HER2 receptors on the surface of the cells, which will no longer be available for the primary antibody during the ELISA. As a result, the cells treated with the anti-HER2-Ab functionalised AuNPs should produce a lower signal at 450 nm as compared to untreated cells or cells treated with non-functionalised AuNPs, in which all the HER2 receptor sites on the surface of the cells are free. The values obtained can be normalised to cell number in each sample by using the whole-cell stain Janus Green.

Janus Green stains whole cells and gives an absorbance value at 615 nm, which is proportional to the number of cells in the sample. The results are shown in **Figure 3.28**.

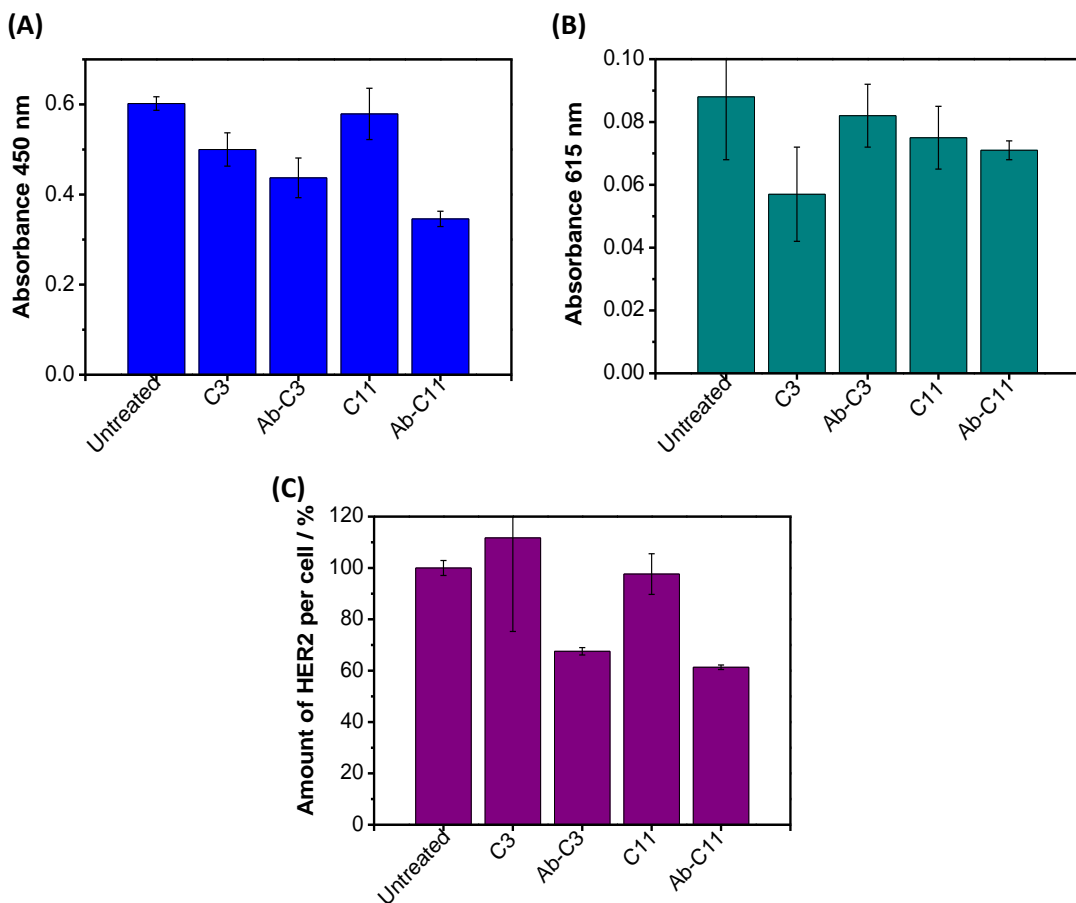


Figure 3.28. InCell ELISA for the detection of the HER2 receptor on the surface of SK-BR-3 cells. **(A)** Absorbance at 450 nm representing the amount of HER2 receptor present in each sample. **(B)** Absorbance at 615 nm representing the number of cells per sample. **(C)** Normalised value of HER2 receptor per cell number in each sample. Untreated refers to cells only treated with McCoy's 5A medium; C3 and C11 refer to cells treated with C3-PEG-AuNPs and C11Pc-PEG-AuNPs, respectively; Ab-C3 and Ab-C11 refer to cells treated with anti-HER2-Ab-C3Pc-PEG-AuNPs and anti-HER2-Ab-C11Pc-PEG-AuNPs, respectively. Error bars represent the SD ($n = 3$) within a 95 % confidence interval.

Figure 3.28 shows the change in HER2 protein expression when the cells are treated with the anti-HER2-Ab functionalised AuNPs relative to untreated cells. For those samples treated with anti-HER2-Ab-C3Pc-PEG-AuNPs there is a 32 % reduction in HER2 expression (**Figure 3.28 C**). For samples treated with anti-HER2-Ab-C11Pc-PEG-AuNPs there is a 38 % reduction in HER2 expression (**Figure 3.28 C**). These results suggest that the anti-HER2-Ab functionalised AuNPs are binding to some of the HER2 receptor sites

on the cell surface. On the other hand, the change in samples treated with either of the non-functionalised nanoparticles, C3Pc-PEG-AuNPs or C11Pc-PEG-AuNPs, is negligible (**Figure 3.28 C**). These results suggest that the anti-HER2-Ab functionalised AuNPs are internalised by the cells *via* receptor-mediated endocytosis, which leads to a higher nanoparticle uptake and thus more efficient photodamage.

3.2.10. Confocal microscopy study of targeted PDT

The uptake and PDT effect of the nanoparticles in SK-BR-3 cells was studied using confocal microscopy to evaluate the difference in internalisation before and after functionalisation of the AuNPs with anti-HER2 antibody. The phthalocyanines were used at a concentration of 0.15 μ M since at this concentration the cell death for targeted PDT was high in both systems with minimal dark toxicity, either containing C11Pc or C3Pc (see **Figure 3.27**). The cells were treated with the anti-HER2-Ab functionalised and non-functionalised AuNPs for 3 h and subsequently washed to eliminate all the non-internalised nanoparticles, as described in **section 2.2.11**. Confocal microscopy images were then taken either right after incubation with the AuNPs (0 h) or 19 h after incubation with the AuNPs. During those 19 h, the cells were kept in an incubator at 37 °C under a 5 % CO₂ atmosphere. As reported in **section 3.2.7**, propidium iodide was used to stain dead cells. The results are shown in **Figure 3.29** for the control samples, **Figure 3.30** for the samples treated with C11Pc-PEG-AuNPs and **Figure 3.31** for the samples treated with C3Pc-PEG-AuNPs.

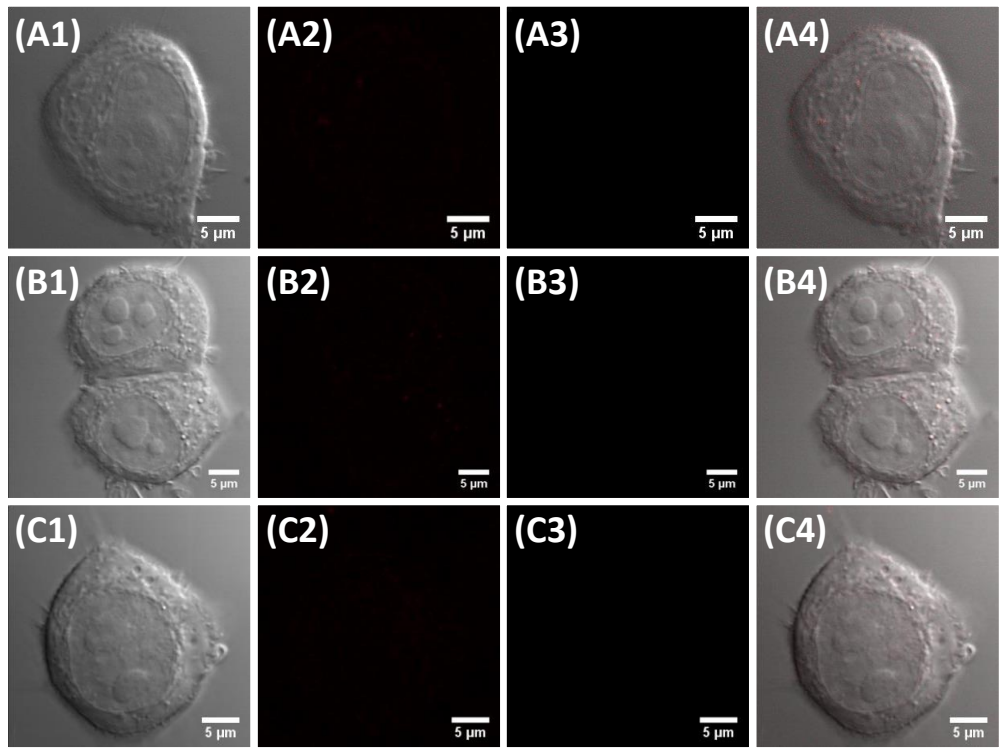


Figure 3.29. Confocal fluorescence microscopy images of SK-BR-3 cells control samples incubated with serum-free McCOY's 5A medium for 3 h. The samples were either non-irradiated and imaged right after incubation with the medium **(A)**, non-irradiated and imaged 19 h following incubation **(B)** or irradiated with a 633 nm HeNe laser 19 h following incubation **(C)**. Images taken from: **1)** DIC, **2)** fluorescence collected in the red channel ($\lambda_{\text{ex}} = 633 \text{ nm}$; above 650 nm), **3)** fluorescence from propidium iodide collected in the pink channel ($\lambda_{\text{ex}} = 543 \text{ nm}$; 560-615 nm) and **4)** composite images of DIC, red channel and pink channel. Scale bars 5 μm .

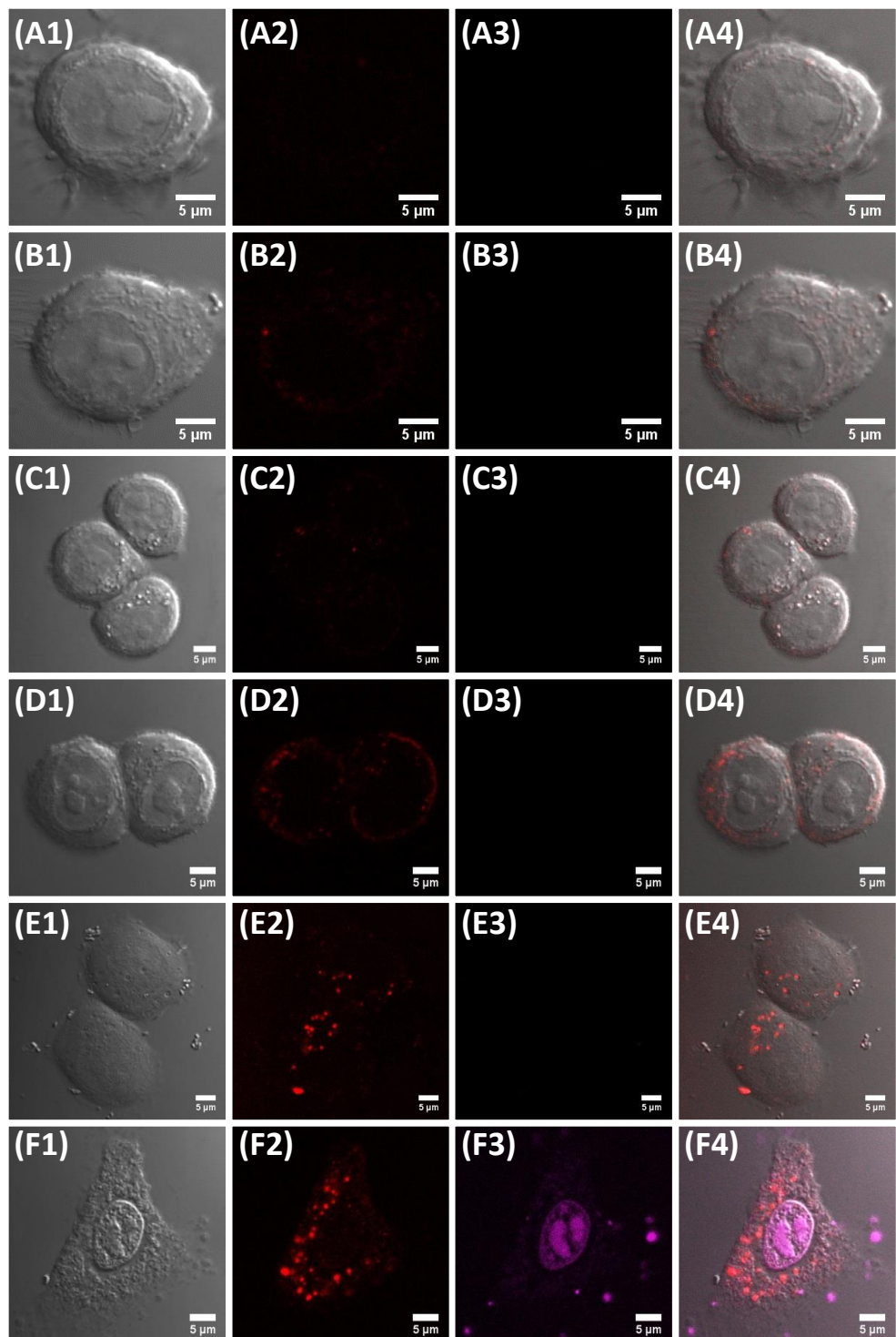


Figure 3.30. Confocal fluorescence microscopy images of SK-BR-3 cells incubated with non-conjugated **(A-C)** or anti-HER2-Ab conjugated **(D-F)** C11Pc-PEG-AuNPs, either non-irradiated and imaged right after incubation with the AuNPs **(A, D)**, non-irradiated and imaged 19 h following incubation **(B, E)** or irradiated with a 633 nm HeNe laser 19 h following incubation **(C, F)**. Images taken from: **1)** DIC, **2)** fluorescence from C11Pc collected in the red channel ($\lambda_{\text{ex}} = 633 \text{ nm}$; above 650 nm), **3)** fluorescence from propidium iodide collected in the pink channel ($\lambda_{\text{ex}} = 543 \text{ nm}$; 560-615 nm) and **4)** composite images of DIC, red channel and pink channel. Scale bars 5 μm .

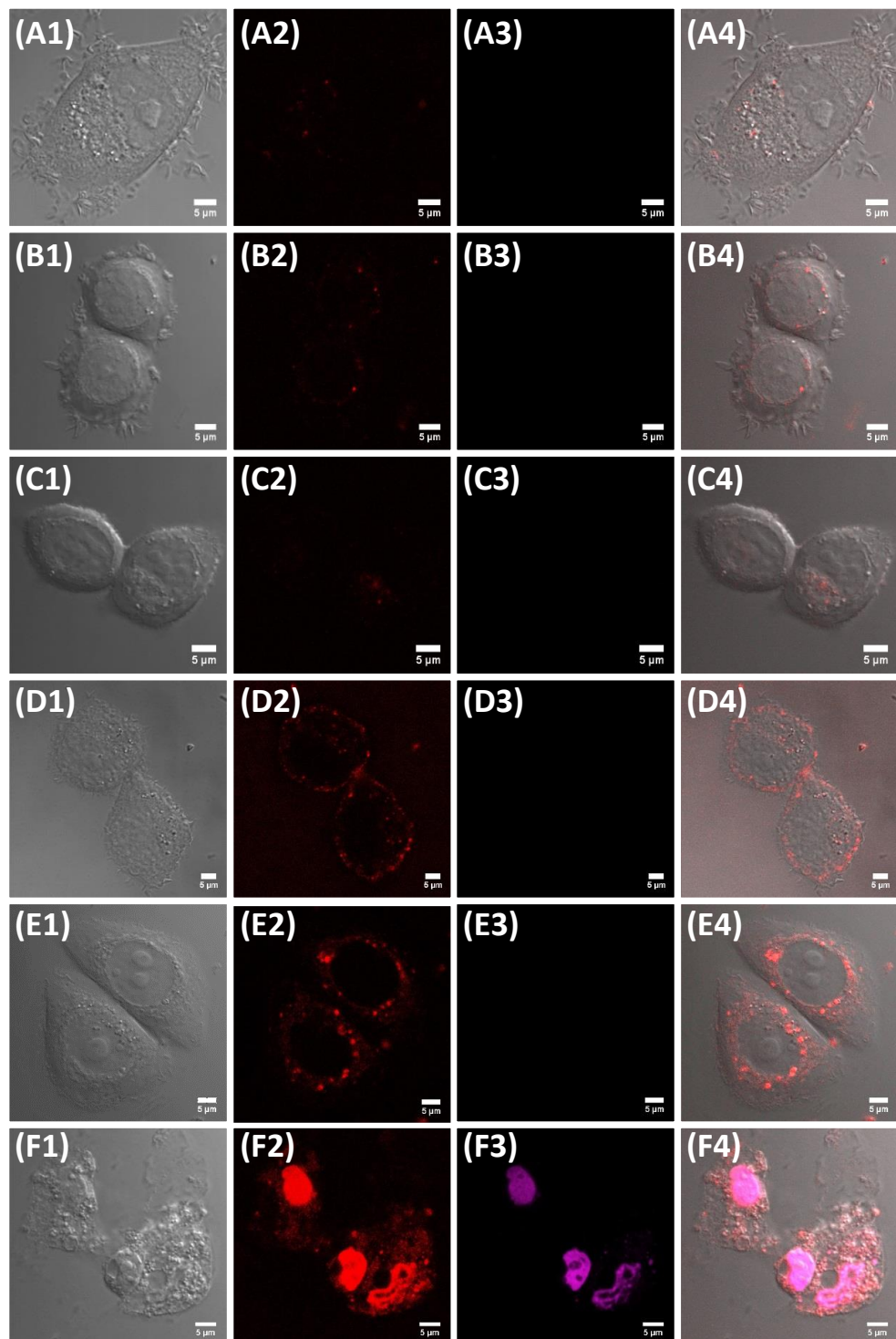


Figure 3.31. Confocal fluorescence microscopy images of SK-BR-3 cells incubated with non-conjugated **(A-C)** or anti-HER2-Ab conjugated **(D-F)** C3Pc-PEG-AuNPs, either non-irradiated and imaged right after incubation with the AuNPs **(A, D)**, non-irradiated and imaged 19 h following incubation **(B, E)** or irradiated with a 633 nm HeNe laser 19 h following incubation **(C, F)**. Images taken from: **1)** DIC, **2)** fluorescence from C3Pc collected in the red channel ($\lambda_{\text{ex}} = 633 \text{ nm}$; above 650 nm), **3)** fluorescence from propidium iodide collected in the pink channel ($\lambda_{\text{ex}} = 543 \text{ nm}$; 560-615 nm) and **4)** composite images of DIC, red channel and pink channel. Scale bars 5 μm .

It can be seen from the images shown above, for both C11Pc (**Figure 3.30**) and C3Pc (**Figure 3.31**), that the functionalisation with anti-HER2 antibody greatly enhances the uptake by SK-BR-3 cells. Additionally, the anti-HER2 antibody functionalised AuNPs are initially located around the cell membrane following a 3 h incubation period (**Figure 3.30 D** and **Figure 3.31 D**). As time progresses (up to 19 h after incubation), the AuNPs appear to be in specific locations within the cells, most likely the acidic organelles (**Figure 3.30 E** and **Figure 3.31 E**). The AuNPs are shown to induce no dark toxicity as non-irradiated samples are not stained with propidium iodide and are thus viable. Furthermore, it can be seen that, at this concentration of 0.15 μ M, C11Pc-PEG-AuNPs only induced cytotoxicity after light irradiation when the antibody is used to target the SK-BR-3 cells, in accordance with the cell viability results shown in **Figures 3.22** and **3.27**. For the 0.15 μ M C3Pc-PEG-AuNPs, targeting the cells with the antibody highly increased the photodynamic efficacy and cell death, as shown in **Figure 3.27**. However, prior to antibody conjugation, the C3Pc-PEG-AuNPs at 0.15 μ M were already able to induce *ca.* 60 % cell death, as shown by the cell viability assays (see **Figure 3.22**). The confocal microscopy images here reported for the SK-BR-3 cells treated with 0.15 μ M C3Pc-PEG-AuNPs following irradiation (**Figure 3.31 C**), show viable cells not stained with propidium iodide. During the confocal microscopy experiments, this coverslip is populated with *ca.* 40 % viable cells and *ca.* 60 % dead cells (see **Figure 3.22**). Therefore, it is easy to find viable cells within the sample. These results further confirmed the cell viability results seen in **sections 3.2.6** and **3.2.9**. Therefore, it can be confirmed that the functionalisation of the AuNPs with anti-HER2 antibody increases the internalisation by the SK-BR-3 cells and thus leads to higher levels of cell death for both the anti-HER2-Ab-C11Pc-PEG-AuNPs and the anti-HER2-Ab-C3Pc-PEG-AuNPs.

3.2.11. Colocalisation studies

The location of the gold nanoparticles functionalised with anti-HER2 antibody within the cells was further studied using confocal microscopy by investigating the colocalisation with the acidic organelle marker LysoSensor™ Green DND-189. LysoSensor™ Green is a fluorescent molecule that marks the acidic organelles inside the cells, namely the lysosomes.¹⁰³ The colocalisation studies were performed using the

anti-HER2-Ab functionalised AuNPs at 0.15 μ M. Following treatment with the anti-HER2-Ab-C11Pc-PEG-AuNPs or the anti-HER2-Ab-C3Pc-PEG-AuNPs for 3 h and removal of the non-internalised AuNPs by washing, the cells were further incubated between 0-19 h before treatment with Lysosensor™ Green and imaging. However, it was not until 19 h after nanoparticle treatment that the nanoparticles were located in the acidic organelles, as shown in **Figure 3.32** by the partial colocalisation between the red fluorescence from the functionalised AuNPs and the green fluorescence from the Lysosensor™ Green. Control cells not incubated with AuNPs (**Figure 3.32 A**) show the green fluorescence from the Lysosensor™ Green, marking the acidic organelles. Cells treated with the anti-HER2-Ab-C11Pc-PEG-AuNPs (**Figure 3.32 B**) and the anti-HER2-Ab-C3Pc-PEG-AuNPs (**Figure 3.32 C**) clearly show that the red fluorescence from the AuNPs (**Figure 3.32 B-C 2**) is in the same locations as the green fluorescence from Lysosensor™ Green (**Figure 3.32 B-C 3**). The colocalisation of the green and red channels suggests that the anti-HER2-Ab functionalised AuNPs are located in the acidic organelles inside the cells, *i.e.*, the lysosomes.

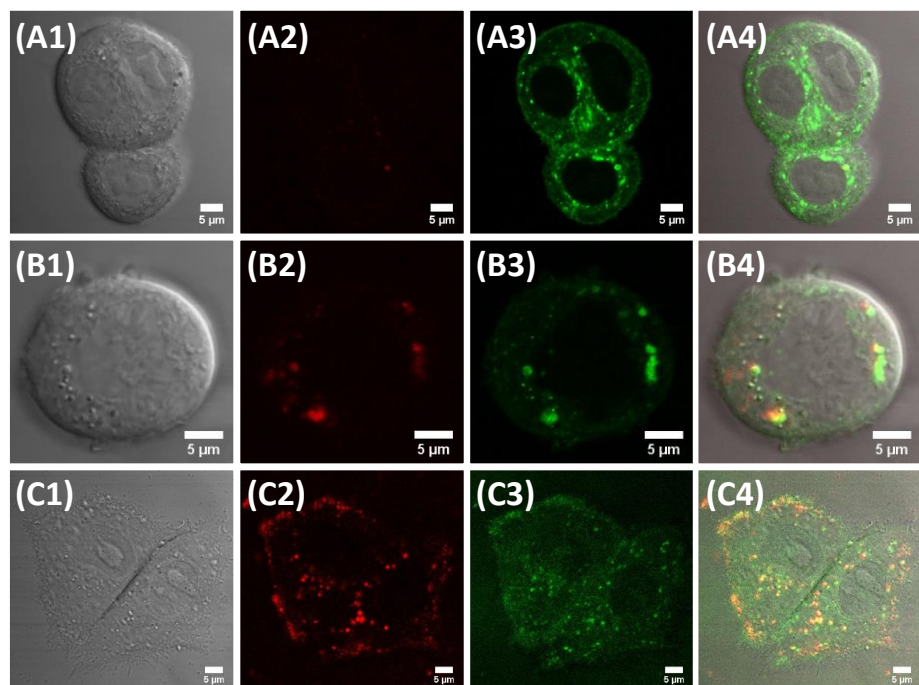


Figure 3.32. Confocal fluorescence microscopy images of SK-BR-3 cells control samples (**A**), incubated with anti-HER2-Ab-C11Pc-PEG-AuNPs (**B**) or anti-HER2-Ab-C3Pc-PEG-AuNPs (**C**). Images were taken 19 h following incubation with the AuNPs. Images taken from **1**) DIC, **2**) fluorescence from C11Pc or C3Pc collected in the red channel ($\lambda_{\text{ex}} = 633$ nm; above 650 nm), **3**) fluorescence from Lysosensor™ Green collected in the green channel ($\lambda_{\text{ex}} = 458$ nm; 475-525 nm) and **4**) composite images from DIC, red and green channels. Scale bars 5 μ m.

3.2.12. Toxicity and PDT effect in non-cancerous mammary epithelial cells

In order to fully compare the photosensitisers C3Pc and C11Pc regarding their PDT efficacy, it was important to test these nanoparticle conjugates using a non-cancerous cell line. The MCF-10A cell line consists of non-cancerous human fibrocystic mammary epithelial cells.¹⁰⁴ Therefore, these cells can be used to assess the effect of the AuNPs on healthy neighbouring cells. The cells were treated with the AuNPs following the procedure developed for the SK-BR-3 cancer cell line. The AuNPs, both non-conjugated and conjugated with anti-HER-Ab, were tested, as shown in **Figure 3.33**.

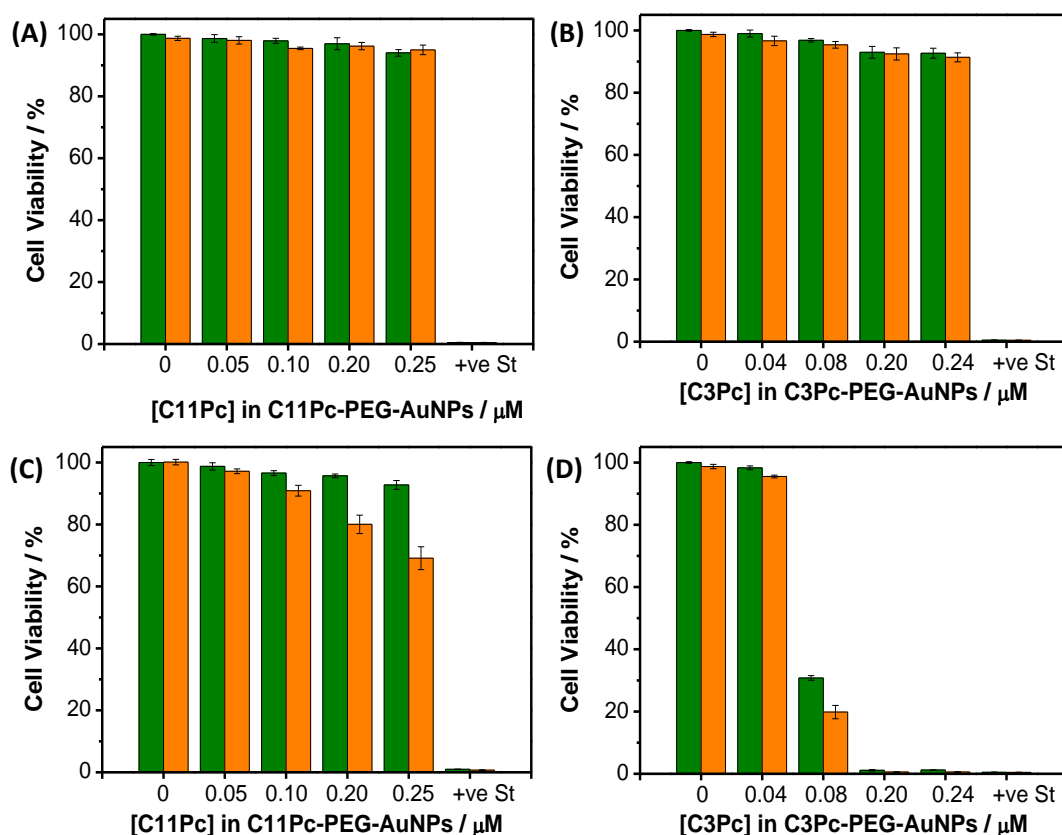


Figure 3.33. CellTiter-Blue® cell viability assay for MCF-10A cells incubated with **(A)** C11Pc-PEG-AuNPs, **(B)** C3Pc-PEG-AuNPs, **(C)** anti-HER2-Ab-C11Pc-PEG-AuNPs and **(D)** anti-HER2-Ab-C3Pc-PEG-AuNPs. Cells were either irradiated with a 633 nm HeNe laser (green) or non-irradiated (orange). Staurosporine (+ve St) was used as a positive control for cytotoxicity. Error bars represent the SD ($n = 3$) within a 95 % confidence interval.

Both the non-conjugated C11Pc-PEG-AuNPs and C3Pc-PEG-AuNPs (**Figure 3.33 A-B**) produce minimal damage to the cells following incubation, even at the highest concentrations. All samples, before and after irradiation at 633 nm, show high levels of cell viability. This suggests the AuNPs are not being internalised by the non-cancerous cells and thus no cell damage is observed. Further studies to investigate the internalisation pathway followed by MCF-10A cells should be performed to understand why MCF-10A cells do not internalise the functionalised AuNPs as readily as the cancerous SK-BR-3 cells. However, when anti-HER2-Ab is conjugated to the AuNPs, the results are significantly different, especially for the anti-HER2-Ab-C3Pc-PEG-AuNPs. The HER2 receptor is expressed in normal healthy cells in lower amounts than cancerous cells, as it is involved in cell growth and differentiation.⁶⁵ As a result, it is expected that at high concentrations, some of the AuNPs will be taken up by the MCF-10A cells *via* receptor-mediated endocytosis facilitated by the presence of the HER2 receptor on the cell surface. This is the case for anti-HER2-Ab-C11Pc-PEG-AuNPs, as seen in **Figure 3.33 C**. When there is no irradiation, the cells show high levels of viability, even at the higher concentrations. However, once the 633 nm light is used to irradiate the samples, the cells die as the concentration is increased. This confirms the hypothesis that the HER2 receptors on the surface of the healthy cells are facilitating the internalisation of the AuNPs. For anti-HER2-Ab-C3Pc-PEG-AuNPs, the cells are killed at concentrations as low as 0.08 μ M, even without light irradiation. The conjugation of anti-HER2-Ab to C3Pc-PEG-AuNPs not only increases the internalisation by the healthy cells, but it also makes the AuNPs toxic for healthy mammary cells even at low C3Pc concentrations. The difference in dark toxicity between anti-HER2-Ab-C11Pc-PEG-AuNPs and anti-HER2-Ab-C3Pc-PEG-AuNPs could be related to the higher amount of AuNPs for the anti-HER2-Ab-C3Pc-PEG-AuNPs at the same concentration as anti-HER2-Ab-C11Pc-PEG-AuNPs, as explained in **section 3.2.9**.

These results, together with the cell viability results reported in **sections 3.2.6** and **3.2.9**, suggest that C3Pc-PEG-AuNPs are superior phototoxic agents than the C11Pc-PEG-AuNPs. Neither of the two types of nanoparticles are toxic for healthy cells. However, C3Pc-PEG-AuNPs induces far more cancerous cell death following PDT than C11Pc-PEG-AuNPs, as shown in **Figure 3.22**. On the other hand, when anti-HER2-Ab is conjugated to the AuNPs, the C11Pc-PEG-AuNPs respond better than the C3Pc-PEG-

AuNPs. This is because while both types of nanoparticles induce high levels of cancerous cell death following PDT (see **Figure 3.27**), the anti-HER2-Ab-C11Pc-PEG-AuNPs do not damage healthy cells, as opposed to the anti-HER2-Ab-C3Pc-PEG-AuNPs, which are toxic even at low concentrations (0.08 μ M C3Pc).

3.2.13. Studies of cell viability 19 h after incubation

As seen in **sections 3.2.10** and **3.2.11**, the AuNPs are initially located around the cell membrane and it is not until 19 h following incubation that they locate in the acidic organelles inside the cells. To study whether the phototoxic effects would have greater efficiency when the AuNPs are located in the lysosomes, a CellTiter-BlueTM cell viability assay was performed in which the cells were irradiated both immediately after incubation with the AuNPs, as previously performed in **sections 3.2.6** and **3.2.9**, and 19 h following incubation with the AuNPs. Following irradiation, the cells were incubated for *ca.* 48 h prior to measuring cell viability. The concentrations of the phthalocyanines were 0.16 μ M for C11Pc and 0.15 μ M for C3Pc.

Figure 3.34 shows the results for the SK-BR-3 cells treated with C11Pc-PEG-AuNPs (**Figure 3.34 A-B**) and C3Pc-PEG-AuNPs (**Figure 3.34 C-D**). When the cells are irradiated immediately after incubation with the nanoparticles (**Figure 3.34 A,C**) the results are similar to those shown in **sections 3.2.6** and **3.2.9**. There is minimal dark toxicity in all samples. Furthermore, the nanoparticles not functionalised with anti-HER2-Ab only induce cell death when they contain C3Pc but not C11Pc, even with the slightly lower concentration of 0.15 μ M vs 0.16 μ M for C3Pc and C11Pc, respectively. When the nanoparticles are functionalised with anti-HER-Ab, cell death reaches 99 % cell death in both cases. On the other hand, when the cells are irradiated 19 h following incubation with the nanoparticles (**Figure 3.34 B,D**) the results are different. No cell death is seen when the nanoparticles are not functionalised with anti-HER-Ab, for either the C3Pc or the C11Pc. Additionally, when the cells are treated with nanoparticles functionalised with anti-HER-Ab, either containing C3Pc or C11Pc, the cell death is considerably less than when irradiation is performed immediately after

nanoparticle incubation. Cell death only reaches up to 60 % for both C3Pc and C11Pc, a considerable difference to the 99 % cell death that was seen previously.

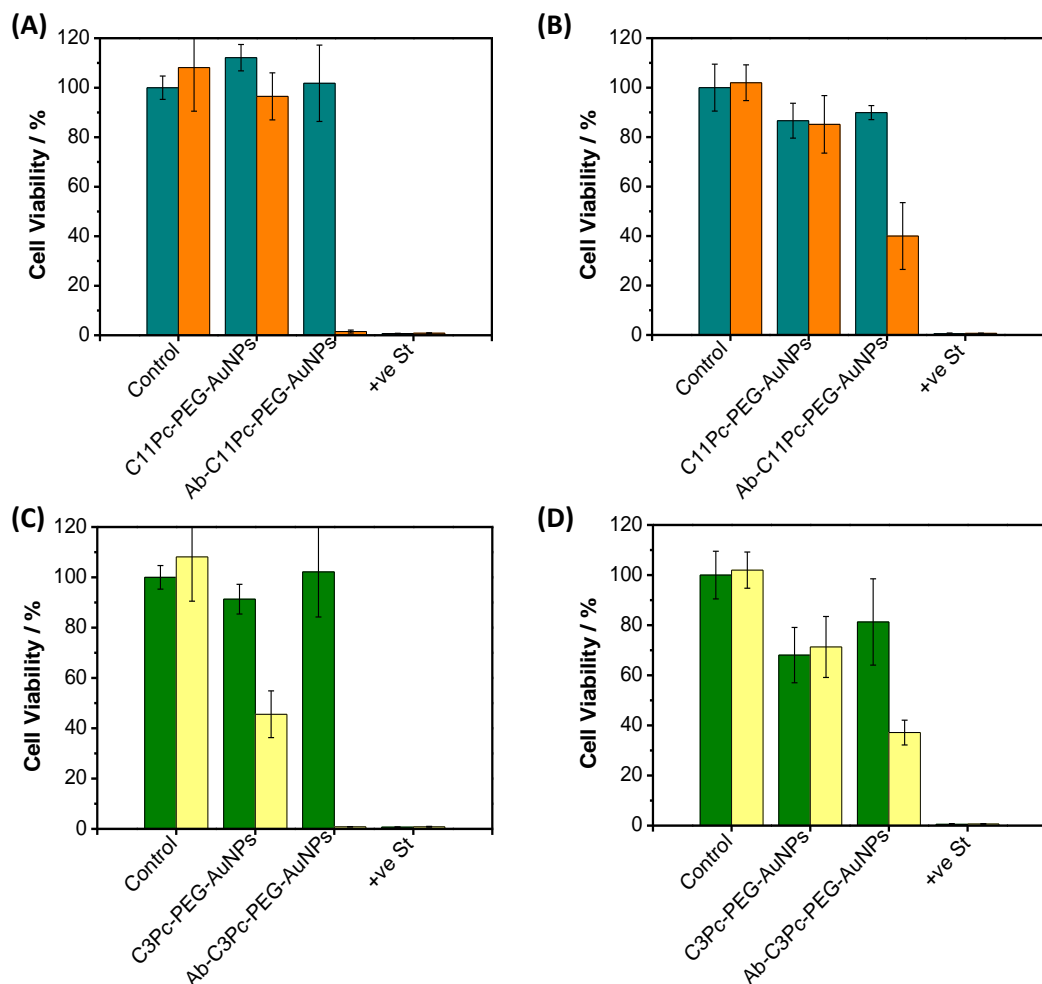


Figure 3.34. CellTiter-Blue® cell viability assay for SK-BR-3 cells incubated with **(A-B)** anti-HER2-Ab functionalised and non-functionalised C11Pc-PEG-AuNPs (0.16 µM C11Pc) or **(C-D)** anti-HER2-Ab functionalised and non-functionalised C3Pc-PEG-AuNPs (0.15 µM C3Pc). Cells were either irradiated with a 633 nm HeNe laser **(A-B)** orange, **(C-D)** yellow) or non-irradiated **(A-B)** dark cyan, **(C-D)** green). Irradiated samples were either irradiated 0 h **(A, C)** or 19 h **(B, D)** following incubation with the AuNPs. Control are samples not incubated with any AuNPs. Staurosporine (+ve St) was used as a positive control for cytotoxicity. Error bars represent the SD (n = 3) within a 95 % confidence interval.

The lower cell death values seen in the *in vitro* experiments when the cells are irradiated 19 h post-incubation could be related to the localisation of the AuNPs inside the cells. As shown in **Figures 3.30-3.32**, the AuNPs are internalised by the cells and are

then encapsulated in the lysosomes, during the 19 h following incubation. The localisation of the AuNPs in the intracellular space enhances the cell destruction as opposed to the localisation inside the lysosomes due to the small radius of action of $^1\text{O}_2$ in the cytoplasm (ca. 10-55 nm).^{105,106} When the AuNPs are located in the lysosomes, the radius of action of $^1\text{O}_2$ allows for the destruction of the lysosomes. Following destruction of the lysosomes, the AuNPs are released into the cytosol, where the production of $^1\text{O}_2$ can lead to the destruction of the whole cell. Therefore, the cell viability of the SK-BR-3 cells treated with the functionalised AuNPs and irradiated 19 h following incubation should be monitored more than 48 h after irradiation, in order to give sufficient time for the AuNPs to be released from the lysosomes and kill the cells. This mechanism has been reported by Berg and co-workers for the destruction of tumour cells *via* photochemical internalisation (PCI).¹⁰⁷⁻¹¹⁰ During PCI, an anti-cancer drug is encapsulated in the lysosomes, which are surrounded by photosensitisers. Activation of the photosensitisers by light irradiation leads to the destruction of the lysosomes and thus the release of the anti-cancer drug into the cytosol, which is then used for cancer therapy.¹⁰⁷⁻¹¹⁰

3.2.14. ApoTox-Glo™ Triplex assay for cell death mechanism

The ApoTox-Glo™ Triplex assay was performed to study the cell death mechanism that the SK-BR-3 cells undergo following PDT with the anti-HER2-Ab conjugated and non-conjugated C11Pc-PEG-AuNPs and C3Pc-PEG-AuNPs. The triplex assay measures three components: cell viability; cell cytotoxicity; and apoptotic response. Cell viability is measured using a cell-permeant peptide substrate, GF-AFC. GF-AFC goes into living cells and is cleaved by a protease activity, creating a fluorescent signal which can be measured at 505 nm following excitation at 400 nm. On the other hand, GF-AFC becomes inactive in the presence of dead cells due to the breakage of the cell membrane, which inactivates the live-cell protease. Cell cytotoxicity is measured using a cell-impermeant peptide substrate, bis-AAF-R110. Bis-AAF-R110 measures the protease activity that has been released into the culture medium by dead cells following breakage of the cell membrane. This reaction produces a fluorescent signal that can be measured at 520 nm following excitation at 485 nm. Bis-AAF-R110 is unable

to recognise healthy cells because their cell membrane is intact. The viability and cytotoxicity component of the assay thus act in a ratiometric manner. When the viability fluorescence values are high, the cytotoxicity fluorescence values should be low and *vice versa*. The apoptotic response of the cells is measured using a substrate for caspase 3/7. Both caspases 3 and 7 become active and promote apoptosis. Therefore, measuring the activity of these caspases is an indication of apoptosis in the sample. The caspase 3/7 substrate contains an aspartate-glutamate-valine-aspartate tetrapeptide sequence, known as DEVD, which is cleaved upon reaction with the active caspases. The final product, aminoluciferin, produces a luminescent signal that is proportional to the amount of caspase activity and thus to the apoptotic response in the sample.¹¹¹

Initially, as explained in **section 2.2.14**, the triplex assay was performed *ca.* 48 h following PDT (results not shown), to mimic the experiments in which cell viability was assessed through MTT and CellTiter-Blue® assays. Staurosporine was used as a positive control for cytotoxicity that follows the apoptotic pathway.⁹⁷ The assay did not show the anticipated results, as they did not agree with the previous assay results. Additionally, the cytotoxicity and apoptosis components produced unexpected results since the positive control did not show high levels of cell cytotoxicity or apoptosis, even though staurosporine is a well-known apoptosis inducer. The unexpected results obtained could be related to the post-PDT incubation period of 48 h. The biomarkers for cytotoxicity and apoptosis are prone to degradation over time. As a result, the cytotoxicity protease activity can be degraded by the time the assay components are added, which would lead to an underestimation of the cytotoxicity levels within the sample. This is also true for drugs that induce cell-cycle arrest (*i.e.*, antiproliferative effects). During the cell-cycle arrest, not only cytotoxicity is underestimated, but also the caspase activation might be underestimated.¹¹² These effects are exacerbated when the drugs induce necrosis, which is a fast-acting cell death pathway. In an attempt to avoid these problems and obtain better results for the triplex assay, the incubation period post-PDT was decreased from 48 h to 4 h. The results for the ApoTox-Glo™ Triplex assay performed 4 h post-PDT are shown in **Figure 3.35 A** for cells treated with C11Pc-PEG-AuNPs and **Figure 3.35 B** for cells treated with C3Pc-PEG-AuNPs. In the viability component (**Figure 3.35 1**), the untreated control cells are viable whereas the

cells treated with the positive control show low levels of viability, as expected. Additionally, the samples treated with the functionalised AuNPs are all shown to induce cell death following PDT. However, the cell death values do not agree with previous results found from the cell viability assays reported in **sections 3.2.6** and **3.2.9**. Furthermore, the dark toxicity for the anti-HER2-Ab-C3Pc-PEG-AuNPs appears to be significantly high, leading to cell death similar to the irradiated sample. This result also disagrees with those previously reported (see **Figure 3.27**).

The cytotoxicity component of the assay (**Figure 3.35 2**) still provides results that are difficult to explain, as shown by the absence of fluorescence in the samples treated with the positive control staurosporine, which is expected to induce the highest values of cytotoxicity. The fact that the cytotoxicity component is producing low fluorescent values for most samples could be an indication that the cells are in a cell-cycle arrest following PDT. The apoptosis component of the assay (**Figure 3.35 3**) shows a significant improvement after reducing the post-PDT incubation time to 4 h, since the positive control has the highest values of luminescence of all samples. The samples treated with the AuNPs show much lower levels of luminescence, especially those treated with the anti-HER2 Ab functionalised AuNPs. The lower luminescence values of the AuNPs-treated cells are a possible indication of cell death occurring *via* a non-apoptotic pathway, such as necrosis. However, a firm conclusion cannot be reached since the results of the assay were difficult to interpret and did not agree with the previous CellTiter-Blue® assay results.

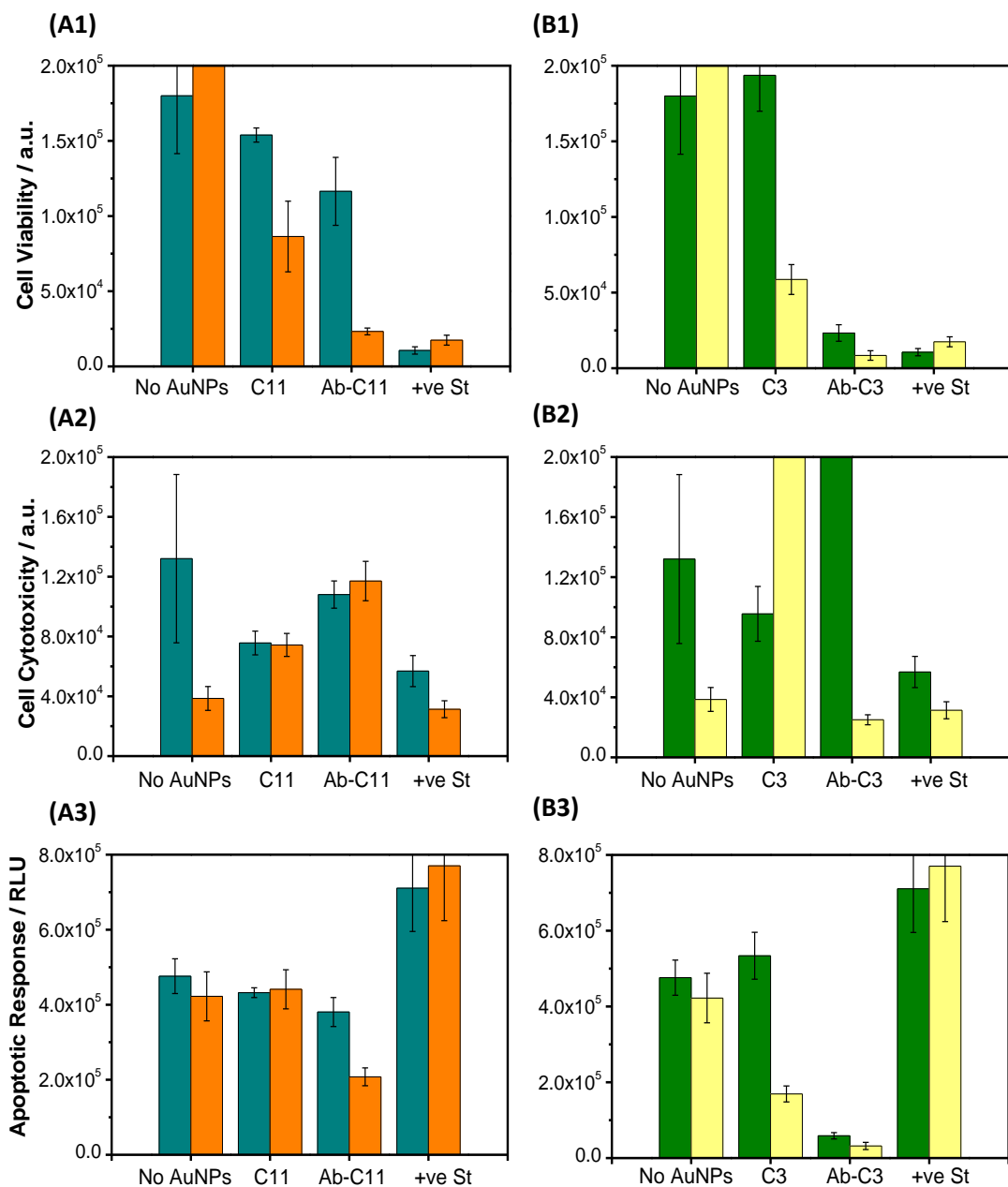


Figure 3.35. ApoTox-Glo™ Triplex assay for SK-BR-3 cells incubated with **(A)** anti-HER2-Ab conjugated and non-conjugated C11Pc-PEG-AuNPs (0.16 μ M C11Pc) or **(B)** anti-HER2-Ab conjugated and non-conjugated C3Pc-PEG-AuNPs (0.16 μ M C3Pc). Cells were either irradiated with a 633 nm HeNe laser (**A** orange, **B** yellow) or non-irradiated (**A** dark cyan, **B** green). The cells were treated with the triplex assay 4 h following PDT. **(1)** Fluorescence from the GF-AFC substrate giving the cell viability values, **(2)** Fluorescence from bis-AAF-R110 substrate giving the cell cytotoxicity values and **(3)** Luminescence from the Caspase 3/7 substrate giving the values for apoptosis. The sample No AuNPs refers to samples not incubated with any AuNP used as the reference negative control. Staurosporine (+ve St) was used as a positive control for cytotoxicity *via* apoptosis. Error bars represent the SD ($n = 3$) within a 95 % confidence interval.

3.3. Conclusions

In this chapter, two zinc phthalocyanines, differing in the length of the carbon chain that connects the macrocycle to the sulfur atom, were compared. C11Pc has a carbon chain consisting of 11 carbon atoms, whereas C3Pc consists of only 3 carbon atoms. Gold nanoparticles were synthesised and functionalised with a mixed monolayer of PEG, to provide aqueous solubility to the system, together with either C11Pc or C3Pc. Gold nanoparticles functionalised with C11Pc-PEG (C11Pc-PEG-AuNPs) had an average size of 3.41 ± 1.16 nm. Gold nanoparticles functionalised with C3Pc-PEG (C3Pc-PEG-AuNPs) had an average size of 3.83 ± 0.99 nm.

The fluorescence of C11Pc-PEG-AuNPs and C3Pc-PEG-AuNPs was analysed and compared to the fluorescence of the free ligands in solution. The fluorescence of the free ligands was found to be more intense for the C11Pc as compared to the C3Pc. On the other hand, when the ligands are on the AuNPs, the fluorescence intensity was greater for the C3Pc-PEG-AuNPs. To confirm this result, the fluorescence quantum yields were estimated and they were found to be 4.8 % for free C11Pc, 2.6 % for free C3Pc, 0.2 % for C11Pc-PEG-AuNPs and 0.42 % for C3Pc-PEG-AuNPs. These results were rationalised by consideration of the interactions between fluorophores and metal nanoparticles. The quenching of the fluorescence of both C11Pc and C3Pc when self-assembled on the surface of the AuNPs, is due to the small size of the nanoparticles, as explained by the RP model.²⁰ The fact that C3Pc-PEG-AuNPs experience less fluorescence quenching than C11Pc-PEG-AuNPs was probably related to the orientation and the distance between the fluorophore and the AuNPs. The enhanced quenching present for the C11Pc could be explained by the orientation of the phthalocyanine molecules in respect to the AuNPs. The orientation of the longer C11 chain is influenced by the important chain-chain intermolecular interactions taking place. As a result, it is possible that the C11 chain will be oriented at an angle more parallel to the gold core, such that the C11Pc molecule lies more horizontal with respect to the AuNPs. By contrast, the chain-chain interactions in the C3Pc will be minimal due to the short nature of the chain. Therefore, it is possible that the C3 chain will be oriented more perpendicular relative to the AuNPs. The relative orientations of the phthalocyanines in respect with the nanoparticles has an effect in their fluorescence

properties. The parallel orientation in which the C11Pc is speculated to be positioned leads to the phthalocyanine's molecular dipole and the dipole of the AuNPs to radiate out of phase, thus decreasing the radiative decay of the fluorophore.¹² The angles at which the chains are positioned influences how close the phthalocyanines will be to the gold core. In the present study, it was speculated that the C11Pc molecule lies closer to the gold core, which could explain the higher quenching effect observed, mainly due to electron transfer between C11Pc and the AuNPs. On the other hand, the C3Pc molecule is speculated to be oriented in a perpendicular orientation, which allows for the enhancement of the radiative decay rate of the fluorophore. Even though the perpendicular orientation of the C3Pc is ideal for MEF, the absence of fluorescence enhancement seen in the present study could be related to the small size of the nanoparticles, which are strong fluorescence quenchers. These results opened the possibility for an increased production of $^1\text{O}_2$ by C3Pc-PEG-AuNPs. Analysis of the production of $^1\text{O}_2$ with ABMA indicated that C3Pc-PEG-AuNPs produced more $^1\text{O}_2$ than the C11Pc-PEG-AuNPs. To confirm these results, the quantum yield of $^1\text{O}_2$ production for both nanoparticle conjugates was analysed. Unfortunately, the AuNPs were dissolved in an aqueous solvent, which leads to the quenching of the $^1\text{O}_2$ signal. Therefore, it was not possible to estimate a value for the $^1\text{O}_2$ quantum yields.

In vitro studies of both C11Pc-PEG-AuNPs and C3Pc-PEG-AuNPs in SK-BR-3 human breast adenocarcinoma cells showed a great difference between the two systems. While C11Pc-PEG-AuNPs do not show any cell death after irradiation with a 633 nm HeNe laser, C3Pc-PEG-AuNPs shows high levels of cell cytotoxicity, which increase with increasing concentration of C3Pc. Additionally, internalisation by the SK-BR-3 cells proved to be similar for C11Pc-PEG-AuNPs and C3Pc-PEG-AuNPs, as shown by confocal microscopy. These results further support the idea that there is an increased production of $^1\text{O}_2$ by the C3Pc-PEG-AuNPs. However, in order to confirm that the internalisation of both nanosystems by the SK-BR-3 cells is the same, a quantification experiments should be performed, such as flow cytometry. *In vitro* studies in MCF-10A human mammary epithelial cells showed no toxicity for neither C11Pc-PEG-AuNPs nor C3Pc-PEG-AuNPs. Therefore, the C3Pc-PEG-AuNPs were shown to be optimal as they induce high cell kill in cancer cells and no damage to healthy cells.

Anti-HER2-Ab was used to target the overexpressed HER2 receptor on the surface of SK-BR-3 cells. Anti-HER2-Ab was conjugated to the terminal end of the PEG in both C11Pc-PEG-AuNPs and C3Pc-PEG-AuNPs *via* EDC-NHS coupling. *In vitro* studies in SK-BR-3 cells showed a marked improvement in the rate of cell death by both AuNPs systems due to the presence of the anti-HER2-Ab. The difference between anti-HER2-Ab-C11Pc-PEG-AuNPs and anti-HER2-Ab-C3Pc-PEG-AuNPs was minimal, as both systems led to similar levels of cell death (99 %) following PDT. Confocal microscopy studies of anti-HER2-Ab functionalised AuNPs to investigate uptake and PDT confirmed the previous results. The anti-HER2-Ab led to higher levels of internalisation as compared to the non-functionalised AuNPs. Additionally, it was found that the anti-HER2-Ab functionalised AuNPs colocalised with the acidic organelles inside the cells 19 h after incubation. Studies in MCF-10A cells showed high levels of cytotoxicity before and after irradiation for anti-HER2-Ab-C3Pc-PEG-AuNPs whereas there was minimal photodamage when anti-HER2-Ab-C11Pc-PEG-AuNPs were used. Therefore, anti-HER2-Ab-C11Pc-PEG-AuNPs were found to be preferred as they induce efficient cell kill in cancer cells while leaving healthy cells unaffected.

The ApoTox-Glo™ Triplex assay was performed to check the cell death pathway followed after PDT. An indication that the cells follow a non-apoptotic cell death pathway, *i.e.*, necrosis, was obtained. However, these results were not conclusive since several components of the assay gave unexpected results and were not in agreement with the other assay results. Further studies to evaluate the cell death mechanism followed by the SK-BR-3 cells after PDT treatment with the C11Pc-PEG-AuNPs and C3Pc-PEG-AuNPs should be performed.

In this chapter, the use of an antibody to target breast cancer cells was found to significantly increase the internalisation and PDT efficacy of the functionalised AuNPs. The use of other types of ligands to target specific receptor overexpressed on the surface of cancer cells has been explored, including the use of carbohydrates, lectins and aptamers, as explained in **Chapter 1**.^{79,113-115} The use of a carbohydrate, lactose, as a potential targeting ligand to improve the PDT efficacy in breast cancer cells will be explored in **Chapter 4**.

3.4. References

- (1) Eustis, S.; El-Sayed, M. A. *Chem. Soc. Rev.* **2006**, *35*, 209.
- (2) Ghosh, S. K.; Pal, T. *Phys. Chem. Chem. Phys.* **2009**, *11*, 3831.
- (3) Anger, P.; Bharadwaj, P.; Novotny, L. *Phys. Rev. Lett.* **2006**, *96*.
- (4) Aslan, K.; Lakowicz, J. R.; Geddes, C. D. *Curr. Opin. Chem. Biol.* **2005**, *9*, 538.
- (5) Swierczewska, M.; Lee, S.; Chen, X. *Phys. Chem. Chem. Phys.* **2011**, *13*, 9929.
- (6) Planas, O.; Macia, N.; Agut, M.; Nonell, S.; Heyne, B. *J. Am. Chem. Soc.* **2016**, *138*, 2762.
- (7) Li, M.; Cushing, S. K.; Wu, N. *Analyst* **2015**, *140*, 386.
- (8) Darvill, D.; Centeno, A.; Xie, F. *Phys. Chem. Chem. Phys.* **2013**, *15*, 15709.
- (9) Kang, K.; Wang, J.; Jasinski, J.; Achilefu, S. *J. Nanobiotechnol.* **2011**, *9*, 16.
- (10) Kotiaho, A.; Lahtinen, R.; Efimov, A.; Metsberg, H.-K.; Sariola, E.; Lehtivuori, H.; Tkachenko, N. V.; Lemmetyinen, H. *J. Phys. Chem. C* **2010**, *114*, 162.
- (11) Aslan, K.; Pérez-Luna, V. H. *J. Fluoresc.* **2004**, *14*, 401.
- (12) Dulkeith, E.; Ringler, M.; Klar, T. A.; Feldmann, J. *Nano Lett.* **2005**, *5*.
- (13) Dulkeith, E.; Morteani, A. C.; Niedereichholz, T.; Klar, T. A.; Feldmann, J.; Levi, S. A.; van Veggel, F. C. J. M.; Reindhoudt, D. N.; Möller, M.; Gittins, D. I. *Phys. Rev. Lett.* **2002**, *89*, 203002.
- (14) Park, S. Y.; Lee, S. M.; Kim, G. B.; Kim, Y. P. *Gold Bull.* **2012**, *45*, 213.
- (15) Mayilo, S.; Kloster, M. A.; Wunderlich, M.; Lutich, A.; Klar, T. A.; Nichtl, A.; Kürzinger, K.; Stefani, F. D.; Feldmann, J. *Nano Lett.* **2009**, *9*, 4558.
- (16) Ipe, B. I.; Thomas, K. G.; Barazzouk, S.; Hotchandani, S.; Kamat, P. V. *J. Phys. Chem. B* **2002**, *106*, 18.
- (17) Aslan, K.; Gryczynski, I.; Malicka, J.; Matveeva, E.; Lakowicz, J. R.; Geddes, C. D. *Curr. Opin. Biotechnol.* **2005**, *16*, 55.
- (18) Geddes, C. D.; Lakowicz, J. R. *J. Fluoresc.* **2002**, *12*, 121.
- (19) Deng, W.; Xie, F.; Baltar, H. T. M. C. M.; Goldys, E. M. *Phys. Chem. Chem. Phys.* **2013**, *15*, 15695.
- (20) Lakowicz, J. R. *Anal. Biochem.* **2005**, *337*, 171.
- (21) Drexhage, K. H.; Kuhn, H.; Schäfer, F. P. *Ber. Bunsen-Ges. Phys. Chem.* **1968**, *72*, 329.
- (22) Thomas, K. G.; Kamat, P. V. *Acc. Chem. Res.* **2003**, *36*, 888.
- (23) Hua, X. M.; Gersten, J. I.; Nitzan, A. *J. Chem. Phys.* **1985**, *83*, 3650.

(24) Garoff, S.; Weitz, D. A.; Alvarez, M. S.; Gersten, J. I. *J. Chem. Phys.* **1984**, *81*, 5189.

(25) Sokolov, K.; Chumanov, G.; Cotton, T. M. *Anal. Chem.* **1998**, *70*, 3898.

(26) Selvan, S. T.; Hayakawa, T.; Nogami, M. *J. Phys. Chem. B* **1999**, *103*, 7064.

(27) Moskovits, M. *Rev. Mod. Phys.* **1985**, *57*, 783.

(28) Metiu, H. *Prog. Surf. Sci.* **1984**, *17*, 153.

(29) Ford, G. W.; Weber, W. H. *Phys. Rep.* **1984**, *113*, 195.

(30) Geddes, C. D. *Phys. Chem. Chem. Phys.* **2013**, *15*, 19537.

(31) Huang, X.; Tian, X.-J.; Yang, W.-I.; Ehrenberg, B.; Chen, J.-Y. *Phys. Chem. Chem. Phys.* **2013**, *15*, 15727.

(32) Karolin, J.; Geddes, C. D. *Phys. Chem. Chem. Phys.* **2013**, *15*, 15740.

(33) Zhang, Y.; Aslan, K.; Previte, M. J. R.; Geddes, C. D. *J. Fluoresc.* **2007**, *17*, 345.

(34) Zhang, Y.; Aslan, K.; Previte, M. J. R.; Malyn, S. N.; Geddes, C. D. *J. Phys. Chem. B* **2006**, *110*, 25108.

(35) Zhang, B.; Aslan, K.; Previte, M. J. R.; Geddes, C. D. *Proc. Natl. Acad. Sci. U.S.A.* **2008**, *105*, 1798.

(36) Zhang, Y.; Dragan, A.; Geddes, C. D. *J. Phys. Chem. C* **2009**, *113*, 12095.

(37) Lakowicz, J. R. *Anal. Biochem.* **2001**, *298*, 1.

(38) Fort, E.; Grésillon, S. *J. Phys. D: Appl. Phys.* **2008**, *41*, 1.

(39) Gryczynski, I.; Malicka, J.; Gryczynski, Z.; Geddes, C. D.; Lakowicz, J. R. *J. Fluoresc.* **2002**, *12*, 11.

(40) Dragan, A. I.; Mali, B.; Geddes, C. D. *Chem. Phys. Lett.* **2013**, *556*, 168.

(41) Dragan, A. I.; Bishop, E. S.; Casas-Finet, J.; Strouse, R. J.; McGivney, J.; Schenerman, M. A.; Geddes, C. D. *Plasmonics* **2012**, *7*, 739.

(42) Zhang, Y.; Mali, B. L.; Geddes, C. D. *Spectrochim. Acta A Mol. Biomol. Spectrosc.* **2012**, *85*, 134.

(43) Aslan, K.; Malyn, S. N.; Geddes, C. D. *J. Fluoresc.* **2007**, *17*, 7.

(44) Zhang, J.; Lakowicz, J. R. *Opt. Express* **2007**, *15*, 2598.

(45) Bardhan, R.; Grady, N. K.; Cole, J. R.; Joshi, A.; Halas, N. J. *ACS Nano* **2009**, *3*, 744.

(46) Huang, X.; El-Sayed, M. A. *J. Adv. Res.* **2010**, *1*, 13.

(47) Teixeira, R.; Paulo, P. M. R.; Viana, A. S.; Costa, S. M. B. *J. Phys. Chem. C* **2011**, *115*, 24674.

(48) Battistini, G.; Cozzi, P. G.; Jalkanen, J.-P.; Montalti, M.; Prodi, L.; Zaccheroni, N.; Zerbetto, F. *ACS Nano* **2007**, *2*, 77.

(49) Mishra, H.; Mali, B. L.; Karolin, J.; Dragan, A. I.; Geddes, C. D. *Phys. Chem. Chem. Phys.* **2013**, *15*, 19538.

(50) Cheng, D.; Xu, Q.-H. *Chem. Commun.* **2007**, 248.

(51) Revell, D. J.; Chambrier, I.; Cook, M. J.; Russell, D. A. *J. Mater. Chem.* **2000**, *10*, 31.

(52) Simpson, T. R. E.; Revell, D. J.; Cook, M. J.; Russell, D. A. *Langmuir* **1997**, *13*, 460.

(53) Ulman, A.; Eilers, J. E.; Tillman, N. *Langmuir* **1989**, *5*, 1147.

(54) Porter, M. D.; Bright, T. B.; Allara, D. L.; Chidsey, C. E. D. *J. Am. Chem. Soc.* **1987**, *109*, 3559.

(55) Nuzzo, R. G.; Dubois, L. H.; Allara, D. L. *J. Am. Chem. Soc.* **1990**, *112*, 558.

(56) Tao, F.; Bernasek, S. L. *Chem. Rev.* **2007**, *107*, 1408.

(57) Thomas, K. G.; Kamat, P. V. *J. Am. Chem. Soc.* **2000**, *122*, 2655.

(58) Bazley, L. A.; Gullick, W. J. *Endocr.-Relat. Cancer* **2005**, *12 Suppl 1*, S17.

(59) Iqbal, N.; Iqbal, N. *Mol. Biol. Int.* **2014**, *2014*, 1.

(60) Ross, J. S.; Fletcher, A. *Stem Cells* **1998**, *16*, 413.

(61) Yu, D.; Hung, M. C. *Oncogene* **2000**, *19*, 6115.

(62) Baselga, J.; Albanell, J. *Ann. Oncol.* **2001**, *12 Suppl 1*, S35.

(63) Brennan, P. J.; Kumogai, T.; Berezov, A.; Murali, R.; Greene, M. I. *Oncogene* **2000**, *19*, 6093.

(64) Seshacharyulu, P.; Ponnusamy, M. P.; Haridas, D.; Jain, M.; Ganti, A. K.; Batra, S. K. *Expert Opin. Ther. Targets* **2012**, *16*, 15.

(65) Rubin, I.; Yarden, Y. *Ann. Oncol.* **2001**, *12 Suppl 1*, S3.

(66) Ross, J. S.; Slodkowska, E. A.; Symmans, W. F.; Pusztal, L.; Ravdin, P. M.; Hortobagyi, G. N. *The Oncologist* **2009**, *14*, 320.

(67) Hatake, K.; Tokudome, N.; Ito, Y. *Breast Cancer* **2007**, *14*, 132.

(68) Pohl, M.; Stricker, I.; Schoeneck, A.; Shulmann, K.; Klein-Scory, S.; Schwartze-Waldholff, I.; Hasmann, M.; Tannapfel, A.; Schmiegel, W.; Reinacher-Schick, A. *J. Cancer Res. Clin. Oncol.* **2009**, *135*, 1377.

(69) Berg, J. M.; Tymoczko, J. L.; Stryer, L. *Biochemistry*; 7th ed.; Freeman and Co.: Basinstoke, 2012.

(70) Steward, M. W. *Antibodies: Their structure and function*; 1st ed.; Chapman and Hall: London, 1984.

(71) Nelson, D. L. *Lehninger principles of biochemistry*; 4th ed.; Freeman and Co.: New York, 2005.

(72) Lydell, E. In *The Immunoassay Handbook*; 4th ed.; Wild, D., John, R., Sheehan, C., Binder, S., He, J., Eds.; Elsevier: Amsterdam, 2013, p 245.

(73) Parija, S. C. *Textbook of Microbiology and Immunology*; 2nd ed.; Elsevier: Manesar, 2012.

(74) Kohler, G.; Milstein, C. *Nature* **1975**, 256, 495.

(75) Brannon-Peppas, L.; Blanchette, J. O. *Adv. Drug Delivery Rev.* **2012**, 64, 206.

(76) Owen, S. C.; Patel, N.; Logie, J.; Pan, G.; Persson, H.; Moffat, J.; Sidhu, S. S.; Shoichet, M. S. *J. Controlled Release* **2013**, 172, 395.

(77) Stuchinskaya, T.; Moreno, M.; Cook, M. J.; Edwards, D. R.; Russell, D. A. *Photochem. Photobiol. Sci.* **2011**, 10, 822.

(78) Obaid, G.; Chambrier, I.; Cook, M. J.; Russell, D. A. *Photochem. Photobiol. Sci.* **2015**, 14, 737.

(79) Obaid, G.; Chambrier, I.; Cook, M. J.; Russell, D. A. *Angew. Chem., Int. Ed.* **2012**, 51, 6158.

(80) Hone, D. C.; Walker, P. I.; Evans-Gowing, R.; FitzGerald, S.; Beeby, A.; Chambrier, I.; Cook, M. J.; Russell, D. A. *Langmuir* **2002**, 18, 2985.

(81) Wieder, M. E.; Hone, D. C.; Cook, M. J.; Handsley, M. M.; Gavrilovic, J.; Russell, D. A. *Photochem. Photobiol. Sci.* **2006**, 5, 727.

(82) Pagano, M.; Gauvreau, K. *Principles of biostatistics*; 2nd ed.; Brooks/Cole: Boston, 2000.

(83) Haiss, W.; Thanh, N. T. K.; Aveyard, J.; Fernig, D. G. *Anal. Chem.* **2007**, 79, 4215.

(84) Staniford, M. C.; Lezhnina, M. M.; Gruener, M.; Stegemann, L.; Kuczus, R.; Bleicher, V.; Strassert, C. A.; Kynast, U. H. *Chem. Commun.* **2015**, 51, 13534.

(85) Sigma-Aldrich.Tetrahydrofuran
<http://www.sigmaaldrich.com/chemistry/solvents/tetrahydrofuran-center.html> [Accessed Nov 13th, 2016].

(86) Sigma-Aldrich.Toluene
<http://www.sigmaaldrich.com/chemistry/solvents/toluene-center.html> [Accessed Nov 13th, 2016].

(87) Curry, A.; Nusz, G.; Chilkoti, A.; Wax, A. *Opt. Express* **2005**, 13, 2668.

(88) Martin, P. C.; Gouterman, M.; Pepich, B. V.; Renzoni, G. E.; Schindele, D. C. *Inorg. Chem.* **1991**, 30, 3305.

(89) Tolbin, A. Y.; Dzuban, A. V.; Shulishov, E. V.; Tomilova, L. G.; Zefirov, N. S. *New J. Chem.* **2016**, 40, 8262.

(90) Tolbin, A. Y.; Pushkarev, V. E.; Balashova, I. O.; Dzuban, A. V.; Tarakanov, P. A.; Trashin, S. A.; Tomilova, L. G.; Zefirov, N. S. *New J. Chem.* **2014**, *38*, 5825.

(91) Kameyama, K.; Morisue, M.; Satake, A.; Kobuke, Y. *Angew. Chem., Int. Ed.* **2005**, *44*, 4763.

(92) van Leeuwen, M.; Beeby, A.; Fernandes, I.; Ashworth, S. H. *Photochem. Photobiol. Sci.* **2014**.

(93) Koerner, Megan M.; Palacio, Luis A.; Wright, Johnnie W.; Schweitzer, Kelly S.; Ray, Bruce D.; Petrache, Horia I. *Biophys. J.* **2011**, *101*, 362.

(94) Wang, M.; Huang, L.; Sharma, S. K.; Jeon, S.; Thota, S.; Sperandio, F. F.; Nayka, S.; Chang, J.; Hamblin, M. R.; Chiang, L. Y. *J. Med. Chem.* **2012**, *55*, 4274.

(95) Penon, O.; Marín, M. J.; Amabilino, D. B.; Russell, D. A.; Pérez-García, L. *J. Colloid Interface Sci.* **2016**, *462*, 154.

(96) Stockert, J. C.; Blázquez-Castro, A.; Cañete, M.; Horobin, R. W.; Villanueva, Á. *Acta Histochem.* **2012**, *114*, 785.

(97) Antonsson, A.; Persson, J. L. *Anticancer Res.* **2009**, *29*, 2893.

(98) Belmokhtar, C. A.; Hillion, J.; Seagal-Bendirdjian, E. *Oncogene* **2001**, *20*, 3354.

(99) Gabrielson, N. P.; Pack, D. W. *Biomacromolecules* **2006**, *7*, 2427.

(100) O'Brien, J.; Wilson, I.; Orton, T.; Pognan, F. *Eur. J. Biochem.* **2000**, *267*, 5421.

(101) Banerjee, A.; Majumder, P.; Sanyal, S.; Singh, J.; Jana, K.; Das, C.; Dasguptaa, D. *FEBS Open Bio* **2014**, *4*, 251.

(102) Hermanson, G. T. *Bioconjugate Techniques*; 3rd ed.; Academic Press: London, 2013.

(103) Thermo Fisher Scientific. LysoSensor™ Green DND-189 - Catalog number L7535 <http://www.thermofisher.com/order/catalog/product/L7535> [Accessed Nov 1st, 2016].

(104) Soule, H.; McGrath, C. M. Immortal human mammary epithelial cell lines. US Patent 5,026,637. June 25, 1991.

(105) Agostinis, P.; Berg, K.; Cengel, K. A.; Foster, T. H.; Girotti, A. W.; Gollnick, S. O.; Hahn, S. M.; Hamblin, M. R.; Juzeniene, A.; Kessel, D.; Korbelik, M.; Moan, J.; Mroz, P.; Nowis, D.; Piette, J.; Wilson, B. C.; Golab, J. *CA-Cancer J. Clin.* **2011**, *61*, 250.

(106) Abrahamse, H.; Hamblin, M. R. *Biochem. J.* **2016**, *473*, 347.

(107) Berg, K.; Selbo, P. K.; Prasmickaite, L.; Tjelle, T. E.; Sandvig, K.; Moan, J.; Gaudernack, G.; Fodstad, Ø.; Kjølsrud, S.; Anholt, H.; Rodal, G. H.; Rodal, S. K.; Høgset, A. *Cancer Res.* **1999**, *59*, 1180.

(108) Høgset, A.; Prasmickaite, L.; Selbo, P. K.; Hellum, M.; Engesæter, B. Ø.; Bonsted, A.; Berg, K. *Adv. Drug Delivery Rev.* **2004**, *56*, 95.

(109) Selbo, P. K.; Høgset, A.; Prasmickaite, L.; Berg, K. *Tumour Biol.* **2002**, *23*, 103.

(110) Selbo, P. K.; Weyergang, A.; Høgset, A.; Norum, O.-J.; Berstad, M. B.; Vikdal, M.; Berg, K. *J. Controlled Release* **2010**, *148*, 2.

(111) Niles, A.; Worzella, T.; Scurria, M.; Daily, W.; Bernad, L.; Guthmiller, P.; Mcnamara, B.; Rashka, K.; Lange, D.; Riss, T. L. *Cell Notes* **2006**, *16*, 12.

(112) Niles, A.; Moravec, R. A.; Riss, T. L. *Expert Opin. Drug Discovery* **2008**, *3*, 655.

(113) Ai, J.; Xu, Y.; Lou, B.; Li, D.; Wang, E. *Talanta* **2014**, *118*, 54.

(114) Brevet, D.; Gary-Bobo, M.; Raehm, L.; Richeter, S.; Hocine, O.; Amro, K.; Loock, B.; Couleaud, P.; Frochot, C.; Morere, A.; Maillard, P.; Garcia, M.; Durand, J. O. *Chem. Commun.* **2009**, 1475.

(115) Gary-Bobo, M.; Hocine, O.; Brevet, D.; Maynadier, M.; Raehm, L.; Richeter, S.; Charasson, V.; Loock, B.; Morere, A.; Maillard, P.; Garcia, M.; Durand, J. O. *Int. J. Pharm.* **2012**, *423*, 509.

Chapter 4

Targeted photodynamic therapy of breast cancer cells using lactose-phthalocyanine gold nanoparticle conjugates

This chapter describes the use of a carbohydrate, lactose, as a targeting agent for the selective uptake of gold nanoparticles functionalised with a zinc phthalocyanine for photodynamic therapy of human breast adenocarcinoma cells.

4.1. Introduction

4.1.1. Aberrant glycosylation in cancer

Glycobiology has become an important field of study in cancer research.¹ Carbohydrates are organic structures widely found in nature.² The most basic structures of carbohydrates, monosaccharides, can be linked *via* glycosidic bonds to form more complex structures, oligosaccharides and polysaccharides also known as glycans.^{2,3} Glycans are not encoded by the genome. Instead, the enzymes glycosyltransferases and glycosidases catalyse the biosynthesis of glycans, which then lead to the formation of glycoproteins and glycolipids.²⁻⁴ Glycans and proteins can be either *N*-linked, when the glycan is bound to the amide group of an asparagine residue on the protein, or *O*-linked, when the glycan is bound to the hydroxyl group of serine or threonine residues on the protein.^{2,3,5,6} Additionally, glycolipids are created *via* sphingolipids, when the glycans are linked to lipid ceramides.^{1,3} Therefore, glycans are expressed in a specific pattern on the surface of all cells.^{2,7}

The surface of all cells also expresses other carbohydrate-related molecules, known as lectins. Lectins are carbohydrate-binding proteins that recognise glycans in a specific manner *via* their carbohydrate-recognising domains (CRDs).^{2,6,7} Lectins preferentially bind those carbohydrates found on glycoproteins and glycolipids, *i.e.*, natural polysaccharides, with dissociation constants (K_d) in the nanomolar range. However, they can also bind free carbohydrates but this interaction is weaker ($K_d = ca. 10^{-4} M$).

The multivalent nature of the lectin-carbohydrate interactions allows for multiple weak binding that can induce high overall affinity.^{2,8-10} Even though there is not a generally accepted classification for endogenous lectins, there are four main categories that include the majority of known animal lectins; C-type, S-type, I-type and P-type lectins.^{2,11} C-type lectins are calcium-dependent lectins that are always found bound to a carbohydrate. They include selectins, collectins, endocytic receptors and proteoglycans.^{2,12} S-type lectins, most commonly known as galectins, are calcium-independent lectins found non-glycosylated that have specificity towards β -galactose-containing glycans.^{2,13} I-type lectins belong to the immunoglobulin superfamily. The most important and well known subgroup involves the siglecs, sialic acid-binding lectins.^{2,14} P-type lectins are specific towards mannose-6-phosphate, also known as M6P receptors.¹¹

Glycans and lectins play important roles in normal healthy tissue. They are involved in embryonic development, cell growth, differentiation and adhesion, apoptosis, cell signalling, cell-cell recognition, interactions between cells and the extracellular matrix (ECM) and protein folding.^{2,5,6} Additionally, they have roles in the immune system in regulating host-pathogen interactions and inflammation.^{2,6} These functions are regulated when lectins on one cell bind their corresponding carbohydrates, present on the surface of other cells.⁷

Changes in the phenotypic distribution of glycans and lectins on the surface of the cells is linked with cancer, since they can promote cell migration and metastasis.^{1-3,5-7,15,16} The most common changes in the phenotype of glycans are related to the under- or over-expression of the enzymes involved in their biosynthesis, glycosyltransferases and glycosidases.^{1,6,16} Aberrant glycosylation usually occurs by two main pathways, the first one being the expression of truncated or shorter glycans as what would normally be seen in healthy cells and the second one being a change in the terminal sequences of the glycans.¹⁵ As a result, an increased expression of α -2,6 sialylation, fucosylation, O-glycan truncation, β -1,6 branching of N-linked glycans and Lewis^{a/x} antigens together with the expression of oncofetal antigens are seen.^{1,5,6,15,16} These changes in the glycosylation pattern are mediated by two mechanisms, neo-synthesis and incomplete synthesis, and are usually linked to poor prognosis in cancers.^{1-3,6,15} Modifications in the

expression of lectins on the surface of the cells is also linked to cancer. The two most important and well-characterised types of lectins in cancer research are selectins and galectins.^{2,7} Galectins and their role in cancer will be further discussed in **section 4.1.2**.

4.1.2. Galectins and their role in cancer

Galectins are a type of lectins that have preference towards β -galactoside carbohydrates.¹⁷ Galectins are encoded by the gene LGALS, which stands for lectin galactoside-binding soluble.^{17,18} To date, fifteen different galectins have been identified, which can be classified into three distinct groups.¹⁸⁻²³ Galectins in the first group are referred to as prototype galectins and they include galectins 1, 2, 5, 7, 10, 13, 14 and 15.¹⁹ Prototype galectins have a dimeric structure and contain one single CRD (**Figure 4.1 A**).^{19,21,22} Galectins in the second group are referred to as tandem-repeat galectins and they include galectins 4, 6, 8, 9 and 12.¹⁹ Tandem-repeat galectins contain two non-identical CRDs linked by a peptide domain and thus they are also known as biCRD (**Figure 4.1 B**).^{19,21,22} Finally, the third group of galectins is known as chimera.¹⁹⁻²¹ Only galectin-3 is part of this group and it is composed of one CRD linked to a proline, tyrosine and glycine rich domain and an NH₂-terminal domain (**Figure 4.1 C**).^{17,21,22,24,25} Galectin-3 is found as a monomer in solution but it can form multivalent aggregates as it binds to a ligand with its carbohydrate specificity.^{17,24}

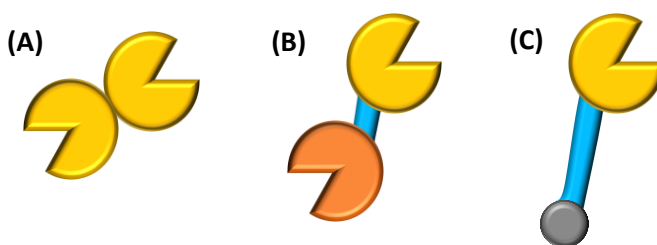


Figure 4.1. Typical structures for each type of galectin: **(A)** prototype galectin **(B)** tandem-repeat (biCRD) galectin and **(C)** chimera galectin. This figure was adapted from Ref. 17.

All galectins are composed of a core CRD sequence consisting of 130 amino acids.^{17,18,26} As it was previously mentioned, galectins recognise the β -galactoside domain of carbohydrates.¹⁷ This definition is not restricted to the monosaccharide galactose. Galectins, especially galectins-1 and 2, have also been found to recognise lactose, via

the galactose residue present within the lactose disaccharide. Surprisingly, in the case of galectins-1 and 2, there must be an interaction with the glucose residue on lactose too. This is because galectins-1 and 2 have a much higher affinity towards lactose than galactose.¹⁷ The problem with lactose is that it needs a high concentration of galectin-1 in the cells for an effective inhibition.^{18,27} Naturally encountered ligands for galectins include glycoconjugates that contain polylactosamine chains within their structure.^{17,24}

Galectins are cytosolic proteins expressed not only intracellularly, specifically within the cytoplasm and in the nucleus of the cells, but also on the cell surface and extracellularly within the ECM. Externalisation of galectins is possible due to their secretion *via* non-classical secretion pathways, unrelated to the standard pathway *via* the endoplasmic reticulum and the Golgi apparatus.^{17,18,20,22-24} Galectins play a variety of roles in the body. Even though their mechanism of action is not yet understood, the main roles of galectins are triggered by the recognition of carbohydrates present on the surface of the cells.²² Some of the most important roles include cell-to-cell and cell-to-ECM adhesion, regulation of cell growth, proliferation, migration and apoptosis, neurite elongation, inflammation, embryogenesis and pre-mRNA splicing.^{20-22,24,26} Additionally, over- or under-expression of galectins has been linked with cancer, especially with tumour spreading, metastasis and angiogenesis.^{21,22} The best characterised and widely studied galectins in cancerous tissue are galectin-1 and galectin-3.^{17,21,24}

Galectin-1 is a 14 kDa pro-tumorigenic galectin encoded by the gene LGALS1 located on chromosome 22q12.^{17,18,22,23,28} Due to its mass, it has also been referred to as L-14 lectin.¹⁷ The dimeric structure of galectin-1 allows it to crosslink inter- and intra-molecularly by binding to more than one galactoside-containing carbohydrate, which leads to the activation of signal transduction pathways and triggers its biological functions.^{22,24} Natural carbohydrates that lead to the activation of galectin-1 include the ECM glycoproteins laminin and fibronectin, polylactosamine-rich lysosome-associated membrane proteins (LAMPs) and the T-cell surface glycoproteins CD43, CD45 and CD7.^{21,24}

Galectin-1 is expressed in a variety of healthy and cancerous tissue. The normal tissue includes the thymus, lymph nodes, prostate, kidney, spleen, lungs, placenta, motor and

sensory neurons, skin and also endothelial cells and fibroblasts.^{17,24} In all these organs, galectin-1 can be found in the nucleus and cytoplasm inside the cells and also anchored onto the cell surface.^{18,23} Additionally, galectin-1 is secreted to the extracellular compartments, where its mass increases to 15 kDa as a result of the post-translational modifications that it undergoes during externalisation.²³ The localisation of galectin-1 within the cells varies from normal healthy tissue to cancerous tissue. In healthy cells, the majority of galectin-1 is found intracellularly, specifically located inside the nucleus of endothelial cells. On the other hand, in cancer cells galectin-1 is located extracellularly in much higher amounts.²³

Expression of galectin-1 within cancer cells is well known. Galectin-1 is found overexpressed in a variety of cancer types including breast, colon, endometrium, ovary, prostate, pancreatic, bladder and head and neck cancers. Additionally, overexpression of galectin-1 has also been linked to thyroid tumours, melanoma, astrocytoma, glioblastoma and the tumour vasculature, mainly endothelial cells.^{18-20,22-24,27,29-31} Overexpression of galectin-1 in cancer is correlated with an increased aggressiveness and poor prognosis because galectin-1 mediates several functions that change the tumour microenvironment and are essential for cancer progression.^{18,27} Galectin-1 induces metastasis and proliferation in cancer cells since it can promote the adhesion of the tumour cells and endothelial cells to the ECM.^{18,23,27} However, this enhancement in cell adhesion depends on the tumour type as well as the cellular localisation of galectin-1. In some cases, the opposite effect, where cell adhesion is inhibited, could be seen.^{23,24,27} As it was previously discussed, galectin-1 is overexpressed in the endothelial cells within the tumours. Endothelial cells are responsible for the creation of new “leaky” blood vessels, which leads to angiogenesis in cancer.¹⁸ The presence of galectin-1 stimulates the migration and proliferation of endothelial cells and provides a support for the formation of angiogenic blood vessels.^{18,27,29} Additionally, galectin-1 has a role in the tumour-immune escape as it induces T-cell apoptosis *via* interaction with the CD glycoproteins mentioned above.^{24,27}

Galectin-3 is another pro-tumorigenic galectin with a mass ranging between 29-34 kDa encoded by the gene LGALS3 located in chromosome 1p13.^{17,19,32} Galectin-3 has been referred to as L-29, L-31 and εBP previously.¹⁷ Galectin-3 is found as a monomer in

solution. However, it has the ability for multimerisation upon binding to its specific receptors.¹⁷ Multimerisation of galectin-3 allows for its ability to cross-link inter- and intra-molecularly. Natural binding ligands specific towards galectin-3 include the ECM glycoproteins laminin and fibronectin, LAMPs 1 and 2, IgE and its receptor, the apoptosis regulator Bcl-2, a 90 kDa glycoprotein found in epithelial cells known as Mac2-BP and the RNA in the nucleus of the cells.^{17,24,33-35}

Galectin-3 is expressed in a variety of healthy tissue including cells of the immune system.^{17,24} The main locations for galectin-3 are macrophages, basophils, mast cells, monocytes, some sensory neurons, endothelial cells and epithelial cells of several tissues such as intestine, kidney, colon and breast.^{17,24} These cells express galectin-3 primarily in the cytoplasm, but it can also be found in the nucleus, cell surface and circulating within the extracellular space.^{21,33,36} Galetin-3 plays important roles in cell adhesion, inflammation, bacterial colonisation, neutrophil and macrophage activation and protection of T-cells against apoptosis.^{17,24}

Expression of galectin-3 in cancerous tissue has been the subject of many studies. There is a well-known correlation between galectin-3 and cancer progression as this lectin is found overexpressed in certain types of cancers including central nervous system (CNS) tumours, lymphoma, melanoma, head and neck, gastric, liver, pancreatic, bladder and non-small cell lung cancer.¹⁹⁻²² For CNS tumours, galectin-3 is only found overexpressed in high grade, *i.e.*, highly aggressive, tumours such as glioblastoma (grade IV) and grade III astrocytoma.^{20,37} Low-grade brain tumours, *i.e.*, slow-growth tumours, do not show galectin-3 expression. The role and expression of galectin-3 in breast, colon, ovary, uterus and thyroid tumours is a conflicting issue. There are studies that show an overexpression of galectin-3 in breast, colon, ovary, uterus and thyroid cancers, which is related to metastatic potential.^{32,34,35,38-40} However, other studies have shown that galectin-3 is highly downregulated in breast, colon, ovary, uterus and thyroid cancers, and it is this downregulation that is correlated with histological grade.^{20,21,25,34,41} The contradicting values of galectin-3 expression in previous studies could be explained by the use of anti-galectin-3 antibodies that have cross-reactivity towards 67 laminin receptor (67LR) to detect galectin-3 levels.⁴¹ The expression of 67LR increases in cancers with increasing metastatic potential, which would explain the reason why

galectin-3 was found in high levels in some studies.⁴¹ The role of galectin-3 in cancer is to promote cell adhesion, invasion, proliferation and metastasis, inhibit T cell apoptosis and nitric oxide (NO) mediated apoptosis and stimulate anoikis resistance and tumour angiogenesis.^{22,24,34,36,40,42-44} However, the level of expression of galectin-3 and its role in cancer progression are dependent on the location of galectin-3 within the cells as well as tumour-specific factors, including the stage in which the tumour is at.^{24,25,34} Cytoplasmic galectin-3 in circulation and galectin-3 circulating in the extracellular space tend to promote tumour progression and metastasis. On the other hand, galectin-3 present in the nucleus has pro-apoptotic properties.^{34,45} Independent of its localisation, galectin-3 free mice are healthy, which suggests inhibition of galectin-3 could be important to prevent cancer progression.³⁴ Additionally, inhibiting galectin-3 has been found to reduce the frequency of lung metastasis by 90 %.⁴³

In this chapter, the cancer of interest is breast adenocarcinoma. There is consensus of the overexpression of galectin-1 in breast cancer epithelial cells, as well as in their associated stromal cells. Therefore, galectin-1 is an ideal candidate for targeted breast cancer therapy since it has been shown that its suppression prevents tumour growth and metastasis.^{24,31} Overexpression of galectin-1 has been particularly shown in MDA-MB-231 human breast adenocarcinoma cells.^{28,30,31,46} The expression of galectin-3 in breast cancer cells has led to the production of conflicting reports. Studies of galectin-3 overexpression in different types of breast cancer have shown an indication that there is an increased expression of galectin-3 only in triple-negative breast cancers (TNBC). TNBC are those that do not overexpress neither of the hormonal receptors, estrogen and progesterone, nor the HER2 receptor and they account for approximately 15 % of breast cancers.^{42,47} One commonly studied TNBC cell line is MDA-MB-231, which has been associated with an increased production of galectin-3.^{44,48} On the other hand, the HER2 positive SK-BR-3 human breast adenocarcinoma cell line has been associated with downregulation and zero-expression of galectin-3.⁴⁸ However, it is only an indication and conflict still exists on the expression of galectin-3 on TNBC as other studies have found no cell-surface galectin-3 in MDA-MB-231 cells.⁴⁶ Therefore, targeting breast cancer cells *via* β -galactoside-containing carbohydrates should be preferentially directed towards galectin-1.

4.1.3. Targeting cancer glycosylation

As it was discussed in **section 4.1.1**, cancer cells present an aberrant glycosylation on their surface. The aberrant glycosylation affects both glycoconjugates and lectins. As a result, carbohydrates and lectins are ideal candidates for targeted cancer therapy. The interaction between lectins and carbohydrates ($k_d = ca. 10^{-3}\text{-}10^{-6} \text{ M}$) is specific but of lower affinity than the interaction between antigens and antibodies ($k_d = 10^{-8}\text{-}10^{-12} \text{ M}$), or enzymes and their substrates.^{49,50} Therefore lectin-targeting can be used for selective cancer treatment. There are two types of lectin-targeting, reverse and direct.^{49,51,52} Reverse lectin-targeting involves the use of exogenous lectins that will be recognised by the glycoconjugates expressed on the surface of cancer cells (**Figure 4.2 A**). Direct lectin-targeting, also known as glycotargeting, involves the use of carbohydrates that are selectively recognised by endogenous lectins expressed on cancer cells (**Figure 4.2 B**).^{49,51,52}

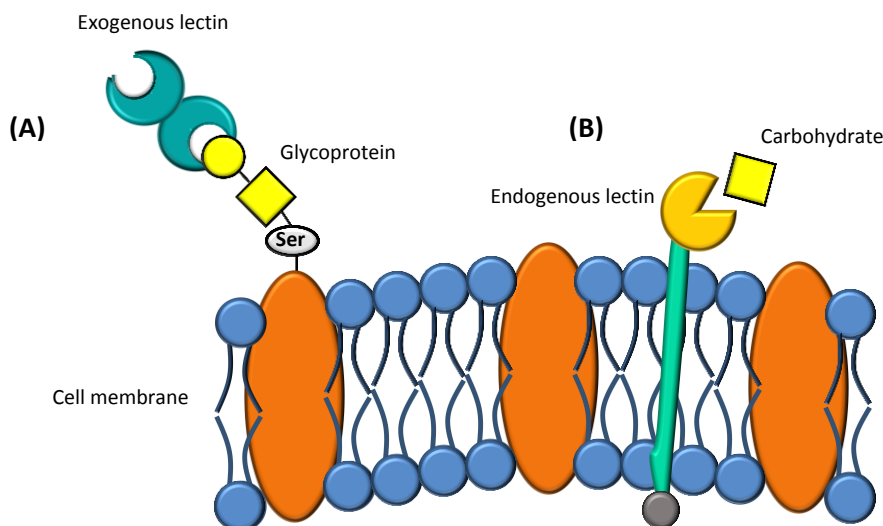


Figure 4.2. Schematic representation showing (A) reverse and (B) direct lectin targeting.

There are numerous studies showing both direct and reverse lectin targeting for cancer therapy. In direct targeting, Durand and co-workers have published several studies.⁵³⁻⁵⁷ These authors use mesoporous silica nanoparticles (MSN) functionalised with a photosensitiser and mannose for targeted PDT.⁵³ The breast cancer cell line MDA-MB-231 was incubated with the functionalised MSN for 24 h followed by 40 min irradiation

for PDT. The functionalisation of mannose proved to be effective in increasing cellular uptake of the MSN as there was a 54 % increase in cell death as compared to MSN not functionalised with mannose.⁵³ These mannose-photosensitiser functionalised MSN were further used for two-photon excitation (TPE)-PDT in breast and colon cancer cells.⁵⁴ Similar results were obtained with no dark toxicity and a higher nanoparticle uptake for mannose functionalised MSN as compared to non-functionalised MSN. For further studies, the Durand group combined mannose functionalised MSN-PDT with drug delivery.^{55,56} The anti-cancer drug camptothecin (Cp) was loaded onto the mannose functionalised MSN yielding Cp-Man-MSN. The Cp-Man-MSN were used to target highly metastatic breast, colon and pancreatic cancer, and retinoblastoma cells. Following a 24 h incubation with either Cp-Man-MSN or non-functionalised MSN, the cellular internalisation was higher for the former, which thus led to a higher cell death after PDT. The presence of the anti-cancer drug in the system was essential for further enhancing the cell death efficacy. Mannose was replaced with galactose, synthesising MSN nanoparticles functionalised with galactose and camptothecin (Cp-Gal-MSN).^{55,56} The use of galactose did not alter the results as it was also thought to be enhancing internalisation of the MSN *via* receptor-mediated endocytosis.^{55,56} Additionally, the retinoblastoma cells were subjected to TPE-PDT, which was shown to induce even better PDT efficiency than one-photon excitation PDT.⁵⁶ The Durand group further studied mannose targeting using a slightly different type of nanoparticles.⁵⁷ In this case, the MSN were modified by introducing a magnetic Fe_3O_4 core. The authors obtained similar results to those reported with other types of nanoparticles previously mentioned. Mannose was found to be essential to provide a good cellular uptake and thus cytotoxic effect after PDT.⁵⁷ The use of mannose and galactose, together with other carbohydrates such as glucose, has been studied in combination with silver nanoparticles (AgNPs).⁵⁸ It was found that the AgNPs were more effectively internalised by Neuro-2A brain neuroblastoma and HepG2 hepatocellular carcinoma cells when the carbohydrates were loaded onto the AgNPs. Additionally, the use of either mannose or galactose showed the least toxicity, which suggests they should be used in preference to glucose.⁵⁸

Further studies using galactose as the targeting agent have been reported. Pereira *et al.* developed a phthalocyanine surrounded by sixteen galactose molecules in a

dendrimer (PcGal_{16}) for targeted PDT of bladder cancer cells.⁵⁹ The galactose molecules specifically recognised the overexpressed galectin-1 receptors on the surface of bladder cancer cells. Additionally, the glucose-transporter-1 (GLUT1) receptor also has specificity towards galactose and it is overexpressed in bladder cancer cells. As a result, PcGal_{16} was easily and quickly internalised, only a 4 h incubation with the cells was required, *via* receptor-mediated endocytosis. PcGal_{16} was found to induce no dark-toxicity but high levels of cell death following PDT.⁵⁹ In another study, Peng *et al.* successfully used galactose functionalised fluorescent nanoparticles to target the asialoglycoprotein receptor on the surface of liver cells.⁶⁰

Carbohydrate ligands have also been used to inhibit the action of certain endogenous lectins that promote tumour growth. Park *et al.* reported the potential use of lactose conjugated chlorins to target the galectin-3 receptor, which is sometimes overexpressed in cancer cells.⁴⁵ Other examples of possible galectin inhibitors include lactulose amines, thiodigalactoside and davanat.²³ The use of orally ingested polysaccharides that can target and inhibit the action of pro-tumorigenic lectins has also been reported. Pienta *et al.* used modified citrus pectin, which contains galactose residues, to reduce metastasis promoted by galectins on the surface of prostate cancer cells.⁶¹ A similar study was performed by Sathisha *et al.* to inhibit the action of galectin-3 on several cancer cells using dietary inhibitors. The dietary galectin inhibitors used included citrus pectin, swallow root and black cumin.⁴⁴

The mannose-6-phosphate/insulin-like growth factor (M6P/IGF-II), overexpressed in breast cancer, pancreatic cancer, gastric cancer, melanoma and hepatocellular carcinoma, has been targeted with human serum albumin modified with M6P moieties (M6P-HSA).⁶² M6P-HSA was effectively internalised *via* receptor-mediated endocytosis by B16 melanoma cells. The addition of the anti-cancer drug doxorubicin (DOX) to the system allowed for efficient internalisation and release of DOX in the cells, which contributed to the inhibition of tumour progression and metastasis.⁶² Another carbohydrate used for cancer targeting is the glycoprotein transferrin.⁶³ Transferrin selectively recognises the transferrin receptor, sometimes overexpressed in cancer cells, including bladder,⁶⁴ brain,⁶⁵ and breast.⁶⁶

Reverse lectin-targeting has also been extensively studied. The lectin *Helix Pomatia* agglutinin (HPA) has been used to target the monosialylated oligosaccharide HPAgl1 receptor overexpressed on the surface of breast cancer cells.⁶⁷ The lectin Wheat Germ agglutinin (WGA), which has a preference towards N-acetyl-D-glucosamine and sialic acid, has also been used to target cancer cells.^{68,69} Polymeric nanoparticles with a quantum dot core were functionalised with WGA and they were used to target Caco-2 colon cancer cells.⁶⁸ Caco-2 cancer cells overexpress WGA binding receptors on their surface, especially the *N*-acetyl-*D*-glucosamine glycoprotein, which facilitates an easy internalisation of the WGA functionalised nanoparticles. The addition of an anti-cancer drug, paclitaxel, to the WGA functionalised polymer nanoparticles allowed for an effective drug delivery inside the cells, which inhibits tumour proliferation.⁶⁹ The lectins *Ricis communis* agglutinin (RCA₁₂₀) and concanavalin A (ConA) have been used to target HeLa cervical cancer cells.⁷⁰ These lectins were conjugated to 13 nm AuNPs and effectively detected glycosyl complexes on the surface of the HeLa cells.

The podoplanin (PDPN) transmembrane receptor, overexpressed in breast, oral and skin cancers has been targeted with a lectin obtained from the seeds of *Maackia amurensis* (MASL).⁷¹ In the experiment by Ochoa-Alvarez *et al.*, the PDPN on the surface of melanoma cells was targeted following oral ingestion of MASL. Ingestion of MASL led to the effective binding of MASL to the PDPN receptors, which induced the inhibition of malignant growth and proliferation.⁷¹ Another example of an orally ingested lectin is the tomato lectin (TL).⁷² TL was conjugated to fluorescent nanoparticles and effectively used to target cells in the intestine of female Wistar rats.

Reverse lectin-targeting has also been used for PDT.⁷³ The lectin Jacalin, obtained from Jackfruit (*Artocarpus integrifolia*), was used to target the oncofetal Thomsen-Friedenreich disaccharide (T antigen) overexpressed on the surface of colon cancer cells. Jacalin was conjugated to 4 nm AuNPs functionalised with the zinc phthalocyanine derivative C11Pc and PEG (Jacalin-C11Pc-PEG-AuNPs). Jacalin-C11Pc-PEG-AuNPs were efficiently internalised by the HT-29 colon cancer cells *via* receptor-mediated endocytosis. Following PDT, a marked enhancement of the cell death (95 % cell death) was observed as compared to C11Pc-PEG-AuNPs without Jacalin (8 % cell death).⁷³

4.1.4. Aims of the research reported in this chapter

In this chapter, direct lectin-targeting of breast adenocarcinoma cells was studied. Lactose was chosen as the targeting agent due to its selective binding towards galectin-1, overexpressed on the surface of breast cancer cells. Two cell lines were used, MDA-MB-231 and SK-BR-3 cells.

Gold nanoparticles (*ca.* 2-4 nm) were synthesised and functionalised with a mixed monolayer of lactose and the zinc phthalocyanine derivative C11Pc (lactose-C11Pc-AuNPs). In this system, lactose was used to provide aqueous dispersibility for the AuNPs as well as used as a potential targeting agent. In order to test the targeting ability of lactose, “control” AuNPs were synthesised and functionalised with C11Pc and sPEG (C11Pc-sPEG-AuNPs). The sPEG was chosen to provide aqueous dispersibility and its chain length was similar to that of the lactose. Lactose-C11Pc-AuNPs and C11Pc-sPEG-AuNPs were tested *in vitro* in MDA-MB-231 and SK-BR-3 cells. Additionally, the ability of lactose to target galectin-1 on the surface of the breast cancer cells was analysed using an InCell ELISA.

In the second part of the research, C3Pc replaced C11Pc as the photosensitiser. Gold nanoparticles (*ca.* 2-4 nm) were synthesised and functionalised with a mixed monolayer of lactose and C3Pc (lactose-C3Pc-AuNPs). “Control” AuNPs were also synthesised (C3Pc-sPEG-AuNPs). Lactose-C3Pc-AuNPs and C3Pc-sPEG-AuNPs were tested *in vitro* in MDA-MB-231 and SK-BR-3 cells. InCell ELISAs were also performed to evaluate the degree of lactose targeting towards each cell line. Additionally, the intracellular uptake and PDT effect were visually studied using confocal microscopy.

4.2. Results and discussion

4.2.1. Lactose and galectin-1 levels

Lactose is a disaccharide composed of a galactose subunit and a glucose subunit. The terminal end of lactose connected to the glucose subunit was modified with a thiol in order to self-assemble the lactose to the surface of the AuNPs. The modified lactose

was kindly provided by Dr Alan Haines (School of Chemistry, University of East Anglia, Norwich, UK). The structure of the thiolated lactose⁷⁴ is shown in **Figure 4.3**.

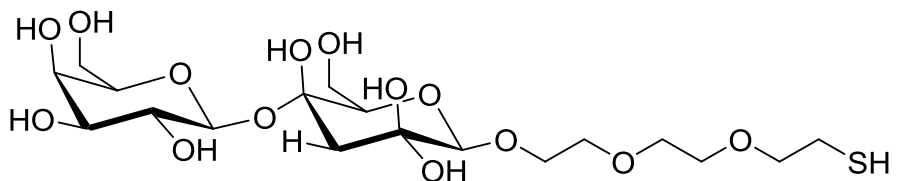


Figure 4.3. Structure of the thiolated lactose, taken from Ref. 74.

As shown in **Figure 4.3**, galactose is the terminal subunit in the lactose derivative molecule. This opens the possibility to use lactose as a targeting agent for galactose-binding cell receptors. As described in **section 4.1.2**, galectins are β -galactoside-binding proteins, which have been found to be potential cancer biomarkers, as they are overexpressed in malignant epithelial and tumour-associated stromal cells.^{19,34} Galectin-1 is the most relevant galectin in breast cancer as there is consensus regarding its overexpression on the surface of breast cancer cells, especially the MDA-MB-231 cell line.³¹ The presence of galectin-3 on breast cancer cells is debated as some reports suggest it is overexpressed and other state it is highly downregulated.^{20,21,25,32,39-41} Furthermore, the overexpression has found to be only related to triple-negative breast cancers in some studies, including MDA-MB-231 cells, but these results are also inconclusive.^{42,46-48} Taking into consideration the previously reported data on galectin overexpression in breast cancer cells, it was decided to evaluate and compare the levels of galectin-1 on MDA-MB-231 and SK-BR-3 human breast adenocarcinoma cells to determine whether galectin-1 could be used as a target for cancer therapy. This was achieved using an InCell ELISA. The InCell ELISA was performed as described in **section 2.3.10**. The results from the InCell ELISA are presented in three different graphs (**Figure 4.4**).

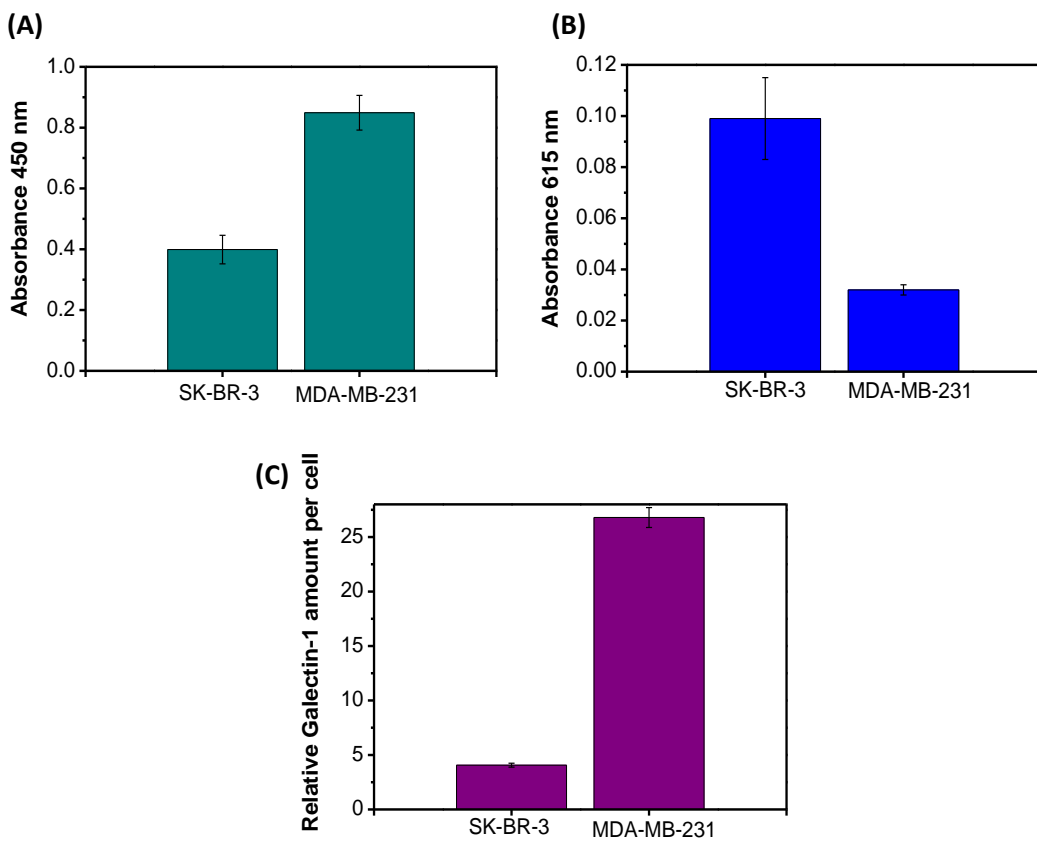


Figure 4.4. InCell ELISA for the detection of galectin-1 on the surface of SK-BR-3 and MDA-MB-231 cells. **(A)** Absorbance at 450 nm representing the amount of galectin-1 in each sample. **(B)** Absorbance at 615 nm representing the number of cells per sample. **(C)** Normalised value of galectin-1 per cell in each sample. Error bars represent the SD ($n = 3$) within a 95 % confidence interval.

Figure 4.4 A shows the absorbance at 450 nm for each cell line. Absorbance at 450 nm is directly proportional to the amount of galectin-1 in the sample. **Figure 4.4 B** shows the absorbance at 615 nm for each cell line. The absorbance at 615 nm detects the amount of Janus Green whole-cell stain in the sample and is thus directly proportional to the amount of cells in each sample. **Figure 4.4 C** shows the ratio between the absorbance at 450 nm and the absorbance at 615 nm. This ratio normalises the amount of galectin-1 to the number of cells in each sample. As a result, the final value gives an estimation of the relative amount of galectin-1 per cell in each sample. The results presented showed that MDA-MB-231 cells present a much higher amount of galectin-1 on their surface as compared to SK-BR-3 cells.

4.2.2. Synthesis and characterisation of lactose-C11Pc-AuNPs

Lactose-C11Pc-AuNPs, a schematic representation of which is shown in **Figure 4.5 A**, were synthesised according to the procedure reported in **section 2.3.1**. Initially, the synthesis was attempted following the method used for the results presented in **Chapter 3** for the synthesis of C11Pc-PEG-AuNPs. The molar concentrations of C11Pc, HAuCl₄ and NaBH₄ were kept constant. The only difference was the addition of lactose instead of PEG. Lactose was dissolved in dH₂O, rather than using THF as the solvent, due to solubility issues. Following overnight incubation, the dark green solution was purified to remove all the AuNPs not functionalised with both C11Pc and lactose. The final purified solution dissolved in MES buffer appeared to be colourless. However, upon measuring the extinction spectrum, as shown in **Figure 4.5 B**, a small absorption band at *ca.* 698 nm was observed. This absorption band showed that there was some functionalisation with the C11Pc, since the characteristic absorption band for Pcs was observed at a low extinction intensity. Additionally, the AuNPs were soluble in an aqueous solution, which confirmed their functionalisation with lactose.

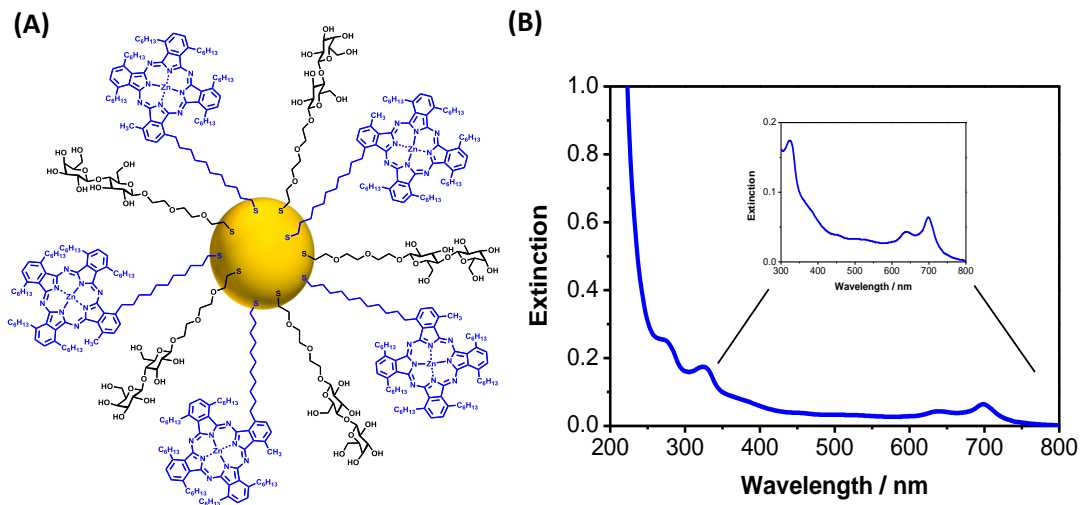


Figure 4.5. (A) Schematic representation of lactose-C11Pc-AuNPs. (B) UV-vis extinction spectrum of the synthesised lactose-C11Pc-AuNPs, with the low loading of C11Pc on the AuNPs surface. **Inset:** UV-vis extinction spectrum of the synthesised lactose-C11Pc-AuNPs amplified in the region 300-800 nm.

In an attempt to increase the loading of C11Pc on the nanoparticles, a few changes were made on the synthetic method, as reported in **section 2.3.1**. Lactose had previously been added at 2.5 μmol . This was in considerable excess as compared to the amount of C11Pc added, only 1.8 μmol . Therefore, the amount of lactose added was reduced to 1.8 μmol to be equimolar to the C11Pc. Additionally, the solution during synthesis contained more dH_2O than THF, since lactose is insoluble in THF. This could cause problems for C11Pc solubility during synthesis. Therefore, the THF: dH_2O ratio was kept at 1:1. Following overnight incubation, the reaction mixture was purified in the same manner as previously described. The synthesised lactose-C11Pc-AuNPs presented a blue colour, characteristic of C11Pc and were dispersed in MES buffer. The UV-vis extinction spectrum shows the band at *ca.* 698 nm, which is typical of these substituted phthalocyanines, thus showing the functionalisation of the nanoparticles with C11Pc. Furthermore, functionalisation with lactose can be confirmed since the AuNPs were soluble in an aqueous buffer, which would not be possible if the nanoparticles were only functionalised with the C11Pc. The UV-vis extinction spectrum and a cuvette containing a solution of the synthesised lactose-C11Pc-AuNPs are shown in **Figure 4.6 A and B** respectively.

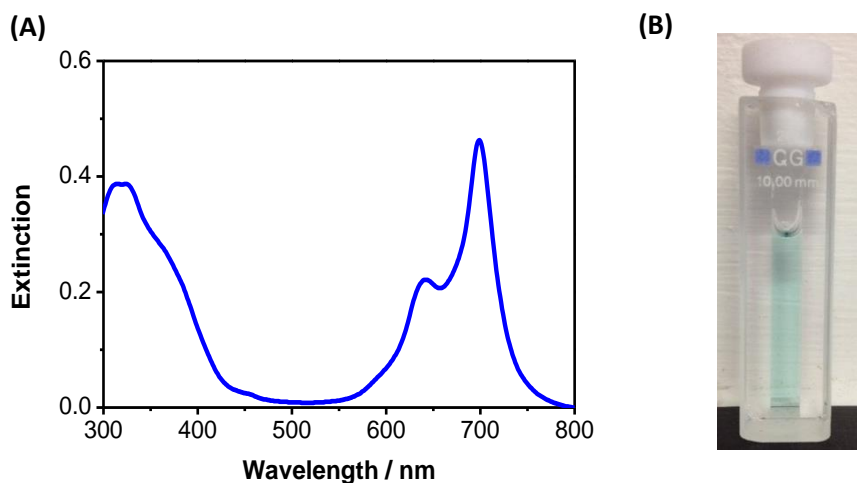


Figure 4.6. **(A)** UV-vis extinction spectrum of lactose-C11Pc-AuNPs and **(B)** image showing a cuvette containing a solution of the synthesised lactose-C11Pc-AuNPs.

The synthesised lactose-C11Pc-AuNPs were further characterised using TEM to evaluate their mean size. TEM analysis indicated that the lactose-C11Pc-AuNPs had an average diameter of 2.37 ± 1.65 nm, following analysis of 340 nanoparticles, with a median value of 1.79 ± 2.71 nm. TEM images of the lactose-C11Pc-AuNPs, together with a histogram showing their size distribution, are shown in **Figure 4.7**. As it can be seen in **Figure 4.7**, the size distribution histogram is positively skewed. In these situations, the median value could sometimes be taken as a better representation of the population than the mean.⁷⁵

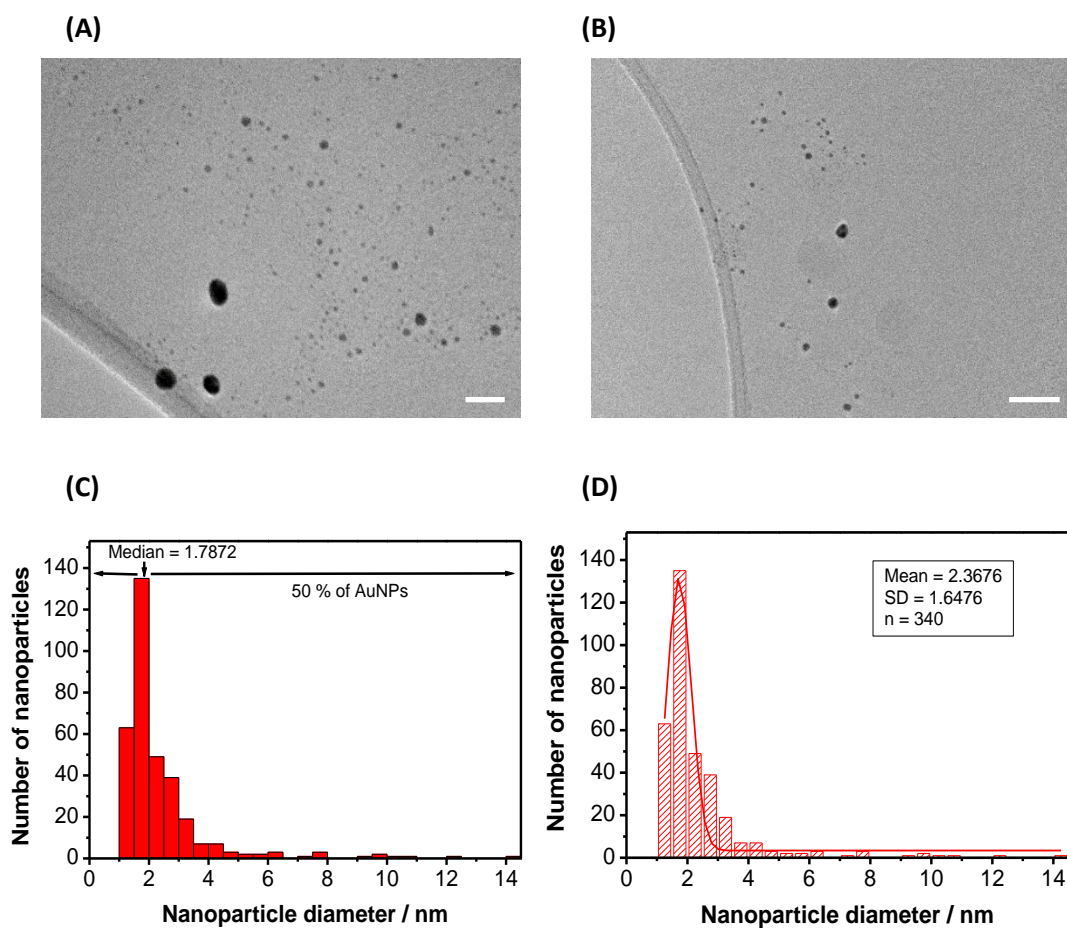


Figure 4.7. **(A-B)** Transmission electron micrographs of a sample of lactose-C11Pc-AuNPs, where the scale bars represent **(A)** 20 nm and **(B)** 50 nm. **(C)** Histogram of the lactose-C11Pc-AuNPs with a median value of 1.79 ± 2.71 nm ($n = 340$). **(D)** Size distribution of the lactose-C11Pc-AuNPs showing the Gaussian fit, with an average size of 2.37 ± 1.65 nm ($n = 340$).

To confirm whether the synthesised lactose-C11Pc-AuNPs could be used for PDT, the production of reactive oxygen species needs to be proven. The singlet oxygen probe ABMA was used to confirm the production of ${}^1\text{O}_2$ by lactose-C11Pc-AuNPs, as described in **sections 2.3.4** and **3.2.4**. The results are shown in **Figure 4.8**. It can be seen that, in the presence of lactose-C11Pc-AuNPs, the fluorescence of ABMA is quenched when the sample is irradiated with a 633 nm HeNe laser. This confirms that ${}^1\text{O}_2$ is being produced by the lactose-C11Pc-AuNPs upon irradiation. Additionally, the negligible fluorescence quenching of ABMA in the presence of control PEG-AuNPs indicates that the C11Pc is essential for the production of ${}^1\text{O}_2$.

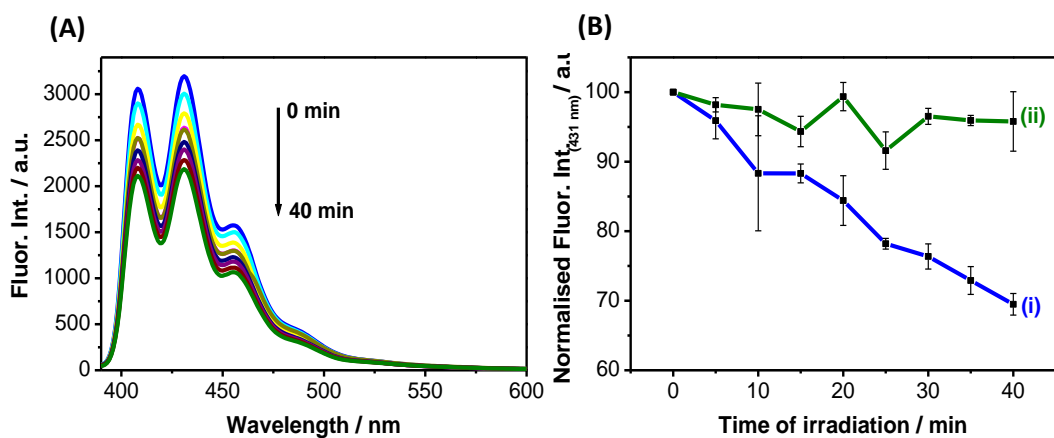


Figure 4.8. (A) Fluorescence emission spectra of ABMA showing the quenching of the fluorescence following irradiation of the lactose-C11Pc-AuNPs, thus confirming the production of ${}^1\text{O}_2$. (B) Photobleaching of ABMA in the presence of (i) lactose-C11Pc-AuNPs (0.734 μM C11Pc) as a function of time. No photobleaching was observed for control PEG-AuNPs (ii). Error bars represent the SD ($n = 3$) within a 95 % confidence interval.

The maximum amount of ABMA photobleaching, *i.e.*, following the first 5 min of irradiation, can be calculated following **Equation 3.4** in **section 3.2.4**. The maximum amount of ABMA photobleaching was found to be $1.1 \pm 0.7\%$ for lactose-C11Pc-AuNPs. This value indicates the ability of the lactose-C11Pc-AuNPs to produce ${}^1\text{O}_2$ after only 5 min irradiation. In **Chapter 3**, the maximum amount of ABMA photobleaching for the C11Pc-PEG-AuNPs was found to be $2.1 \pm 0.1\%$, which is considerably higher than the rate found for lactose-C11Pc-AuNPs. This result indicates that the C11Pc-PEG-AuNPs produce more ${}^1\text{O}_2$ and thus, at the same concentration, should have a higher PDT efficiency than the lactose-C11Pc-AuNPs presented in this chapter.

4.2.3. Synthesis and characterisation of control C11Pc-sPEG-AuNPs

In order to provide a control for the study of the targeting ability of lactose towards the overexpressed galectin-1 on the surface of breast cancer cells, AuNPs without a targeting agent were synthesised. Similarly to that reported in **Chapter 3**, a PEG chain was used to provide the aqueous solubility to the nanoparticle system. In this case, the PEG chain (282.35 g/mol) was shorter than that used in **Chapter 3** (PEG; 3,073 Da) so that the molecule would provide a similar length to that of the lactose derivative of the lactose-C11Pc-AuNPs for a direct comparison. This shorter PEG chain will be labelled as sPEG. The structure of sPEG, together with a schematic representation of the gold nanoparticles functionalised with a mixed monolayer of C11Pc and sPEG (C11Pc-sPEG-AuNPs) are shown in **Figure 4.9**.

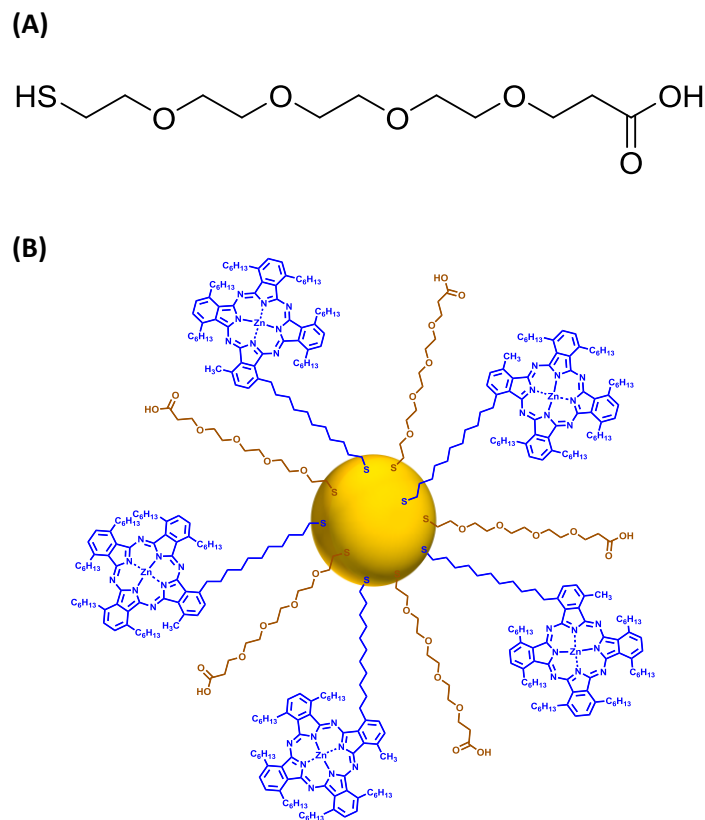


Figure 4.9. (A) Structure of the sPEG used throughout the results presented in **Chapter 4**. **(B)** Schematic representation of C11Pc-sPEG-AuNPs.

C11Pc-sPEG-AuNPs were synthesised following the improved method for lactose-C11Pc-AuNPs as described in **section 2.3.5**. Given the short nature of this sPEG chain, solubility of C11Pc within the C11Pc-sPEG-AuNPs became more challenging. Therefore, this particular synthetic route does not provide a high loading of C11Pc on the nanoparticles, which were obtained in a low yield. The extinction spectrum of the synthesised C11Pc-sPEG-AuNPs dispersed in MES buffer, together with an image to show the final colour of a solution of the nanoparticles, are shown in **Figure 4.10 A** and **B** respectively.

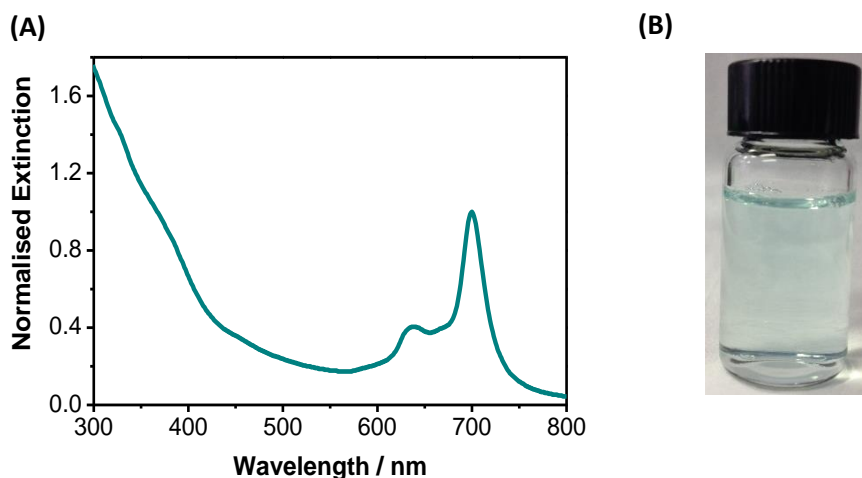


Figure 4.10. **(A)** UV-vis extinction spectra of C11Pc-sPEG-AuNPs and **(B)** image showing a vial containing a solution of the synthesised C11Pc-sPEG-AuNPs.

The synthesised C11Pc-sPEG-AuNPs were used as a control to the lactose-C11Pc-AuNPs to evaluate the targeting ability of the lactose ligand towards the galectin-1 receptor on the surface of breast cancer cells.

4.2.4. *In vitro* studies in MDA-MB-231 cells using lactose-C11Pc-AuNPs

Initially, MDA-MB-231 human breast adenocarcinoma cells were used to test the potential targeting ability of the synthesised lactose-C11Pc-AuNPs. MDA-MB-231 cells were chosen since, as discussed in **section 4.2.1**, there is an increased expression of galectin-1 in this cell line as compared to SK-BR-3 cells, see **Figure 4.4**. As a result, it would be expected that the lactose would target the MDA-MB-231 cells more

efficiently than the SK-BR-3 cells and so the nanoparticles would be internalised more readily, potentially leading to higher cell death following PDT.

A CellTiter-Blue® cell viability assay was performed, as described in **section 2.3.8**. MDA-MB-231 cells were seeded on 96-well microplates and incubated with the lactose-C11Pc-AuNPs and C11Pc-sPEG-AuNPs (0.25 μ M C11Pc) for 3 h. Following incubation with the AuNPs, the cells were washed to eliminate the non-internalised AuNPs and irradiated with a 633 nm HeNe laser for 6 min. Cell viability was measured *ca.* 48 h following PDT. The results of the viability assay are shown in **Figure 4.11**.

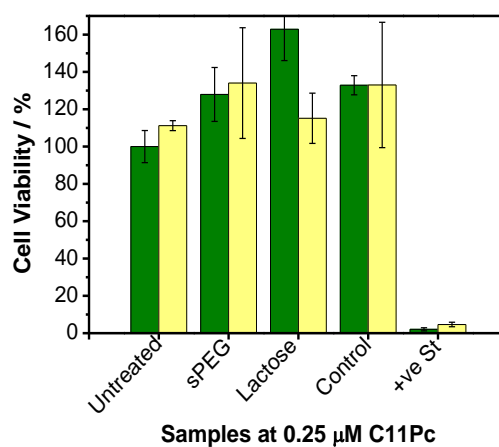


Figure 4.11. CellTiter-Blue® cell viability assay results for MDA-MB-231 cells incubated with C11Pc-sPEG-AuNPs (sPEG) or lactose-C11Pc-AuNPs (lactose) for 3 h. Cells were either irradiated with a 633 nm HeNe laser (yellow) or non-irradiated (green). Control refers to samples treated with sPEG-AuNPs without the presence of C11Pc. Untreated refers to cells treated with growth medium only. Staurosporine (+ve St) was used as a positive control for cytotoxicity. Error bars represent the SD ($n = 3$) within a 95 % confidence interval.

Figure 4.11 shows that there is no cell death in any of the samples. These results were highly reproducible in a further four attempts. The inability of any of the nanoparticle conjugates to induce cell death following PDT could be related to the incubation time of the AuNPs with the cells. The lactose-C11Pc-AuNPs and C11Pc-sPEG-AuNPs were incubated with the MDA-MB-231 cells for only 3 h. The CellTiter-Blue® cell viability assay results suggest that a 3 h incubation period is not sufficient for efficient AuNPs internalisation. Therefore, the incubation period was increased to 24 h. Other than changing the incubation period, the MDA-MB-231 cells were treated with the AuNPs in

the same manner as described previously ($0.25 \mu\text{M}$ C11Pc). The results of the extended incubation period experiments are shown in **Figure 4.12**.

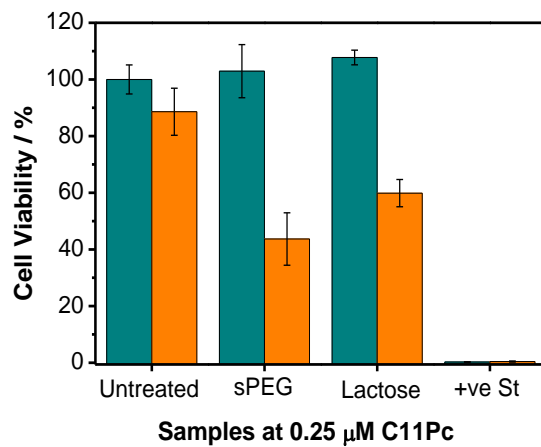


Figure 4.12. CellTiter-Blue® cell viability assay results for MDA-MB-231 cells incubated with C11Pc-sPEG-AuNPs (sPEG) or lactose-C11Pc-AuNPs (lactose) for 24 h. Cells were either irradiated with a 633 nm HeNe laser (orange) or non-irradiated (dark cyan). Untreated refers to cells treated with growth medium only. Staurosporine (+ve St) was used as a positive control for cytotoxicity. Error bars represent the SD ($n = 3$) within a 95 % confidence interval.

As shown in **Figure 4.12**, following the 24 h incubation period of the nanoparticles with the MDA-MB-231 cells, cell death was observed after irradiation with a 633 nm HeNe laser for both lactose-C11Pc-AuNPs and C11Pc-sPEG-AuNPs. The non-irradiated samples, with either type of nanoparticles, showed no dark toxicity. The cell death levels induced after irradiation were higher for the C11Pc-sPEG-AuNPs (56 %) than the lactose-C11Pc-AuNPs (40 %). This seems to suggest that the lactose is not effectively targeting the galectin-1 receptor on the surface of the MDA-MB-231 cells. To confirm these results, the CellTiter-Blue® cell viability assay, together with MTT cell viability assays, were repeated. **Figure 4.13** shows the results of the repeated CellTiter-Blue® and MTT cell viability assays, using the same conditions for the assay performed for **Figure 4.12**. Unfortunately, the results from the CellTiter-Blue® and MTT cell viability assays were found to be non-reproducible. As shown in **Figure 4.13**, the results from the cell viability assays are very different every time the experiment is performed under the same conditions.

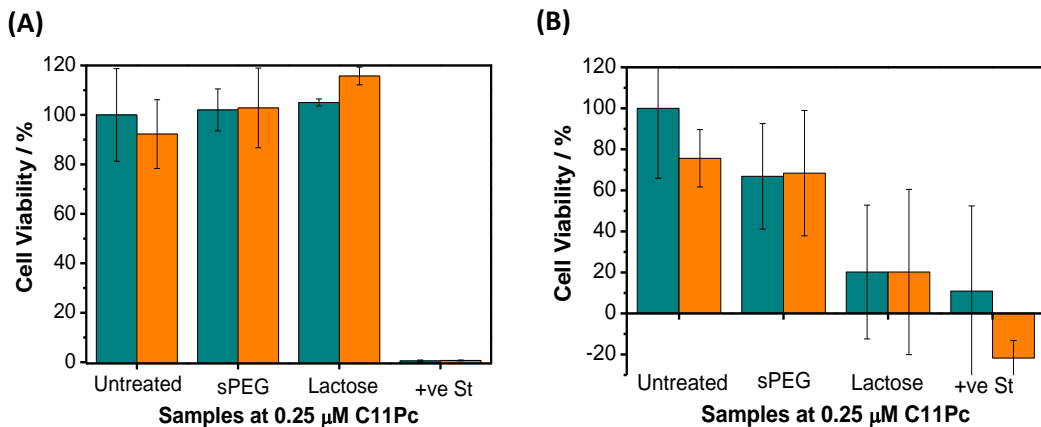


Figure 4.13. (A) CellTiter-Blue® cell viability assay results and (B) MTT cell viability assay results for MDA-MB-231 cells incubated with C11Pc-sPEG-AuNPs (sPEG) or lactose-C11Pc-AuNPs (lactose) for 24 h. Cells were either irradiated with a 633 nm HeNe laser (orange) or non-irradiated (dark cyan). Untreated refers to cells only treated with growth medium. Staurosporine (+ve St) was used as a positive control for cytotoxicity. Error bars represent the SD ($n = 3$) within a 95 % confidence interval.

As shown in **Figure 4.13**, the results of PDT treatment of MDA-MB-231 cells incubated with lactose-C11Pc-AuNPs or C11Pc-sPEG-AuNPs for 24 h were inconclusive. Out of the five performed cell viability assays, only one CellTiter-Blue® assay showed an indication of cell death following irradiation, as seen in **Figure 4.12**, but these results were not reproducible. Even when cell death was observed, there was no evidence of targeting by the lactose ligand. The majority of the assays performed showed no effect from lactose, which suggests that the lactose-C11Pc-AuNPs are not effective for targeted PDT of MDA-MB-231 cells.

4.2.5. *In vitro* studies in SK-BR-3 cells using lactose-C11Pc-AuNPs

Given the negative results for PDT with lactose-C11Pc-AuNPs and C11Pc-sPEG-AuNPs in MDA-MB-231 cells following 3 h incubation with the nanoparticles, and the non-reproducible results following 24 h incubation with the nanoparticles, it was decided to test the effects of the nanoparticles with SK-BR-3 cells. Even though SK-BR-3 cells have a lower level of galectin-1 on their surface (**Figure 4.4**), there is a possibility that the lactose ligand also recognises the GLUT1 receptor, which has been reported to be

overexpressed in breast cancer.⁷⁶⁻⁸¹ GLUT1 is known to react with galactose moieties.⁵⁹ Therefore, there is a potential for the targeting of SK-BR-3 cells with lactose *via* receptors other than galectin-1.

CellTiter-Blue® cell viability assays were performed on SK-BR-3 cells incubated with either lactose-C11Pc-AuNPs or C11Pc-sPEG-AuNPs for 3 h. The assays were repeated multiple times to evaluate the reproducibility. Typical results are shown in **Figure 4.14**. The assays were repeated 9 times and the results were obtained with 67 % reproducibility.

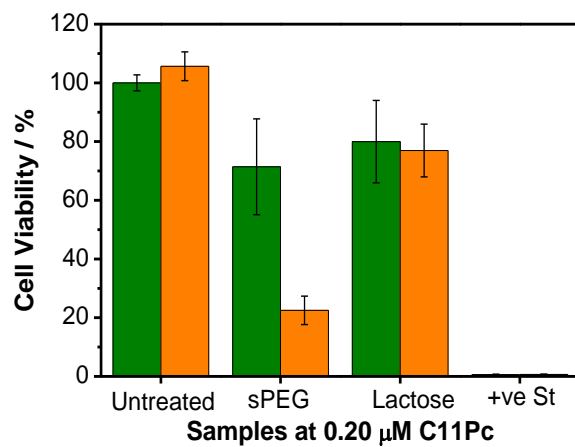


Figure 4.14. CellTiter-Blue® cell viability assay for SK-BR-3 cells incubated with C11Pc-sPEG-AuNPs (sPEG) or lactose-C11Pc-AuNPs (lactose) for 3 h. Cells were either irradiated with a 633 nm HeNe laser (orange) or non-irradiated (green). Untreated refers to cells only treated with growth medium. Staurosporine (+ve St) was used as a positive control for cytotoxicity. Error bars represent the SD ($n = 3$) within a 95 % confidence interval.

The results shown in **Figure 4.14** show low dark toxicity for the samples treated with either C11Pc-sPEG-AuNPs or lactose-C11Pc-AuNPs. Following irradiation, phototoxicity was only induced in cell samples treated with the C11Pc-sPEG-AuNPs, leading to 77 % cell death. These results suggest that the lactose-C11Pc-AuNPs are not effective for PDT and the lactose ligand is not enhancing the uptake and subsequent PDT effect. In an attempt to improve these results reported above, the SK-BR-3 cells were further treated with either lactose-C11Pc-AuNPs or C11Pc-sPEG-AuNPs increasing the incubation period from 3 h to 24 h. Increasing the incubation period with the nanoparticles could enhance the uptake by the SK-BR-3 cells and lead to more reliable results. CellTiter-Blue® and MTT cell viability assays were performed. The results for

the CellTiter-Blue® assay are shown in **Figure 4.15**. In this case, the reproducibility was significantly improved since for 4 repetitions of this assay, 75 % of the times the results reported below were obtained.

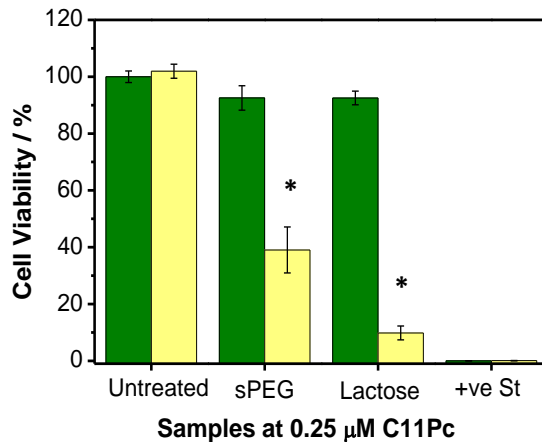


Figure 4.15. CellTiter-Blue® cell viability assay for SK-BR-3 cells incubated with C11Pc-sPEG-AuNPs (sPEG) or lactose-C11Pc--AuNPs (lactose) for 24 h. Cells were either irradiated with a 633 nm HeNe laser (yellow) or non-irradiated (green). Untreated refers to cells only treated with growth medium. Staurosporine (+ve St) was used as a positive control for cytotoxicity. Error bars represent the SD ($n = 3$) within a 95 % confidence interval. Statistically significant difference between C11Pc-sPEG-AuNPs and lactose-C11Pc-AuNPs is indicated by * at $P < 0.006$, obtained using a two-tailed Student's *t*-test, where $P < 0.05$ is considered statistically significant.

The results shown in **Figure 4.15** suggest that, following a 24 h incubation with the AuNPs, there is targeting *via* the lactose ligand towards the SK-BR-3 cells, as confirmed by the P values that show there is a statistically significant difference between the samples. The samples treated with lactose-C11Pc-AuNPs induced up to 90 % cell death, while the samples treated with C11Pc-sPEG-AuNPs only led to 61 % cell death. Surprisingly, the cells treated with C11Pc-sPEG-AuNPs for 24 h were killed less efficiently than those cells treated with C11Pc-sPEG-AuNPs for 3 h (77 % cell death), see **Figure 4.14**. The longer incubation period of 24 h enables the cancer cells to grow for a longer period of time. Therefore, if there is a plateau in the level of C11Pc-sPEG-AuNPs internalised, this could help explain why less cells die after 24 h incubation compared to 3 h incubation. With an increased growth of cells and similar levels of C11Pc-sPEG-AuNPs internalised, the cell death is not as high.

In order to evaluate whether the galectin-1 receptor is involved in this possible targeting by lactose towards SK-BR-3 cells, an InCell ELISA was performed, following the procedure described in **section 2.3.11**. InCell ELISA was used to detect the amount of galectin-1 on the surface of the cells. As explained in **section 3.2.9**, prior to treating the cells with anti-galectin1 antibody, the cells were incubated with either lactose-C11Pc-AuNPs or C11Pc-sPEG-AuNPs for 24 h. This treatment can lead to the targeting of the galectin-1 receptors on the surface of the cells, which would then be no longer available for the anti-galectin1 primary antibody during the ELISA. Therefore, the lactose-C11Pc-AuNPs should produce a lower absorbance signal as compared to C11Pc-sPEG-AuNPs, in which all the galectin-1 receptors are free, if selective targeting between lactose and galectin-1 is taking place. The results, shown in **Figure 4.16**, indicate that the levels of galectin-1 after treatment with either the lactose-C11Pc-AuNPs or the C11Pc-sPEG-AuNPs are similar to the levels of galectin-1 in untreated SK-BR-3 cells. These results suggest that the galectin-1 receptor is not involved in lactose targeting of SK-BR-3 cells. Other galactose-binding receptors on the surface of SK-BR-3 cells, such as the GLUT1 receptor previously discussed, should be studied to verify the possible selective targeting by lactose. This could be done using an InCell ELISA or *via* Western blotting, with the specific antibodies towards the GLUT1 receptor.

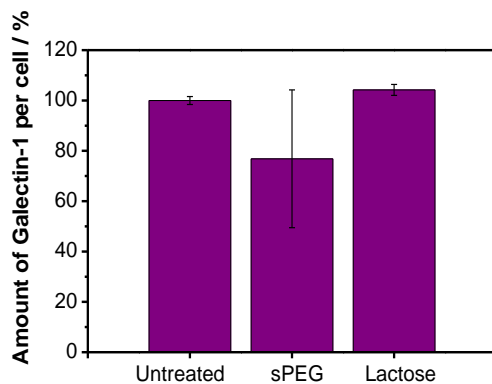


Figure 4.16. InCell ELISA for the detection of galectin-1 on the surface of SK-BR-3 cells showing the normalised value of galectin-1 per cell number in each sample. Untreated refers to cells treated with McCoy's 5A medium only, for 24 h; sPEG refers to cells treated with C11Pc-sPEG-AuNPs for 24 h; and Lactose refers to cells treated with lactose-C11Pc-AuNPs for 24 h. Error bars represent the SD ($n = 3$) within a 95 % confidence interval.

The results reported in this section of the thesis suggest that targeting SK-BR-3 cells with lactose-C11Pc-AuNPs requires a 24 h incubation with the nanoparticles before any

cytotoxic effects can be observed. Additionally, an indication of targeting was found as the levels of cell death induced by the lactose-C11Pc-AuNPs (90 %) were much higher than those induced by the C11Pc-sPEG-AuNPs (61 %). However, an InCell ELISA suggested that galectin-1 is not involved as the receptor for such lactose targeting. Other receptors, overexpressed on the surface of SK-BR-3 cells, should be investigated to establish why the lactose-C11Pc-AuNPs preferentially induce a significant PDT effect following a 24 h incubation.

4.2.6. Synthesis and characterisation of lactose-C3Pc-AuNPs

The use of C3Pc as the photosensitiser in the lactose-AuNPs system rather than the C11Pc could be a way to increase the targeting ability of lactose. C3Pc has a shorter carbon chain than C11Pc and thus it allows the lactose ligand to extend slightly further away from the surface of the AuNPs than C3Pc photosensitiser. As a result, the lactose ligand should be able to interact with galectin-1, or other receptors, on the surface of the cells easier without hinderance by the longer chain attached to the Pc macrocycle. This can be readily seen in **Figure 4.17**, where a schematic representation of both the lactose-C11Pc-AuNPs and the lactose-C3Pc-AuNPs is shown.

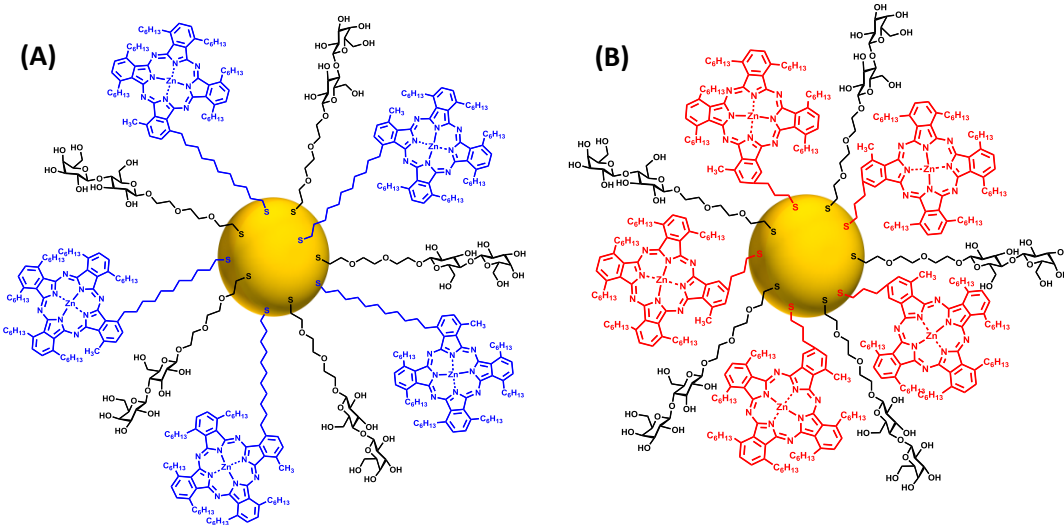


Figure 4.17. Schematic representation of (A) lactose-C11Pc-AuNPs and (B) lactose-C3Pc-AuNPs.

The synthesis of lactose-C3Pc-AuNPs was performed *via* the optimal method described for the lactose-C11Pc-AuNPs in **section 2.3.2**. The use of lactose as a means to provide aqueous solubility to the phthalocyanine-gold nanoparticle system is more effective with the C3Pc than the C11Pc. This is possibly related to the shorter nature of the C3Pc carbon chain, which allows the lactose to surround the C3Pc molecule. The synthesis of the lactose-C3Pc-AuNPs is thus more facile and gives a higher yield than the synthesis of lactose-C11Pc-AuNPs. The higher yield of lactose-C3Pc-AuNPs is the first advantage of using the C3Pc as compared to C11Pc. The UV-vis extinction spectrum and an image of the synthesised lactose-C3Pc-AuNPs dissolved in MES buffer are shown in **Figure 4.18 A** and **B** respectively. The extinction spectrum clearly shows the characteristic C3Pc phthalocyanine absorption band at *ca.* 698 nm and the solution presents a deep blue colour, a lot more intense than that observed for the lactose-C11Pc-AuNPs (**Figure 4.6**) because, in the final 5 mL solutions of synthesised AuNPs, the amount of C3Pc (1.8×10^{-8} mol) immobilised in the AuNPs is significantly greater than that of C11Pc (7.2×10^{-9} mol).

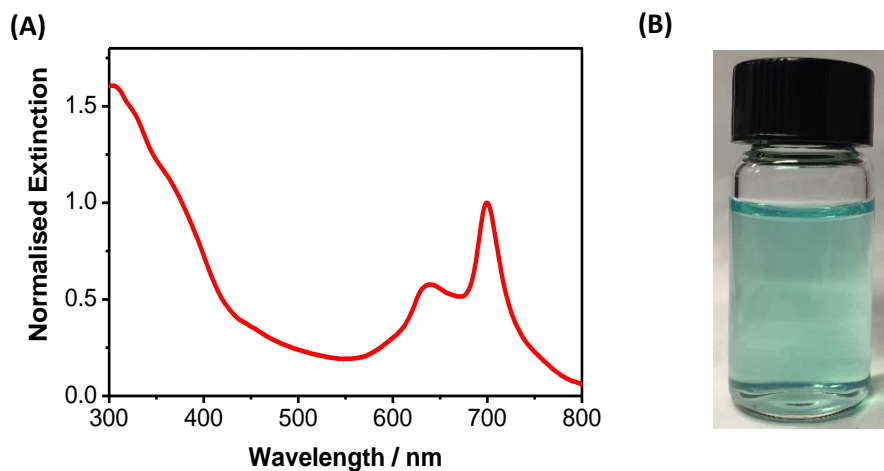


Figure 4.18. **(A)** UV-vis extinction spectrum of lactose-C3Pc-AuNPs and **(B)** image showing a vial containing a solution of the synthesised lactose-C3Pc-AuNPs in MES buffer.

The synthesised lactose-C3Pc-AuNPs were further characterised using TEM to evaluate their mean size. TEM analysis indicated that the lactose-C3Pc-AuNPs had an average diameter of 3.10 ± 1.32 nm, following analysis of 466 nanoparticles, with a median value of 2.72 ± 1.74 nm. TEM images of the lactose-C3Pc-AuNPs, together with a histogram showing their size distribution, are shown in **Figure 4.19**. The size

distribution is slightly skewed to the left. In these situations, the median value could sometimes be taken as a better representation of the population than the mean.⁷⁵

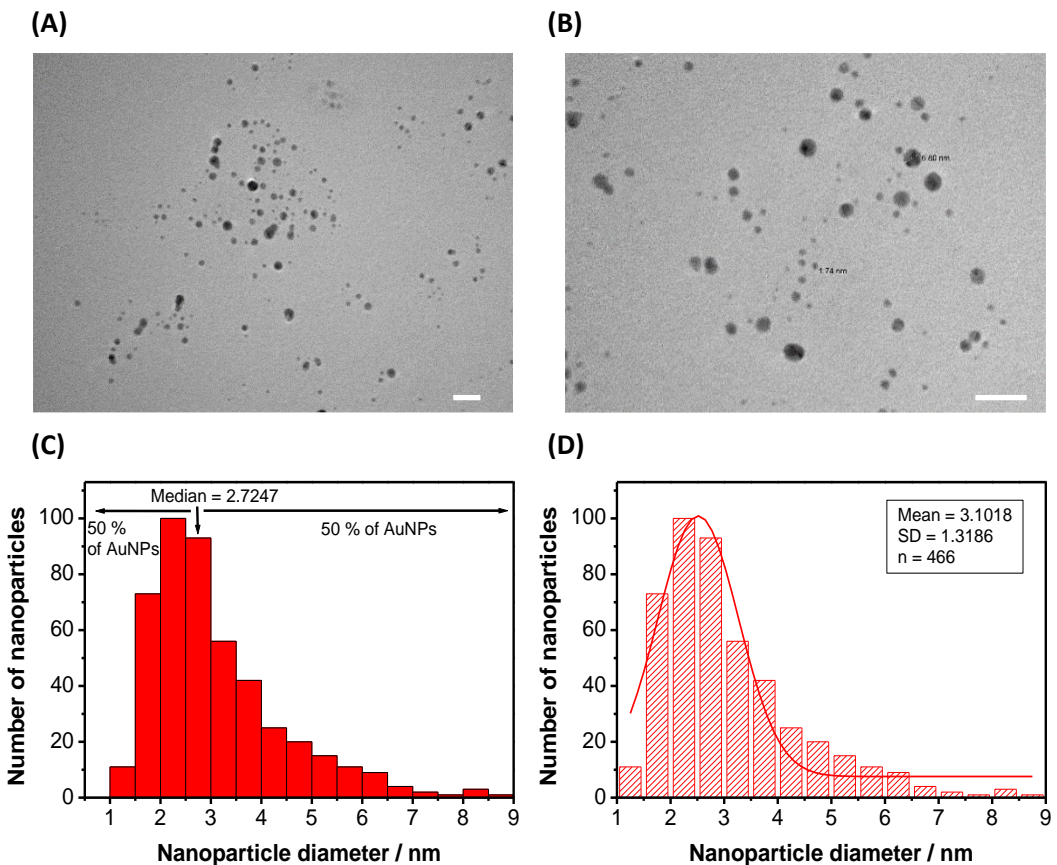


Figure 4.19. **(A-B)** Transmission electron micrographs of a sample of lactose-C3Pc-AuNPs, where the scale bars represent 20 nm. **(C)** Histogram of the lactose-C3Pc-AuNPs with a median value of 2.72 ± 1.74 nm ($n = 466$). **(D)** Size distribution of the lactose-C3Pc-AuNPs showing the Gaussian fit, with an average size of 3.10 ± 1.32 nm ($n = 466$).

To confirm the production of ${}^1\text{O}_2$ by the lactose-C3Pc-AuNPs, the probe ABMA was used, as previously described in **sections 2.3.4** and **3.2.4**. The results confirm the photobleaching of ABMA in the presence of lactose-C3Pc-AuNPs as ${}^1\text{O}_2$ is being produced upon irradiation with a 633 nm HeNe laser (**Figure 4.20**). On the contrary, PEG-AuNPs not functionalised with C3Pc show no photobleaching, indicating the importance of the photosensitiser for the generation of ${}^1\text{O}_2$. The maximum amount of photobleaching of ABMA in the presence of lactose-C3Pc-AuNPs was calculated, following **Equation 3.4** in **section 3.2.4**, and it was found to be 2.5 ± 1.5 %. This value is higher to that obtained for the lactose-C11Pc-AuNPs (1.1 ± 0.7 %), which constitutes a

further advantage of the use of C3Pc over C11Pc, but similar to the value obtained for C3Pc-PEG-AuNPs ($2.5 \pm 1.5\%$) in **Chapter 3**.

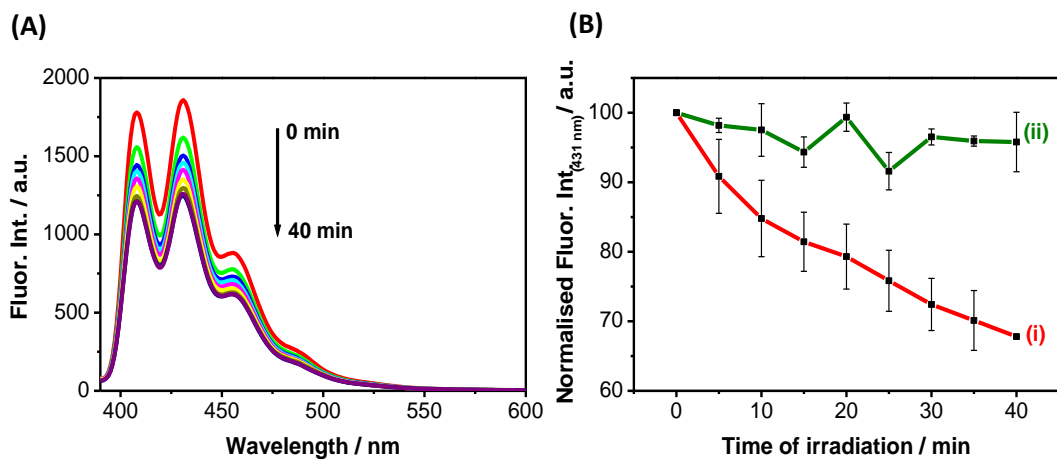


Figure 4.20. (A) Fluorescence emission spectra of ABMA showing the quenching of the fluorescence, thus confirming the formation of ${}^1\text{O}_2$ following irradiation at 633 nm of lactose-C3Pc-AuNPs. (B) Photobleaching of ABMA in the presence of (i) lactose-C3Pc-AuNPs (0.734 μM C3Pc) as a function of time. No photobleaching was observed for the control PEG-AuNPs (ii). The photobleaching shown for the control PEG-AuNPs is the same as that previously reported in **Figure 4.8**. Error bars represent the SD ($n = 3$) within a 95 % confidence interval.

4.2.7. Synthesis and characterisation of control C3Pc-sPEG-AuNPs

As previously described for C11Pc nanoparticles, control C3Pc-sPEG-AuNPs were synthesised. The sPEG chain used, see **Figure 4.9**, was shorter than that used in **Chapter 3** so that the molecule would provide a similar length to that of the lactose derivative in the lactose-C3Pc-AuNPs for a direct comparison of the cell viability results. A schematic representation of the C3Pc-sPEG-AuNPs is shown in **Figure 4.21**.

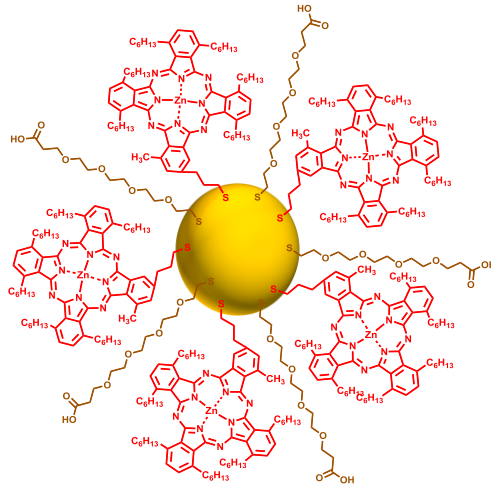


Figure 4.21. Schematic representation of the C3Pc-sPEG-AuNPs.

Similarly to the results obtained with the lactose-C3Pc-AuNPs, the C3Pc-sPEG-AuNPs were easier to synthesise and were produced with a higher yield than the C11Pc-sPEG-AuNPs. **Figure 4.22** shows the UV-vis extinction spectrum and an image of a solution of the synthesised C3Pc-sPEG-AuNPs.

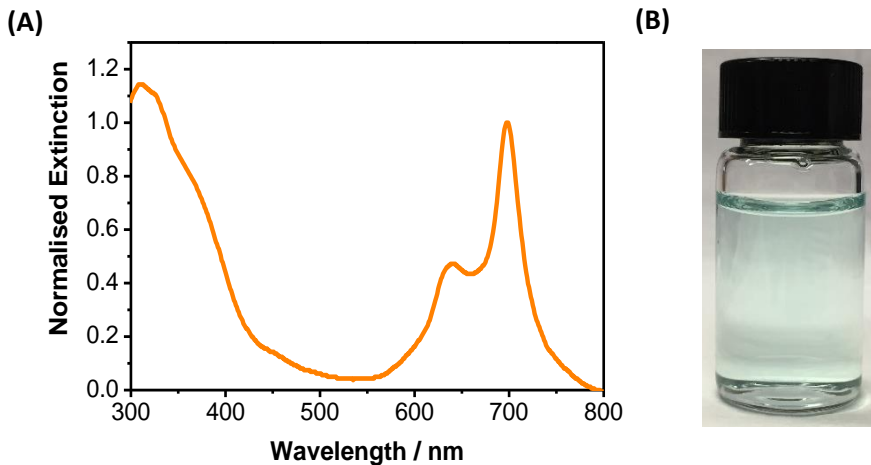


Figure 4.22. (A) UV-vis extinction spectrum of C3Pc-sPEG-AuNPs and (B) image showing a vial containing a solution of the synthesised C3Pc-sPEG-AuNPs in MES buffer.

4.2.8. *In vitro* studies in MDA-MB-231 cells using lactose-C3Pc-AuNPs

Initially, intracellular studies using lactose-C3Pc-AuNPs and their corresponding control C3Pc-sPEG-AuNPs were performed in MDA-MB-231 cells aiming to target the galectin-

1 receptor on the cell surface. The cells were incubated with the AuNPs for 3 h and CellTiter-Blue® cell viability assays were performed. The lactose-C3Pc-AuNPs and C3Pc-sPEG-AuNPs were added to the cells at various concentrations. Following incubation, the cells were washed to eliminate all the non-internalised AuNPs, irradiated for 6 min with a 633 nm HeNe laser and cell viability was measured *ca.* 48 h following PDT. The results are shown in **Figure 4.23**. Reproducibility for these assays was found to be good since the same results were obtained the three times the assays were performed.

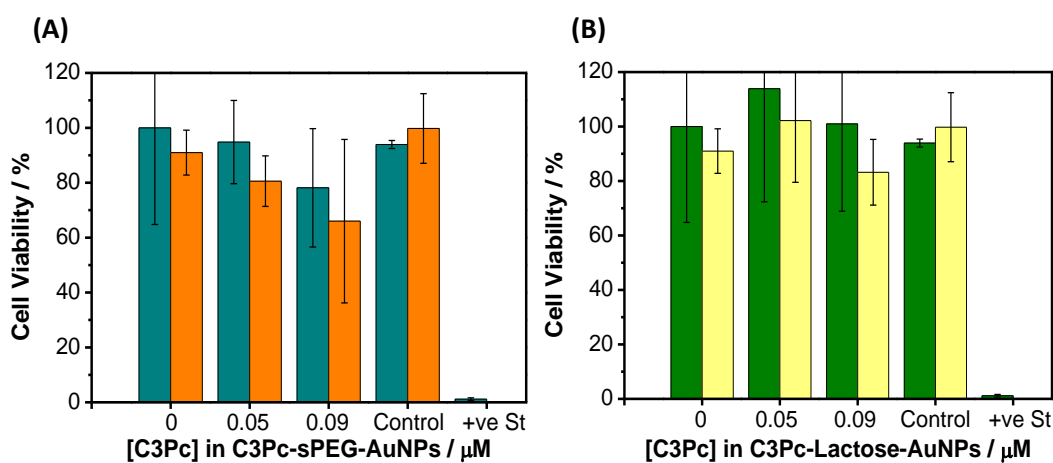


Figure 4.23. CellTiter-Blue® cell viability assay results for MDA-MB-231 cells incubated with (A) C3Pc-sPEG-AuNPs or (B) lactose-C3Pc-AuNPs for 3 h. Cells were either irradiated with a 633 nm HeNe laser (A orange, B yellow) or non-irradiated (A dark cyan, B green). Control refers to samples treated with sPEG-AuNPs without the presence of the C3Pc photosensitiser. Staurosporine (+ve St) was used as a positive control for cytotoxicity. Error bars represent the SD ($n = 3$) within a 95 % confidence interval.

As it can be seen from **Figure 4.23**, neither the lactose-C3Pc-AuNPs nor the C3Pc-sPEG-AuNPs produce any visible cell death following a 3 h incubation and irradiation with the 633 nm laser. Similar to the results obtained with lactose-C11Pc-AuNPs and C11Pc-sPEG-AuNPs following a 3 h incubation with MDA-MB-231 cells (see **Figure 4.11**), the incubation period appears to be too short for any efficient internalisation. Therefore, no cell death is seen following PDT. However, the concentrations reported in **Figure 4.23** were lower than those used for the C11Pc photosensitiser ($0.25 \mu\text{M}$). To confirm that the concentration was not the reason why cell death was not observed, the concentration of the C3Pc photosensitiser in both lactose-C3Pc-AuNPs and C3Pc-sPEG-AuNPs was increased to $0.20 \mu\text{M}$ and a further cell viability assay was performed

(Figure 4.24). The results shown in Figure 4.24 confirmed that the concentration was not the issue as, with a higher concentration of C3Pc, cell death is still negligible following PDT.

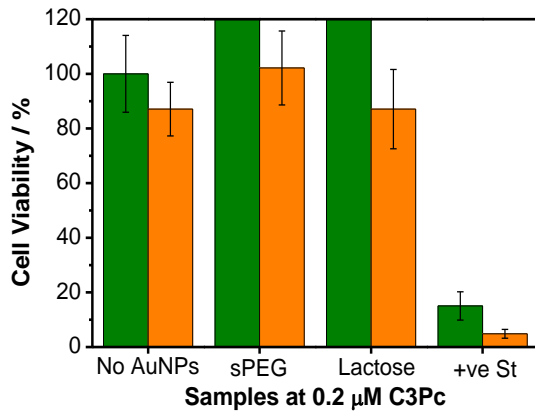


Figure 4.24. MTT cell viability assay for MDA-MB-231 cells incubated with C3Pc-sPEG-AuNPs (sPEG) or lactose-C3Pc-AuNPs (lactose) for 3 h. Cells were either irradiated with a 633 nm HeNe laser (orange) or non-irradiated (green). No AuNPs refers to cells treated with growth medium only. Staurosporine (+ve St) was used as a positive control for cytotoxicity. Error bars represent the SD ($n = 3$) within a 95 % confidence interval.

Since higher concentrations did not lead to increase in cell death, it was decided to increase the incubation period of the nanoparticles with the cells prior to irradiation. MDA-MB-231 cells were incubated with lactose-C3Pc-AuNPs and C3Pc-sPEG-AuNPs (0.20 μ M C3Pc) for 24 h. CellTiter-Blue® and MTT cell viability assays were performed *ca.* 48 h after PDT. The assays were repeated seven times. Typical results (63 % reproducibility) are shown in Figure 4.25.

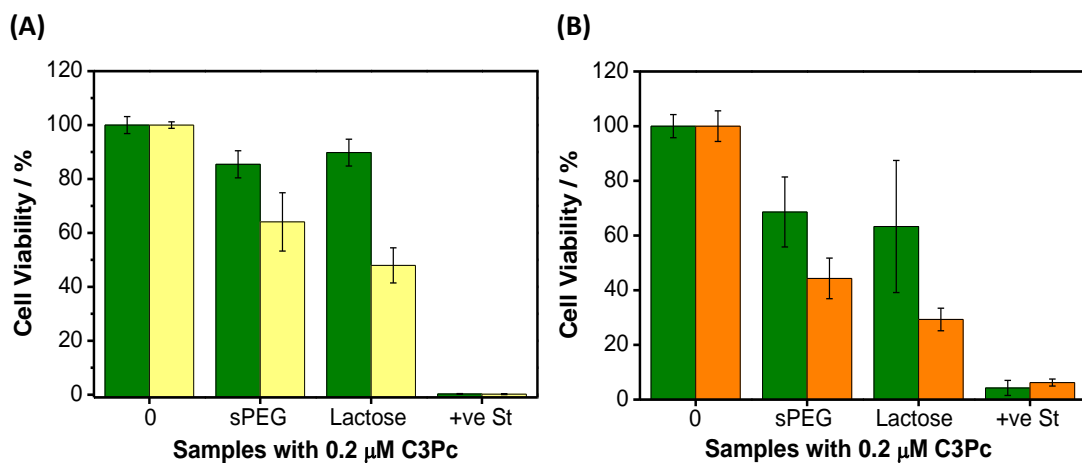


Figure 4.25. **(A)** CellTiter-Blue® and **(B)** MTT cell viability assays for MDA-MB-231 cells incubated with C3Pc-sPEG-AuNPs (sPEG) or lactose-C3Pc-AuNPs (lactose) for 24 h. Cells were either irradiated with a 633 nm HeNe laser (**A** yellow, **B** orange) or non-irradiated (green). Staurosporine (+ve St) was used as a positive control for cytotoxicity. Error bars represent the SD ($n = 3$) within a 95 % confidence interval. No statistically significant difference between C3Pc-sPEG-AuNPs and lactose-C3Pc-AuNPs, as indicated by the P values ($P < 0.09$) obtained using a two-tailed Student's *t*-test, where $P < 0.05$ is considered statistically significant.

As shown in **Figure 4.25**, following a 24 hour incubation period, the results are different to those obtained previously. Both the lactose-C3Pc-AuNPs and the C3Pc-sPEG-AuNPs are shown to induce cell death following irradiation, while there is minimal dark toxicity. The results are supported by both cell viability assays, CellTiter-Blue® and MTT. The MTT assay (**Figure 4.25 B**) has larger error bars as compared to the CellTiter-Blue® assay (**Figure 4.25 A**). This was previously discussed in **Chapter 3 section 3.2.6**. Even with the large error bars, both the MTT and the CellTiter-Blue® assays give similar results, showing cell death only after irradiation. Additionally, there is an indication of improved PDT with the lactose-C3Pc-AuNPs with possible targeting *via* lactose (**Figure 4.25**), but this indication is not statistically significant as shown by the P values obtained ($P < 0.09$) using a two-tailed Student's *t*-test. The values of cell death, taken from the CellTiter-Blue® assay, are higher for the samples treated with lactose-C3Pc-AuNPs (52 %) than for samples treated with C3Pc-sPEG-AuNPs (36 %) (**Figure 4.25 A**).

In order to confirm the potential targeting of lactose-C3Pc-AuNPs towards galectin-1 on the surface of MDA-MB-231 cells, an InCell ELISA for the detection of galectin-1 was

performed. The InCell ELISA was performed using the same method previously described in **section 4.2.5**, incubating the AuNPs for both 3 h and 24 h. The results are shown in **Figure 4.26**.

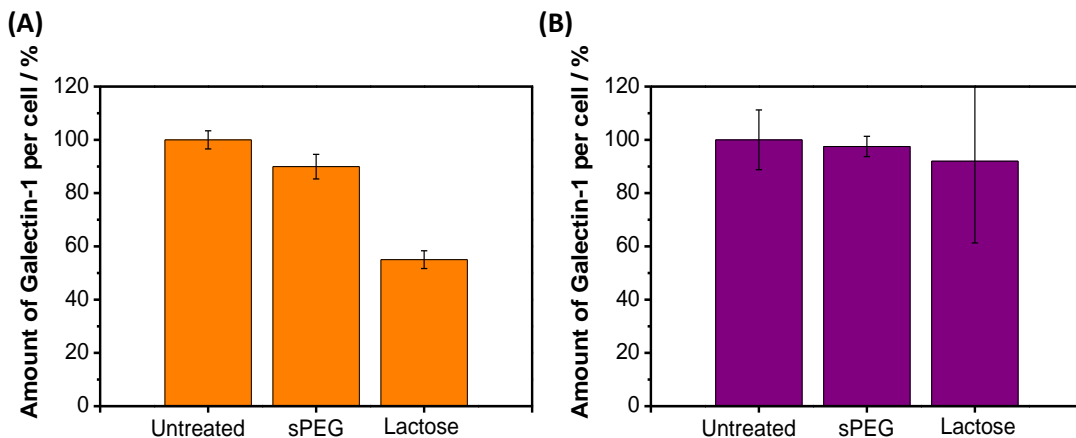


Figure 4.26. InCell ELISA for the detection of galectin-1 on the surface of MDA-MB-231 cells. The graphs show the normalised values of galectin-1 per cell in each sample. The samples were incubated with C3Pc-sPEG-AuNPs (sPEG) or lactose-C3Pc-AuNPs (lactose) for either **(A)** 3 h or **(B)** 24 h. Error bars represent the SD (n = 3) within a 95 % confidence interval.

The results from the InCell ELISA shown in **Figure 4.26 A** indicate that lactose selectively targets the galectin-1 receptor on the surface of the MDA-MB-231 cells following a 3 h incubation with the AuNPs. These results, however, do not match those results seen previously with the cell viability assays. The cell viability assays showed no cell death following a 3 h incubation with either lactose-C3Pc-AuNPs or C3Pc-sPEG-AuNPs (**Figures 4.23-4.24**). This could possibly be due to a low uptake of nanoparticles by the cells following a 3 h incubation and hence why no cell death is observed. However, the galectin-1 receptors on the surface of the MDA-MB-231 cells are selectively recognising the lactose ligand on the AuNPs and they appear to require longer incubation periods for complete internalisation.

Additionally, when the AuNPs were incubated for 24 h, **Figure 4.26 B**, there is also an indication of selective targeting. However, the error bars from the samples treated with lactose-C3Pc-AuNPs are so large that it cannot be completely confirmed. Selective targeting *via* the galectin-1 receptor on the surface of MDA-MB-231 cells can

potentially explain the higher cell death seen for samples treated with lactose-C3Pc-AuNPs as compared to the control C3Pc-sPEG-AuNPs (**Figure 4.25**) following PDT.

4.2.9. Studies of lactose-C3Pc-AuNPs internalisation by MDA-MB-231 cells

The cell viability assays reported in **section 4.2.8** showed that cell death was induced by lactose-C3Pc-AuNPs when they were incubated with the MDA-MB-231 cells for 24 h. To understand what the difference in AuNPs uptake following either 3 h or 24 h incubation was due to, internalisation studies using confocal microscopy were performed, as described in **section 2.3.9**. MDA-MB-231 cells were incubated with the lactose-C3Pc-AuNPs for either 3 h or 24 h, washed to remove all the non-internalised AuNPs and irradiated to visually assess the PDT effect. Following irradiation, the cells were incubated for a further *ca.* 24 h prior to imaging. The results are shown in **Figure 4.27** for the cells incubated with lactose-C3Pc-AuNPs for 3 h and **Figure 4.28** for the cells incubated with lactose-C3Pc-AuNPs for 24 h.

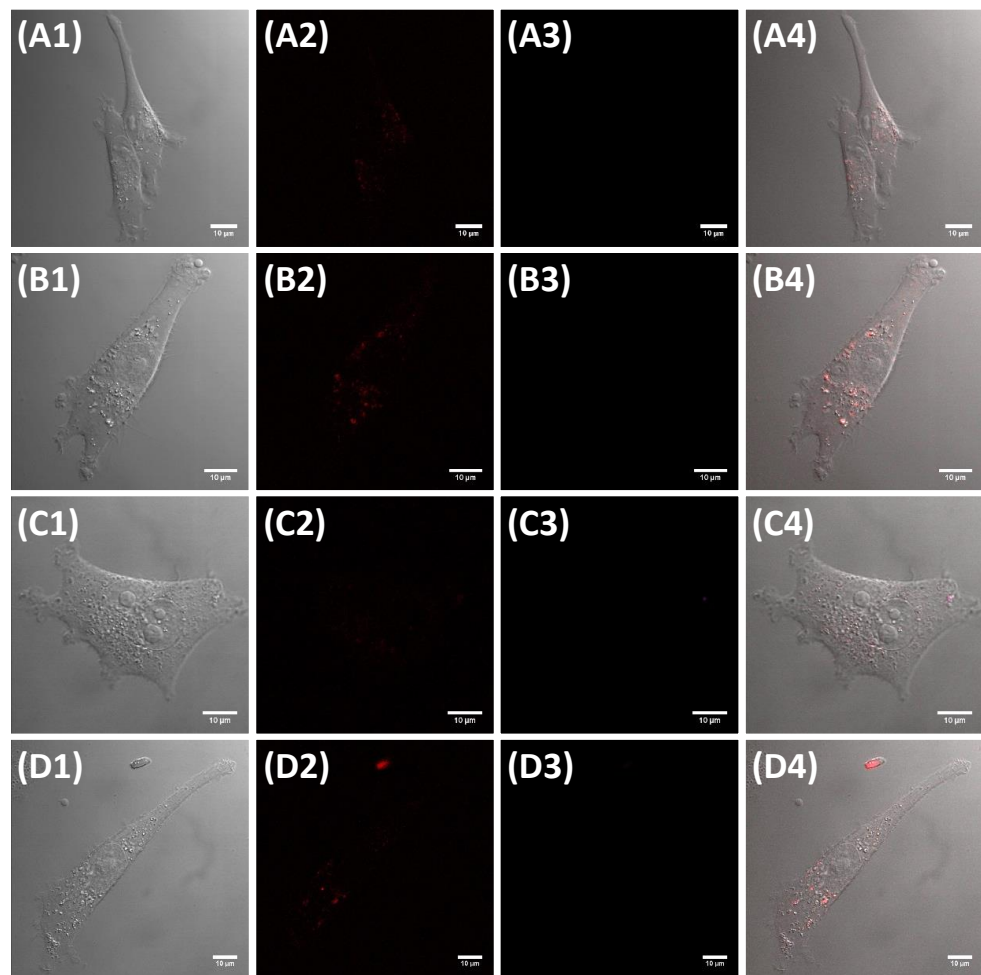


Figure 4.27. Confocal fluorescence microscopy images of MDA-MB-231 cells. **(A, C)** control cells incubated only with growth medium for 3 h and **(B, D)** cells incubated with lactose-C3Pc-AuNPs for 3 h. The cells were either non-irradiated **(A, B)** or irradiated **(C, D)** with a 633 nm HeNe laser. All samples were imaged 24 h following treatment. Images taken from: **1**) DIC, **2**) fluorescence from C3Pc collected in the red channel ($\lambda_{\text{ex}} = 633$ nm; above 650 nm), **3**) fluorescence from propidium iodide collected in the pink channel ($\lambda_{\text{ex}} = 543$ nm; 560-615 nm) and **4**) composite images of DIC, fluorescence from C3Pc collected in the red channel and fluorescence from propidium iodide collected in the pink channel. Scale bars represent 10 μm .

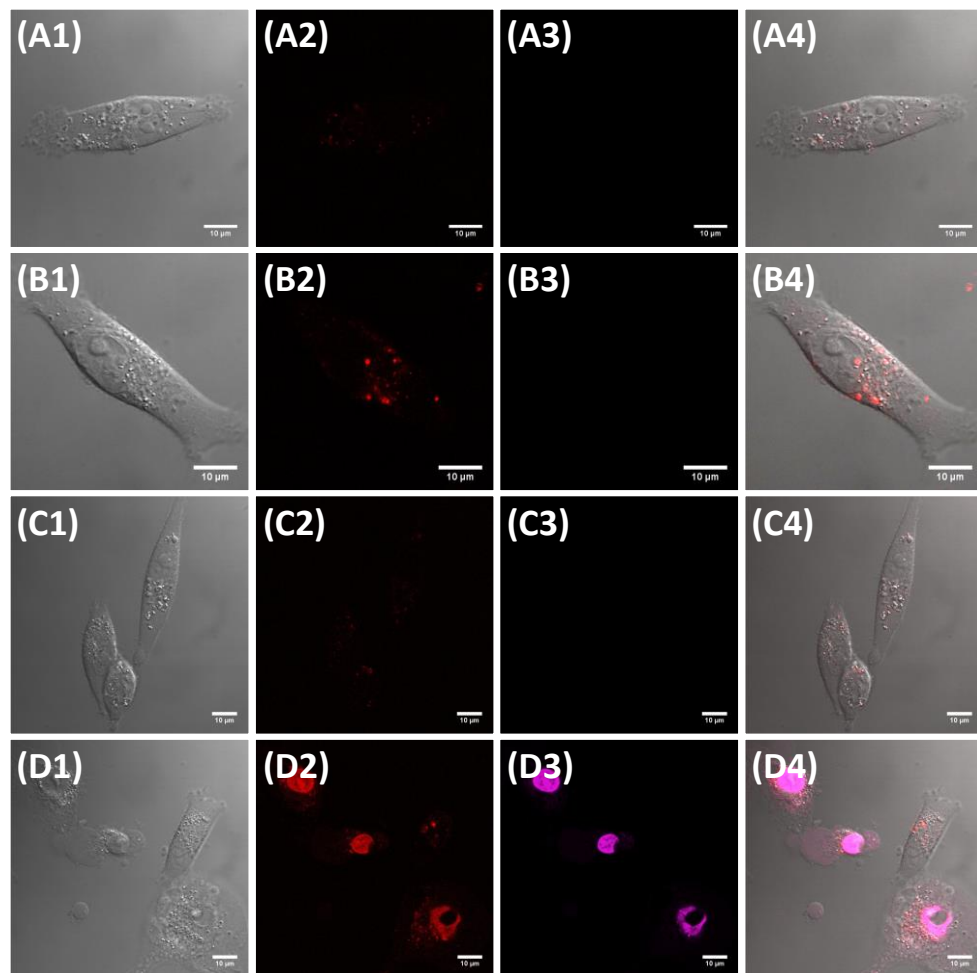


Figure 4.28. Confocal fluorescence microscopy images of MDA-MB-231 cells. **(A, C)** control cells incubated only with growth medium for 24 h and **(B, D)** cells incubated with lactose-C3Pc-AuNPs for 24 h. The cells were either non-irradiated **(A, B)** or irradiated **(C, D)** with a 633 nm HeNe laser. All samples were imaged 24 h following treatment. Images taken from: **1)** DIC, **2)** fluorescence from C3Pc collected in the red channel ($\lambda_{\text{ex}} = 633$ nm; above 650 nm), **3)** fluorescence from propidium iodide collected in the pink channel ($\lambda_{\text{ex}} = 543$ nm; 560-615 nm) and **4)** composite images of DIC, fluorescence from C3Pc collected in the red channel and fluorescence from propidium iodide collected in the pink channel. Scale bars represent 10 μ m.

Figure 4.27 B shows that there is low internalisation of lactose-C3Pc-AuNPs by MDA-MB-231 cells following a 3 h incubation. The fluorescence seen in the red channel is similar in the cells treated with lactose-C3Pc-AuNPs and the control cells that were only treated with growth medium during the incubation period (**Figure 4.27 A**). This is an indication that there is some background fluorescence in the MDA-MB-231 cell line. In addition, following a 3 h incubation period, the internalisation of lactose-C3Pc-AuNPs

is not significant enough to see any cytotoxicity following PDT as shown in **Figure 4.27 D**, highlighted by the lack of propidium iodide staining.

When the MDA-MB-231 cells were subjected to a 24 h incubation period, the results were different. In this case, there is a significant difference in the red fluorescence seen in the control cells treated only with growth medium (**Figure 4.28 A**) as compared to those cells treated with lactose-C3Pc-AuNPs (**Figure 4.28 B**). Additionally, the red fluorescence seen for the cells treated with lactose-C3Pc-AuNPs for 24 h (**Figure 4.28 B**) is significantly more intense than that seen after only a 3 h incubation period (**Figure 4.27 B**). As a result, following irradiation with a 633 nm HeNe laser for 6 min, cell death can be visualised in the MDA-MB-231 cells treated with lactose-C3Pc-AuNPs for 24 h, as confirmed by the staining with the dead cell marker propidium iodide and the change in cell morphology, *i.e.*, disintegration of the cell membrane, (**Figure 4.28 D**). After irradiation, there is a mixture of dead and live cells in the samples since the cell viability was 48 %, as indicated by the cell viability assays (**Figure 4.25**). These results indicate that the lactose-C3Pc-AuNPs should be incubated for 24 h with the MDA-MB-231 cells in order to achieve an efficient internalisation that will thus lead to cell death following PDT treatment.

MDA-MB-231 cells are thus efficiently targeted using the lactose-C3Pc-AuNPs when they are incubated with the AuNPs for 24 h. These results present an improvement to those seen when C11Pc was used as the photosensitiser. Lactose-C11Pc-AuNPs were unable to induce cytotoxicity following PDT of the MDA-MB-231 cells at either 3 h or 24 h incubation. It can be concluded that the use of C3Pc rather than C11Pc does facilitate the targeting ability of lactose towards MDA-MB-231 cells.

4.2.10. *In vitro* studies in SK-BR-3 cells using lactose-C3Pc-AuNPs

Lactose-C11Pc-AuNPs were shown to induce targeting and cytotoxicity following PDT in SK-BR-3 cells after a 24 h incubation (**section 4.2.5**). Therefore, the lactose-C3Pc-AuNPs were also tested in SK-BR-3 cells to confirm whether these nanoparticles would improve the results previously shown by the lactose-C11Pc-AuNPs.

SK-BR-3 cells were incubated with lactose-C3Pc-AuNPs and their corresponding control C3Pc-sPEG-AuNPs for 3 h at various C3Pc concentrations. Following incubation, the cells were washed to remove all of the non-internalised AuNPs and then irradiated with a 633 nm HeNe laser for 6 min. Before measuring cell viability using a CellTiter-Blue® cell viability assay, the cells were further incubated for *ca.* 48 h. The results, as shown in **Figure 4.29**, indicate that both lactose-C3Pc-AuNPs and C3Pc-sPEG-AuNPs were effectively internalised by the cells. Furthermore, all of the nanoparticle samples show minimal dark toxicity, which highlights that they were not toxic in the absence of light. More importantly, both C3Pc-lactose-AuNPs and C3Pc-sPEG-AuNPs show cell death following irradiation. However, the targeting *via* lactose is only limited as the amount of cell death induced by lactose-C3Pc-AuNPs (95 % with 0.20 μ M C3Pc) is similar to that induced by C3Pc-sPEG-AuNPs (92 % with 0.20 μ M C3Pc), indicating both types of nanoparticles are internalised in a similar manner. However, at the lowest concentration of 0.5 μ M C3Pc, there is an indication of targeting by lactose, as shown by the P values in **Figure 4.29**. The fact that the cell death values are lower than with higher concentration of lactose-C3Pc-AuNPs indicates that there could be an error in this part of the assay. The study of lower concentrations of C3Pc within the sample could help understand whether there is selective lactose targeting towards the SK-BR-3 cells. The present results show that, even though lactose is not inducing specific targeting, the nanoparticles are effective at inducing cell death following PDT after only a 3 h incubation period. The cell viability assays, repeated five times, were highly reproducible (80 %).

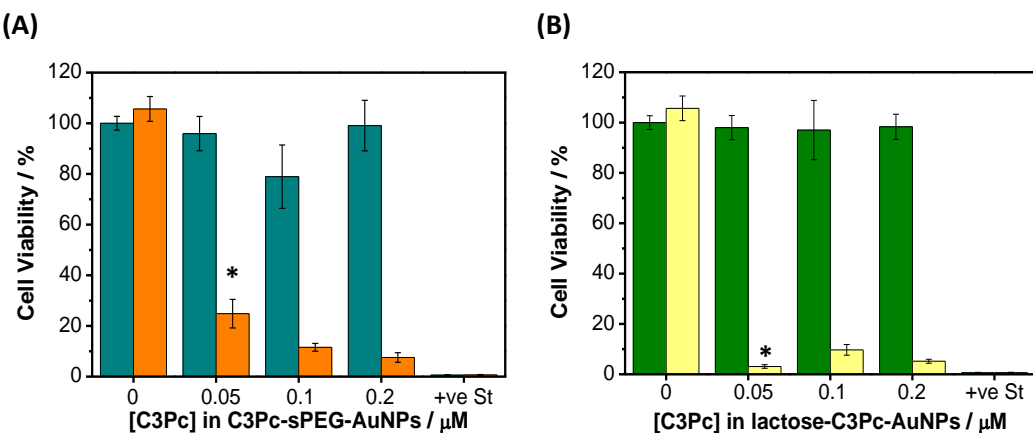


Figure 4.29. CellTiter-Blue® cell viability assay results for SK-BR-3 cells incubated with **(A)** C3Pc-sPEG-AuNPs or **(B)** lactose-C3Pc-AuNPs for 3 h. Cells were either irradiated with a 633 nm HeNe laser **(A** orange, **B** yellow) or non-irradiated (**A** dark cyan, **B** green). Staurosporine (+ve St) was used as a positive control for cytotoxicity. Error bars represent the SD ($n = 3$) within a 95 % confidence interval. Statistically significant difference between C3Pc-sPEG-AuNPs and lactose-C3Pc-AuNPs (0.05 μM C3Pc) is indicated by * at $P < 0.003$, obtained using a two-tailed Student's *t*-test, where $P < 0.05$ is considered statistically significant. At higher concentrations ($> 0.1 \mu\text{M}$), the difference is not statistically significant ($P < 0.2$).

The results shown in **Figure 4.29** display a marked improvement to those seen with lactose-C11Pc-AuNPs (see **Figure 4.14**), where after a 3 h incubation period no cell death was observed. For lactose-C11Pc-AuNPs, a 24 h incubation period was required before targeting and cytotoxicity was seen. Therefore, for comparison purposes, the lactose-C3Pc-AuNPs were also incubated with the SK-BR-3 cells for 24 h and the cell viability was assessed. SK-BR-3 cells were incubated for 24 h only with 0.20 μM C3Pc for both lactose-C3Pc-AuNPs and C3Pc-sPEG-AuNPs since this concentration produced the highest levels of cell death following a 3 h incubation. The results are shown in **Figure 4.30**. Following a 24 h incubation, the results are similar to those shown previously in **Figure 4.29**. There was cell death after irradiation for both types of AuNPs and only a slight indication that there could be targeting *via* lactose. The lactose-C3Pc-AuNPs induced 96 % cell death and C3Pc-sPEG-AuNPs induced 95 % cell death. The dark toxicity of the lactose-C3Pc-AuNPs did appear to be less than that observed for the C3Pc-sPEG-AuNPs.

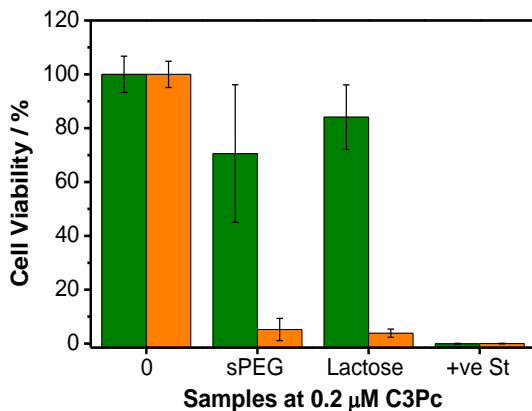


Figure 4.30. CellTiter-Blue® cell viability assay results for SK-BR-3 cells incubated with C3Pc-sPEG-AuNPs (sPEG) or lactose-C3Pc-AuNPs (lactose) (0.2 μ M C3Pc) for 24 h. Cells were either irradiated with a 633 nm HeNe laser (orange) or non-irradiated (green). Staurosporine (+ve St) was used as a positive control for cytotoxicity. Error bars represent the SD ($n = 3$) within a 95 % confidence interval. No statistically significant difference between C3Pc-sPEG-AuNPs and lactose-C3Pc-AuNPs, as confirmed by the P values ($P < 0.1$) obtained with a two-tailed Student's *t*-test, where $P < 0.05$ is considered to be statistically significant.

Once again, to confirm whether this limited targeting was due to the galectin-1 receptor on the surface of the SK-BR-3 cells, an InCell ELISA was performed. The results, shown in **Figure 4.31**, indicate that the levels of galectin-1 in untreated cells and cells treated with either lactose-C3Pc-AuNPs or C3Pc-sPEG-AuNPs are similar. Therefore, the results shown in **Figure 4.31** suggest that there is no effective targeting towards the galectin-1 receptor. These results are consistent with the fact that galectin-1 is not expressed in high amounts on the surface of SK-BR-3 cells.⁴⁸ As previously mentioned, other receptors such as the GLUT1 receptor, could be responsible for the selective targeting with galactose-containing carbohydrates. Further studies would need to be performed to confirm this possibility.

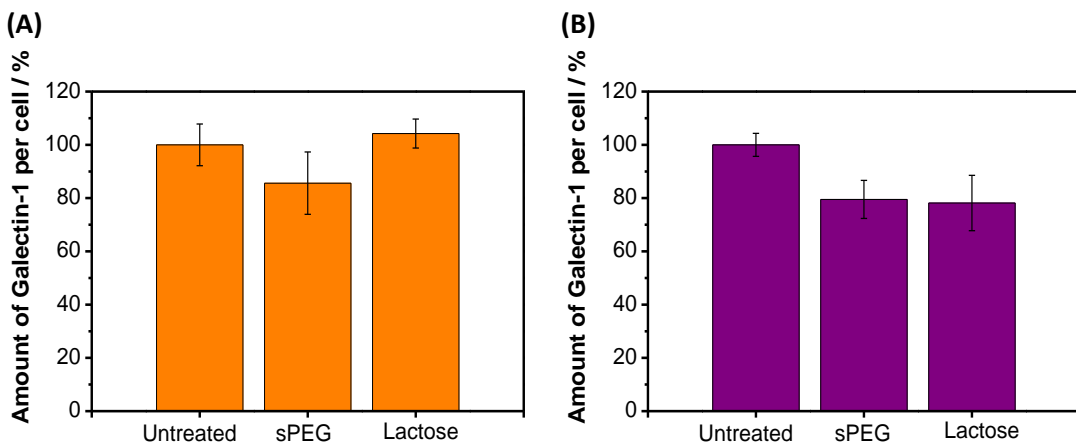


Figure 4.31. InCell ELISA for the detection of galectin-1 on the surface of SK-BR-3 cells. The figure shows the normalised values of galectin-1 per cell in each sample. The samples were incubated with C3Pc-sPEG-AuNPs (sPEG) or lactose-C3Pc-AuNPs (lactose) for either **(A)** 3 h or **(B)** 24 h. Error bars represent the SD ($n = 3$) within a 95 % confidence interval.

The results with SK-BR-3 cells suggest that the use of lactose-C3Pc-AuNPs should be preferred over lactose-C11Pc-AuNPs. Lactose-C3Pc-AuNPs induce cell death after only 3 h incubation, whereas the lactose-C11Pc-AuNPs require a longer incubation period of 24 h before any cell death following irradiation is observed.

4.2.11. Internalisation of lactose-C3Pc-AuNPs and PDT effect in SK-BR-3 cells

Confocal microscopy was used for a visual inspection of the SK-BR-3 cells following incubation and PDT with lactose-C3Pc-AuNPs. The lactose-C3Pc-AuNPs were incubated with the SK-BR-3 cells for 3 h, since this incubation period was enough to induce high cytotoxic effects following PDT (see **Figure 4.29**). The results for the confocal microscopy study are shown in **Figure 4.32** and they confirm the results obtained with the cell viability assays. SK-BR-3 cells show good internalisation of the lactose-C3Pc-AuNPs as the red fluorescence is intense (**Figure 4.32 B**) in contrast to control cells not incubated with any AuNPs (**Figure 4.32 A**), where there is no red fluorescence. Furthermore, cell death can be seen following irradiation with a 633 nm HeNe laser (**Figure 4.32 D**) indicated by the staining with the dead cell marker propidium iodide, in pink. To observe cell death, the presence of the lactose-C3Pc-AuNPs is essential, as

irradiation of the control cells not treated with AuNPs does not induce any cell death (Figure 4.32 C).

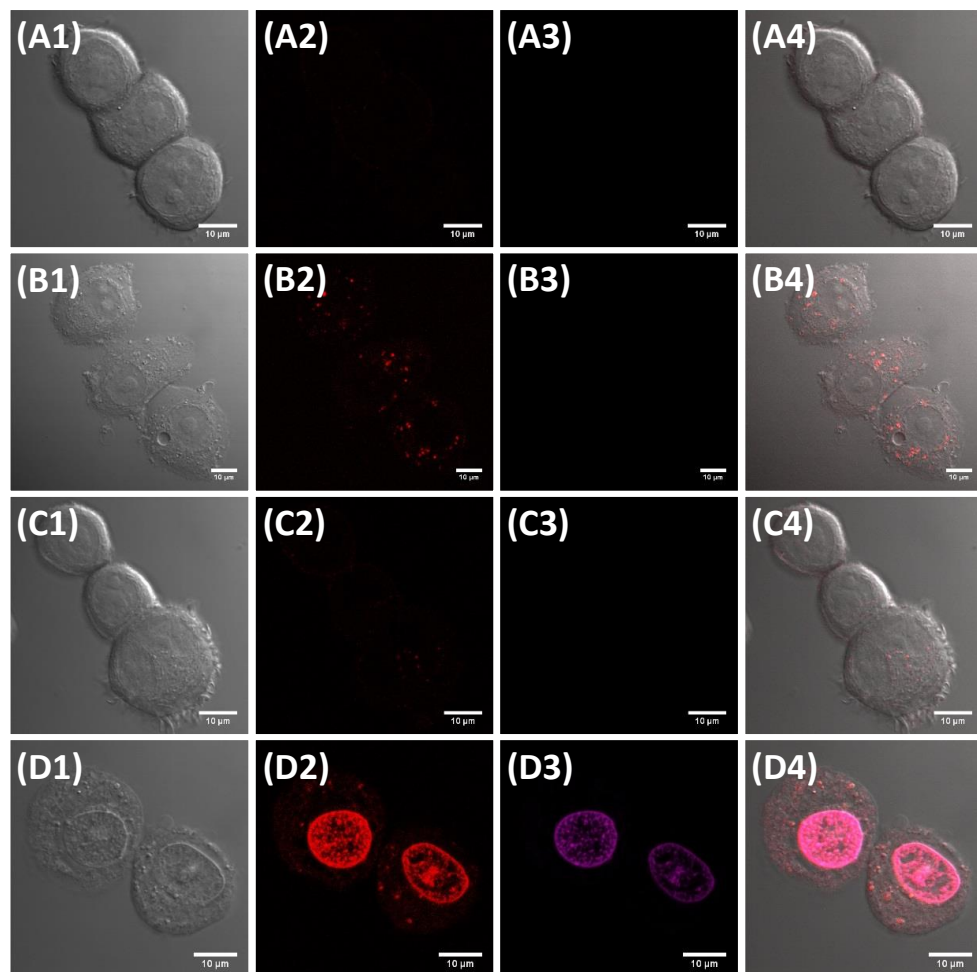


Figure 4.32. Confocal fluorescence microscopy images of SK-BR-3 cells. **(A, C)** control cells incubated only with growth medium for 3 h and **(B, D)** cells incubated with C3Pc-lactose-AuNPs for 3 h. The cells were either non-irradiated **(A, B)** or irradiated **(C, D)** with a 633 nm HeNe laser. All samples were imaged 24 hours following treatment. Images taken from: **1)** DIC, **2)** fluorescence from C3Pc collected in the red channel ($\lambda_{ex} = 633$ nm; above 650 nm), **3)** fluorescence from propidium iodide collected in the pink channel ($\lambda_{ex} = 543$ nm; 560-615 nm) and **4)** composite images of DIC, fluorescence from C3Pc collected in the red channel and fluorescence from propidium iodide collected in the pink channel. Scale bars represent 10 μ m.

4.2.12. Mechanism of cell death post-PDT by lactose-C3Pc-AuNPs

The ApoTox-Glo™ Triplex assay was performed to study the cell death mechanism that the SK-BR-3 and MDA-MB-231 cells undergo following PDT with the lactose-C3Pc-AuNPs and C3Pc-sPEG-AuNPs. The ApoTox-Glo™ Triplex assay measures cell viability, cell cytotoxicity and apoptosis as three different components. The mechanisms behind this assay were described in **section 3.2.14**.

The ApoTox-Glo™ Triplex assay was performed with the optimal incubation times found for each cell line, using the AuNPs with a 0.20 μ M C3Pc concentration. For SK-BR-3 cells, a short incubation time of 3 h with the lactose-C3Pc-AuNPs was enough to induce high levels of cytotoxicity after PDT (**section 4.2.10**). On the other hand, for MDA-MB-231 cells a longer incubation period of 24 h was required for cell death to be observed following PDT (**section 4.2.8**).

Following the procedure described in **section 2.3.12**, the triplex assay was performed *ca.* 4 h after the cells were treated with PDT. The incubation period post-PDT of 4 h is considerably lower than the 48 h used during the MTT and CellTiter-Blue® cell viability assays previously reported. However, it was chosen in order to reproduce the experiments reported in **section 3.2.14**, where a 48 h post-PDT incubation period was found to be too long for the ApoTox-Glo™ Triplex assay, which led to the degradation of the cytotoxicity and apoptosis biomarkers and thus produced erroneous results. The results for SK-BR-3 and MDA-MB-231 cells incubated with lactose-C3Pc-AuNPs and C3Pc-sPEG-AuNPs incubated for 3 h and 24 h, respectively, are shown in **Figure 4.33**.

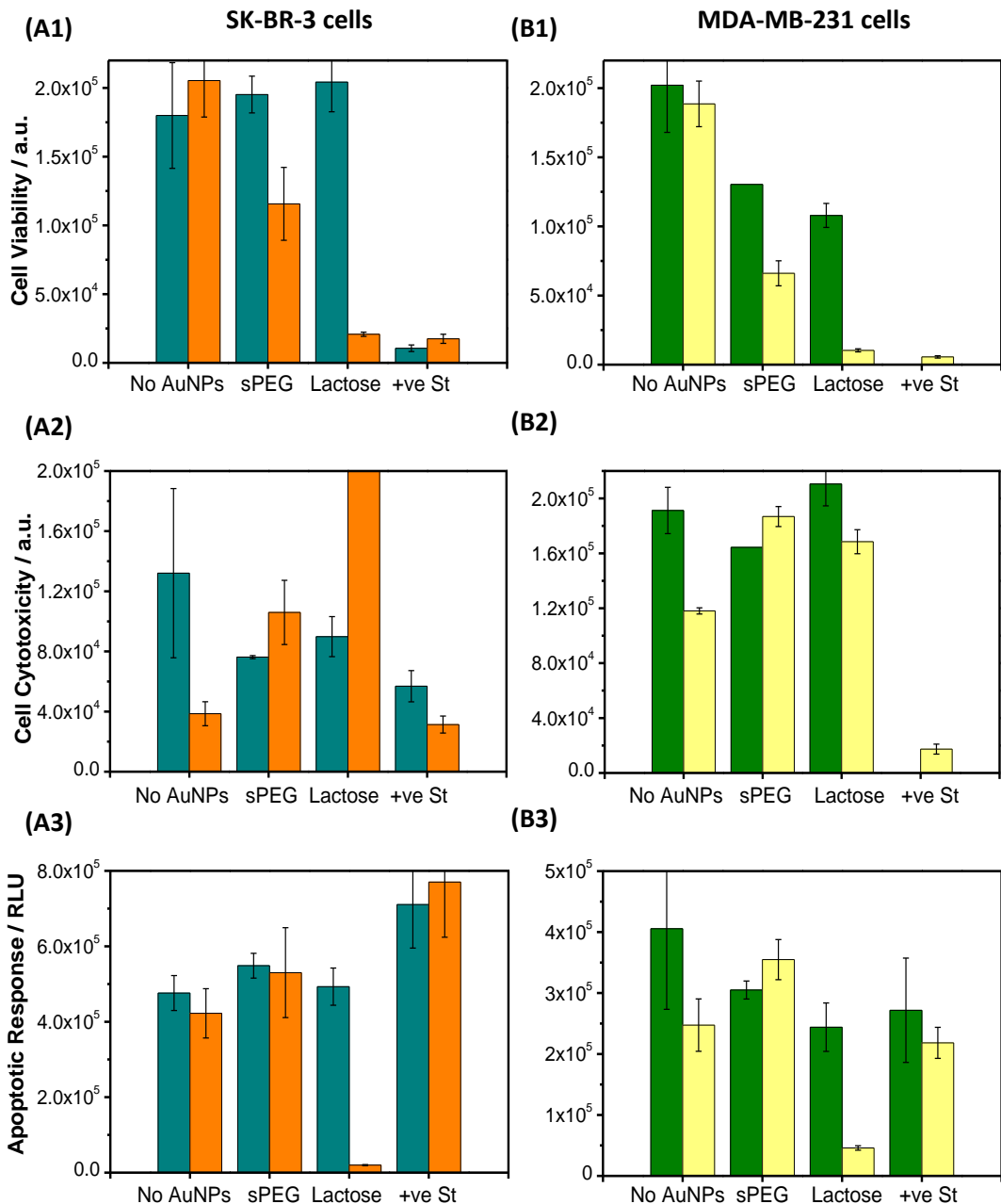


Figure 4.33. ApoTox-Glo™ Triplex assay for **(A)** SK-BR-3 cells incubated for 3 h and **(B)** MDA-MB-231 cells incubated for 24 h with lactose-C3Pc-AuNPs and C3Pc-sPEG-AuNPs (0.2 μ M C3Pc). Cells were either irradiated with a 633 nm HeNe laser (**A** orange, **B** yellow) or non-irradiated (**A** dark cyan, **B** green). The cells were treated with the triplex assay *ca.* 4 h following PDT. **(1)** Fluorescence from the GF-AFC substrate giving the cell viability values, **(2)** fluorescence from bis-AAF-R110 substrate giving the cell cytotoxicity values and **(3)** luminescence from the Caspase 3/7 substrate giving the values for apoptosis. The sample 'No AuNPs' refers to samples not incubated with any AuNPs used as the reference negative control. Staurosporine (+ve St) was used as a positive control for cytotoxicity *via* apoptosis. Error bars represent the SD ($n = 3$) within a 95 % confidence interval.

The results presented in **Figure 4.33** show the three different components of the ApoTox-Glo™ Triplex assay. For the viability part of the assay (**Figure 4.33 A1-B1**), the results indicate targeting by lactose in both SK-BR-3 and MDA-MB-231 cells. However, the values for cell death following irradiation to the samples treated with lactose-C3Pc-AuNPs (95 % MDA-MB-231 cells and 88 % SK-BR-3 cells) and C3Pc-sPEG-AuNPs (67 % MDA-MB-231 cells and 36 % SK-BR-3 cells) are not the same as those reported with the cell viability assays; lactose-C3Pc-AuNPs (52 % MDA-MB-231 cells and 95 % SK-BR-3 cells) and C3Pc-sPEG-AuNPs (36 % MDA-MB-231 cells and 92 % SK-BR-3 cells). The Triplex assay was only performed once, whereas the cell viability assays were performed multiple times, as previously reported. Therefore, the values obtained from the cell viability assays are taken to be more accurate than those for the ApoTox-Glo™ Triplex assay. For the cytotoxicity part of the assay (**Figure 4.33 A2-B2**), the results obtained are difficult to interpret. The positive control (+ve St) should produce the highest fluorescence signals but this is not the case. In fact, the fluorescence values from +ve St are amongst the lowest of all samples. Additionally, the apoptosis part of the assay (**Figure 4.33 A3-B3**) also gives results that are difficult to explain. Once again, the positive control (+ve St) should give the highest luminescent values since it is a known apoptosis inducer. On the other hand, the luminescent intensity values for viable cells should be low. However, even though the positive control gives the highest luminescence intensity for SK-BR-3 cells (**Figure 4.33 A3**), this is not the case for MDA-MB-231 cells (**Figure 4.33 B3**). Additionally, the luminescence intensity values for the viable cells are also relatively high (**Figure 4.33 A3-B3**). It can be concluded that there is indication that the cells treated with lactose-C3Pc-AuNPs do not follow an apoptotic cell death pathway because the luminescent values for these samples are the lowest for both cell lines. However, this conclusion cannot be confirmed since the assay is producing results that are difficult to interpret in all three components, cell viability, cytotoxicity and apoptosis. It is possible that a necrotic cell death pathway may be the mechanism induced by the lactose-C3Pc-AuNPs. However, this mechanism of action would need further confirmation.

4.2.13. Effects of lactose-C3Pc-AuNPs in non-cancerous MCF-10A cells

Analysis of PDT induced by both lactose-C11Pc-AuNPs and lactose-C3Pc-AuNPs indicated that lactose-C3Pc-AuNPs are better at inducing cell death in both SK-BR-3 and MDA-MB-231 cells. As a result, it was decided to study the effect of PDT of lactose-C3Pc-AuNPs, and its corresponding control C3Pc-sPEG-AuNPs, in non-cancerous mammary epithelial cells, MCF-10A cells. MCF-10A cells were incubated with lactose-C3Pc-AuNPs and C3Pc-sPEG-AuNPs at a concentration of 0.20 μ M as described in **section 2.3.8**. The cells were incubated with the AuNPs for either 3 h or 24 h. Following incubation, the cells were washed to remove all non-internalised AuNPs. MCF-10A cells were irradiated using a 633 nm HeNe laser for 6 min and incubated for a further *ca.* 48 h before cell viability was measured. The results are shown in **Figure 4.34**.

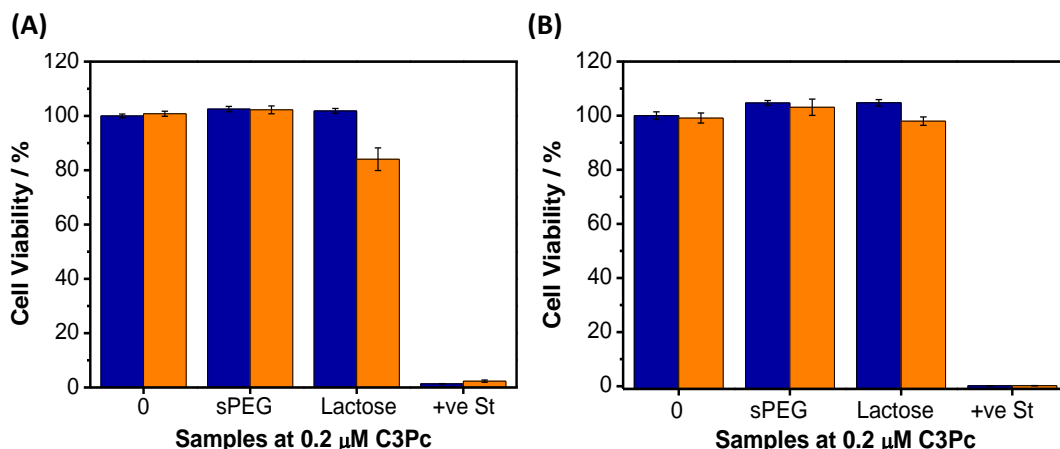


Figure 4.34. CellTiter-Blue® cell viability assay for MCF-10A cells incubated with C3Pc-sPEG-AuNPs (sPEG) and lactose-C3Pc-AuNPs (lactose) (0.2 M C3Pc) for either **(A)** 3 h or **(B)** 24 h. Cells were either irradiated with a 633 nm HeNe laser (orange) or non-irradiated (blue). Staurosporine (+ve St) was used as a positive control for cytotoxicity. Error bars represent the SD ($n = 3$) within a 95 % confidence interval.

As it can be seen in **Figure 4.34**, non-cancerous MCF-10A cells are not damaged by either lactose-C3Pc-AuNPs or C3Pc-sPEG-AuNPs. Therefore, the AuNPs reported in this chapter can be used for efficient PDT since they induce cell death to cancerous cells but leave healthy cells undamaged. Further studies on the internalisation of lactose-C3Pc-AuNPs and C3Pc-sPEG-AuNPs by the MCF-10A cells should be performed to understand why the cells do not internalise the nanoparticles as readily as cancer cells and thus no cell death is observed.

4.3. Conclusions

In this chapter, the use of lactose as a targeting agent for breast adenocarcinoma cells was explored. MDA-MB-231 and SK-BR-3 cells were compared for the expression of galectin-1 on their surface. Galectin-1 is a β -galactoside-binding lectin that has been found to be overexpressed on the surface of certain cancers, including breast cancer.^{18,23,24,31} MDA-MB-231 cells were found to have a higher amount of galectin-1 on their surface as compared to SK-BR-3 cells. Therefore, it was expected that MDA-MB-231 cells would be better candidates for targeted PDT using lactose.

Lactose-C11Pc-AuNPs were successfully synthesised and dissolved in an aqueous buffer, MES buffer, with a mean diameter of 2.37 ± 1.65 nm, as confirmed by TEM analysis. The production of $^1\text{O}_2$ by the lactose-C11Pc-AuNPs was confirmed using the $^1\text{O}_2$ probe ABMA. Additionally, a PEG ligand (sPEG) with a short chain that would resemble the length of the lactose derivative was used to synthesise C11Pc-sPEG-AuNPs. These nanoparticles were used as a control to confirm targeting by lactose. Lactose-C11Pc-AuNPs and C11Pc-sPEG-AuNPs were initially used to target MDA-MB-231 cells, with incubation periods of either 3 h or 24 h, as summarised below:

- Incubation of MDA-MB-231 cells with the lactose-C11Pc-AuNPs and C11Pc-sPEG-AuNPs for 3 hours led to no cell death following PDT, suggesting the incubation period was too short for effective internalisation of the AuNPs.
- Increasing the incubation period of MDA-MB-231 cells with the lactose-C11Pc-AuNPs and C11Pc-sPEG-AuNPs to 24 hours led to inconclusive results, suggesting that the PDT efficacy was low or negligible.

Since the results were negative for MDA-MB-231 cells, it was decided to attempt the use of lactose-C11Pc-AuNPs to target SK-BR-3 cells. The main findings are summarised below:

- Initial incubation of SK-BR-3 cells with the lactose-C11Pc-AuNPs and C11Pc-sPEG-AuNPs for 3 hours led to no cell death following PDT. This was an indication that a 3-hour incubation period was not sufficient for effective internalisation of the AuNPs.

- An increase in the incubation period of SK-BR-3 cells with lactose-C11Pc-AuNPs and C11Pc-sPEG-AuNPs to 24 hours led to PDT cytotoxicity being induced. Moreover, the lactose-C11Pc-AuNPs induced more cell death (90 %) than the C11Pc-sPEG-AuNPs (61 %), with statistical significance ($P < 0.006$). This was an indication that the lactose ligand was selectively targeting the SK-BR-3 cells.
- To confirm whether the selective targeting between lactose-C11Pc-AuNPs and SK-BR-3 cells following a 24 h incubation period was indeed due to the presence of galectin-1 on the surface of the SK-BR-3 cells, an InCell ELISA was performed. Unfortunately, there was no indication of targeting the galectin-1 receptor. Therefore, the possible targeting seen in the viability assays could be due to the selective recognition between lactose and another receptor on the surface of the SK-BR-3 cells, such as GLUT1. Additional studies with GLUT1 should be performed to confirm this possibility.

In the second part of the research reported in this chapter, C3Pc was used as a photosensitiser in an attempt to facilitate the targeting ability of the lactose ligand. C3Pc has a shorter carbon chain than C11Pc, and slightly shorter than the lactose ligand. As a result, the lactose ligand extends further than the C3Pc from the surface of the AuNPs, which could allow for an unhindered binding between lactose and galectin-1. Lactose-C3Pc-AuNPs were successfully synthesised and dissolved in an aqueous buffer, MES buffer, with a mean diameter of 3.10 ± 1.32 nm. The first advantage of lactose-C3Pc-AuNPs over lactose-C11Pc-AuNPs was that the former were easier to synthesise since the shorter chain of C3Pc allows for a better dispersibility in water and thus a higher C3Pc loading on the AuNPs. Control C3Pc-sPEG-AuNPs were synthesised to directly assess the targeting ability of lactose-C3Pc-AuNPs. The ability of lactose-C3Pc-AuNPs to produce ${}^1\text{O}_2$ was also confirmed using ABMA.

Lactose-C3Pc-AuNPs were initially incubated with MDA-MB-231 cells for either 3 h or 24 h. A summary of the main findings are reported below:

- Incubation of MDA-MB-231 cells with the lactose-C3Pc-AuNPs and C3Pc-sPEG-AuNPs for 3 hours led to no cell death following PDT, as shown by the cell viability assays as well as using confocal microscopy, indicating that 3 hours was too short for effective internalisation of the AuNPs.

- Increasing the incubation period of MDA-MB-231 cells with lactose-C3Pc-AuNPs and C3Pc-sPEG-AuNPs to 24 hours was effective at inducing cell death following PDT, as confirmed by the cell viability assays together with visual inspection using confocal microscopy. There was a slight evidence of targeting by lactose since the lactose-C3Pc-AuNPs induced higher levels of cell death (52 %) than the C3Pc-sPEG-AuNPs (36 %). However, this evidence was not statistically significant.
- To confirm whether the possible targeting seen between lactose-C3Pc-AuNPs and MDA-MB-231 cells following a 24 h incubation period was due to the interaction between lactose and galectin-1, an InCell ELISA was performed. Indeed, there was an indication that galectin-1 was involved in the internalisation of lactose-C3Pc-AuNPs.
- These results present an advantage of the use of lactose-C3Pc-AuNPs over lactose-C11Pc-AuNPs, which did not induce cell death in MDA-MB-231 cells at either incubation period.

The effect of lactose-C3Pc-AuNPs was also tested on SK-BR-3 cells. The main conclusions are reported below:

- Incubation of SK-BR-3 cells with lactose-C3Pc-AuNPs and C3Pc-sPEG-AuNPs for 3 hours effectively induced cytotoxicity following PDT, as confirmed by cell viability assays and confocal microscopy. Additionally, at low concentrations (0.05 μ M C3Pc) there was an indication of targeting by lactose, as confirmed statistically ($P < 0.003$).
- Incubation of SK-BR-3 cells with lactose-C3Pc-AuNPs and C3Pc-sPEG-AuNPs for 24 hours was also effective at inducing cell death following PDT.
- With reference to lactose targeting, there was an indication of targeting with the cell viability assays, especially following a 3 h incubation period with low concentrations of C3Pc. However, an InCell ELISA revealed that the possible targeting seen in the cell viability assays did not involve the galectin-1 receptor on the surface of SK-BR-3 cells.

- These results present an advantage of lactose-C3Pc-AuNPs over lactose-C11Pc-AuNPs, which were only effective at inducing PDT cell death when the SK-BR-3 cells were incubated with AuNPs for 24 h.

Considering that the lactose-C3Pc-AuNPs were more efficient than the lactose-C11Pc-AuNPs, the effect of lactose-C3Pc-AuNPs on non-cancerous mammary epithelial cells (MCF-10A cells) was assessed. It was found that neither lactose-C3Pc-AuNPs nor C3Pc-sPEG-AuNPs induce any damage to healthy cells. This suggests that lactose-C3Pc-AuNPs are ideal candidates for PDT since they only target cancerous cells and induce no damage to healthy cells. The mechanism of cell death followed by SK-BR-3 and MDA-MB-231 cells following PDT with lactose-C3Pc-AuNPs was studied. There was an indication that the most likely route was a non-apoptotic pathway such as necrosis. However, the results of the ApoTox-Glo™ Triplex assay were difficult to interpret and thus inconclusive.

The research in **Chapter 4** has revealed that lactose can be used, rather than PEG, to synthesise aqueous-dispersable AuNPs with either C3Pc or C11Pc. Additionally, lactose-C3Pc-AuNPs were found to be more efficient than lactose-C11Pc-AuNPs for ${}^1\text{O}_2$ production and PDT of both cell lines, MDA-MB-231 and SK-BR-3:

- Lactose-C11Pc-AuNPs only targeted and induced cell death to SK-BR-3 cells following a 24 h incubation period. On the contrary, lactose-C11Pc-AuNPs were inefficient on MDA-MB-231 cells.
- Lactose-C3Pc-AuNPs efficiently targeted and induced cell death of SK-BR-3 cells after only a 3 h incubation period. Additionally, lactose-C3Pc-AuNPs targeted and induced cell death of MDA-MB-231 cells following a 24 h incubation period.
- The galectin-1 receptor on the surface of the SK-BR-3 cells was not involved in the targeting seen by lactose-AuNPs. On the contrary, the galectin-1 receptor on the surface of the MDA-MB-231 cells showed an indication of selective recognition of the lactose on the lactose-C3Pc-AuNPs.

4.4. References

- (1) Pinho, S. S.; Reis, C. A. *Nat. Rev. Cancer* **2015**, *15*, 540.
- (2) Ghazarian, H.; Idoni, B.; Oppenheimer, S. B. *Acta Histochem.* **2011**, *113*, 236.
- (3) Dube, D. H.; Bertozzi, C. R. *Nat. Rev. Drug Discov.* **2005**, *4*, 477.
- (4) Seeberger, P. H.; Finney, N.; Rabuka, D.; Bertozzi, C. R. In *Essentials of Glycobiology*; 3rd ed.; Varki, A., Cummings, R. D., Esko, J. D., Freeze, H. H., Stanley, P., Bertozzi, C. R., Hart, G. W., Etzler, M. E., Eds.; Cold Spring Harbor Laboratory Press: Cold Spring Harbor (NY), 2009
- (5) Tuccillo, F. M.; de Laurentiis, A.; Pamieri, C.; Fiume, G.; Bonelli, P.; Borrelli, A.; Tassone, P.; Scala, I.; Buonaguro, F. A.; Quinto, I.; Scala, G. *BioMed Res. Int.* **2014**, *2014*, 742831.
- (6) Häuselmann, I.; Borsig, L. *Front. Oncol.* **2014**, *4*, 1.
- (7) Nangia-Makker, P.; Conklin, J.; Hogan, V.; Raz, A. *Trends Mol. Med.* **2002**, *8*, 187.
- (8) Rabinovich, G. A.; Toscano, M. A.; Jackson, S. S.; Vasta, G. R. *Curr. Opin. Struct. Biol.* **2007**, *17*, 513.
- (9) Brewer, C. F.; Miceli, M. C.; Baum, L. G. *Curr. Opin. Struct. Biol.* **2002**, *12*, 616.
- (10) Weis, W. I.; Drickamer, K. *Annu. Rev. Biochem.* **1996**, *65*, 441.
- (11) Varki, A.; Etzler, M. E.; Cummings, R. D.; Esko, J. D. In *Essentials of Glycobiology*; Varki, A., Cummings, R. D., Esko, J. D., Freeze, H. H., Stanley, P., Bertozzi, C. R., Hart, G. W., Etzler, M. E., Eds.; Cold Spring Harbor Laboratory Press: Cold Spring Harbor (NY), 2009.
- (12) Cummings, R. D.; McEver, R. P. In *Essentials of Glycobiology*; 3rd ed.; Varki, A., Cummings, R. D., Esko, J. D., Freeze, H. H., Stanley, P., Bertozzi, C. R., Hart, G. W., Etzler, M. E., Eds.; Cold Spring Harbor Laboratory Press: Cold Spring Harbor (NY), 2009.
- (13) Cummings, R. D.; Liu, F. T. In *Essentials of Glycobiology*; 3rd ed.; Varki, A., Cummings, R. D., Esko, J. D., Freeze, H. H., Stanley, P., Bertozzi, C. R., Hart, G. W., Etzler, M. E., Eds.; Cold Spring Harbor Laboratory Press: Cold Spring Harbor (NY), 2009.
- (14) Varki, A.; Crocker, P. R. In *Essentials of Glycobiology*; 3rd ed.; Varki, A., Cummings, R. D., Esko, J. D., Freeze, H. H., Stanley, P., Bertozzi, C. R., Hart, G. W., Etzler, M. E., Eds.; Cold Spring Harbor Laboratory Press: Cold Spring Harbor (NY), 2009.
- (15) Kim, Y. J.; Varki, A. *Glycoconj. J.* **1997**, *14*, 569.
- (16) Meany, D. L.; Chan, D. W. *Clin. Proteomics* **2011**, *8*, 1.
- (17) Barondes, S. H.; Cooper, D. N. W.; Gitt, M. A.; Leffle, H. J. *J. Biol. Chem.* **1994**, *269*, 20807.

(18) Ito, K.; Stannard, K.; Gabutero, E.; Clark, A. M.; Neo, S.-Y.; Onturk, S.; Blanchard, H.; Ralph, S. *J. Cancer Metastasis Rev.* **2012**, *31*, 763.

(19) Balan, V.; Nangia-Makker, P.; Raz, A. *Cancers* **2010**, *2*, 592.

(20) Danguy, A.; Camby, I.; Kiss, R. *Biochim. Biophys. Acta, Gen. Subj.* **2002**, *1572*, 285.

(21) Gorelik, E.; Galili, U.; Raz, A. *Cancer Metastasis Rev.* **2001**, *20*, 245.

(22) Rabinovich, G. A. *Cell Death Differ.* **1999**, *6*, 711.

(23) Astorgues-Xerri, L.; Riveiro, M. E.; Tijeras-Raballand, A.; Serova, M.; Neuzillet, C.; Albert, S.; Raymond, E.; Faivre, S. *Cancer Treat. Rev.* **2014**, *40*, 307.

(24) Perillo, N. L.; Marcus, M. E.; Baum, L. G. *J. Mol. Med.* **1998**, *76*, 402.

(25) Takenaka, Y.; Fukumori, T.; Ra, A. *Glycoconj. J.* **2004**, *19*, 543.

(26) Cooper, D. N. W.; Barondes, S. H. *Glycobiology* **1999**, *9*, 979.

(27) Rabinovich, G. A. *Br. J. Cancer* **2005**, *92*, 1188.

(28) Jung, E.-J.; Moon, H.-G.; Cho, B. I.; Jeong, C.-Y.; Joo, Y.-T.; Lee, Y.-J.; Hong, S.-C.; Choi, S.-K.; Ha, W.-S.; Kim, J. W.; Lee, C.-W.; Lee, J. S.; Park, S.-T. *Int. J. Cancer* **2007**, *120*, 2331.

(29) Thijssen, V. L.; Barkan, B.; Shoji, H.; Aries, I. M.; Mathieu, V.; Deltour, L.; Hackeng, T. M.; Kiss, R.; Kloog, Y.; Poirier, F.; Griffioen, A. W. *Cancer Res.* **2010**, *70*, 6216.

(30) Demydenko, D.; Berest, I. *Exp. Oncol.* **2009**, *31*, 74.

(31) Dalotto-Moreno, T.; Croci, D. O.; Cerliani, J. P.; Martinez-Allo, V. C.; Dergan-Dylon, S.; Méndez-Huergo, S. P.; Stupirski, J. C.; Mazal, D.; Osinaga, E.; Toscano, M. A.; Sundblad, V.; Rabinovich, G. A.; Salatino, M. *Cancer Res.* **2013**, *73*, 1107.

(32) Nangia-Makker, P.; Honjo, Y.; Sarvis, R.; Akahani, S.; Hogan, V.; Pienta, K. J.; Raz, A. *Am. J. Pathol.* **2000**, *156*, 899.

(33) Iurisci, I.; Tinari, N.; Natoli, C.; Angelucci, D.; Cianchetti, E.; Iacobelli, S. *Clin. Cancer Res.* **2000**, *6*, 1389.

(34) Liu, W.; Watabe, K. In *Cancer Metastasis Biologic Basis and Therapeutics*; Lyden, D., Welch, D. R., Psaila, B., Eds.; Cambridge University Press: New York, 2011, p 131.

(35) Bresalier, R. S.; Byrd, J. C.; Wang, L.; Raz, A. *Cancer Res.* **1996**, *56*, 4354.

(36) Yang, R. Y.; Hsu, D. K.; Liu, F. T. *Proc. Natl. Acad. Sci. U.S.A.* **1996**, *93*, 6737.

(37) Bresalier, R. S.; Yan, P.-S.; Byrd, J. C.; Lotan, R.; Raz, A. *Cancer* **1997**, *80*, 776.

(38) Schoeppner, H. L.; Raz, A.; Ho, S. B.; Bresalier, R. S. *Cancer* **1995**, *75*, 2818.

(39) Akahani, S.; Nangia-Makker, P.; Inohara, H.; Kim, H.-R. C.; Raz, A. *Cancer Res.* **1997**, *57*, 5272.

(40) Moon, B. K.; Lee, Y. J.; Battle, P.; Jessup, J. M.; Raz, A.; Kim, H. R. C. *Am. J. Pathol.* **2001**, *159*, 1055.

(41) Castronovo, V.; van Den Brule, F. A.; Jackers, P.; Clausse, N.; Liu, F. T.; Gillet, C.; Sobel, M. E. *J. Pathol.* **1996**, *179*, 43.

(42) Zhang, H.; Liang, X.; Duan, C.; Liu, C.; Zhao, Z. *PLoS one* **2014**, *9*, e103482.

(43) Zou, J.; Glinsky, V. V.; Landon, L. A.; Matthews, L.; Deutscher, S. L. *Carcinogenesis* **2005**, *26*, 309.

(44) Sathisha, U. V.; Jayaram, S.; Harish Nayaka, M. A.; Dharmesh, S. *Glycoconj. J.* **2007**, *24*, 497.

(45) Park, Y. K.; Bold, B.; Cui, B. C.; Bai, J. Q.; Lee, W. K.; Shim, Y. K. *Bull. Korean Chem. Soc.* **2008**, *29*, 130.

(46) Lin, T. W.; Chang, H. T.; Chen, C. H.; Chen, C. H.; Lin, S. W.; Hsu, T. L.; Wong, C. H. *J. Am. Chem. Soc.* **2015**, *137*, 9685.

(47) Koo, J. S.; Jung, W. H. *Yonsei Med. J.* **2011**, *52*, 89.

(48) Inohara, H.; Akahani, S.; Koths, K.; Raz, A. *Cancer Res.* **1996**, *56*, 4530.

(49) Minko, T. *Adv. Drug Delivery Rev.* **2004**, *56*, 491.

(50) Liang, P.-H.; Wang, S.-K.; Wong, C.-H. *J. Am. Chem. Soc.* **2007**, *129*, 11177.

(51) Cho, K.; Wang, X.; Nie, S.; Chen, Z.; Shin, D. M. *Clin. Cancer Res.* **2008**, *14*, 1310.

(52) Sinha, R.; Kim, G. J.; Nie, S.; Shin, D. M. *Mol. Cancer Ther.* **2006**, *5*, 1909.

(53) Brevet, D.; Gary-Bobo, M.; Raehm, L.; Richeter, S.; Hocine, O.; Amro, K.; Loock, B.; Couleaud, P.; Frochot, C.; Morere, A.; Maillard, P.; Garcia, M.; Durand, J. O. *Chem. Commun.* **2009**, 1475.

(54) Gary-Bobo, M.; Mir, Y.; Rouxel, C.; Brevet, D.; Basile, I.; Maynadier, M.; Vaillant, O.; Mongin, O.; Blanchard-Desce, M.; Morere, A.; Garcia, M.; Durand, J. O.; Raehm, L. *Angew. Chem., Int. Ed.* **2011**, *50*, 11425.

(55) Gary-Bobo, M.; Hocine, O.; Brevet, D.; Maynadier, M.; Raehm, L.; Richeter, S.; Charasson, V.; Loock, B.; Morere, A.; Maillard, P.; Garcia, M.; Durand, J. O. *Int. J. Pharm.* **2012**, *423*, 509.

(56) Gary-Bobo, M.; Mir, Y.; Rouxel, C.; Brevet, D.; Hocine, O.; Maynadier, M.; Gallud, A.; Da Silva, A.; Mongin, O.; Blanchard-Desce, M.; Richeter, S.; Loock, B.; Maillard, P.; Morere, A.; Garcia, M.; Raehm, L.; Durand, J. O. *Int. J. Pharm.* **2012**, *432*, 99.

(57) Perrier, M.; Gary-Bobo, M.; Lartigue, L.; Brevet, D.; Morere, A.; Garcia, M.; Maillard, P.; Raehm, L.; Guari, Y.; Larionova, J.; Durand, J. O.; Mongin, O.; Blanchard-Desce, M. *J. Nanopart. Res.* **2013**, *15*, 1602.

(58) Kennedy, A. C.; Orts-Gil, G.; Lai, C. H.; Mller, L.; Haase, A.; Luch, A.; Seeberger, P. H. *J. Nanobiotechnol.* **2014**, *12*.

(59) Pereira, P. M. R.; Silva, S.; Cavaleiro, J. A. S.; Ribeiro, C. A. F.; Tomé, J. P. C.; Fernandes, R. *PLoS one* **2014**, 9, e95529.

(60) Peng, J.; Wang, K.; Tan, W.; He, X.; He, C.; Wu, P.; Liu, F. *Talanta* **2007**, 71, 833.

(61) Pienta, K. J.; Nailk, H.; Akhtar, A.; Yamazaki, K.; Replogle, T. S.; Lehr, J.; Donat, T. L.; Tait, L.; Hogan, V.; Raz, A. *J. Natl. Cancer Inst.* **1995**, 87, 348.

(62) Prakash, J.; Beljaars, L.; Harapanahalli, A. K.; Zeinstra-Smith, M.; de Jager-Krikken, A.; Hessing, M.; Steen, H.; Poelstra, K. *Int. J. Cancer* **2010**, 126, 1966.

(63) Bertrand, N.; Wu, J.; Xu, X.; Kamaly, N.; Farokhzad, O. C. *Adv. Drug Delivery Rev.* **2014**, 66, 2.

(64) Başar, I.; Ayhan, A.; Bircan, K.; Ergen, A.; Taşar, C. *Br. J. Urol.* **1991**, 67, 165.

(65) Recht, L.; Torres, C. O.; Smith, T. W.; Raso, V.; Griffin, T. W. *J. Neurosurg.* **1990**, 72, 941.

(66) Shindelman, J. E.; Ortmeyer, A. E.; Sussman, H. H. *Int. J. Cancer* **1981**, 27, 329.

(67) Dwek, M. V.; Ross, H. A.; Streets, A. J.; Brooks, S. A.; Adam, E.; Titcomb, A.; Woodside, J. V.; Schumacher, U.; Leathem, A. J. *Int. J. Cancer* **2001**, 95, 79.

(68) Gao, X.; Wang, T.; Wu, B.; Chen, J.; Chen, J.; Yue, Y.; Dai, N.; Chen, H.; Jiang, X. *Biochem. Biophys. Res. Commun.* **2008**, 377, 35.

(69) Wang, C.; Ho, P. C.; Lim, L. Y. *Int. J. Pharm.* **2010**, 400, 201.

(70) Wang, J.; Duan, T.; Sun, L.; Liu, D.; Wang, Z. *Anal. Biochem.* **2009**, 392, 77.

(71) Ochoa-Alvarez, J. A.; Krishnan, H.; Shen, Y.; Acharya, N. K.; Han, M.; McNulty, D. E.; Hasegawa, H.; Hyodo, T.; Senga, T.; Geng, J.-G.; Kosciuk, M.; Shin, S. S.; Goydos, J. S.; Temiakov, D.; Nagele, R. G.; Goldberg, G. S. *PLoS one* **2012**, 7, e41845.

(72) Hussain, N.; Jani, P. U.; Florence, A. T. *Pharm. Res.* **1997**, 14, 613.

(73) Obaid, G.; Chambrier, I.; Cook, M. J.; Russell, D. A. *Angew. Chem., Int. Ed.* **2012**, 51, 6158.

(74) Reynolds, A. J.; Haines, A. H.; Russell, D. A. *Langmuir* **2006**, 22, 1156.

(75) Pagano, M.; Gauvreau, K. *Principles of biostatistics*; 2nd ed.; Brooks/Cole: Boston, 2000.

(76) Grover-McKay, M.; Walsh, S.; Seftor, E.; Thomas, P.; Hendrix, M. *Pathol. Oncol. Res.* **1998**, 4, 115.

(77) Hussein, Y. R.; Bandyopadhyay, S.; Semaan, A.; Ahmed, Q.; Albasiti, B.; Jazaerly, T.; Nahleh, Z.; Ali-Fehmi, R. *Transl. Oncol.* **2011**, 4, 321.

(78) Krzeslak, A.; Wojcik-Krowiranda, K.; Forma, E.; Jozwiak, P.; Romanowicz, H.; Bienkiewicz, A.; Brys, M. *Pathol. Oncol. Res.* **2012**, 18, 721.

(79) Brown, R. S.; Wahl, R. L. *Cancer* **1993**, 72, 2979.

(80) Venturelli, L.; Nappini, S.; Bulfoni, M.; Gianfranceschi, G.; Dal Zilio, S.; Coceano, G.; Del Ben, F.; Turetta, M.; Scoles, G.; Vaccari, L.; Cesselli, D.; Cojoc, D. *Sci. Rep.* **2016**, *6*.

(81) Young, C. D.; Lewis, A. S.; Rudolph, M. C.; Ruehle, M. D.; Jackman, M. R.; Yun, U. J.; Ilkun, O.; Pereira, R.; Abel, E. D.; Anderson, S. M. *PLoS one* **2011**, *6*.

Chapter 5

The potential use of upconverting nanoparticles as drug carriers for photodynamic therapy of cancer

This chapter describes the potential use of upconverting nanoparticles as drug carriers for photodynamic therapy of cancer. The upconverting nanoparticles, functionalised with Rose Bengal (RB) as a photosensitiser, were tested for near-infrared (NIR)-PDT with human breast adenocarcinoma cells.

5.1. Introduction

5.1.1. Upconverting nanoparticles

Upconverting nanoparticles (UCNPs), as described in **Chapter 1**, have recently received much attention due to their ability to emit light in the visible region (high energy, short-wavelength radiation) upon excitation with light in the NIR region (long-wavelength radiation, usually 980 nm), in a process known as upconversion.¹⁻⁶ Upconversion disobeys classical linear optics, by which absorption of high energy photons leads to the Stokes emission of low energy, long wavelength radiation, due to the loss of energy that occurs when the system relaxes back to the ground state.^{1,7,8} Therefore, upconversion can be defined as an anti-Stokes non-linear optical process.^{1,2,6-10} It is important to note the difference between upconversion and another non-linear optical process, two-photon or multiphoton absorption (TPA). While TPA refers to the simultaneous absorption of two or more photons, upconversion occurs upon sequential absorption of those photons.^{5,11-13} As a result, upconversion is a more efficient process, which allows for the use of a low-cost continuous wave diode NIR laser as the excitation source rather than the more expensive ultrashort pulsed lasers required for TPA.^{11,12}

The mechanisms by which upconversion takes place can be classified into three main groups; excited-state absorption (ESA), energy transfer upconversion (ETU) and photon

avalanche (PA).^{1,2,8,9,14,15} All these mechanisms have in common the sequential absorption of photons leading to a highly excited state from which emission then takes place.¹ Excited-state absorption (**Figure 5.1 A**), discovered by Bloembergen in 1959,¹⁶ involves the absorption of two photons by a single ion. Absorption of the first photon promotes the excitation of the ion in the ground state (G) into an intermediate excited state (E1) with a long half-life. The ion in E1 is then excited into the higher level E2 *via* absorption of a second photon. Relaxation of the ion from E2 to the ground state leads to the upconverted luminescence emission.^{9,12,15} Energy transfer upconversion (**Figure 5.1 B**) was discovered by Auzel in 1966, which he termed APTE (from the French ‘addition de photon par transferts d’energie’), and it is the most efficient upconversion phenomenon.^{1,8,9,14,15} ETU involves sequential energy transfer between two neighbouring ions, one acting as the donor (*i.e.*, sensitiser) and the second one acting as the acceptor (*i.e.*, activator). Both the sensitiser and the activator are excited to the E1 level upon absorption of a photon. The sensitiser in the E1 level transfers its energy to the activator, also in the E1 level. As a result, the activator is excited to level E2 and the sensitiser relaxes back to the ground state. Relaxation of the activator from level E2 to the ground state leads to upconverted luminescence emission.^{1,9,12,15} The ETU phenomenon resulting from identical sensitiser and activator ions is known as cross-relaxation (CR).^{9,14} CR involves the interaction between an ion in the E2 state and an ion in the ground state. The ETU between the two ions leads to both ions transitioning to the E1 excited level (**Figure 5.1 C**).¹² Additionally, cooperative processes, namely cooperative sensitisation and cooperative luminescence, are a type of energy transfer upconversion but with a much lower efficiency.^{9,12,14} Cooperative processes can take place between two ions or between a pair of ions and a third ion.¹⁴ Finally, photon avalanche (**Figure 5.1 D**) was discovered by Chivian in 1979.¹⁷ It is the most complex process and it is initiated by the excitation of an ion to its E1 level, followed by excitation to the E2 level *via* ESA. The excited ion in level E2 interacts with a near-by ion in the ground state *via* CR. The ions can readily be excited to the E2 level and the process is repeated, in an avalanche manner, leading to strong upconversion.^{9,15}

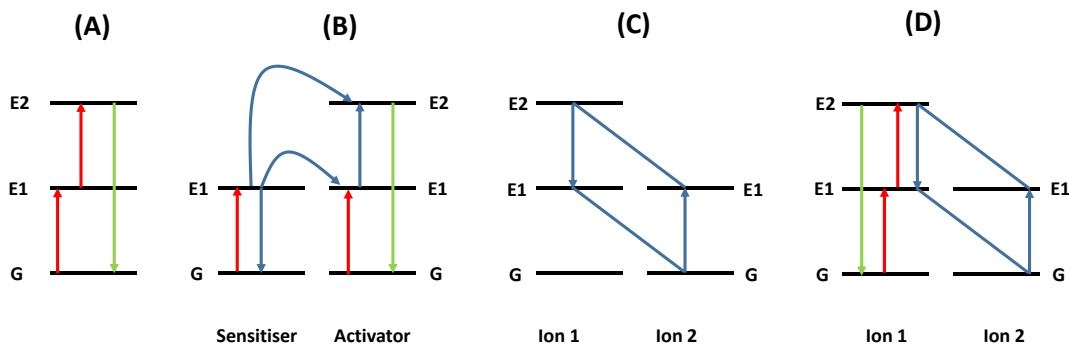


Figure 5.1. Energy level diagrams showing the upconversion mechanisms: **(A)** excited-state absorption (ESA), **(B)** energy transfer upconversion (ETU), **(C)** cross-relaxation (CR) and **(D)** simplified figure of photon avalanche (PA). The red arrows represent photon excitation, the blue lines and arrows represent energy transfer and the green arrows represent upconverted emission. The figure was adapted from Ref. 1 and Ref. 12.

Requirements for the formation of upconversion are the presence of two metastable excited states and a ladder-like arrangement of the energy levels with similar distances between one another.^{1,13} Both requirements are fulfilled by some d and f elements. Rare-earth ions, *i.e.*, lanthanides, provide high upconversion efficiency and are thus normally used for the synthesis of UCNPs.¹ UCNPs consist of a crystalline host lattice and lanthanide dopants.^{1,7,9,12,15,18} The selection of both the host lattice and the dopants is important in order to achieve high upconversion efficiency.¹² The host lattice plays an essential role within the UCNPs, as it will regulate the distance between the dopants, their relative position and coordination number as well as the chemical environment surrounding the dopants.^{1,7} As a result, the host lattices are required to be chemically and physically stable, transparent in the spectral region of interest and should have low phonon energies to minimise non-radiative loss and maximise upconverted emission.^{1,2,7,9,12,15} Considering all of these prerequisites, a combination of alkali (*i.e.*, Na^{2+} , Ca^{2+}) and rare-earth metal (*i.e.*, Y^{3+} , Gd^{3+}) fluorides are ideal as host lattices for UCNPs. Common examples are sodium yttrium fluoride (NaYF_4) or sodium gadolinium fluoride (NaGdF_4) crystal lattices. The geometry of the crystal structure has also been found to contribute to a higher or lower upconverted emission. For example, the use of hexagonal (β -phase) NaYF_4 leads to much higher upconversion efficiencies as compared to the cubic (α -phase) NaYF_4 structure.^{1,2,7,9,12,15}

The selection of the dopants has also been studied. As it was previously mentioned, the most important upconversion mechanism in UCNPs is ETU, with considerably higher efficiency than ESA. As a result, the host lattice is co-doped with a sensitiser and an activator.¹ The most commonly used sensitiser is ytterbium (Yb³⁺), whose energy level is simple and facilitates the energy transfer to the activators.^{1,7,9,12,15} For the selection of the activators, they should have an energy level compatible with that of the sensitiser, Yb³⁺, and metastable excited states. The lanthanides erbium (Er³⁺), thulium (Tm³⁺) and holmium (Ho³⁺) are ideal candidates to be used as activators. Additionally, the concentration of the dopants is important in order to avoid loss of energy *via* CR. Typically, sensitisers are included at high concentrations (≥ 20 mol %) but activators are added at low concentrations (≤ 2 mol %).^{1,7,9,12,15} Lithium ions (Li⁺) have also been reported as potential dopants for UCNPs since Li⁺ can lead to a 30-fold enhancement of the luminescence efficiency as compared to other lanthanide dopants.¹⁹

The most efficient structure for UCNPs has been found to be β -phase NaYF₄ co-doped with Yb³⁺ and Er³⁺.^{3,5-7,15,18,20-22} However, the combination NaYF₄ co-doped with Yb³⁺ and Tm³⁺ is also being widely studied as it leads to high upconversion efficiency.⁷ The ETU diagrams for both combinations can be seen in **Figure 5.2**, where it is clearly shown that NaYF₄ co-doped with Yb³⁺/Er³⁺ leads to red, green and blue emission while NaYF₄ co-doped with Yb³⁺/Tm³⁺ leads to only red and blue emission.^{1,7,15,18,22,23} The addition of Gd³⁺ to these systems is encouraged because it facilitates the conversion of NaYF₄ from the cubic phase to the hexagonal phase crystal structure and it provides the possibility to use the UCNPs as contrast agents for bioimaging.^{6,10,20,23,24}

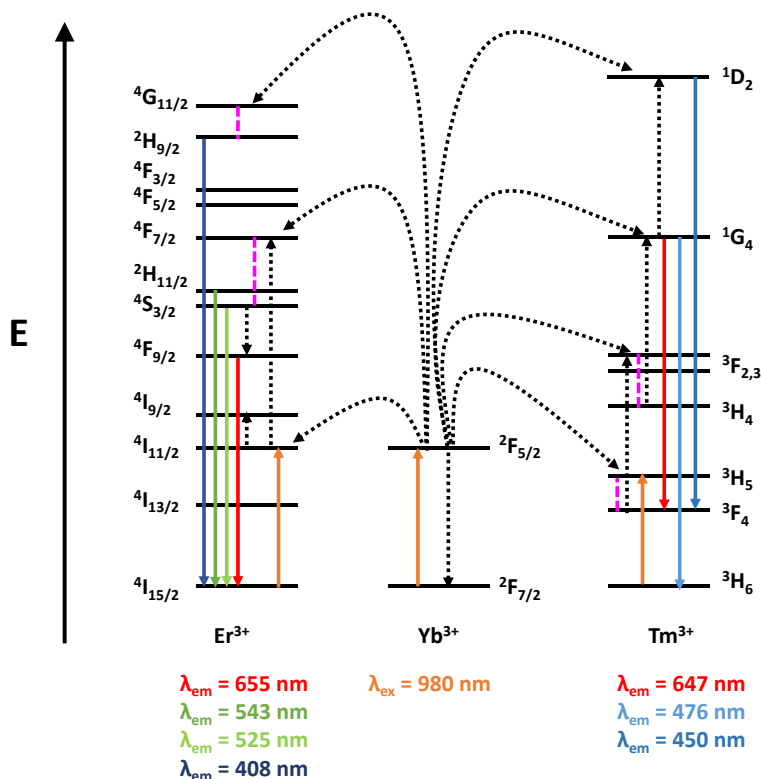


Figure 5.2. Energy level diagrams showing the upconversion mechanisms for NaYF_4 co-doped with the sensitisier Yb^{3+} and either Er^{3+} or Tm^{3+} as activator. The arrows indicate absorption (orange), energy transfer (black dots), non-radiative relaxation (pink dash) and upconverted luminescence emission at different wavelengths (red, green and blue). The $^{2S+1}L_J$ notation used to label the f energy levels refer to spin (S), orbital (L) and angular momentum (J) quantum numbers according to the Russell-Saunders notation. The diagram was adapted from Ref. 1.

UCNPs have a lower luminescence efficiency than their bulk counterparts due to their large surface-to-volume ratio.^{1,12} As a result, the dopants are exposed to surface deactivation processes, which can lead to the quenching and energy loss of the upconverted luminescence and thus low efficiency.^{1,12} A technique to solve this problem is to cover the surface of the UCNPs with a shell. The core-shell structure of the UCNPs could either be homogeneous or heterogeneous relative to the host material.¹² Additionally, the shell can either be active or passive. Passive shells do not contain any dopants whereas active shells are doped with lanthanides in the same way as the core.^{1,12} As a result, core-shell UCNPs will have much higher luminescence intensities and their use is encouraged.

The synthesis of UCNPs can be performed *via* several methods. The most common synthetic routes followed are thermal decomposition, co-precipitation, solvothermal synthesis, sol-gel processing, Ostwald-Ripening strategy, combustion synthesis, flame synthesis and microwave-assisted heating.^{5,12,15,19} The main challenge in these syntheses is that the final UCNPs are capped with organic ligands containing long alkyl chains, usually oleate, and are thus highly hydrophobic. As a result, to obtain water-dispersable or water-soluble UCNPs, the hydrophobic UCNPs need to be subjected to post-synthesis surface modifications.^{1,5,12,25} Common strategies of surface modification include: The addition of a water soluble inorganic shell (SiO_2 or TiO_2); The chemical modification of the organic ligand *via* ligand oxidation; The coating of the UCNPs with amphiphilic polymers such as phospholipids, PEG or polyacrylic acid (*i.e.*, ligand attraction); The layer-by-layer assembly of charged molecules through electrostatic interactions; and the complete elimination of the organic ligand *via* ligand exchange.^{5,7,12} Ligand exchange is divided in two methods. Firstly, a one-step exchange process. Secondly, a two-step process in which the UCNPs are either treated with nitrosonium tetrafluoroborate (NOBF_4) or a strong acid for the removal of the organic ligand, followed by the addition of a water-soluble coating.⁵

5.1.2. Biological applications of UCNPs

The use of UCNPs for biomedicine has recently received considerable attention.²⁶ The ability of UCNPs to convert NIR light into higher energy visible or UV light provides them with several advantages over currently used nanomaterials such as quantum dots (QDs) and nanoparticles functionalised with organic dyes.^{2,3,12,26-30} Excitation in the NIR region allows for a deeper penetration into the tissue, due to the low absorbance of biological tissue in that region, as well as reduced photodamage towards the cells under long-term irradiation. Additionally, unlike QDs, the luminescence emission of UCNPs is not size-dependent, it allows for the possibility to tune multicolour emission, and the emission bands are narrow, which is another advantage for multiplexed imaging. Further advantages over QDs include the non-blinking, non-bleaching nature of the UCNPs, which provides less scattering and a high resistance to photobleaching. Adding to these qualities, UCNPs are biocompatible, synthesised with a narrow size

distribution and have enhanced photostability as well as low cytotoxicity. Furthermore, the NIR excitation also contributes to lower autofluorescence, which essentially leads to no background noise during bioimaging and thus increases the signal-to-noise ratio. As a result, UCNPs are ideal candidates for bioimaging, biosensing, drug delivery and therapeutic applications.^{2,3,7,9,12,26-39}

It was previously discussed that UCNPs have low cytotoxicity. Studies on the toxicity of UCNPs are challenging since toxicity is dependent on many factors including UCNPs size, shape, composition, charge and surface ligands but also on cell and tissue type and the route of exposure and incubation conditions used.^{7,8} Therefore, results cannot be easily extrapolated from one UCNP model to another and cannot be directly compared with the toxicity of other types of nanoparticles.^{7,8} Additionally, results from *in vitro* and *in vivo* studies do not always correlate. *In vitro* studies are usually performed on cells cultured on a monolayer so the concentration of UCNPs used are in direct contact with the cells. Most *in vitro* studies, up to date, have shown that UCNPs at concentrations as high as 400-500 µg/mL incubated with cell cultures for as long as 48 h do not show any cytotoxicity.⁷ *In vivo* studies are more complex because only a partial dose of the UCNPs being used actually reaches the site of interest, *i.e.*, the tumour cells, and it is highly dependent on the route of exposure, metabolism, excretion pathway and immune response.⁷ One of the most important *in vivo* studies for the toxicity of UCNPs was reported by Xiong *et al.*⁴⁰ The authors studied NaYF₄ nanoparticles, co-doped with Yb³⁺ and Tm³⁺ and functionalised with polyacrylic acid, in mice. It was found that accumulation of the UCNPs in the liver and spleen is slowly cleared from the animal during a four-month period and no health damage was observed to the treated mice.^{7,8,40} UCNPs functionalised with other ligands such as PEG and polyethylenimine (PEI) have also been reported to accumulate in several organs including lungs, kidney, liver and spleen but eliminated from the body *ca.* 7 days post injection.^{7,8} The use of UCNPs containing Gd, considered the most toxic element upon release of free Gd³⁺ ions in the body, have also been shown to induce no harm in mice up to 150 days following injection.⁸ The inclusion of the Gd strongly bonded to the host lattice avoids the release of the ions and thus reduces the toxicity associated with free Gd³⁺ ions.⁸ The majority of the studies performed to date indicate UCNPs have a low toxicity and are thus good candidates for biomedical applications. However, long-term

toxicity, decomposition of UCNPs leading to secondary toxicity effects *via* their decomposition products and the possibility of the chemical properties of UCNPs activating unwanted cellular signalling have not been studied. Therefore, it cannot be fully concluded that UCNPs do not pose any health risks. The results reported up to date are promising but further studies on the toxicology of UCNPs are required to effectively assess the possible hazards towards humans.⁸

Current investigation on the use of UCNPs involve several applications, as previously discussed. The use of Förster resonance energy transfer (FRET), a non-radiative process of energy transfer between an excited donor and an acceptor in the ground state, plays an important role in the use of UCNPs for biomedicine.³⁸ The UCNPs, excited with NIR light, act as the energy donor to a molecule placed on the nanoparticle surface, which can be excited with the light being emitted by the UCNPs. Therefore, the key requirement for FRET to occur is the spectral overlap between the fluorescence emission of the donor, *i.e.*, the UCNPs, and the UV-vis absorption of the acceptor, *i.e.*, the fluorophore placed on the surface of the UCNPs. FRET has been used for applications such as biosensing, bioassays, bioimaging and cancer therapeutics, especially PDT.³⁸ One of the most relevant and researched applications of UCNPs is PDT (for a review on the use of UCNPs for PDT see **Chapter 1**). The use of FRET in UCNPs-mediated PDT is essential for the effective production of singlet oxygen. Excitation of the UCNPs at 980 nm leads to upconverted luminescence emission, which can then be used to excite the photosensitiser on the nanoparticle surface and induce the generation of singlet oxygen. An energy level diagram showing the FRET process between UCNPs and the photosensitiser Rose Bengal, which leads to the generation of singlet oxygen, is shown in **Figure 5.3**.

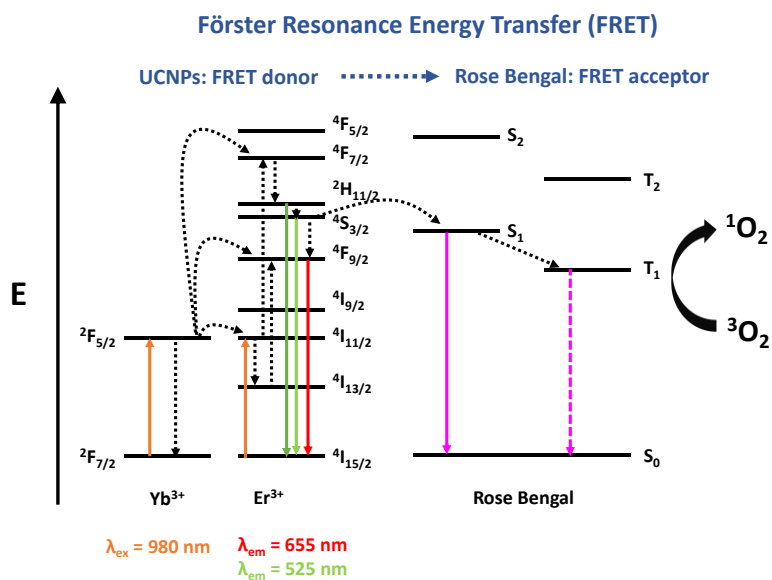


Figure 5.3. Energy level diagrams showing the upconversion mechanisms for NaYF_4 co-doped with the sensitiser Yb^{3+} and the activator Er^{3+} . Efficient FRET between the UCNPs and Rose Bengal leads to the generation of singlet oxygen (${}^1\text{O}_2$) upon reaction of the excited photosensitiser with molecular oxygen (${}^3\text{O}_2$). The arrows indicate absorption (orange), energy transfer (black dots), fluorescence (pink), phosphorescence (pink dash) and upconverted luminescence emission at different wavelengths (red and green). The Russell-Saunders (${}^{2S+1}\text{L}_J$) notation used to label the f energy levels refer to spin (S), orbital (L) and angular (J) quantum numbers. The diagram was adapted from Ref. 38.

The use of UCNPs as biosensors has been reported for the detection of oxygen,³⁷ glutathione,³⁶ avidin,⁴¹ temperature,⁴² and small interference RNA (siRNA).⁴³ UCNPs cannot directly detect the analytes of interest. Therefore, the use of a molecule sensitive to the analyte of interest, that will receive energy transfer from the UCNPs emission, *i.e.*, FRET, is required. In the case of oxygen sensing, an iridium (III) complex (Ir) that has a fluorescence signal known to be quenched in the presence of oxygen was used.³⁷ Effective FRET between the UCNPs and Ir led to the fluorescence emission of Ir, which was then used for sensing oxygen in the environment.³⁷ In the case of glutathione sensing, sheets of MnO_2 were used to cover the surface of the UCNPs.³⁶ FRET between the UCNPs and MnO_2 lead to the quenching of the UCNPs luminescence, which was recovered upon addition of glutathione. As a result, quantification of glutathione in the environment was possible.³⁶ For the detection of trace amounts of avidin, UCNPs were conjugated to gold nanoparticles and efficient FRET between the two systems led to the successful detection of avidin.⁴¹

The use of UCNPs for both *in vitro* and *in vivo* imaging has been widely studied.² The use of UCNPs for *in vivo* imaging is restricted to several conditions; biocompatibility, water-solubility, bright luminescence, small diameter (< 10 nm) and the possibility to attach targeting ligands to the surface of the UCNPs.^{30,44} For bright luminescence, the use of UCNPs with a core-shell structure is encouraged because the addition of a shell can increase the luminescence of the UCNPs,⁴⁵ as explained in **section 5.1.1**. The synthesis of UCNPs with these characteristics has been reported and successfully used for *in vitro* imaging⁴⁶ but more importantly *in vivo* imaging, including vascular imaging.^{30,44} The addition of targeting ligands has also been used for tumour-targeted imaging. Chatterjee *et al.* coated PEI modified NaYF₄ UCNPs with folic acid to specifically target the folic acid receptors overexpressed on certain types of cancer. The presence of folic acid increased the uptake of the UCNPs by the cells and led to successful *in vitro* but also *in vivo* imaging.²⁹ Other groups have reported the use of peptides as the targeting moiety. In particular, cyclic arginine-glycine-aspartic acid (RGD) has been used to target the $\alpha_v\beta_3$ integrin receptor overexpressed in cancer. The RGD functionalised UCNPs have been effectively used to image tumours *in vivo*.^{2,47} The use of targeted imaging shows great potential for successful cancer imaging. Additionally, another important contribution of UCNPs to imaging is the use of multimodal imaging.² The inclusion of Gd³⁺ in the UCNPs formulation allows for dual imaging *via* the UCNPs luminescence emission and the ability of Gd³⁺ to be used as a contrast agent in magnetic resonance imaging (MRI). An alternative to Gd³⁺ is the use of iron oxide nanoparticles (IONPs) for dual MRI and UCNPs imaging.²

Drug delivery is also an important application for which UCNPs can be used. The use of UCNPs to deliver drugs such as doxorubicin (DOX) and ibuprofen (IBU) has been particularly studied.^{31,33,35,48-50} Lin and co-workers used pH-sensitive UCNPs for the delivery of the anticancer drug DOX into cancerous cells.^{31,48} UCNPs synthesised with NaYF₄ co-doped with Yb³⁺ and Tm³⁺ were functionalised with hydrazine, to which DOX was attached *via* a hydrazone bond. The hydrazone bond was pH sensitive and easily cleaved under mildly acidic conditions (pH 4.5-5.0). As a result, DOX was effectively released upon endocytosis, which leads to the formation of acidic endosomes and lysosomes. The DOX release could be easily monitored using confocal microscopy *via* FRET, since the luminescence of the UCNPs is quenched in the presence of DOX, but

recovered as DOX is released into the environment. The release of DOX into cancer cells was effective at inducing cell death.³¹ The use of pH-sensitive drug release was also studied by Hou *et al.*^{49,50} The authors synthesised silica nanofibers *via* electrospinning to which UCNPs were attached. The release of both DOX and IBU into cancer cells was effective in both of their studies. The delivery of DOX has also been possible *via* NIR light-triggered release.³³ Liu *et al.* synthesised NaYF₄ UCNPs co-doped with Yb³⁺ and Tm³⁺, which were covered with a mesoporous silica shell to which azobenzene groups were attached. Additionally, DOX was loaded on the silica shell of the UCNPs. Excitation of the UCNPs with NIR light led to FRET with the azobenzene groups. The absorption of light by the azobenzene groups induced a continuous rotation-inversion movement, which is responsible for the release of DOX into the environment, *i.e.*, the cancer cells.³³ This NIR light-triggered release has also been used for the release and activation of caged compounds, which can be used for cancer therapy and gene expression.⁵¹⁻⁵³

Importantly, the use of UCNPs as multifunctional agents for both therapy and imaging has also been studied. Multifunctional UCNPs have received a lot of interest and have become the subject of many studies.^{3,26-28,54-58} The Liu group synthesised NaYF₄ UCNPs, decorated these nanoparticles with a layer of IONPs, further covered the surface with a gold shell and finally functionalised the resultant particles with PEG.^{28,58} As a result, these nanoparticles could be used for a combination of dual MRI and UCNPs imaging due to the presence of the IONPs, and PTT due to the presence of the Au shell. Additionally, the use of folic acid as a targeting agent allowed for tumour-targeted imaging. *In vitro* and *in vivo* studies showed a good response of these multifunctional nanoparticles for dual MRI and luminescence imaging, as well as PTT. The use of PTT was further improved by magnetically guiding the nanoparticles towards the tumour cells *via* an external magnet, thanks to the presence of the IONPs within the system. As a result, these multifunctional nanoparticles were effective for a range of applications; imaging *via* the luminescence of the UCNPs and MRI together with magnetically-guided PTT.^{28,58} The use of UCNPs decorated with IONPs has also been studied by Xu *et al.*²⁷ The authors further functionalised the UCNPs with an amphiphilic polymer and DOX, which could be used for novel imaging-guided therapy and magnetic-targeted drug delivery both *in vitro* and *in vivo*. Additionally, Zhang *et al.* further used UCNPs functionalised with IONPs and DOX for effective magnetic-targeted drug delivery and

MRI.⁵⁶ The combination of PTT and PDT together with dual MRI and UCNPs imaging was developed by Chen *et al.*⁵⁵ The authors fabricated Gd-based UCNPs, useful for MRI, and further functionalised these nanoparticles with Rose Bengal for PDT, the NIR absorbing dye IR825 for PTT and the protein bovine serum albumin (BSA) to provide good stability in aqueous solutions.⁵⁵

It can be readily seen that UCNPs hold great potential in biomedicine. The use of NIR light, typically 980 nm, offers important advantages for both imaging and therapeutic applications. More recently, the use of lower excitation wavelengths, 808 nm or 915 nm, have been explored, as discussed in **section 1.2.3.**^{59,60} The use of these lower wavelengths for excitation of the UCNPs offer further advantages. Absorption of water at 808 nm or even 915 nm is minimised, which avoids overheating of the biological sample while allowing larger imaging depth.^{59,60} The use of neodymium (Nd³⁺) as the sensitiser agent rather than Yb³⁺ to allow excitation at lower wavelengths is being studied and reported in the literature.⁶⁰

In this chapter, UCNPs functionalised with the photosensitiser Rose Bengal were used for PDT. As it has been previously mentioned, an extensive review on the current use of UCNPs for *in vitro* and *in vivo* PDT was covered in **Chapter 1**.

5.1.3. Aim of the research reported in this chapter

The application of UCNPs in biomedicine, especially in the field of PDT, is becoming increasingly popular. The interest in the use of UCNPs for PDT relies on the NIR excitation of the UCNPs, which allows for a better penetration into the tissue, reaching deeper tumours. Additionally, FRET between the UCNPs and a photosensitiser attached to their surface leads to the generation of ${}^1\text{O}_2$ for effective cell death.

In this chapter, the use of core-shell NaYF₄ UCNPs co-doped with Yb³⁺/Er³⁺/Gd³⁺, the most luminescence efficient UCNPs found to date, surface-modified with lysine and functionalised with the photosensitiser Rose Bengal for PDT was studied. Initially, the ability of the UCNPs to generate ${}^1\text{O}_2$ *via* the efficient FRET between the UCNPs and RB was investigated. Additionally, *in vitro* studies were performed on SK-BR-3 human breast adenocarcinoma cells. The internalisation of the UCNPs by the SK-BR-3 cells was

investigated *via* confocal laser scanning microscopy and multi-photon microscopy. Furthermore, studies on cell viability and cytotoxicity before and after PDT treatment were performed to evaluate the use of these UCNPs as potential candidates for PDT.

In the second part of the research reported in this chapter, UCNPs without the RB photosensitiser were analysed. First, the potential production of ${}^1\text{O}_2$ by the UCNPs without the presence of a photosensitiser was studied. Furthermore, *in vitro* studies on SK-BR-3 cells were also performed to evaluate the potential cytotoxicity associated with RB-free UCNPs both before and after PDT treatment.

5.2. Results and discussion

5.2.1. Synthesis and characterisation of the UCNPs

The UCNPs used throughout the research reported in this thesis were synthesised, characterised and kindly provided by Markus Buchner, PhD student in the group of Dr Thomas Hirsch (Institute for Analytical Chemistry, University of Regensburg, Regensburg, Germany).

The UCNPs used in the first part of **Chapter 5** were based on a hexagonal sodium yttrium fluoride ($\beta\text{-NaYF}_4$) structure doped with the lanthanides Yb^{3+} (20 %), Er^{3+} (2 %) and Gd^{3+} (20 %) with an average size of 16.2 nm. In order to enhance the luminescence intensity of the UCNPs, a cubic shell of NaYF_4 ($\alpha\text{-NaYF}_4$; 2-3 nm) was grown around the core of the UCNPs. The luminescence spectra of the core and core-shell UCNPs (**Figure 5.4 A**) show distinctive emission bands at *ca.* 550 nm and *ca.* 650 nm. These two bands are responsible for the green and red emission of the UCNPs, respectively. It can be clearly seen that the luminescence intensity of the core-shell UCNPs (**Figure 5.4 A (ii)**) is much higher than the luminescence of the core UCNPs (**Figure 5.4 A (i)**). The size of the core-shell UCNPs was analysed by TEM (**Figure 5.4 B-D**). Analysis of the TEM indicates that the nanoparticles are uniform and spherical and have an average

diameter of 17.2 ± 0.98 nm, following analysis of 991 nanoparticles, with a median value of 17.2 ± 0.95 nm.

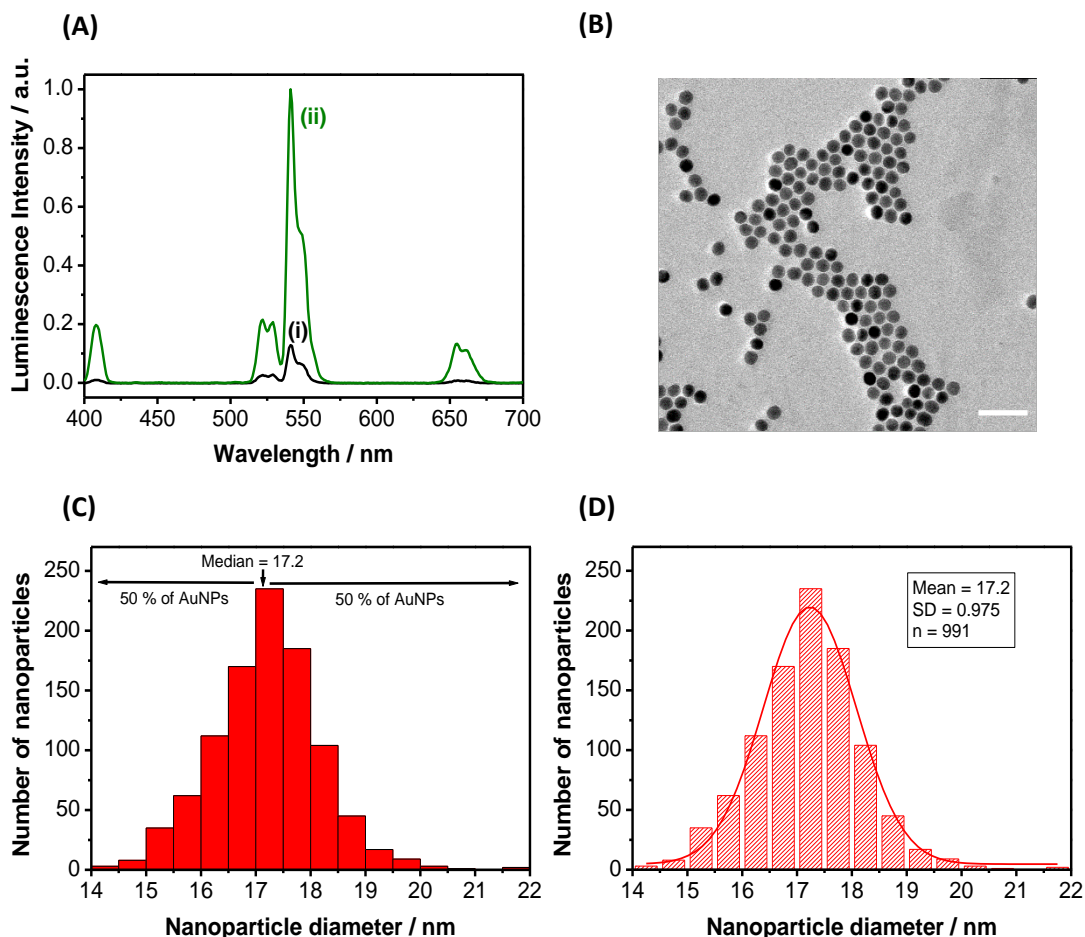


Figure 5.4. (A) Luminescence spectra of the core NaYF₄ (Yb³⁺, Er³⁺, Gd³⁺) UCNPs (i) and of the core-shell NaYF₄ (Yb³⁺, Er³⁺, Gd³⁺)-NaYF₄ UCNPs (ii) in cyclohexane. (B) Transmission electron micrograph of a sample of core-shell NaYF₄ (Yb³⁺, Er³⁺, Gd³⁺)-NaYF₄ UCNPs, where the scale bar represents 60 nm. (C) Histogram of the core-shell NaYF₄ (Yb³⁺, Er³⁺, Gd³⁺)-NaYF₄ UCNPs with a median value of 17.2 ± 0.95 nm (n = 991). (D) Size distribution of the core-shell NaYF₄ (Yb³⁺, Er³⁺, Gd³⁺)-NaYF₄ UCNPs showing the Gaussian fit, with an average size of 17.2 ± 0.98 nm (n = 991). Data obtained by Markus Buchner at the University of Regensburg (Germany).

The surface of the core-shell NaYF₄ (Yb³⁺, Er³⁺, Gd³⁺)-NaYF₄ UCNPs was modified with lysine, to which the photosensitiser Rose Bengal was attached (NaYF₄-lysine-RB) (**Figure 5.5 A**). The functionalised UCNPs were soluble in DMSO. The luminescence spectra of the functionalised and non-functionalised UCNPs are shown in **Figure 5.5 B**. NaYF₄-lysine-RB UCNPs (**Figure 5.5 B (ii)**) is distinctly different to that of the non-

functionalised UCNPs (**Figure 5.5 B (i)**). The green emission of the UCNPs was significantly decreased due to the energy transfer from the UCNPs to the RB, which absorbs light in that region (*ca.* 550 nm). Additionally, emission from RB at *ca.* 600 nm following NIR excitation clearly shows the functionalisation of the surface of the UCNPs with the RB photosensitiser.

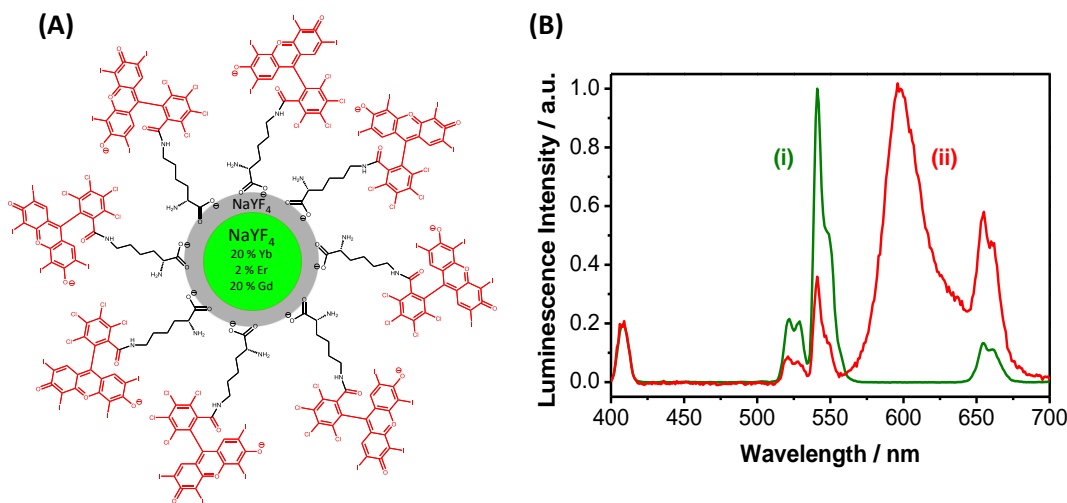


Figure 5.5. **(A)** Schematic representation of the NaYF_4 -lysine-RB UCNPs in DMSO, RB shown in red. **(B)** Luminescence spectra of non-functionalised NaYF_4 UCNPs **(i)** and NaYF_4 -lysine-RB UCNPs in DMSO **(ii)**. Spectra obtained by Markus Buchner at the University of Regensburg (Germany).

In the second part of **Chapter 5**, UCNPs dispersed in dH_2O were used. The structure was again based on $\beta\text{-NaYF}_4$ doped with Yb^{3+} (20 %), Er^{3+} (2 %) and Gd^{3+} (10 %), with an average size of 22 nm. These UCNPs were also modified with an $\alpha\text{-NaYF}_4$ shell, for luminescence intensity enhancement. The size of the core-shell UCNPs was analysed by TEM. Analysis of the TEM indicated that the nanoparticles were uniform and spherical and have an average diameter of 28 ± 3.17 nm, following analysis of 266 nanoparticles, with a median value of 28.5 ± 10 nm. The TEM results are shown in

Figure 5.6.

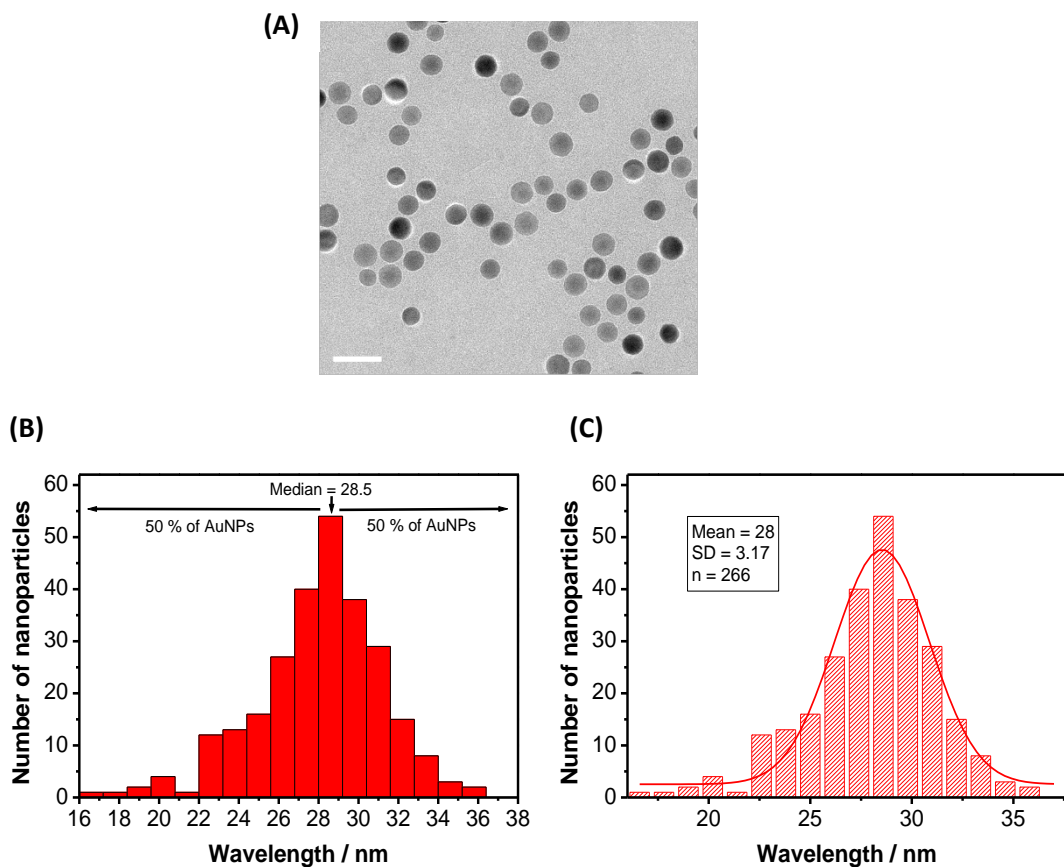


Figure 5.6. (A) Transmission electron micrograph of a sample of core-shell NaYF_4 (Yb^{3+} , Er^{3+} , Gd^{3+})- NaYF_4 UCNPs in dH_2O , where the scale bar represents 60 nm. (B) Histogram of the core-shell NaYF_4 (Yb^{3+} , Er^{3+} , Gd^{3+})- NaYF_4 UCNPs with a median value of 28.5 ± 10 nm ($n = 266$). (C) Size distribution of the core-shell NaYF_4 (Yb^{3+} , Er^{3+} , Gd^{3+})- NaYF_4 UCNPs showing the Gaussian fit, with an average size of 28 ± 3.17 nm ($n = 266$). Data obtained by Markus Buchner (University of Regensburg, Germany).

To provide the aqueous dispersibility, the UCNPs were functionalised with polyacrylic acid (PAA) ligands. A schematic representation of the NaYF_4 -PAA UCNPs together with a luminescence spectrum are shown in **Figure 5.7 A** and **B** respectively. As previously mentioned, the luminescence spectrum shows the green and red emission from the UCNPs at *ca.* 550 and 650 nm, respectively. These UCNPs in dH_2O , not functionalised with RB, were used to test the cytotoxic effects of the UCNPs alone and their potential ability to induce cell death before and after irradiation with a 980 nm NIR laser.

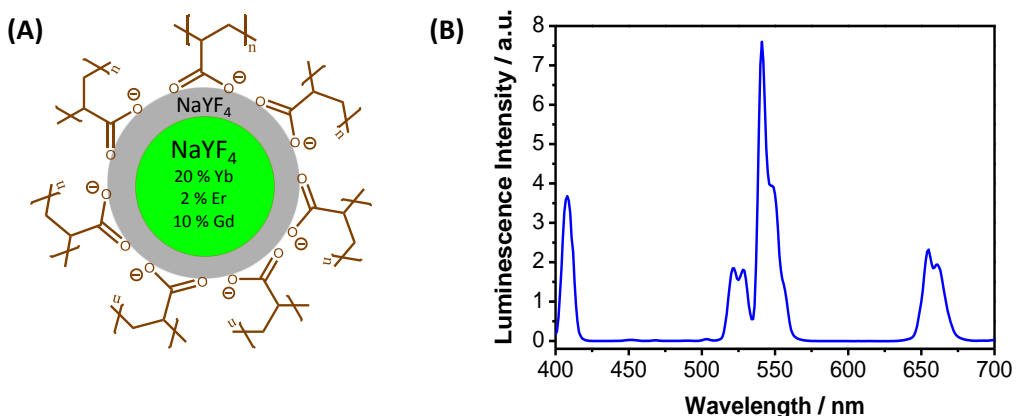


Figure 5.7. (A) Schematic representation of the NaYF_4 -PAA UCNP in dH_2O . **(B)** Luminescence spectrum of NaYF_4 -PAA UCNP in dH_2O . Spectrum obtained by Markus Buchner at the University of Regensburg (Germany).

5.2.2. Singlet oxygen production by the NaYF_4 -lysine-RB UCNP

The RB-functionalised UCNP, dissolved in DMSO, were analysed for ${}^1\text{O}_2$ production. In order to use these UCNP for PDT, RB should produce ${}^1\text{O}_2$ upon excitation of the UCNP at 980 nm. Energy transfer between the UCNP and the RB should occur for efficient ${}^1\text{O}_2$ production. Specifically, the green emission ($\lambda_{\text{max}} = 541 \text{ nm}$) from the UCNP following excitation at 980 nm should excite the RB (absorption $\lambda_{\text{max}} = 540\text{--}550 \text{ nm}$) on the surface, leading to the production of ${}^1\text{O}_2$. The probe ABMA was used to study the production of ${}^1\text{O}_2$. ABMA, as described in **section 3.2.4**, is photobleached in the presence of ${}^1\text{O}_2$. As a result, the fluorescence of ABMA is quenched upon reaction with ${}^1\text{O}_2$.

The NaYF_4 -lysine-RB UCNP were dispersed in either DMSO (100 %) or McCoy's 5A medium (containing between 6-10 % DMSO) to evaluate the production of ${}^1\text{O}_2$ in each solvent. The concentration of the UCNP was either 1 mg/mL or 25 $\mu\text{g}/\text{mL}$. The latter concentration was used to simulate the typical low concentrations that were used in the intracellular experiments. The fluorescence quenching of ABMA over time (**Figure 5.8**) clearly confirms that ${}^1\text{O}_2$ is being produced by the RB on the surface of the NaYF_4 -lysine-RB UCNP upon irradiation at 980 nm. This confirms the energy transfer between the UCNP and RB. As expected, the production of ${}^1\text{O}_2$ is significantly higher when the UCNP are dispersed in DMSO as compared to that obtained when the nanoparticles

are dispersed in McCoy's 5A medium. The reduced production of ${}^1\text{O}_2$ in McCoy's 5A medium is probably due to the higher quenching of the fluorescence in the presence of an aqueous solution. A similar result with lower ${}^1\text{O}_2$ production for the samples dispersed in McCoy's 5A medium was obtained for both concentrations at 1 mg/mL and 25 $\mu\text{g}/\text{mL}$ of UCNPs. As would be expected, the 1 mg/mL sample led to a higher ABMA photobleaching both in DMSO and McCoy's 5A medium. These results confirm that the production of ${}^1\text{O}_2$ is dependent on both the concentration of the UCNPs and the solvent in which they are dissolved. Conclusively, it can be confirmed that the NaYF_4 -lysine-RB UCNPs are able to generate ${}^1\text{O}_2$ upon irradiation at 980 nm, even at low concentrations, and can thus be potentially used for NIR-PDT.

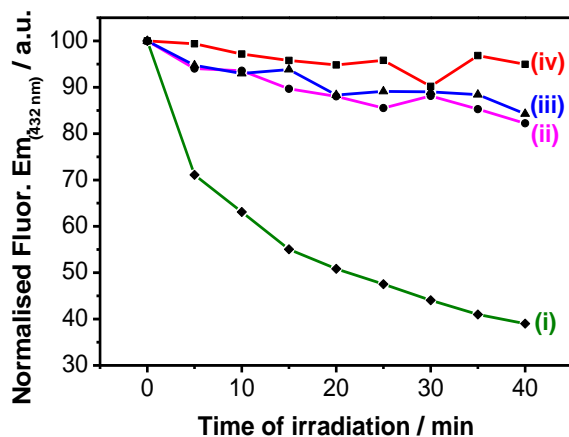


Figure 5.8. Quenching of ABMA fluorescence at 432 nm in the presence of NaYF_4 -lysine-RB UCNPs dispersed in either DMSO (i, ii) or McCoy's 5A medium (iii, iv) upon irradiation with a 980 nm NIR laser. The RB on the NaYF_4 -lysine-RB UCNPs was at a concentration of either 1 mg/mL (i, iii) or 25 $\mu\text{g}/\text{mL}$ (ii, iv).

5.2.3. Internalisation studies of the NaYF_4 -lysine-RB UCNPs by SK-BR-3 cells

The results shown in **section 5.2.2** clearly demonstrate the production of ${}^1\text{O}_2$ by the RB on the NaYF_4 -lysine-RB UCNPs upon irradiation with a 980 nm NIR laser. Therefore, these UCNPs are potential candidates for PDT. *In vitro* studies using SK-BR-3 human breast adenocarcinoma cells were performed to evaluate the suitability of the NaYF_4 -lysine-RB UCNPs for PDT.

The internalisation of the NaYF_4 -lysine-RB UCNPs by the SK-BR-3 cells was initially studied using confocal laser scanning microscopy. The main challenge with the use of confocal microscopy for this purpose, with the available lasers, was that the UCNPs could not be directly excited due to the NIR wavelength (980 nm) required. Therefore, to prove the presence of the UCNPs inside the cells *via* confocal microscopy, the RB in the sample was directly excited using a HeNe laser at 543 nm. As described in **section 2.4.4**, the UCNPs at a concentration of 25 $\mu\text{g}/\text{mL}$ were incubated with the SK-BR-3 cells for 3 h prior to imaging. Following incubation, the internalisation of the UCNPs by the cells was investigated. The emission due to the RB ($\lambda_{\text{max}} \approx 567 \text{ nm}$) in the UCNPs was collected in the red channel using a band pass filter between 560-615 nm. Additionally, the morphology of the cells was evaluated from the DIC images, which were obtained using a 488 nm argon-ion laser. Confocal microscopy images are shown in **Figure 5.9**.

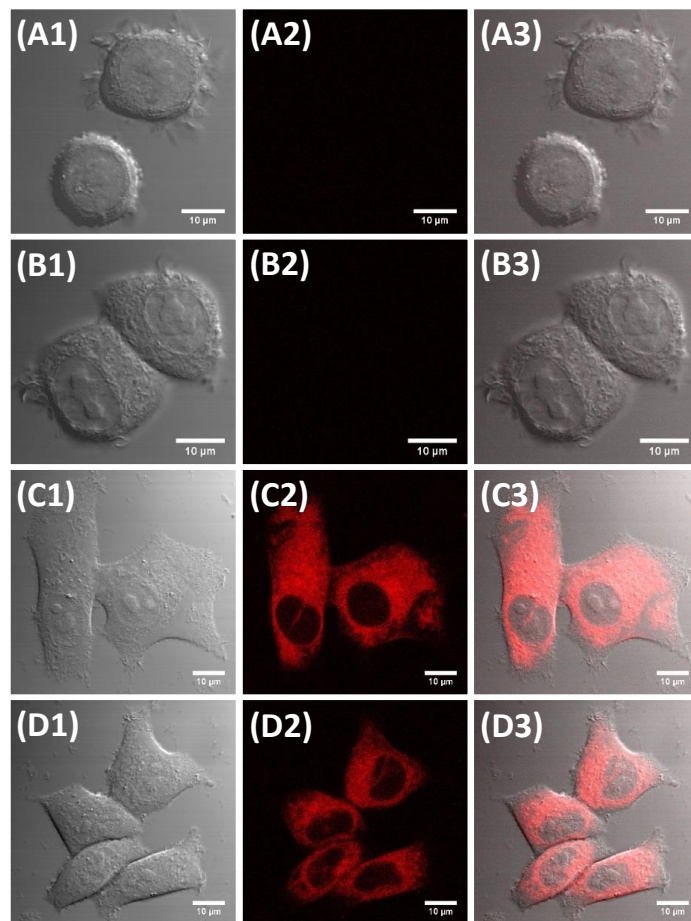


Figure 5.9. Confocal fluorescence microscopy images of SK-BR-3 cells: control cells incubated with McCoy's 5A phenol red-free medium **(A-B)** or cells incubated with 25 $\mu\text{g}/\text{mL}$ NaYF_4 -lysine-RB UCNPs **(C-D)**. Images taken from: **1**) DIC, **2**) fluorescence from RB collected in the red channel ($\lambda_{\text{ex}} = 543 \text{ nm}$; 560-615 nm), **3**) composite images of DIC and red channel. Scale bars 10 μm .

Samples treated with the UCNPs (**Figure 5.9 C-D**) clearly show the red fluorescence emitted from the RB functionalised on the surface of the UCNPs. The intense red fluorescence is located only inside the cells, as confirmed by **Figure 5.9 C3, D3**, where it is clearly seen that the space surrounding the cells does not show any fluorescence. On the other hand, control cells, not treated with the UCNPs (**Figure 5.9 A-B**), do not show any fluorescence. The cell morphology of the cells treated with the UCNPs is shown to be intact. This confirms that the cells remain viable following incubation with the UCNPs.

The results obtained from the confocal microscope confirm that the cells have efficiently internalised the RB, which suggests that the UCNPs themselves have been fully internalised. However, for definitive proof of internalisation of the UCNPs, the UCNPs should be excited at 980 nm to obtain the green and red emission from the UCNPs directly, and not the emission from RB alone. For this purpose, a multi-photon microscope was used, which allows the excitation of NIR-exitable fluorophores. The cells were treated in the same manner as previously described for the confocal microscope experiments. For imaging in the multi-photon microscope, the cells were excited at two different wavelengths, 880 nm and 980 nm (**Figure 5.10**). Excitation at 880 nm should enable the production of the DIC images (**Figure 5.10 A-D (1)**) as well as the excitation of the RB on the surface of the UCNPs (**Figure 5.10 A-D (2)**). Excitation at 980 nm should lead to the direct excitation of the UCNPs (**Figure 5.10 A-D (4-5)**). Fluorescence emission was collected in either the green channel (550 ± 42.5 nm) or the red channel (655 ± 20 nm). Both the green and the red channel show emission from the UCNPs upon excitation at 980 nm (**Figure 5.10 A-D (4-5)**). Additionally, the green channel also shows emission from the RB on the surface of the UCNPs upon excitation at 880 nm (**Figure 5.10 C-D (2)**).

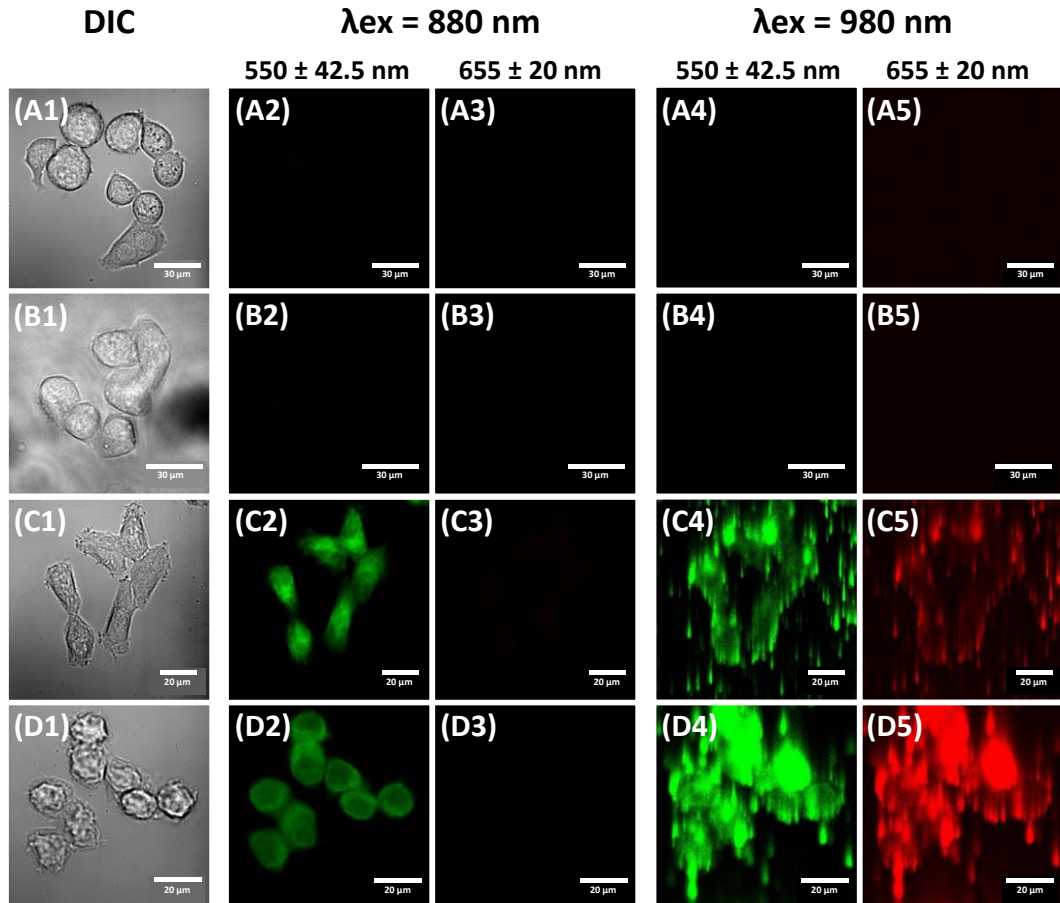


Figure 5.10. Multi-photon microscopy images of SK-BR-3 cells control cells incubated with McCoy's 5A phenol red-free medium **(A-B)** or incubated with 25 μ g/mL NaYF₄-lysine-RB UCNPs **(C-D)**. Images taken from: **1**) DIC ($\lambda_{\text{ex}} = 880 \text{ nm}$), **2**) fluorescence from RB collected in the green channel ($\lambda_{\text{ex}} = 880 \text{ nm}$; $550 \pm 42.5 \text{ nm}$), **3**) fluorescence collected in the red channel ($\lambda_{\text{ex}} = 880 \text{ nm}$; $655 \pm 20 \text{ nm}$), **4**) luminescence from UCNPs collected in the green channel ($\lambda_{\text{ex}} = 980 \text{ nm}$; $550 \pm 42.5 \text{ nm}$), **5**) luminescence from UCNPs collected in the red channel ($\lambda_{\text{ex}} = 980 \text{ nm}$; $655 \pm 20 \text{ nm}$). Scale bars **(A-B)** 30 μm or **(C-D)** 20 μm .

It is important to note that fluorescence or luminescence emission is only seen in samples incubated with the NaYF₄-lysine-RB UCNPs (**Figure 5.10 C-D**), whereas the control samples not incubated with UCNPs do not show any fluorescence or luminescence in any of the four channels (**Figure 5.10 A-B**). Following excitation at 880 nm, fluorescence emission is only seen in the green channel but not in the red channel (**Figure 5.10 C-D (2)**). This indicates that the fluorescence seen is due to the RB on the surface of the UCNPs. Following excitation at 980 nm, fluorescence emission is seen in both the green and red channels (**Figure 5.10 C-D (4-5)**), as expected from the luminescence spectrum of the UCNPs (**Figure 5.5**). The emission of the SK-BR-3 cells incubated with the NaYF₄-lysine-RB UCNPs upon excitation at 980 nm (**Figure 5.10 C-D**

(4-5)) provided images of low resolution with a distorted representation of the luminescence of the UCNPs, with the nanoparticles appearing to be aggregated. Similar low quality images have previously been reported.⁶¹ Yu *et al.* associated this lack of definition to several interferences in the sample. Axial interference coming from the out-of-focus luminescence of the UCNPs, in combination with lateral interference coming from the scattering within the focal plane greatly contributed to the absence of in-focus detail, leading to the images shown in **Figure 5.10 C-D (4-5)**. Yu *et al.* reported that the use of a multi-photon microscope fitted with a pinhole leads to the suppression of the axial and lateral interferences and thus to clear images with high quality and resolution.⁶¹ While such a ‘pinhole’ was not available for these studies, the results reported in **Figure 5.10** confirm the internalisation of the UCNPs by the SK-BR-3 cells, not only by the fluorescence emission of the RB but also with the luminescence of the UCNPs, which is only seen in those samples treated with NaYF₄-lysine-RB UCNPs.

5.2.4. PDT using NaYF₄-lysine-RB UCNPs – CellTiter-Blue® cell viability assays

Following confirmation that SK-BR-3 cells effectively internalise the NaYF₄-lysine-RB UCNPs, the efficacy of the UCNPs for PDT was investigated. A CellTiter-Blue® cell viability assay was used to evaluate the PDT effect. The CellTiter-Blue® assay has been previously described in **section 3.2.6**.

As described in **section 2.4.6**, SK-BR-3 cells were incubated with the NaYF₄-lysine-RB UCNPs at various concentrations for 3 h. Following incubation, the cells were thoroughly washed with PBS-B to remove all of the non-internalised UCNPs. At this point, some samples were subjected to PDT irradiation for 6 min using a 980 nm NIR laser. The non-irradiated samples were kept in the dark under the same conditions. Cell viability was studied *ca.* 48 h later. **Figure 5.11** shows that, following PDT treatment (*i.e.*, post-irradiation), there is a decrease in the viability of the SK-BR-3 cells, concomitant with an increase in the concentration of the UCNPs in the sample. The main drawback was that at high concentrations, the UCNPs become toxic even before irradiation with a 980 nm NIR laser. This dark toxicity starts to appear with increasing concentration and it is especially high when the cells are incubated with 25 µg/mL of

the UCNPs. Four control samples were included in this assay. The first one, denoted as '0' in **Figure 5.11**, shows the viability of the cells that were not incubated with UCNPs. It can be seen that the cells remain viable before and after irradiation, confirming that the 980 nm NIR laser light does not induce toxicity to the cells. The second control sample, denoted as 'a' in **Figure 5.11**, refers to cells incubated with DMSO. In this case, the DMSO was completely toxic for the cells as almost 100 % of the cells were killed. The third control sample, denoted as 'b' in **Figure 5.11**, refers to cells incubated with DMSO dispersed in McCoy's 5A phenol red-free medium (0.25 % DMSO). This control sample simulates the amount of DMSO in all UCNPs samples. It was confirmed that, under the conditions used to perform the cell viability assay, DMSO is not toxic for the cells as the SK-BR-3 cells remain viable (*ca.* 97 %). Therefore, dispersing the UCNPs in McCoy's 5A medium is a good way to decrease the toxicity that would otherwise be induced by DMSO. The final control sample, '+ve St', was a solution of staurosporine in McCoy's 5A phenol red-free medium, a positive control for cytotoxicity.

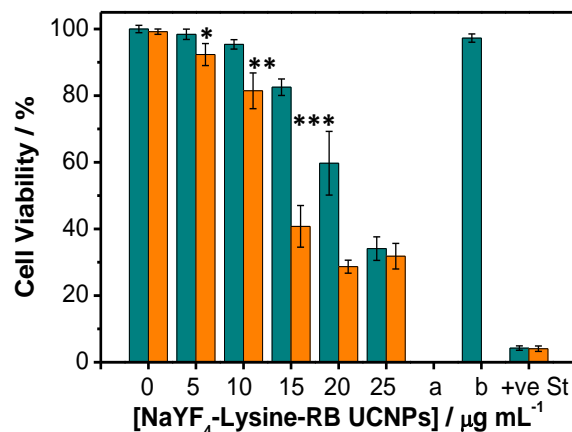


Figure 5.11. CellTiter-Blue® cell viability assay for SK-BR-3 cells incubated with NaYF₄-lysine-RB UCNPs. Cells were either irradiated with a 980 nm NIR laser (orange) or non-irradiated (dark cyan). DMSO (a) was used as a control to test its cytotoxic effect in SK-BR-3 cells. DMSO diluted to 0.25 % (b) was also used as a control to test the effects of DMSO under the conditions used to perform the cell viability assay. Staurosporine (+ve St) was used as a positive control for cytotoxicity. Error bars represent the standard deviation ($n = 3$) within a 95 % confidence interval. Statistically significant difference between non-irradiated and irradiated samples is indicated by * at $P < 0.04$, ** at $P < 0.01$ and *** at $P < 0.0004$, obtained using a two-tailed Student's *t*-test, where $P < 0.05$ is considered statistically significant.

Further studies to determine the ideal concentration of the UCNPs for maximum PDT efficacy were performed. The lowest concentration of 5 $\mu\text{g/mL}$ was removed since it did not lead to any significant cell death following PDT, as shown in **Figure 5.11**. Additionally, the highest concentration of 25 $\mu\text{g/mL}$ was also removed due to its high dark toxicity. A new concentration of 17 $\mu\text{g/mL}$ was added to the following cell viability assays. The results are shown in **Figure 5.12**. In nine repetitions, the majority of the assays always provided the same trend in relation to cell viability and cell death. The exact values for each sample were variable but the error was usually included within a 95 % confidence interval. As seen in **Figure 5.12**, a decrease in cell viability after PDT treatment (*i.e.*, after irradiation with a 980 nm laser) is concomitant with an increase in the concentration of the UCNPs, and thus an increase in the concentration of RB. Dark toxicity levels remained low, but they were also seen to grow as the concentration of UCNPs increased.

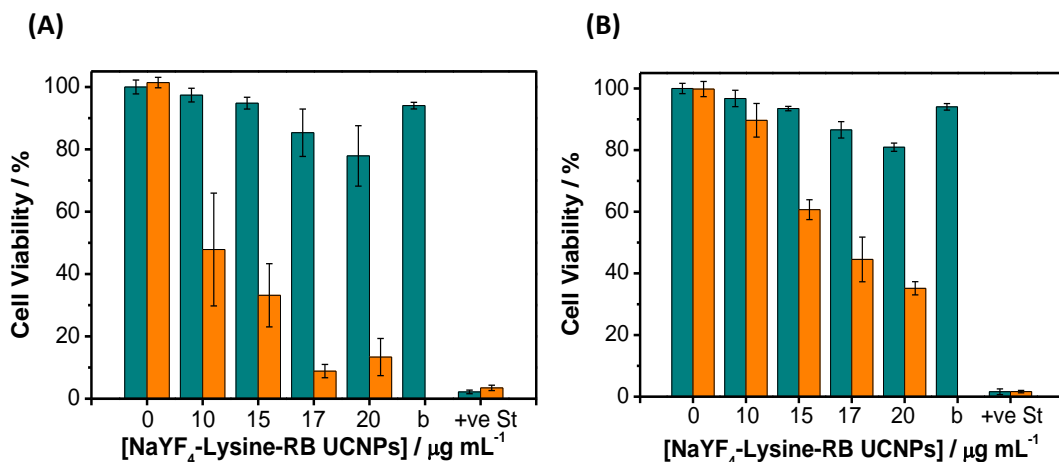


Figure 5.12. CellTiter-Blue® cell viability assay for SK-BR-3 cells incubated with NaYF₄-Lysine-RB UCNPs, where **(A)** and **(B)** are repetitions of the same assay under the same conditions. Cells were either irradiated with a 980 nm NIR laser (orange) or non-irradiated (dark cyan). DMSO diluted to 0.25 % (b) was also used as a control to test the effects of DMSO under the conditions used to perform the cell viability assay. Staurosporine (+ve St) was used as a positive control for cytotoxicity. Error bars represent the standard deviation ($n = 3$) within a 95 % confidence interval.

From all of the cell viability assays, it was found that 15 $\mu\text{g/mL}$ was the ideal concentration for PDT. Cells incubated with 15 $\mu\text{g/mL}$ showed minimal levels of dark toxicity (*ca.* 5-15 %) while inducing effective cell death (*ca.* 40-67 %) following PDT. Higher concentrations (17-20 $\mu\text{g/mL}$) are also effective at inducing cell death. However,

the greater levels of dark toxicity should be considered. As a result, 15 $\mu\text{g}/\text{mL}$ was chosen as the ideal concentration for further studies.

5.2.5. Estimation of the concentration of RB on the UCNPs

The concentration of RB on the UCNPs can be estimated by recording the UV-vis extinction spectrum of the UCNP samples. Additionally, a value for the extinction coefficient of RB needs to be estimated. The extinction coefficient of RB was estimated in dH_2O at 549 nm (**Figure 5.13**) and it was found to be $87,334 \pm 1,010 \text{ M}^{-1}\cdot\text{cm}^{-1}$. A literature value of $95,000 \text{ M}^{-1}\cdot\text{cm}^{-1}$ at 545 nm has been previously reported.⁶²

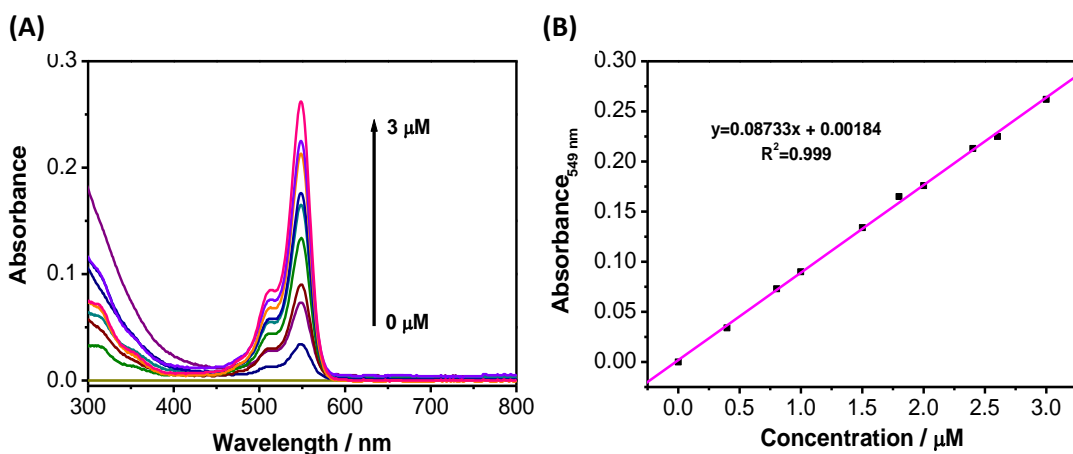


Figure 5.13. (A) UV-vis absorption spectrum of RB in dH_2O at various concentrations and (B) its corresponding calibration curve at 549 nm.

Once a value for the extinction coefficient of RB had been estimated, the UV-vis extinction spectrum of a sample of NaYF_4 -lysine-RB UCNPs in DMSO at a concentration of 1 mg/mL was recorded (**Figure 5.14**). Using the absorbance intensity of RB with a maximum at 549 nm (1.006) and the extinction coefficient of RB, the concentration of RB can be calculated using the Beer-Lambert law, which was found to be 11.52 μM . From this value, several dilutions were prepared to reach the concentrations used in the cell viability assays ($[\text{UCNPs}] = 5, 10, 15, 17, 20, 25 \mu\text{g}/\text{mL}$). The concentrations of RB in each of these dilutions was then calculated using **Equation 5.1**. The results are shown in **Table 5.1**.

$$M_1 V_1 = M_2 V_2$$

Equation 5.1. Equation used to calculate the concentration of RB in each of the diluted UCNPs samples. Where V_1 is the volume of UCNPs at 1 mg/mL used; M_1 is the concentration of RB in the 1 mg/mL solution (11.52 μ M); M_2 is the concentration of RB to be calculated in each sample; and V_2 is the final volume.

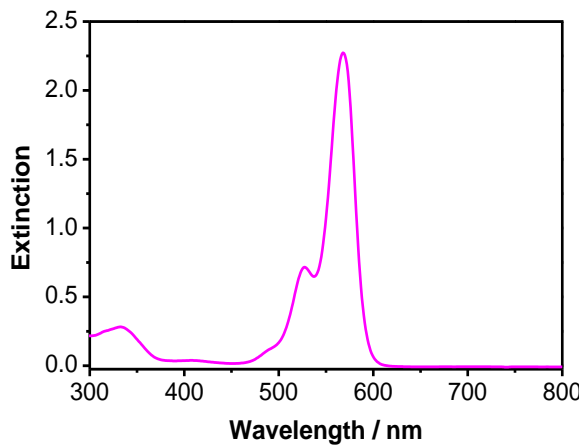


Figure 5.14. Extinction spectrum of a sample of NaYF₄-lysine-RB UCNPs diluted to 1 mg/mL in DMSO.

Table 5.1. Calculated values of the concentration of RB in different UCNPs samples.

[UCNPs] / μ g · mL ⁻¹	V_1 / μ L	V_2 / μ L	[RB] / μ M
5	5	1,000	0.058
10	10	1,000	0.115
15	15	1,000	0.173
17	17	1,000	0.196
20	20	1,000	0.230
25	25	1,000	0.288

As reported in **section 5.2.4**, an ideal concentration of the UCNPs for PDT was found to be 15 μ g/mL. At a 15 μ g/mL concentration of UCNPs, there is 0.173 μ M of RB in the sample.

5.2.6. Evaluation of PDT effect using confocal microscopy

To further establish the potential of the NaYF₄-lysine-RB UCNPs as PDT agents, the PDT effect in SK-BR-3 cells was studied using laser scanning confocal microscopy. As it was

previously explained in **Chapter 3**, the evaluation of cell death *via* confocal microscopy can be achieved in two ways. Firstly, the morphology of the cells significantly changes following cell death. The change in cell morphology can be easily evaluated using the DIC brightfield image of the confocal microscope. Additionally, the dead cell marker propidium iodide can be used in order to fluorescently stain dead cells.

The fluorescence from RB on the surface of the UCNPs overlaps with that of propidium iodide (**Figure 5.15**). As a result, the excitation and emission parameters in which the fluorescence was collected using the confocal microscope are exactly the same; *i.e.*, fluorescence from RB and propidium iodide were collected in the same channel (**Figure 5.15**) with excitation at 543 nm and emission collected between 560-615 nm.

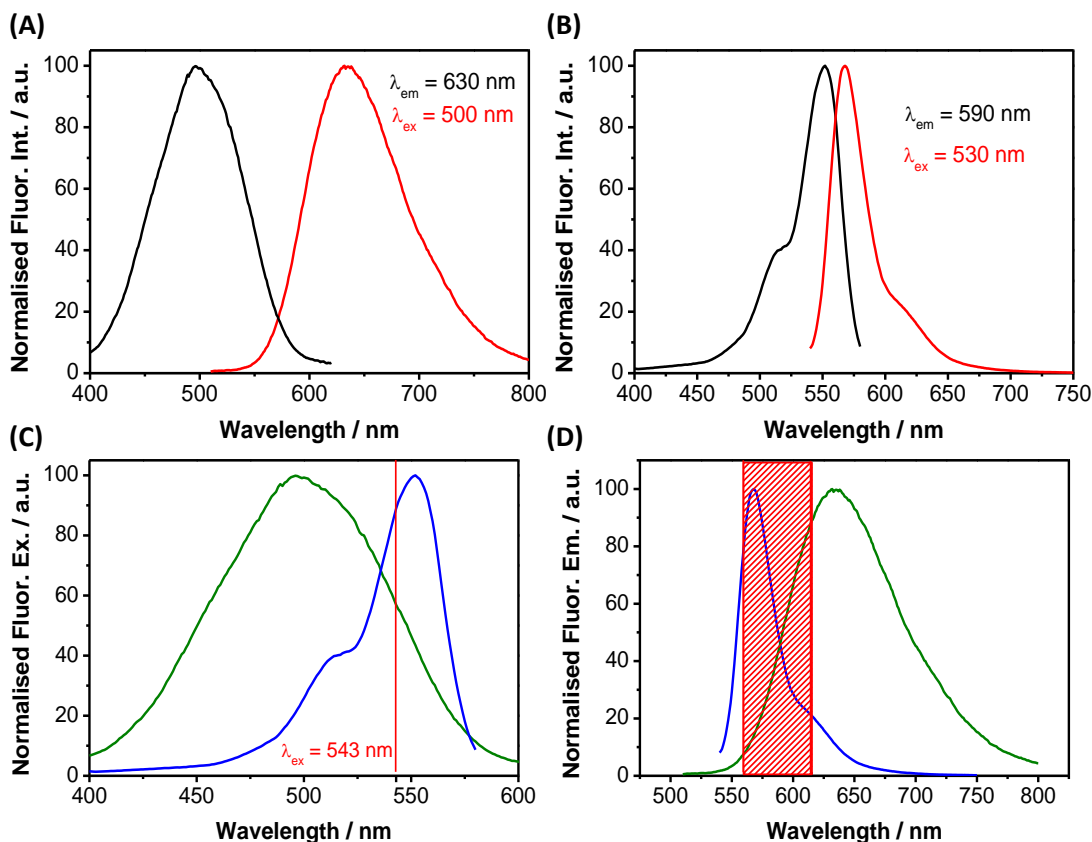


Figure 5.15. Normalised fluorescence intensity excitation and emission spectra of **(A)** propidium iodide ($\lambda_{\text{ex}} = 500 \text{ nm}$, $\lambda_{\text{em}} = 630 \text{ nm}$) and **(B)** Rose Bengal ($\lambda_{\text{ex}} = 530 \text{ nm}$, $\lambda_{\text{em}} = 590 \text{ nm}$). **(C)** Comparison of the fluorescence excitation spectra of propidium iodide (green line) and Rose Bengal (blue line), showing the excitation wavelength ($\lambda_{\text{ex}} = 543 \text{ nm}$) used with the confocal microscope (red line). **(D)** Comparison of the fluorescence emission spectra of propidium iodide (green line) and Rose Bengal (blue line), showing where the emission ($\lambda_{\text{em}} = 560\text{--}615 \text{ nm}$) is collected with the confocal microscope (red box).

Collecting the fluorescence of RB and propidium iodide in the same channel could create a challenge to distinguish the fluorescence from RB on the UCNPs to that of the propidium iodide. However, it was found that by modulating the laser power, from 100 % to only 4 %, this problem could be solved. At low laser powers, the fluorescence of the RB on the UCNPs is low and remains undetectable. However, upon staining of propidium iodide, the fluorescence at 4 % laser power is intense. Therefore, the detection of propidium iodide staining can be easily identified upon excitation with a laser power of 4 % intensity.

As explained in **section 2.4.5**, SK-BR-3 cells were incubated with 15 μ g/mL NaYF₄-lysine-RB UCNPs for 3 h. The concentration of 15 μ g/mL was chosen since it was found to be ideal for PDT, as shown in **section 5.2.4**. Following incubation, the cells were thoroughly washed with PBS-B to remove all of the non-internalised UCNPs. Additionally, the cells were irradiated for 6 min using a 980 nm NIR laser, to stimulate the generation of $^1\text{O}_2$. The cells were then imaged *ca.* 24 h later. Three control experiments were also performed. In the first one, SK-BR-3 cells were not incubated with UCNPs and non-irradiated (**Figure 5.16 A**). In the second control, SK-BR-3 cells were not incubated with UCNPs but were irradiated with the 980 nm laser for 6 min (**Figure 5.16 B**). In the third control, SK-BR-3 cells were incubated with the NaYF₄-lysine-RB UCNPs and non-irradiated (**Figure 5.16 C**).

Cells treated with the NaYF₄-lysine-RB UCNPs and irradiated with the 980 nm laser (**Figure 5.16 D-E**) show clear changes in cell morphology, as compared to healthy cells. The disintegration of the cell membrane can be easily identified in these images (**Figure 5.16 D-E (1)**), which is a strong indicator of cell death. Additionally, the UCNPs were preferentially located within the nucleus of dead cells (**Figure 5.16 D (2-3)**), which is in contrast to the location of the UCNPs in viable cells (**Figure 5.9 section 5.2.3**). Following incubation with propidium iodide, the intensity of the fluorescence in the red channel drastically increases (**Figure 5.16 E**), which is an indication of the positive staining with propidium iodide and thus further confirms the death of the SK-BR-3 cells after PDT treatment. On the other hand, all control cells have a very healthy appearance in the DIC channel and show no indication of staining with propidium iodide. This confirms that neither the 980 nm NIR laser nor the NaYF₄-lysine-RB UCNPs by themselves induce

toxicity in the cells. The irradiation of the NaYF_4 -lysine-RB UCNPs is required in order to induce production of ${}^1\text{O}_2$, which leads to cell death.

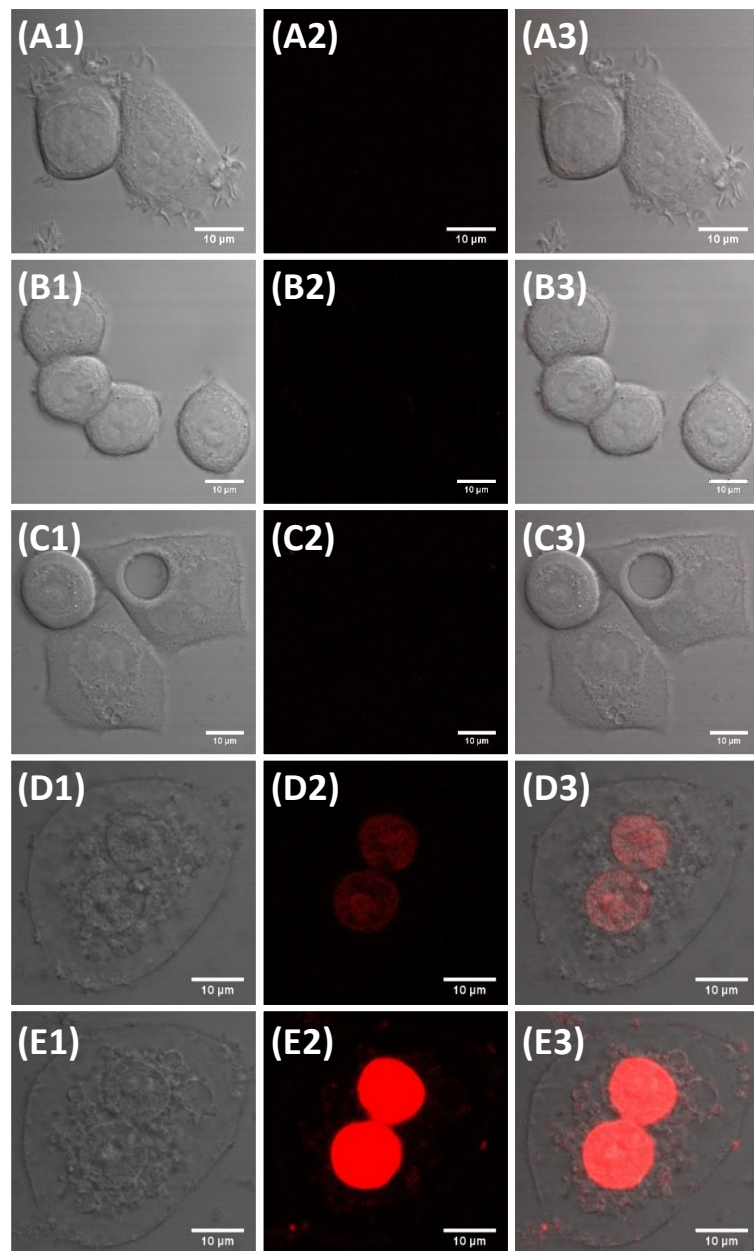


Figure 5.16. Confocal fluorescence microscopy images of SK-BR-3 cells. Control cells incubated with McCoy's 5A phenol red-free medium containing 0.25 % DMSO and treated with propidium iodide before (A) or after (B) irradiation with a 980 nm NIR laser. SK-BR-3 cells incubated with 15 $\mu\text{g}/\text{mL}$ NaYF_4 -lysine-RB UCNPs and treated with propidium iodide before irradiation with a 980 nm NIR laser (C). SK-BR-3 cells incubated with 15 $\mu\text{g}/\text{mL}$ NaYF_4 -lysine-RB UCNPs following irradiation with a 980 nm laser either before (D) or after (E) treatment with propidium iodide. Images taken from: **1)** DIC, **2)** fluorescence from RB and propidium iodide collected in the red channel ($\lambda_{\text{ex}} = 543 \text{ nm}$ with a 4 % laser power; 560-615 nm), **3)** composite images of DIC and red channel. Scale bars 10 μm .

The images shown in **Figure 5.16** were taken with a laser power of 4 % for the red channel ($\lambda_{\text{ex}} = 543 \text{ nm}$). This low laser power was chosen to be able to identify and distinguish the fluorescence from propidium iodide from that of the RB on the surface of the UCNPs, as previously explained. As a result, the fluorescence of the RB on the UCNPs is undetected for the non-irradiated cells incubated with NaYF_4 -lysine-RB UCNPs and treated with propidium iodide (**Figure 5.16 C**). In order to confirm the internalisation of the UCNPs by these non-irradiated cells, the laser power was increased to 100 % and further images were collected, as shown in **Figure 5.17**. Indeed, increasing the laser power confirmed the internalisation of the NaYF_4 -lysine-RB UCNPs by non-irradiated SK-BR-3 cells (**Figure 5.17 B**), which was not seen in control cells only incubated with growth medium containing 0.25 % DMSO (**Figure 5.17 A**). It is worth noting that the UCNPs do not accumulate in the nucleus of SK-BR-3 cells prior to PDT irradiation (**Figure 5.17 B**). The preferential location of the UCNPs inside the nucleus was only seen following PDT (**Figure 5.16 D-E**), which was another indicator for cell death.

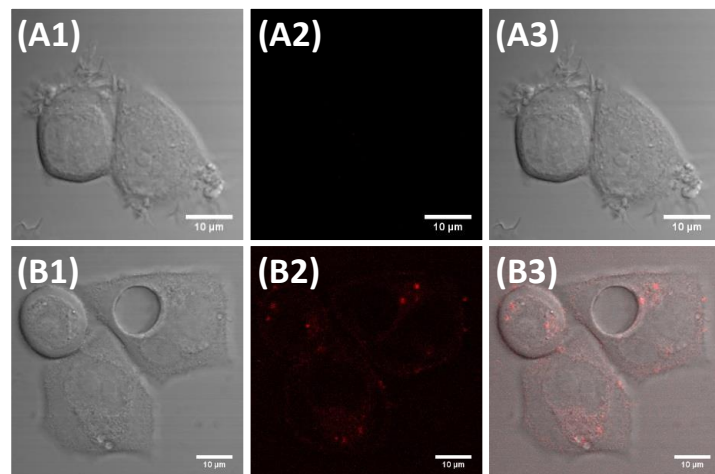


Figure 5.17. Confocal fluorescence microscopy images of non-irradiated SK-BR-3 cells control cells incubated with McCoy's 5A phenol red-free medium containing 0.25 % DMSO (**A**) or incubated with 15 $\mu\text{g}/\text{mL}$ NaYF_4 -lysine-RB UCNPs (**B**). These images were taken prior to treatment with propidium iodide. Images taken from: **1**) DIC, **2**) fluorescence from RB collected in the red channel ($\lambda_{\text{ex}} = 543 \text{ nm}$ with a 100 % laser power; 560-615 nm), **3**) composite images of DIC and red channel. Scale bars 10 μm .

In order to fully show the extent of cell death following irradiation with a 980 nm NIR laser (*i.e.*, after PDT), images with a larger cell sample size were recorded. These are

shown in **Figure 5.18**. Images of control cells incubated with growth medium containing 0.25 % DMSO and irradiated with the 980 nm laser were also recorded for comparison (**Figure 5.18 A**). These images were recorded following treatment of the cells with propidium iodide and using a laser power of 4 % to excite the red channel ($\lambda_{ex} = 543$ nm). It can be clearly seen that following PDT, SK-BR-3 cells stain positive for propidium iodide (**Figure 5.18 B**), as compared to control cells. Additionally, the morphology of the cell membrane is drastically different, since the cell membrane in the PDT-treated cells is shown to be disintegrated.

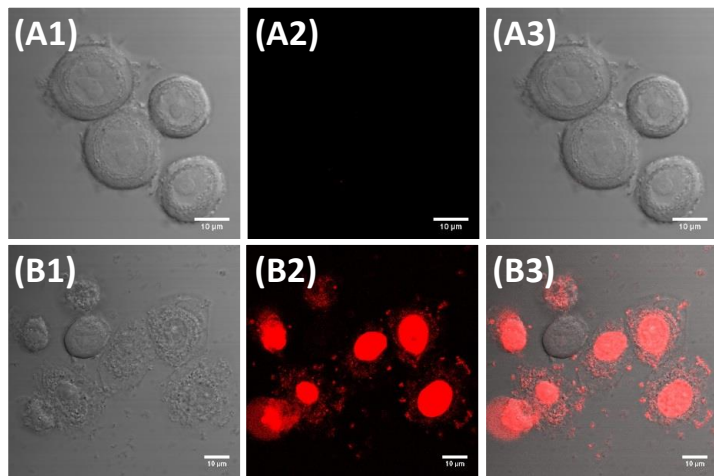


Figure 5.18. Confocal fluorescence microscopy images of non-irradiated SK-BR-3 cells. Control cells incubated with McCoy's 5A phenol red-free medium containing 0.25 % DMSO (**A**) or cells incubated with 15 μ g/mL NaYF₄-lysine-RB UCNPs (**B**). All cells were irradiated with a 980 nm laser for 6 min and treated with propidium iodide. Images taken from: **1)** DIC, **2)** fluorescence from RB and propidium iodide collected in the red channel ($\lambda_{ex} = 543$ nm with a 4 % laser power; 560-615 nm), **3)** composite images of DIC and red channel. Scale bars 10 μ m.

The results obtained from the confocal microscopy, together with the results from the CellTiter-Blue® assays shown in **section 5.2.4**, clearly show that the NaYF₄-lysine-RB UCNPs in DMSO are good candidates for PDT. The NaYF₄-lysine UCNPs were readily internalised by SK-BR-3 cells. Additionally, these UCNPs at 15 μ g/mL are only toxic to the SK-BR-3 cells following irradiation with a 980 nm NIR laser, which induces generation of ${}^1\text{O}_2$ by the RB following energy transfer between the UCNPs and the RB. Neither the NIR laser nor the UCNPs themselves induce any toxicity of the SK-BR-3 cells.

5.2.7. ApoTox-Glo™ Triplex assay to investigate the mechanism of cell death

The mechanism of cell death followed by the SK-BR-3 cells post NIR-PDT using the NaYF₄-lysine-UCNPs was studied *via* an ApoTox-Glo™ Triplex assay. As explained in **section 3.2.14**, the ApoTox-Glo™ Triplex assay measures cell viability, cell cytotoxicity and apoptotic response within the sample using three different biomarkers for each of these processes.

SK-BR-3 cells were incubated with the NaYF₄-lysine-RB UCNPs for 3 h. The NaYF₄-lysine-RB UCNPs were used at a concentration of 15 µg/mL, which was found to be ideal for PDT *via* both cell viability assays (**section 5.2.4**) and confocal microscopy (**section 5.2.6**). Following incubation with the UCNPs, the cells were thoroughly washed to remove all non-internalised UCNPs and they were subjected to irradiation with a 980 nm NIR laser for 6 min. The ApoTox-Glo™ Triplex assay was performed 4 h following PDT. This incubation period of 4 h was used considering the results of the ApoTox-Glo™ Triplex assay obtained and explained in **section 3.2.14** and **section 4.2.12**.

The cell viability results (**Figure 5.19 A**) show that the positive control (+ve St) has killed the cells since the assay results in low viability. Both control samples not incubated with UCNPs have high viability. These values indicate that the viability component of the assay is working correctly. However, the cells incubated with the UCNPs display dark toxicity and no significant cell death following irradiation. These results contradict those results already reported for cell viability assays (with the CellTiter®-Blue assays) and confocal microscopy. The cell cytotoxicity measures a biomarker that can only fluoresce when the cells in the sample are dead. As a result, it was expected that the positive control (+ve St) would give the highest fluorescence intensity values. However, the results obtained (**Figure 5.19 B**) show relatively high levels for all samples, always higher for the irradiated samples than the non-irradiated samples. The fact that the negative control also produced high values, together with the lower values obtained for the positive control prior to irradiation, indicate that the assay is giving erroneous results.

Finally, the apoptosis results (**Figure 5.19 C**) show that the positive control (+ve St) has the highest luminescence intensity values of all samples. This is expected because staurosporine is a known apoptosis inducer.⁶³ Additionally, the values obtained for the negative control cells not incubated with UCNPs, are among the lowest as expected for viable samples. On the other hand, those cells incubated with the UCNPs, show high levels of luminescence both before and after irradiation with the 980 nm NIR laser. The non-irradiated sample, according to the results previously described in **section 5.2.4**, are non-toxic and thus their luminescence values should be as low as those seen for the negative controls. However, the luminescence values for the non-irradiated sample is high, almost at the same level as the values for the irradiated sample. The fact that the luminescence values for the irradiated samples are almost as high as the positive control indicates that the most likely route of cell death followed by cells treated with NIR PDT would be apoptosis. However, the mechanism of cell death cannot be fully confirmed due to the erroneous results seen in this assay. The most likely explanation for these results possibly could be the degradation of the biomarkers in solution.

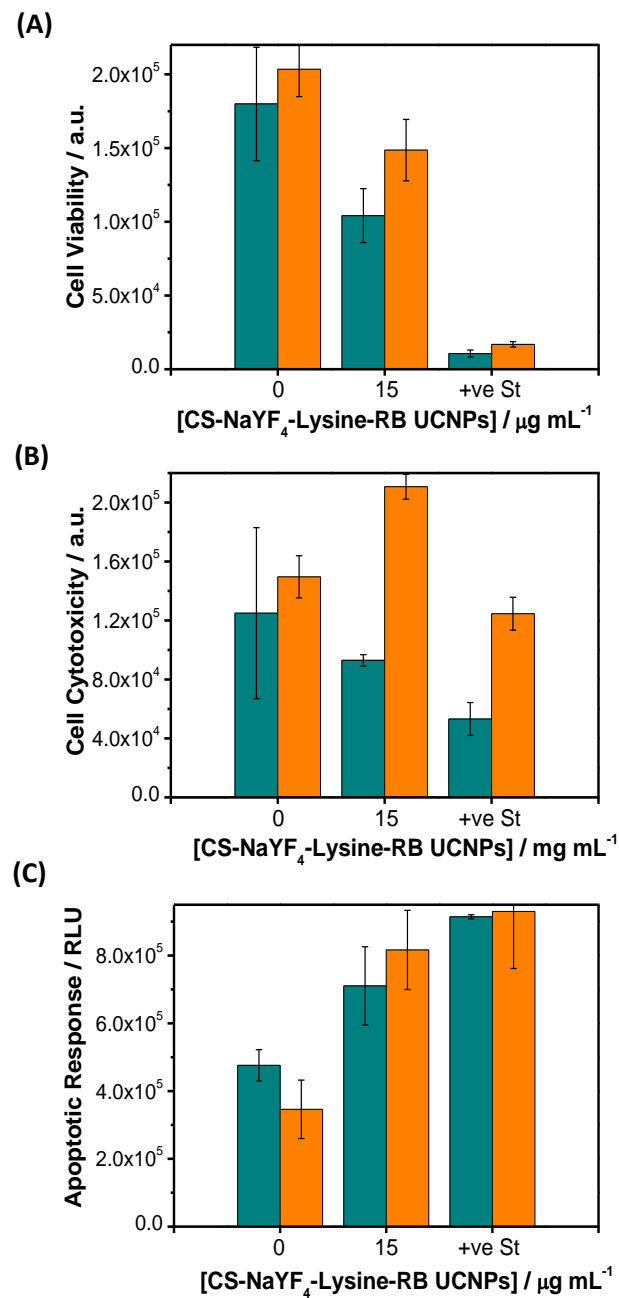


Figure 5.19. ApoTox-Glo™ Triple assay for SK-BR-3 cells incubated for 3 h with 15 $\mu\text{g/mL}$ NaYF₄-lysine-RB UCNPs. Cells were either irradiated with a 980 nm NIR laser (orange) or non-irradiated (dark cyan). The cells were treated with the triple assay *ca.* 4 h following PDT. **(A)** Fluorescence from the GF-AFC substrate giving the cell viability values, **(B)** fluorescence from bis-AAF-R110 substrate giving the cell cytotoxicity values and **(C)** luminescence from the Caspase 3/7 substrate giving the values for apoptosis. Staurosporine (+ve St) was used as a positive control for cytotoxicity *via* apoptosis. Error bars represent the standard deviation ($n = 3$) with a 95 % confidence interval.

5.2.8. Analysis of UCNPs without Rose Bengal

In this section, the results of *in vitro* studies using UCNPs not functionalised with RB to investigate the potential cytotoxic effects of the UCNPs alone without the presence of a photosensitiser are reported. In this case, core-shell NaYF_4 -PAA UCNPs were used. The surface modification of the UCNPs with polyacrylic acid (PAA) is similar to that of lysine, which was previously used. The advantage of using PAA rather than lysine is that PAA will provide a higher stability in aqueous media as compared to lysine. As a result, the NaYF_4 -PAA UCNPs can be dissolved in dH_2O . The average diameter of the NaYF_4 -PAA UCNPs was found to be 28 nm. This is slightly larger than the NaYF_4 -lysine-RB UCNPs, which had an average diameter of 17.2 nm. The larger diameter means that the NaYF_4 -PAA UCNPs will show greater luminescence and potentially could be more toxic than the smaller UCNPs.

The first study performed on the NaYF_4 -PAA UCNPs in dH_2O was to evaluate the production of ${}^1\text{O}_2$ by the system. Production of ${}^1\text{O}_2$ was investigated using the ${}^1\text{O}_2$ probe ABMA, as previously described in **section 3.2.4**. It was expected that the quenching of ABMA would be negligible or limited since the UCNPs do not present any photosensitisers on their surface. However, the results showed a decrease in the fluorescence of ABMA upon irradiation of the UCNPs with a 980 nm NIR laser (**Figure 5.20**). The generation of ${}^1\text{O}_2$ by the NaYF_4 -PAA UCNPs in dH_2O was studied at two different concentrations, either 0.5 mg/mL (**Figure 5.20 i**) or 25 $\mu\text{g}/\text{mL}$ (**Figure 5.20 ii**). The 0.5 mg/mL NaYF_4 -PAA UCNPs led to a maximum photobleaching of ABMA of 12 % following a 5 min irradiation period. On the other hand, the 25 $\mu\text{g}/\text{mL}$ NaYF_4 -PAA UCNPs only led to a maximum photobleaching of ABMA of 6 %. This indicates that the photobleaching of ABMA is dependent on the concentration of UCNPs. Additionally, a control sample consisting of ABMA dissolved in dH_2O without the presence of UCNPs was used as a control (**Figure 5.20 iii**). Control ABMA is not photobleached upon irradiation at 980 nm, which suggests that the photobleaching seen in the UCNPs samples (**Figure 5.20 i-ii**) is due to the production of ${}^1\text{O}_2$ upon irradiation of the samples.

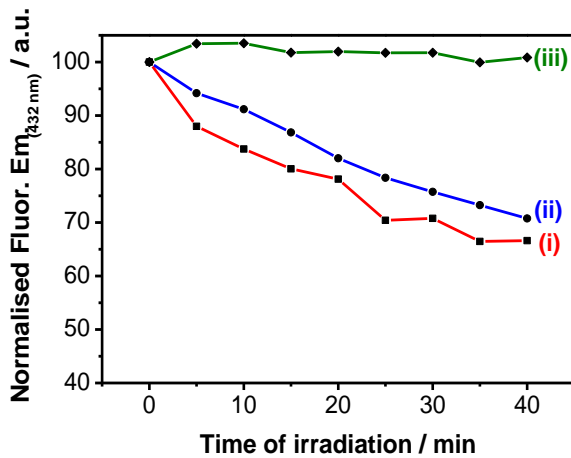


Figure 5.20. Quenching of ABMA fluorescence at 432 nm in the presence of 0.5 mg/mL (i) or 25 μ g/mL (ii) NaYF₄-PAA UCNPs dispersed in dH₂O. No photobleaching is observed for a control sample of ABMA in dH₂O (iii).

The results presented in **Figure 5.20** indicate that the NaYF₄-PAA UCNPs in dH₂O induce the generation of $^1\text{O}_2$. Previous studies have reported a limited production of $^1\text{O}_2$ by naked UCNPs not functionalised with a photosensitiser.⁶⁴ In the study by Idris *et al.*, the production of $^1\text{O}_2$ by UCNPs functionalised with a single photosensitiser was similar to that of the naked UCNPs. However, generation of $^1\text{O}_2$ was enhanced by the conjugation of the UCNPs to two photosensitisers.⁶⁴ In the present study, a direct comparison between the non-functionalised NaYF₄-PAA UCNPs and the RB functionalised NaYF₄-lysine-RB UCNPs cannot be done. This is due to two factors. Firstly, the NaYF₄-PAA UCNPs without RB are larger in size (28 nm) than the NaYF₄-lysine-RB UCNPs (17.2 nm). Secondly, the UCNPs are soluble in different solvents, dH₂O vs DMSO. The solvent plays a key role in the photobleaching of the ABMA probe, as previously seen in **section 5.2.2** for the NaYF₄-lysine-RB UCNPs. The solubilisation of the NaYF₄-lysine-RB UCNPs in either DMSO or McCoy's 5A medium had a big impact in the production of $^1\text{O}_2$. As a result, the photobleaching of ABMA for NaYF₄-lysine-RB UCNPs and NaYF₄-PAA UCNPs cannot be directly compared. The synthesis of water-soluble NaYF₄-PAA-RB UCNPs of the same size as the NaYF₄-PAA UCNPs will be necessary to compare the production of $^1\text{O}_2$ with and without the presence of RB.

Following the analysis of ${}^1\text{O}_2$ production, the NaYF_4 -PAA UCNPs were tested *in vitro* using SK-BR-3 cells. The cell viability assays were performed in the same manner as those assays previously performed for the NaYF_4 -lysine-RB UCNPs, following the procedure described in **section 2.4.9**.

Figure 5.21 shows that the NaYF_4 -PAA UCNPs do not induce any cytotoxicity in SK-BR-3 cells under the concentrations studied (10-25 $\mu\text{g}/\text{mL}$). Cells treated with the UCNPs remain viable before and after irradiation. Additionally, control cells not loaded with UCNPs also remain viable, confirming that the 980 nm NIR laser light is not toxic. These results indicate that the production of ${}^1\text{O}_2$ in UCNPs without a photosensitiser is not efficient enough to induce cell death.

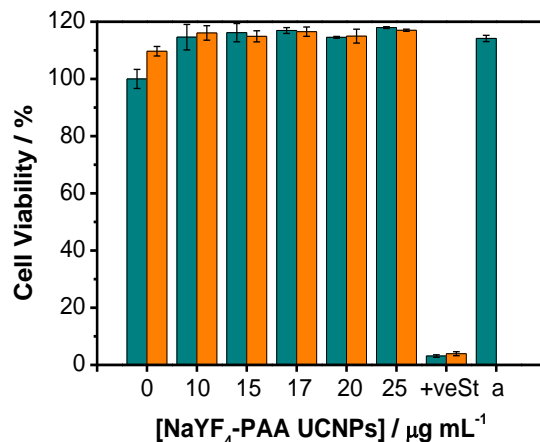


Figure 5.21. CellTiter-Blue® cell viability assay for SK-BR-3 cells incubated with NaYF_4 -PAA UCNPs. Cells were either irradiated with a 980 nm NIR laser (orange) or non-irradiated (dark cyan). H_2O diluted to 0.63 % with McCoy's 5A medium (a) was used as a control to test the effects of dH_2O under the conditions used to perform the cell viability assay. Staurosporine (+ve St) was used as a positive control for cytotoxicity. Error bars represent the standard deviation ($n = 3$) within a 95 % confidence interval.

The absence of PDT-induced cytotoxicity was further confirmed *via* confocal laser scanning microscopy, which was used to evaluate the morphology of the cells and the potential staining with propidium iodide. Control cells not loaded with UCNPs appear to be healthy both before (**Figure 5.22 A**) and after (**Figure 5.22 B**) irradiation with a 980 nm NIR laser. Additionally, there was no staining with propidium iodide, which further confirmed that the cells remained viable. This result is a further confirmation

that the 980 nm NIR is not, by itself, toxic to the SK-BR-3 cells. For cells treated with NaYF₄-PAA UCNPs, the cell morphology also indicated that the cells were healthy both before (**Figure 5.22 C**) and after (**Figure 5.22 D**) PDT treatment. Staining with propidium iodide of the cell nucleus following PDT was not observed. Therefore, these results indicate that NaYF₄-PAA UCNPs, without a photosensitiser, are not effective candidates for PDT. The functionalisation of the NaYF₄-PAA UCNPs with a photosensitiser, such as RB, could improve the results and lead to effective cell kill following PDT treatment.

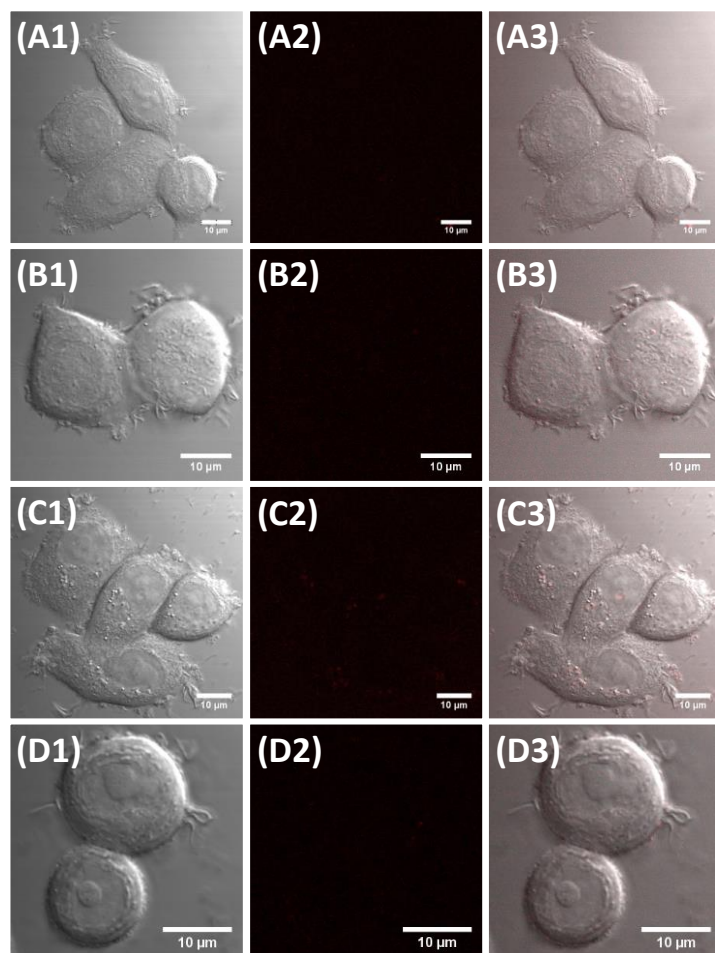


Figure 5.22. Confocal fluorescence microscopy images of SK-BR-3 cells (**A-B**) control cells incubated with McCoy's 5A phenol red-free medium containing 0.63 % dH₂O or (**C-D**) cells incubated with 25 µg/mL NaYF₄-PAA UCNPs dispersed in McCoy's 5A phenol red-free medium. Prior to imaging, all samples were treated with propidium iodide. Images taken from: **1**) DIC, **2**) fluorescence from propidium iodide collected in the red channel ($\lambda_{\text{ex}} = 543$ nm with a 10 % laser power; 560-615 nm), **3**) composite images of DIC and red channel. Scale bars (**A-C**) 10 µm and (**D**) 5 µm.

The microscopy experiments shown in **Figure 5.22** do not confirm the internalisation of the NaYF_4 -PAA UCNPs by the SK-BR-3 cells. The UCNPs are not functionalised with RB and thus, there is no fluorescence signal seen in the confocal microscopy images. Further experiments using the multi-photon microscope should be performed to evaluate the uptake of the NaYF_4 -PAA UCNPs by the SK-BR-3 cells, following excitation with a 980 nm NIR laser.

5.3. Conclusions

In this chapter, the potential use of UCNPs for PDT has been described. The UCNPs, synthesised and characterised by Markus Buchner at the University of Regensburg, contained a hexagonal β -phase NaYF_4 host lattice co-doped with Yb^{3+} , Er^{3+} and Gd^{3+} . Additionally, the UCNPs were covered with a cubic α -phase NaYF_4 passive shell to maximise the luminescence efficiency emitted by the system. The UCNPs were surface modified with lysine and functionalised with the photosensitiser Rose Bengal for PDT. The NaYF_4 -lysine-RB UCNPs were soluble in DMSO. Upon TEM characterisation, it was found that the core-shell NaYF_4 -lysine-RB UCNPs had an average size of 17.2 ± 0.98 nm. Furthermore, the luminescence spectrum of the NaYF_4 -lysine-RB UCNPs successfully confirmed FRET energy transfer between the UCNPs and the RB because the green emission of the UCNPs was visibly quenched due to absorption of the RB at this region. On the other hand, the red emission of the UCNPs remained as high as that observed prior to functionalisation with RB.

The ability of the NaYF_4 -lysine-RB UCNPs to generate singlet oxygen was evaluated using the ${}^1\text{O}_2$ probe ABMA. It was found that the RB in the sample led to the generation of ${}^1\text{O}_2$ upon excitation of the UCNPs at 980 nm. The generation of ${}^1\text{O}_2$ was found to be both concentration-dependent and solvent-dependent. This result further confirmed the efficient FRET taking place between the UCNPs and RB. Once the ability to produce ${}^1\text{O}_2$ was confirmed, the NaYF_4 -lysine-RB UCNPs were used for *in vitro* studies with SK-BR-3 human breast adenocarcinoma cells. Initially, the internalisation of the UCNPs by the SK-BR-3 cells was investigated *via* confocal laser scanning microscopy as well as multi-photon microscopy. Results from the confocal microscope confirmed the

presence of RB inside the cells following only a 3 h incubation, with the fluorescence from RB only seen in those cells treated with the UCNPs but not in the untreated controls. More importantly, the results from the multi-photon microscope, where excitation at 980 nm was possible, confirmed that the UCNPs were efficiently internalised by the treated SK-BR-3 cells. The results from the multi-photon microscopy were important to confirm that the RB was still on the surface of the UCNPs and had not been released. The presence of the RB on the surface of the UCNPs is important in order to achieve NIR-PDT.

Cell viability studies were then performed to evaluate the PDT potential of the NaYF₄-lysine-RB UCNPs. Following a 3 h incubation, SK-BR-3 cells were irradiated with a 980 nm NIR laser to induce the generation of ¹O₂. Cell viability was measured 48 h after PDT treatment. The results showed that the UCNPs induce minimal levels of dark toxicity with the SK-BR-3 cells, *i.e.*, minimal cell death prior to irradiation with the 980 nm laser, at a concentration range between 5-20 µg/mL. Importantly, post-PDT the SK-BR-3 cells were effectively killed in a concentration-dependent manner. The ideal concentration for PDT was found to be 15 µg/mL since it led to *ca.* 40-67 % cell death following irradiation but induced minimal levels of dark toxicity. Control cells not incubated with UCNPs but irradiated with the 980 nm light remained viable, showing that the NIR laser does not pose a hazard to the SK-BR-3 cells by itself. The promising results obtained with the cell viability assays were further confirmed *via* confocal laser scanning microscopy. The drastic changes in cell morphology together with the positive staining with the dead cell marker propidium iodide confirmed cell death of the SK-BR-3 cells treated with 15 µg/mL of the UCNPs during 3 h. Furthermore, control cells not treated with UCNPs, and treated with UCNPs but non-irradiated were not stained by propidium iodide, confirming those cells remained viable after the treatment. An ApoTox-Glo™ Triplex assay was performed in order to assess the cell death pathway followed by SK-BR-3 cells post-NIR-PDT with the NaYF₄-lysine-RB UCNPs. Unfortunately, the assay produced erroneous results, most likely due to the degradation of the cell viability, cytotoxicity and apoptosis biomarkers in solution. However, there was an indication that the most probable cell death pathway followed would be apoptosis.

In the second part of the research, UCNPs not functionalised with RB were used. The UCNPs, again synthesised and characterised by Markus Buchner at the University of Regensburg, contained a hexagonal β -phase NaYF_4 host lattice co-doped with Yb^{3+} , Er^{3+} and Gd^{3+} and were covered with a cubic α -phase NaYF_4 passive shell. The UCNPs were surface modified with polyacrylic acid to enable water-dispersibility. Upon TEM characterisation, it was found that the core-shell NaYF_4 -PAA UCNPs had an average size of 28 ± 3.17 nm. The ability of the NaYF_4 -PAA UCNPs to generate ${}^1\text{O}_2$ was studied using the ${}^1\text{O}_2$ probe ABMA. It was found that the fluorescence of ABMA was quenched upon irradiation with a 980 nm NIR laser. This result was an indication that the NaYF_4 -PAA UCNPs induce the generation of ${}^1\text{O}_2$ without the presence of a photosensitiser. Direct comparison to the ${}^1\text{O}_2$ production by the NaYF_4 -lysine-RB UCNPs in DMSO was not possible due to differences in the solvent and the size of each of the UCNPs.

In vitro cell viability and confocal laser scanning microscopy studies on SK-BR-3 cells using the NaYF_4 -PAA UCNPs showed that these UCNPs induced no cytotoxicity either before or after irradiation with a 980 nm NIR laser. These results highlight the need of a photosensitiser for effective PDT using UCNPs. However, it should be noted that the results here presented for the NaYF_4 -PAA UCNPs do not confirm the internalisation of the UCNPs by the cells. The confocal microscopy images are unable to show the fluorescence of the UCNPs due to the absence of a NIR laser for the excitation of the nanoparticles. Therefore, future studies should be performed using a multi-photon microscope to confirm the presence of the water-soluble UCNPs inside the SK-BR-3 cells.

5.4. References

- (1) Haase, M.; Schäfer, H. *Angew. Chem., Int. Ed.* **2011**, *50*, 5808.
- (2) Cheng, L.; Wang, C.; Liu, Z. *Nanoscale* **2013**, *5*, 23.
- (3) Jiang, S.; GnanaSammudhan, M. K.; Zhang, Y. *J. R. Soc., Interface* **2010**, *7*, 3.
- (4) Shanmugam, V.; Selvakumar, S.; Yeh, C.-S. *Chem. Soc. Rev.* **2014**, *43*, 6254.
- (5) Muhr, V.; Wilhelm, S.; Hirsch, T.; Wolfbeis, O. S. *Acc. Chem. Res.* **2014**, *47*, 3481.
- (6) Zhang, J.; Mi, C.; Wu, H.; Huang, H.; Mao, C.; Xu, S. *Anal. Biochem.* **2012**, *421*, 673.
- (7) Arguinzoniz, A. G.; Ruggiero, E.; Habtemariam, A.; Hernández-Gil, J.; Salassa, L.; Mareque-Rivas, J. C. *Part. Part. Syst. Charact.* **2014**, *31*, 46.
- (8) Gnach, A.; Lipinski, T.; Bednarkiewicz, A.; Rybka, J.; Capobianco, J. A. *Chem. Soc. Rev.* **2015**, *44*, 1561.
- (9) Wang, M.; Abbineni, G.; Clevenger, A.; Mao, C.; Xu, S. *Nanomed. Nanotech. Biol. Med.* **2011**, *7*, 710.
- (10) Wilhelm, S.; Kaiser, M.; Wurth, C.; Heiland, J.; Carrillo-Carrion, C.; Muhr, V.; Wolfbeis, O. S.; Parak, W. J.; Resch-Genger, U.; Hirsch, T. *Nanoscale* **2015**, *7*, 1403.
- (11) Yan, B.; Boyer, J.-C.; Branda, N. R.; Zhao, Y. *J. Am. Chem. Soc.* **2011**, *133*, 19714.
- (12) Chen, G.; Qiu, H.; Prasad, P. N.; Chen, X. *Chem. Rev.* **2014**, *114*, 5161.
- (13) Gamelin, D. R.; Güdel, H. U. *Acc. Chem. Res.* **2000**, *33*, 235.
- (14) Auzel, F. *Chem. Rev.* **2004**, *104*, 139.
- (15) Wang, F.; Liu, X. *Chem. Soc. Rev.* **2009**, *38*, 976.
- (16) Bloembergen, N. *Phys. Rev. Lett.* **1959**, *2*, 84.
- (17) Chivian, J. S.; Case, W. E.; Eden, D. D. *Appl. Phys. Lett.* **1979**, *35*, 124.
- (18) Zeng, J. H.; Su, J.; Li, Z. H.; Yan, R. X.; Li, Y. D. *Adv. Mater.* **2005**, *17*, 2119.
- (19) Wang, H.-Q.; Nann, T. *ACS Nano* **2009**, *3*, 3804.
- (20) Klier, D. T.; Kumke, M. U. *J. Phys. Chem. C* **2015**, *119*, 3363.
- (21) Krämer, K. W.; Biner, D.; Frei, G.; Güdel, H. U.; Hehlen, M. P.; Lüthi, S. R. *Chem. Mater.* **2004**, *16*, 1244.
- (22) Mai, H.-X.; Zhang, Y.-W.; Sun, L.-D.; Yan, C.-H. *J. Phys. Chem. C* **2007**, *111*, 13721.
- (23) Klier, D. T.; Kumke, M. U. *RSC Adv.* **2015**, *5*, 67149.
- (24) Tian, G.; Yin, W.; Jin, J.; Zhang, X.; Xing, G.; Li, S.; Gu, Z.; Zhao, Y. *J. Mater. Chem. B* **2014**, *2*, 1379.

(25) Wilhelm, S.; Hirsch, T.; Patterson, W. M.; Scheucher, E.; Mayr, T.; Wolfbeis, O. S. *Theranostics* **2013**, *3*, 239.

(26) Wang, C.; Cheng, L.; Liu, Z. *Biomaterials* **2011**, *32*, 1110.

(27) Xu, H.; Cheng, L.; Wang, C.; Ma, X.; Li, Y.; Liu, Z. *Biomaterials* **2011**, *32*, 9364.

(28) Cheng, L.; Yang, K.; Li, Y.; Chen, J.; Wang, C.; Shao, M.; Lee, S.-T.; Liu, Z. *Angew. Chem., Int. Ed.* **2011**, *50*, 7385.

(29) Chatterjee, D. K.; Rufaihah, A. J.; Zhang, Y. *Biomaterials* **2008**, *29*, 937.

(30) Hilderbrand, S. A.; Shao, F.; Salthouse, C.; Mahmood, U.; Weissleder, R. *Chem. Commun.* **2009**, 4188.

(31) Dai, Y.; Yang, D.; Ma, P. a.; Kang, X.; Zhang, X.; Li, C.; Hou, Z.; Cheng, Z.; Lin, J. *Biomaterials* **2012**, *33*, 8704.

(32) Cui, S.; Chen, H.; Zhu, H.; Tian, J.; Chi, X.; Qian, Z.; Achilefu, S.; Gu, Y. *J. Mater. Chem.* **2012**, *22*, 4861.

(33) Liu, J.; Bu, W.; Pan, L.; Shi, J. *Angew. Chem., Int. Ed.* **2013**, *52*, 4375.

(34) Mader, H. S.; Kele, P.; Saleh, S. M.; Wolfbeis, O. S. *Curr. Opin. Chem. Biol.* **2010**, *14*, 582.

(35) Gai, S.; Yang, P.; Li, C.; Wang, W.; Dai, Y.; Niu, N.; Lin, J. *Adv. Funct. Mater.* **2010**, *20*, 1166.

(36) Deng, R.; Xie, X.; Vendrell, M.; Chang, Y.-T.; Liu, X. *J. Am. Chem. Soc.* **2011**, *133*, 20168.

(37) Achatz, D. E.; Meier, R. J.; Fischer, L. H.; Wolfbeis, O. S. *Angew. Chem., Int. Ed.* **2011**, *50*, 260.

(38) Wang, Y.; Liu, K.; Liu, X.; Dohnalov, K.; Gregorkiewicz, T.; Kong, X.; Aalders, M. C. G.; Buma, W. J.; Zhang, H. *J. Phys. Chem. Lett.* **2011**, *2*, 2083.

(39) Zhang, F. *Near-infrared Nanomaterials: Preparation, Bioimaging and Therapy Applications*; The Royal Society of Chemistry: Croydon, 2016.

(40) Xiong, L.; Yang, T.; Yang, Y.; Xu, C.; Li, F. *Biomaterials* **2010**, *31*, 7078.

(41) Wang, L.; Yan, R.; Huo, Z.; Wang, L.; Zeng, J.; Bao, J.; Wang, X.; Peng, Q.; Li, Y. *Angew. Chem., Int. Ed.* **2005**, *44*, 6054.

(42) Sedlmeier, A.; Achatz, D. E.; Fischer, L. H.; Gorris, H. H.; Wolfbeis, O. S. *Nanoscale* **2012**, *4*, 7090.

(43) Jiang, S.; Zhang, Y. *Langmuir* **2010**, *26*, 6689.

(44) Liu, Q.; Sun, Y.; Yang, T.; Feng, W.; Li, C.; Li, F. *J. Am. Chem. Soc.* **2011**, *133*, 17122.

(45) Chen, G.; Shen, J.; Ohulchanskyy, T. Y.; Patel, N. J.; Kutikov, A.; Li, Z.; Song, J.; Pandey, R. K.; Ågren, H.; Prasad, P. N.; Han, G. *ACS Nano* **2012**, *6*, 8280.

(46) Nyk, M.; Kumar, R.; Ohulchanskyy, T. Y.; Bergey, E. J.; Prasad, P. N. *Nano Lett.* **2008**, *8*, 3834.

(47) Shen, J.; Zhao, L.; Han, G. *Adv. Drug Delivery Rev.* **2013**, *65*, 744.

(48) Dai, Y.; Ma, P. a.; Cheng, Z.; Kang, X.; Zhang, X.; Hou, Z.; Li, C.; Yang, D.; Zhai, X.; Lin, J. *ACS Nano* **2012**, *6*, 3327.

(49) Hou, Z.; Li, C.; Ma, P.; Li, G.; Cheng, Z.; Peng, C.; Yang, D.; Yang, P.; Lin, J. *Adv. Funct. Mater.* **2011**, *21*, 2356.

(50) Hou, Z.; Li, C.; Ma, P. a.; Cheng, Z.; Li, X.; Zhang, X.; Dai, Y.; Yang, D.; Lian, H.; Lin, J. *Adv. Funct. Mater.* **2012**, *22*, 2713.

(51) Carling, C.-J.; Nourmohammadian, F.; Boyer, J.-C.; Branda, N. R. *Angew. Chem., Int. Ed.* **2010**, *49*, 3782.

(52) Jayakumar, M. K. G.; Idris, N. M.; Zhang, Y. *Proc. Natl. Acad. Sci. U.S.A.* **2012**, *109*, 8483.

(53) Yang, Y.; Shao, Q.; Deng, R.; Wang, C.; Teng, X.; Cheng, K.; Cheng, Z.; Huang, L.; Liu, Z.; Liu, X.; Xing, B. *Angew. Chem., Int. Ed.* **2012**, *51*, 3125.

(54) Liu, K.; Liu, X.; Zeng, Q.; Zhang, Y.; Tu, L.; Liu, T.; Kong, X.; Wang, Y.; Cao, F.; Lambrechts, S. A. G.; Aalders, M. C. G.; Zhang, H. *ACS Nano* **2012**, *6*, 4054.

(55) Chen, Q.; Wang, C.; Cheng, L.; He, W.; Cheng, Z.; Liu, Z. *Biomaterials* **2014**, *35*, 2915.

(56) Zhang, F.; Braun, G. B.; Pallaoro, A.; Zhang, Y.; Shi, Y.; Cui, D.; Moskovits, M.; Zhao, D.; Stucky, G. D. *Nano Lett.* **2012**, *12*, 61.

(57) Tian, G.; Gu, Z.; Zhou, L.; Yin, W.; Liu, X.; Yan, L.; Jin, S.; Ren, W.; Xing, G.; Li, S.; Zhao, Y. *Adv. Mater.* **2012**, *24*, 1226.

(58) Cheng, L.; Yang, K.; Li, Y.; Zeng, X.; Shao, M.; Lee, S.-T.; Liu, Z. *Biomaterials* **2012**, *33*, 2215.

(59) Zhan, Q.; Qian, J.; Liang, H.; Somesfalean, G.; Wang, D.; He, S.; Zhang, Z.; Andersson-Engels, S. *ACS Nano* **2011**, *5*, 3744.

(60) Wang, D.; Xue, B.; Kong, X.; Tu, L.; Liu, X.; Zhang, Y.; Chang, Y.; Luo, Y.; Zhao, H.; Zhang, H. *Nanoscale* **2015**, *7*, 190.

(61) Yu, M.; Li, F.; Chen, Z.; Hu, H.; Zhan, C.; Yang, H.; Huang, C. *Anal. Chem.* **2009**, *81*, 930.

(62) Wu, C.-W.; Wu, F. Y. H. *Biochemistry* **1973**, *12*, 4349.

(63) Belmokhtar, C. A.; Hillion, J.; Seagal-Bendirdjian, E. *Oncogene* **2001**, *20*, 3354.

(64) Idris, N. M.; Gnanasammandhan, M. K.; Zhang, J.; Ho, P. C.; Mahendran, R.; Zhang, Y. *Nat. Med.* **2012**, *18*, 1580.

Chapter 6

Conclusions and future work

This thesis describes the use of nanoparticles for photodynamic therapy of breast adenocarcinoma cells. This chapter summarises the conclusions of the investigations reported throughout this thesis, including the use of metal-enhanced fluorescence and antibody targeting, the potential use of lactose as a breast-cancer specific targeting ligand and the use of upconverting nanoparticles for deep-penetration PDT. Furthermore, suggestions of experiments to be performed in the future to continue this research are given.

6.1. Gold nanoparticle enhanced and selective antibody targeting photodynamic therapy

Chapter 3 explored the use of metal-enhanced fluorescence for PDT. Two zinc phthalocyanines, C11Pc and C3Pc, differing in the length of the carbon chain that connects the macrocycle to the gold core were compared. The chain for C11Pc consisted of 11 carbon atoms, and only 3 carbon atoms for C3Pc. Gold nanoparticles (AuNPs) functionalised with a mixed monolayer of polyethylene glycol (PEG) and either C11Pc (C11Pc-PEG-AuNPs) or C3Pc (C3Pc-PEG-AuNPs) were synthesised. PEG provides aqueous solubility to the system and allows for an increased circulation time in the serum, thus increasing the ability of the AuNPs to be internalised by the tumour.^{1,2} The C11Pc-PEG-AuNPs had an average diameter of 3.41 ± 1.16 nm while the C3Pc-PEG-AuNPs had an average diameter of 3.83 ± 0.99 nm.

A fluorescence spectroscopic comparison between C11Pc-PEG-AuNPs and C3Pc-PEG-AuNPs was performed in order to investigate the potential for metal-enhanced fluorescence within these nanosystems. The fluorescence intensity of the free photosensitisers, dissolved in THF, was found to be significantly greater for C11Pc ($\phi_F = 4.80\%$) than C3Pc ($\phi_F = 2.60\%$). On the contrary, the fluorescence of the nanosystems dissolved in an aqueous buffer was found to be much higher for C3Pc-

PEG-AuNPs ($\phi_F = 0.42\%$) as compared to C11Pc-PEG-AuNPs ($\phi_F = 0.20\%$). The interaction between fluorophores and metal nanoparticles is complex. The effect of the metal on the fluorescence emitted by the fluorophore depends on many parameters, including the size and shape of the metal nanoparticles,³⁻⁶ the distance between the metal core and the fluorophore,⁶⁻⁹ the nature of the anchor chain that connects the fluorophore to the metal surface,¹⁰ the angle at which the fluorophore is positioned relative to the metal surface,^{6,8,10} and the spectral overlap between the metal nanoparticle and the fluorophore.^{6,9} According to the radiating plasmon model developed by Lakowicz in 2005, small nanoparticles will induce a strong quenching effect while larger nanoparticles will induce a fluorescence enhancement, due to the relative contributions of the scattering and absorption components of the nanoparticle extinction.^{3,11,12} In relation to the distance between the metal and the fluorophore, there are three main regions of interest.^{7,9} When the fluorophore is placed too close ($\leq 5\text{ nm}$) to the metal, the fluorescence is highly quenched.⁷⁻⁹ When the fluorophore is placed far away from the metal ($\geq 20\text{ nm}$), the interaction between the metal and the fluorophore is negligible. For metal-enhanced fluorescence, the key relies on locating the fluorophore at an optimal distance (*ca.* 5-20 nm, usually $\geq 10\text{ nm}$), at which the fluorescence emission is enhanced.^{7,13,14} In the C11Pc-PEG-AuNPs and C3Pc-PEG-AuNPs, the fluorescence of the photosensitisers is quenched by presence of the AuNPs as compared to the free photosensitisers in solution, as confirmed by the fluorescence quantum yields. This quenching could be explained by the small size of the AuNPs ($< 5\text{ nm}$). However, interestingly, the fluorescence of C11Pc is more effectively quenched than that of C3Pc. The enhanced quenching effect seen by the C11Pc-PEG-AuNPs might be related to the orientation of the phthalocyanines with respect to the AuNPs. Russell and co-workers investigated the orientation of the same phthalocyanines used in this thesis, C3Pc and C11Pc, as self-assembled monolayers on a planar gold surface.¹⁵ The authors found that the fluorescence emission of the C3Pc was quenched more intensely than that of C11Pc. This observation was attributed to the position of each phthalocyanine with respect to the gold surface; the C3Pc lies more horizontal while the C11Pc is more perpendicular. The perpendicular orientation induces a larger distance between the gold surface and the phthalocyanine and thus the fluorescence is not quenched as much.¹⁵ Even though this study used the same

phthalocyanines that are reported in the present thesis, a direct comparison cannot be performed due to the different nature of the metal, either planar gold surface or gold nanoparticles. Given that the results obtained in this thesis are in disagreement to what was reported previously, it can be concluded that the planar or spherical nature of the metal is the most important parameter that dictates the relative orientation of the fluorophores with respect to the metal. In another study by Battistini *et al.*, the authors investigated the relative orientation of a pyrene connected to gold nanoparticles by either a four (C4) or eleven (C11) carbon chain.¹⁰ The authors reported similar results to what is seen in this thesis, as the C4 pyrene was found to have a higher fluorescence on the surface of the AuNPs as compared to the C11 pyrene. These authors speculated that the shorter C4 chain will adopt a perpendicular orientation relative to the AuNPs, while the longer C11 chain will lead to a conformation flatter towards the AuNPs. As a result, the charge and energy transfer between the AuNPs and the pyrenes will only take place for the C11 chain, which leads to the higher quenching effect. The orientations adopted by each pyrene chain were attributed to the intermolecular chain interactions, which are stronger in the longer chain and lead to the C11 chains positioning closer together to one another to maximise chain-chain interactions.¹⁰ In the present study, the results are similar to those reported by Battistini *et al.* since the phthalocyanine with the longer chain (C11Pc) experiences more quenching than the phthalocyanine with the shorter chain (C3Pc). Therefore, it is speculated that the C11Pc is oriented more parallel towards the gold core than C3Pc. The parallel conformation induces the cancellation of the dipoles from the C11Pc and the AuNPs, which radiate out of phase, and induce a decrease in the radiative decay rate of the C11Pc. Additionally, the angle at which the C11Pc is located might lead to the macrocycle being closer to the gold core than the C3Pc macrocycle, thus facilitating electron transfer between the C11Pc and the AuNPs, which also leads to fluorescence quenching. On the contrary, it was speculated that the C3Pc will adopt a more perpendicular orientation with respect to the AuNPs. The perpendicular orientation allows for the interaction between the dipoles, which induces metal-enhanced fluorescence. However, the absence of metal-enhanced fluorescence reported in this study could be related to the small size of the AuNPs, in agreement with Lakowicz's RP model, as previously discussed.

The fluorescence spectroscopy results opened the possibility for an increased production of ${}^1\text{O}_2$ by the C3Pc-PEG-AuNPs given that the fluorescence of C3Pc-PEG-AuNPs is higher than that of C11Pc-PEG-AuNPs. The production of ${}^1\text{O}_2$ was analysed using the probe ABMA, which suggested that the C3Pc-PEG-AuNPs were producing more ${}^1\text{O}_2$ than the C11Pc-PEG-AuNPs. To confirm these results, the quantum yields of ${}^1\text{O}_2$ were analysed. Unfortunately, the AuNPs were dissolved in an aqueous buffer, which led to the quenching of the ${}^1\text{O}_2$ signal. The use of D_2O as an alternative to avoid the quenching of the ${}^1\text{O}_2$ signal was attempted. However, the ${}^1\text{O}_2$ signal obtained was low and the ${}^1\text{O}_2$ quantum yields could not be determined.

In vitro studies with SK-BR-3 human breast adenocarcinoma cells were performed in order to compare the photodynamic efficiency of C11Pc-PEG-AuNPs and C3Pc-PEG-AuNPs. Confocal laser scanning microscopy confirmed that both C11Pc-PEG-AuNPs and C3Pc-PEG-AuNPs were effectively internalised by the SK-BR-3 cells following a 3 h incubation period. Cell viability was assessed using a CellTiter-Blue® and MTT cell viability assays. Prior to irradiation, both C11Pc-PEG-AuNPs and C3Pc-PEG-AuNPs were biocompatible and non-toxic, since the cells remain viable as shown by the cell viability assays. Following irradiation with a 633 nm HeNe laser for 6 min, only the cells treated with C3Pc-PEG-AuNPs showed high levels of cytotoxicity, concomitant with an increase in the concentration of C3Pc in the sample. These results further the idea that there is an increased production of ${}^1\text{O}_2$ by the C3Pc-PEG-AuNPs as compared to the C11Pc-PEG-AuNPs. *In vitro* studies with MCF-10A human mammary epithelial cells showed that there was no toxicity associated with either the C11Pc-PEG-AuNPs or the C3Pc-PEG-AuNPs, before or after irradiation. Therefore, the use of C3Pc-PEG-AuNPs is encouraged since these nanoparticles induce high cell kill in cancer cells (*ca.* 85 % at 0.23 μM C3Pc) and no damage to healthy cells.

In the second part of **Chapter 3**, anti-HER2 antibody (Ab) was used as a targeting agent for the HER2 receptor. The HER2 receptor is overexpressed in *ca.* 10-34 % aggressive breast cancers,¹⁶ including SK-BR-3 cells. The Ab was conjugated to the terminal end of PEG in both C11Pc-PEG-AuNPs and C3Pc-PEG-AuNPs through an amide bond, using EDC/NHS coupling. Confocal laser scanning microscopy confirmed that the addition of anti-HER2 antibody increased the internalisation of the AuNPs by the SK-BR-3 cells. The

internalisation was confirmed to occur *via* receptor-mediated endocytosis using both an InCell ELISA and confocal microscopy, which showed partial colocalisation with the acidic organelles 19 h after incubation. The increased internalisation resulted in increased levels of cell death following PDT. The levels of cell death induced by either Ab-C11Pc-PEG-AuNPs or Ab-C3Pc-PEG-AuNPs were similar (*ca.* 99 % cell death at 0.2 μ M Pc). However, while the Ab-C11Pc-PEG-AuNPs were non-toxic in the dark, Ab-C3Pc-PEG-AuNPs induced high levels of dark toxicity, *ca.* 70 % cell death, at a concentration as low as 0.08 μ M. Studies in MCF-10A cells showed high levels of cytotoxicity both before and after irradiation for Ab-C3Pc-PEG-AuNPs, whereas there was minimal photodamage for Ab-C11Pc-PEG-AuNPs. In conclusion, the use of Ab-C11Pc-PEG-AuNPs is preferred since these nanoparticles induced high levels of cell death following PDT and no dark toxicity in cancer cells together with no damage to healthy cells.

The mechanism of cell death followed by the C3Pc-PEG-AuNPs and C11Pc-PEG-AuNPs with or without conjugation to anti-HER2 antibody was investigated using an ApoTox-GloTM Triplex assay. The results suggested that apoptosis was not the mechanism of cell death, opening the possibility for other cell death pathways such as necrosis. Unfortunately, the results obtained from this assay were difficult to interpret and a conclusion could not be drawn.

In conclusion, **Chapter 3** showed that metal-enhanced fluorescence is possible for C3Pc-PEG-AuNPs as compared to C11Pc-PEG-AuNPs. However, the small size of the AuNPs could limit the rate of fluorescence enhancement. The enhanced fluorescence of C3Pc-PEG-AuNPs as compared to C11Pc-PEG-AuNPs leads to enhanced photodynamic efficacy. As a result, C3Pc-PEG-AuNPs perform better than C11Pc-PEG-AuNPs *in vitro*. Additionally, the use of a breast cancer-specific targeting agent, anti-HER2 antibody, effectively increased the internalisation of the conjugated nanoparticles by the cells, leading to enhanced photodynamic efficacy.

6.2. Targeting breast cancer cells with lactose

Chapter 4 investigated the use of lactose as a potential targeting agent for breast cancer cells. Lactose is a disaccharide composed of a glucose subunit and a galactose subunit. The lactose derivative used to obtain the results presented in this chapter was thiolated at the terminal end connected to the glucose subunit,¹⁷ to allow self-assembly to the surface of the AuNPs. Lactose is selectively recognised by galectins, β -galactoside-binding lectins, *via* the galactose residue.¹⁸ Galectins are expressed on the surface of the cells, and their under- or over-expression has been linked with cancer.^{19,20} Overexpression of galectin-1 in breast cancer cells has been previously reported.²¹⁻²⁴ The expression of galectin-1 was assessed using two breast cancer cell lines, SK-BR-3 and MDA-MB-231 human breast adenocarcinoma cells. Using an InCell ELISA, MDA-MB-231 cells were found to have a higher expression of galectin-1 on their surface as compared to SK-BR-3 cells. Therefore, targeting with lactose was expected to be more efficient towards MDA-MB-231 cells.

The thiolated lactose derivative was used to synthesise lactose-C11Pc-AuNPs and act as both the targeting ligand and the water-solubility inducer. Lactose-C11Pc-AuNPs were successfully synthesised with a mean diameter of 2.37 ± 1.65 nm, as confirmed by TEM analysis. Production of $^1\text{O}_2$ by these nanoparticles was confirmed using ABMA. Additionally, a PEG ligand (sPEG) with a short chain that resembles the length of the lactose derivative was used to synthesise C11Pc-sPEG-AuNPs, used as a control to confirm lactose targeting. Lactose-C11Pc-AuNPs and C11Pc-sPEG-AuNPs were incubated with MDA-MB-231 cells for either 3 h or 24 h. Unfortunately, CellTiter-Blue[®] cell viability assays showed no cell death following PDT at 633 nm for 6 min. Therefore, the incubation time was increased to 24 h to give more time for the nanoparticles to be internalised. The results of the cell viability assays following a 24 h incubation were non-reproducible and cell death following PDT could not be confirmed. Since the results were negative for MDA-MB-231 cells, *in vitro* studies in SK-BR-3 cells were performed. A 3 h incubation period with the lactose-C11Pc-AuNPs and C11Pc-sPEG-AuNPs was found to be insufficient for effective internalisation since no cell death was observed in the cell viability assays. However, the increase of the incubation time to 24 h was successful as cell death was induced with both lactose-C11Pc-AuNPs (90 %)

and C11Pc-sPEG-AuNPs (61 %), indicating selective targeting *via* the lactose ligand. However, an InCell ELISA did not show any indication of targeting the galectin-1 receptor. As a result, the possible targeting seen in the viability assays could be due to the selective recognition between lactose and another receptor on the surface of the SK-BR-3 cells.

In an attempt to improve the targeting ability of lactose, C3Pc was used as the photosensitiser. The carbon chain of C3Ps is not only shorter than the C11Pc, but also slightly shorter than the lactose ligand. As a result, binding between the galectin-1 receptor and lactose should not be hindered by the large C11Pc carbon chain. Lactose-C3Pc-AuNPs were successfully synthesised with an average diameter of 3.10 ± 1.32 nm, as confirmed by TEM analysis. The synthesis and aqueous solubilisation of lactose-C3Pc-AuNPs was found to be easier than lactose-C11Pc-AuNPs, since the shorter carbon chain of C3Pc in combination with the lactose derivative allowed for a better dispersibility in water and a higher loading of C3Pc on the surface of the AuNPs. Production of $^1\text{O}_2$ by lactose-C3Pc-AuNPs was confirmed using ABMA. Control C3Pc-sPEG-AuNPs were also synthesised to assess the targeting ability of lactose. MDA-MB-231 cells were incubated with lactose-C3Pc-AuNPs and C3Pc-sPEG-AuNPs for either 3 h or 24 h. A 3 h incubation period was found to be insufficient for efficient internalisation, as confirmed by confocal laser scanning microscopy and by the absence of cell death following PDT observed in the cell viability assays. On the contrary, a 24 h incubation period was sufficient time for the internalisation of the nanoparticles, as shown by confocal microscopy. Following PDT at 633 nm for 6 min, cytotoxicity was effectively induced in MDA-MB-231 cells by both lactose-C3Pc-AuNPs (52 %) and C3Pc-sPEG-AuNPs (36 %), with slight evidence of lactose targeting, even though not statistically significant. An InCell ELISA indicated that the galectin-1 receptor on the surface of the MDA-MB-231 cells was involved in the internalisation of lactose-C3Pc-AuNPs, suggesting internalisation *via* receptor-mediated endocytosis. SK-BR-3 cells were also studied for the PDT effect of lactose-C3Pc-AuNPs and C3Pc-sPEG-AuNPs. With this cell line, a 3 h incubation period was sufficient for effective nanoparticle internalisation and cell death post-PDT, confirmed by the cell viability assays as well as confocal microscopy. Additionally, a 24 h incubation period showed similar results. Even though the cell death levels induced by both lactose-C3Pc-AuNPs and C3Pc-sPEG-AuNPs were

comparable, lactose-C3Pc-AuNPs induced less dark toxicity as compared to C3Pc-sPEG-AuNPs, which provides an advantage for their use. An InCell ELISA confirmed that the galectin-1 receptor on the surface of SK-BR-3 cells was not involved in the internalisation of the lactose-C3Pc-AuNPs.

These results indicate that lactose-C3Pc-AuNPs are more efficient than lactose-C11Pc-AuNPs. The mechanism of cell death followed by both SK-BR-3 and MDA-MB-231 cells incubated with the more efficient lactose-C3Pc-AuNPs was investigated using an ApoTox-Glo™ Triplex assay. The results suggested that the most likely cell death route was necrosis. However, the results from the assay were inconclusive. The effect of lactose-C3Pc-AuNPs was also assessed with non-cancerous MCF-10A cells. Neither lactose-C3Pc-AuNPs nor C3Pc-sPEG-AuNPs induced damage to the cells either before or after PDT treatment.

In conclusion, the results presented in **Chapter 4** have shown that lactose can be used as an alternative to PEG to provide water-solubility of the Pc-AuNPs. Lactose-C3Pc-AuNPs were found to be more efficient at targeting and inducing PDT than lactose-C11Pc-AuNPs in both cell lines, MDA-MB-231 and SK-BR-3 cells. For SK-BR-3 cells, lactose-C3Pc-AuNPs were found to be efficiently internalised and induce good cytotoxicity effects after only a 3 h incubation period. On the contrary, lactose-C11Pc-AuNPs required a 24 h incubation period in order to see efficient cytotoxicity post-PDT. The use of lactose in SK-BR-3 cells suggested that selective targeting could be taking place. However, galectin-1 was not involved in this targeting, as confirmed by InCell ELISA. For MDA-MB-231 cells, only lactose-C3Pc-AuNPs were efficiently internalised and induced cell death following a 24 h incubation and PDT, with evidence for targeting galectin-1. As a result, the use of lactose-C3Pc-AuNPs is preferred due to the low dark toxicity, effective phototoxicity and selective targeting towards galectin-1.

6.3. Upconverting nanoparticles for photodynamic therapy

The results presented in **Chapter 5** investigated the use of upconverting nanoparticles (UCNPs), synthesised and characterised by Markus Buchner at the University of Regensburg (Germany), for PDT. The UCNPs consisted of hexagonal β -phase NaYF_4

(Yb³⁺, Er³⁺, Gd³⁺) covered with a cubic α -phase NaYF₄ shell and surface modified with lysine and Rose Bengal (NaYF₄-lysine-RB UCNPs), dissolved in DMSO. The average size of the NaYF₄-lysine-RB UCNPs was 17.2 \pm 0.98 nm. Generation of ¹O₂ by the NaYF₄-lysine-RB UCNPs was evaluated using the probe ABMA. Irradiation using a 980 nm NIR laser induced the effective excitation of RB upon emission of the UCNPs. Excitation of RB led to the generation of ¹O₂, which was concentration-dependent and solvent-dependent, confirming efficient FRET between the UCNPs and RB.

The breast cancer cell line SK-BR-3 was used for the *in vitro* studies. Firstly, the internalisation of the NaYF₄-lysine-RB UCNPs needed to be confirmed. Confocal laser scanning microscopy confirmed the presence of Rose Bengal inside the cells following a 3 h incubation with 25 μ g/mL NaYF₄-lysine-RB UCNPs. Excitation of the RB for the confocal microscopy images was performed using a 543 nm laser. These results, while confirming the presence of RB inside the cells, do not confirm uptake of the NaYF₄-lysine-RB UCNPs due to the absence of a 980 nm laser in the confocal microscope to directly excite the UCNPs. In order to see the fluorescence emission of the NaYF₄-lysine-RB UCNPs inside the cells, a multi-photon microscope was used, which was able to excite the samples at 980 nm. Direct excitation of the UCNPs confirmed the internalisation of the NaYF₄-lysine-RB UCNPs by the cells, since the luminescence emission was only detected inside the cells. The results from the microscopy experiments confirmed that the RB was still attached to the surface of the NaYF₄-lysine-RB UCNPs and the whole system was efficiently internalised by SK-BR-3 cells. The PDT effect was evaluated using CellTiter-Blue[®] cell viability assays and confocal microscopy. The results showed that the NaYF₄-lysine-RB UCNPs were efficient at inducing cell death following a 3 h incubation and irradiation with a 980 nm NIR laser for 6 min, in a concentration-dependent manner. The ideal concentration for PDT was found to be 15 μ g/mL, which contains 0.173 μ M of RB, since it induced minimal levels of dark toxicity and *ca.* 40-67 % cell death post-PDT. Control cells, not incubated with UCNPs but irradiated at 980 nm, remained highly viable, showing that the NIR laser is not toxic to the SK-BR-3 cells by itself. The mechanism of cell death was investigated using an ApoTox-Glo[™] Triplex assay, which showed an indication of apoptosis following NIR-PDT with the NaYF₄-lysine-RB UCNPs. Unfortunately, this conclusion could not be confirmed since the results were difficult to interpret.

In the second part of **Chapter 5**, UCNPs not functionalised with RB were synthesised and characterised by Markus Buchner at the University of Regensburg (Germany). The UCNPs consisted of hexagonal β -phase NaYF_4 (Yb^{3+} , Er^{3+} , Gd^{3+}) covered with a cubic α -phase NaYF_4 shell and modified with polyacrylic acid (PAA) to provide water-solubility (NaYF_4 -PAA), with an average size of 28 ± 3.17 nm. Using ABMA, it was found that the NaYF_4 -PAA UCNPs were able to induce ${}^1\text{O}_2$ production. Even though direct comparison with the NaYF_4 -lysine-RB UCNPs was not possible due to the difference in size and solvent, there was an indication that the NaYF_4 -lysine-RB UCNPs produced higher amounts of ${}^1\text{O}_2$. The NaYF_4 -PAA UCNPs were studied *in vitro* in SK-BR-3 cells. Cell viability assays showed that NaYF_4 -PAA UCNPs induce no cytotoxicity either before or after NIR-PDT, highlighting the need of a photosensitiser for effective PDT.

In conclusion, **Chapter 5** has shown that the NaYF_4 -lysine-RB UCNPs can be used for PDT since they induce good phototoxicity following irradiation at 980 nm but no dark toxicity in a concentration range of 10-20 $\mu\text{g/mL}$.

6.4. Future work

In this thesis, the use of AuNPs and UCNPs for PDT was explored. In **Chapter 3**, the potential of metal-enhanced fluorescence for PDT was studied using two phthalocyanines, C3Pc and C11Pc. The use of inductively-coupled plasma mass spectrometry should be performed to confirm the estimation of the number of C11Pc and C3Pc molecules immobilised per AuNPs reported in **Chapter 3**. To obtain a better understanding of the interactions between the phthalocyanines and the AuNPs here reported, the synthesis of a similar phthalocyanine with a carbon chain somewhere in between 3 and 11 carbon atoms, *i.e.*, 5-9 atoms, should be performed. The fluorescence intensity of a third phthalocyanine will provide a better understanding of the orientation adopted by the macrocycles relative to the gold nanoparticles as well as their distance. Additionally, the application for PDT of such a phthalocyanine should also be performed to further evaluate how the chain length affects the efficiency of PDT *in vitro*. Furthermore, following Lakowicz's RP model, the synthesis and application of larger nanoparticles could lead to increased MEF and increased production of ${}^1\text{O}_2$.

As a result, PDT could be improved, leading to higher cell death at lower concentrations.

In **Chapter 4**, SK-BR-3 cells were found to have a low expression of galectin-1. As a result, the potential targeting ability of lactose was not related to the galectin-1 receptor. To understand whether the lactose ligand is targeting SK-BR-3 cells, other galactose-binding receptors should be studied. Previous studies report that the glucose transport receptor 1 (GLUT1) is selectively recognised by galactose-binding carbohydrates.²⁵ Therefore, the possibility of lactose binding the GLUT1 receptor should be studied. The levels of galectin-1 on the surface of MDA-MB-231 cells were found to be significantly higher than on the surface of SK-BR-3 cells. InCell ELISAs suggested that lactose is selectively recognising the galectin-1 receptor on the surface of MDA-MB-231 cells. To fully confirm this selective targeting, competition studies to block the galectin-1 receptor should be performed. Competition studies will assess whether the internalisation of the lactose-C3Pc-AuNPs and thus the PDT efficacy are inhibited when the galectin-1 receptor is blocked. Additionally, the use of other ligands such as galactose should be explored to evaluate a better targeting towards breast cancer cells. Finally, the ability of lactose to target other cancers overexpressing galectin-1, such as pancreatic cancer, should be explored.

In **Chapter 5**, the NaYF₄-lysine-RB UCNPs were dissolved in DMSO. The preparation of water-soluble UCNPs functionalised with RB should be performed to further minimise the potential toxicity of the UCNPs. Furthermore, the synthesis of NaYF₄-lysine-RB UCNPs in water will enable the direct comparison with the NaYF₄-PAA UCNPs to evaluate the generation of ¹O₂ with and without the presence of a photosensitiser. The investigation of NaYF₄-PAA UCNPs presented in **Chapter 5** did not confirm the internalisation of the UCNPs, since only confocal microscopy studies were performed. Consequently, investigations into the uptake of the water soluble NaYF₄-PAA UCNPs by SK-BR-3 cells should be performed using a multi-photon microscope, which allows for the direct excitation of the UCNPs at 980 nm. This investigation will give value to the cell viability assays presented in this thesis, where the NaYF₄-PAA UCNPs were shown to induce no toxicity to the cells either before or after PDT treatment. The use of the NaYF₄-lysine-RB UCNPs for deep-penetration PDT should be studied. Previous reports

have placed pork tissue between the cells and the laser. As a result, the penetration of NIR light (980 nm) can be compared to visible light (543 nm for RB). The disadvantages of using excitation at 980 nm is the notable absorption of such wavelengths by water and thus the overheating effect. The use of UCNPs with excitation at 808 nm can avoid such problems and should be studied for PDT.

In all chapters, the study of the cell death mechanism was inconclusive. The use of alternative assays for the investigation of the mechanism of cell death followed should be used, including apoptosis/necrosis detection kits or apoptosis detection based on annexin v. The AuNPs and UCNPs studied throughout this thesis were found to be ideal candidates for PDT. However, *in vitro* studies are limited due to the one-dimensional culture of the cells. To further confirm the promising results obtained and reported in this thesis, 3D culture models could be used. The cell culture in a 3D model provides a structure that is more similar to tumour tissue. Furthermore, *in vivo* studies should be performed. Investigations in animal models will show the selective uptake of each of the nanoparticles described in this thesis by the tumour tissue. Additionally, the rate of tumour growth and tumour destruction will also be obtained. More importantly, the use of *in vivo* models is useful to evaluate the toxicity associated with the nanoparticles towards the body and their potential excretion routes. The internalisation of the nanoparticles by certain organs, such as the liver, can lead to undesired toxicity, which should be diminished for effective PDT treatment.

6.5. References

- (1) Obaid, G.; Broekgaarden, M.; Bulin, A.-L.; Huang, H.-C.; Kuriakose, J.; Liu, J.; Hasan, T. *Nanoscale* **2016**, *8*, 12471.
- (2) Obaid, G.; Russell, D. A. In *Handbook of photomedicine*; Hamblin, M. R., Huang, Y.-Y., Eds.; Taylor & Francis: Boca Raton, 2013, p 365.
- (3) Lakowicz, J. R. *Anal. Biochem.* **2005**, *337*, 171.
- (4) Swierczewska, M.; Lee, S.; Chen, X. *Phys. Chem. Chem. Phys.* **2011**, *13*, 9929.
- (5) Li, M.; Cushing, S. K.; Wu, N. *Analyst* **2015**, *140*, 386.
- (6) Dulkeith, E.; Morteani, A. C.; Niedereichholz, T.; Klar, T. A.; Feldmann, J.; Levi, S. A.; van Veggel, F. C. J. M.; Reindhoudt, D. N.; Möller, M.; Gittins, D. I. *Phys. Rev. Lett.* **2002**, *89*, 203002.
- (7) Ghosh, S. K.; Pal, T. *Phys. Chem. Chem. Phys.* **2009**, *11*, 3831.
- (8) Lakowicz, J. R. *Anal. Biochem.* **2001**, *298*, 1.
- (9) Darvill, D.; Centeno, A.; Xie, F. *Phys. Chem. Chem. Phys.* **2013**, *15*, 15709.
- (10) Battistini, G.; Cozzi, P. G.; Jalkanen, J.-P.; Montalti, M.; Prodi, L.; Zaccheroni, N.; Zerbetto, F. *ACS Nano* **2007**, *2*, 77.
- (11) Aslan, K.; Lakowicz, J. R.; Geddes, C. D. *Curr. Opin. Chem. Biol.* **2005**, *9*, 538.
- (12) Bardhan, R.; Grady, N. K.; Cole, J. R.; Joshi, A.; Halas, N. J. *ACS Nano* **2009**, *3*, 744.
- (13) Anger, P.; Bharadwaj, P.; Novotny, L. *Phys. Rev. Lett.* **2006**, *96*.
- (14) Kang, K.; Wang, J.; Jasinski, J.; Achilefu, S. *J. Nanobiotechnol.* **2011**, *9*, 16.
- (15) Revell, D. J.; Chambrier, I.; Cook, M. J.; Russell, D. A. *J. Mater. Chem.* **2000**, *10*, 31.
- (16) Ross, J. S.; Fletcher, A. *Stem Cells* **1998**, *16*, 413.
- (17) Reynolds, A. J.; Haines, A. H.; Russell, D. A. *Langmuir* **2006**, *22*, 1156.
- (18) Barondes, S. H.; Cooper, D. N. W.; Gitt, M. A.; Leffle, H. *J. Biol. Chem.* **1994**, *269*, 20807.
- (19) Gorelik, E.; Galili, U.; Raz, A. *Cancer Metastasis Rev.* **2001**, *20*, 245.
- (20) Rabinovich, G. A. *Cell Death Differ.* **1999**, *6*, 711.
- (21) Ito, K.; Stannard, K.; Gabutero, E.; Clark, A. M.; Neo, S.-Y.; Onturk, S.; Blanchard, H.; Ralph, S. *J. Cancer Metastasis Rev.* **2012**, *31*, 763.
- (22) Astorgues-Xerri, L.; Riveiro, M. E.; Tijeras-Raballand, A.; Serova, M.; Neuzillet, C.; Albert, S.; Raymond, E.; Faivre, S. *Cancer Treat. Rev.* **2014**, *40*, 307.
- (23) Perillo, N. L.; Marcus, M. E.; Baum, L. G. *J. Mol. Med.* **1998**, *76*, 402.

- (24) Dalotto-Moreno, T.; Croci, D. O.; Cerliani, J. P.; Martinez-Allo, V. C.; Dergan-Dylon, S.; Méndez-Huergo, S. P.; Stupirski, J. C.; Mazal, D.; Osinaga, E.; Toscano, M. A.; Sundblad, V.; Rabinovich, G. A.; Salatino, M. *Cancer Res.* **2013**, *73*, 1107.
- (25) Pereira, P. M. R.; Silva, S.; Cavaleiro, J. A. S.; Ribeiro, C. A. F.; Tomé, J. P. C.; Fernandes, R. *PLoS one* **2014**, *9*, e95529.

Publications and presentations

Publications

“Metallic nanoparticles for targeted delivery of photosensitisers for photodynamic therapy” Paula García Calavia and David A. Russell, in *“Photodynamic Medicine: from bench to clinic”*, ed. H. Kostron and T. Hasan, Royal Society of Chemistry, Chapter 7, pp.113-135 (2016).

“Metal-enhanced fluorescence and antibody targeting for photodynamic therapy of breast adenocarcinoma cells” Paula García Calavia, María J. Marín, Isabelle Chambrier, Michael J. Cook and David A. Russell. Manuscript in preparation.

“Targeted photodynamic therapy of breast adenocarcinoma cells using lactose-phthalocyanine gold nanoparticle conjugates” Paula García Calavia, Isabelle Chambrier, Michael J. Cook and David A. Russell. Manuscript in preparation.

“Photosensitiser functionalised luminescent upconverting nanoparticles for photodynamic therapy” Markus Buchner, María J. Marín, Paula García Calavia, Verena Muhr, Antje Baeumner, David A. Russell and Thomas Hirsch. Manuscript in preparation.

Oral presentations

“Phthalocyanine-gold nanoparticle conjugates for photodynamic cancer therapy” Paula García Calavia, María J. Marín, Isabelle Chambrier, Michael J. Cook and David A. Russell, **School of Chemistry – Annual Research Colloquium**, University of East Anglia, Norwich, UK. September 2016.

“Nanoparticles for photodynamic therapy of cancer” Paula García Calavia, María J. Marín, Isabelle Chambrier, Michael J. Cook and David A. Russell, **COST meeting of Workgroup 4 (Assays, Sensors and Imaging) part of The European Upconversion Network COST Action CM1403**, Regensburg, Germany. October 2015.

Poster presentations

“Zinc phthalocyanine functionalised gold nanoparticles for photodynamic cancer therapy” Paula García Calavia, María J. Marín, Isabelle Chambrier, Michael J. Cook and David A. Russell, **38th Meeting of the ASP, American Society for Photobiology**, Tampa, FL, USA. May 2016.

"Phthalocyanine gold nanoparticle conjugates for photodynamic therapy of cancer"
Paula García Calavia, María J. Marín, Isabelle Chambrier, Michael J. Cook and David A. Russell, **16th ESP Congress, European Society for Photobiology**, Aveiro, Portugal. September 2015.

"Fighting breast cancer with red light and gold" Paula García Calavia, **UEA in the city – A festival of student research**, The Forum, Norwich, UK. June 2015.

"Phthalocyanine gold nanoparticle conjugates for photodynamic therapy of cancer"
Paula García Calavia, María J. Marín, Isabelle Chambrier, Michael J. Cook and David A. Russell, **School of Chemistry – Annual Research Colloquium**, University of East Anglia, Norwich, UK. September 2015.

"Photosensitiser gold nanoparticle conjugated for photodynamic therapy of cancer"
Paula García Calavia, María J. Marín, Isabelle Chambrier, Michael J. Cook and David A. Russell, **School of Chemistry – Annual Research Colloquium**, University of East Anglia, Norwich, UK. September 2014.

"Photosensitiser gold nanoparticles for photodynamic therapy of cancer" Paula García Calavia, María J. Marín, Isabelle Chambrier, Michael J. Cook and David A. Russell, **ESP Photobiology School, European Society for Photobiology**, Brixen/Bressanone, Italy. June 2014.